AD-A178 590 NEW METHODS FOR OBTAINING SCATTERING AND ABSORPTION FROM TROPOSPHERIC VIS... (U) VIZ ABILITY CORVALLIS OR J I GORDON 28 FEB 87 VA187-1 ARO-21655.8-GS-S 1/2

UNCLASSIFIED DAAG29-84-C-0014 F/G 20/6 NL

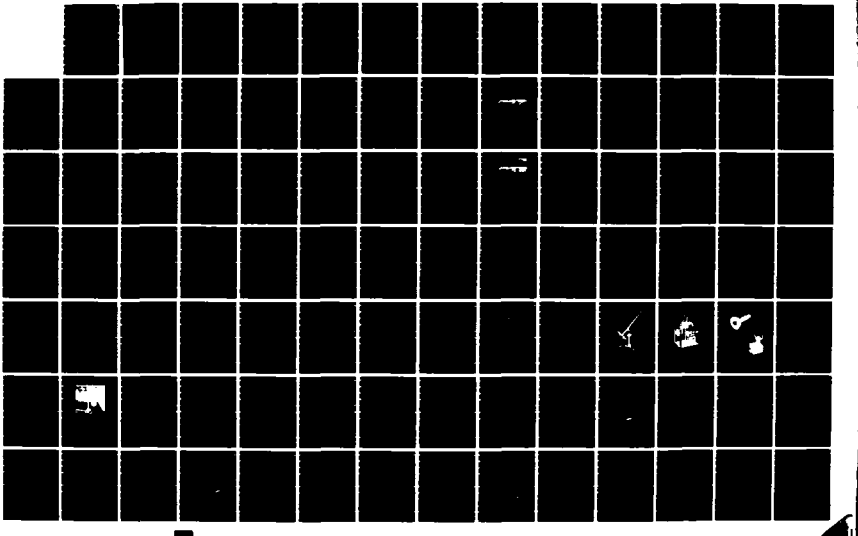

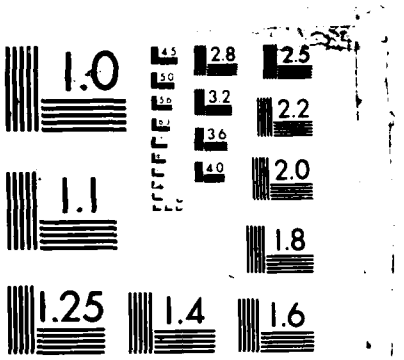

ARO 21655.8-GS-S

VAI87-1

(2)

New Methods for Obtaining Scattering and Absorption from Tropospheric Visible Spectrum Data

Final Report

By

Jacqueline I. Gordon

February 28, 1987

U.S. Army Research Office

Contract: DAAG29-84-C-0014

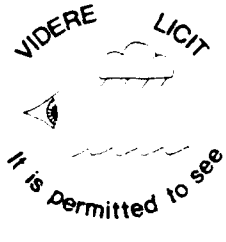

Viz. Ability, Inc.

2941 Ashwood Dr.

Corvallis, OR. 97330-1255

The view, opinions, and/or findings contained in this report are those of the author(s) and should not be construed as an official department of the army position, policy, or decision, unless so designated by other documentation.

UNCLASSIFIED

SECURITY CLASSIFICATION OF THIS PAGE (When Data Entered)

REPORT DOCUMENTATION PAGE		READ INSTRUCTIONS BEFORE COMPLETING FORM
1. REPORT NUMBER ARO 21655.8-GS-S	2. GOVT ACCESSION NO.	3. RECIPIENT'S CATALOG NUMBER
4. TITLE (and Subtitle) NEW METHODS FOR OBTAINING SCATTERING AND ABSORPTION FROM TROPOSPHERIC VISIBLE SPECTRUM DATA		5. TYPE OF REPORT & PERIOD COVERED Final Report 1 Jul 84 - 31 Dec 86 6. PERFORMING ORG. REPORT NUMBER
7. AUTHOR(s) Jacqueline I. Gordon		8. CONTRACT OR GRANT NUMBER(s) DAAG29-84-C-0014
9. PERFORMING ORGANIZATION NAME AND ADDRESS Viz. Ability, Inc. Code IY540 2941 NW Ashwood Dr. Corvallis, OR 97330-1255		10. PROGRAM ELEMENT, PROJECT, TASK AREA & WORK UNIT NUMBERS
11. CONTROLLING OFFICE NAME AND ADDRESS U. S. Army Research Office Post Office Box 12211 Research Triangle Park, NC 27709		12. REPORT DATE February 28,1987 13. NUMBER OF PAGES 156
14. MONITORING AGENCY NAME & ADDRESS(if different from Controlling Office)		15. SECURITY CLASS. (of this report) Unclassified 15a. DECLASSIFICATION/DOWNGRADING SCHEDULE

16. DISTRIBUTION STATEMENT (of this Report)

Approved for public release; distribution unlimited.

17. DISTRIBUTION STATEMENT (of the abstract entered in Block 20, if different from Report)

NA

18. SUPPLEMENTARY NOTES

The view, opinions, and/or findings contained in this report are those of the author(s) and should not be construed as an official Department of the Army position, policy, or decision, unless so designated by other documentation.

19. KEY WORDS (Continue on reverse side if necessary and identify by block number)

scattering
absorption
visible spectrum
troposphere

20. ABSTRACT (Continue on reverse side if necessary and identify by block number)

This is the final report of Contract DAAG29-84-C-0014. This work was carried out over a two and one half year period, resulting in successful completion of the proposed work and seven articles.

During the contract period, new methods for obtaining absorption, aerosol and total scattering optical thickness, and single scattering albedo from tropospheric visible spectrum data were published and then used on two extant sets of tropospheric optical data in the visible spectrum. One ground-based set of measurements predated heavy atmospheric pollution. The other set of

DD FORM 1 JAN 73 1473 EDITION OF 1 NOV 65 IS OBSOLETE

UNCLASSIFIED

SECURITY CLASSIFICATION OF THIS PAGE (When Data Entered)

20. ABSTRACT CONTINUED

airborne measurements was from a metropolitan area containing pollution sources.

Application of the methods to these data sets further developed the methods, provided substantial examples of their use, served to update the data, and provided a means to access all the atmospheric optical data measured prior to 1976 by the Visibility Laboratory, University of California at San Diego. A significant finding was that the aerosol scattering optical thickness of the total atmosphere or of separate haze layers can be described by a modified Angstrom equation in which the constant is a function of the power of the wavelength.

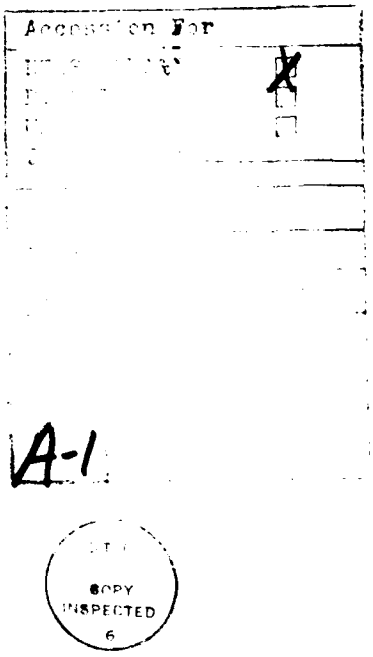

TABLE OF CONTENTS

TABLE OF CONTENTS (continued)

New methods for obtaining scattering and absorption from tropospheric visible spectrum data.

by

Jacqueline I. Gordon

ABSTRACT

This is the final report of Contract DAAG29-84-C-0014. This work was carried out over a two and one half year period, resulting in successful completion of the proposed work and seven articles.

During the contract period, new methods for obtaining absorption, aerosol and total scattering optical thickness, and single scattering albedo from tropospheric visible spectrum data were published and then used on two extant sets of tropospheric optical data in the visible spectrum. One ground-based set of measurements predated heavy atmospheric pollution. The other set of airborne measurements was from a metropolitan area containing pollution sources.

Application of the methods to these data sets further developed the methods, provided substantial examples of their use, served to update the data, and provided a means to access all the atmospheric optical data measured prior to 1976 by the Visibility Laboratory, University of California at San Diego. A significant finding was that the aerosol scattering optical thickness of the total atmosphere or of separate haze layers can be described by a modified Angstrom equation in which the constant is a function of the power of the wavelength.

1. STATEMENT OF PROBLEM

The word aerosol is used herein to describe the liquid and/or solid particulates exclusive of the gas phase in which they are embedded. This is consistent with Prospero, et al. (1983).

1.1 Technical Problem

New methods for obtaining scattering and absorption from atmospheric visible spectrum data were to be used on two data sets (the sets are described in detail in Appendices F and G). These data sets belong to a larger body of atmospheric optical data at the Visibility Laboratory, University of California, San Diego, measured prior to 1976. The large tropospheric optical data bank was taken primarily under the aegis of the Air Force Geophysics Laboratory. All the data were in a binary format no longer in use, and stored on unmaintained, 7-track magnetic tapes. In the process of using these two data sets a procedure was to be developed providing ready access to this large body of atmospheric data.

The plan was to use the Cyber at Oregon State University to read the data from the 7-track tapes, translate the data to ASCII, and transfer it directly to the STRIDE computer at Viz. Ability, Inc. Obstacles included the inability to directly connect the two computers and unacceptable telephone data transfer rates. The solution required the development of a 9-track tape drive system for the STRIDE computer (none was previously available). These unexpected obstacles resulted in a portion of the no-cost extension to the contract

period.

These data sets are unique in character and over the years have been extremely useful for checking analytical methods, theories and modeling. Developing the program for translating the binary tape, transferring the data to 9-track tapes, and using ASCII format, insured the continuing accessibility of a large optical data bank.

1.2 Scientific Problem

Scattering and absorption in the visible

Modelers tend to use AFGL's Program LOWTRAN [Kneizys, et al. (1980)] to specify the absorption for broad band spectrum problems. LOWTRAN neglects absorption for the visible except for the ozone Chappuis bands. Comparison of space-to-earth total radiance transmittance values to scattering transmittance values [Johnson and Gordon (1982) and Gordon and Johnson (1984)] indicated that this was probably true for the spectrum below 550 nm but not above, although the absorption was not large. This was borne out by Tashenov (1970) although he did not interpret his results in this manner. It was proposed to obtain atmospheric absorption for passbands in the visible and to check whether the absorption is related to the overall total transmittance or whether it is relatively constant.

Seven new methods

A technical report [Gordon (1982)] by the principal investigator contained the theoretical bases for several innovative methods for obtaining scattering and absorption optical thickness from atmospheric visible spectrum data. We proposed publishing three articles on the scattering and absorption methods (Appendices B, C and D). We also proposed further developing and testing those methods (Appendices F and G).

To further develop and test these methods, they were applied to two data sets. Both data sets had been processed to the point that all measurements were in calibrated radiometric form. Both had sky scanner data with full 2π sky radiance coverage using a 5 degree resolution, neither contained values of total, absorption, scattering, aerosol absorption, or aerosol scattering optical thicknesses. The objective was to specify in detail the separate roles of absorption, emission and scattering as they relate to the troposphere and the total atmosphere in the visible and near-infrared.

Four of the new methods were: aerosol optical thickness from solar almucantar radiances, scattering from sky radiance ratios, absorption optical thickness from net flux, and the critical scattering angle for radiometer error. These will be further explained in the results section.

Equation of transfer for scalar irradiance. Reviewers discovered an error in the equation of transfer for scalar irradiance. This was corrected and an analysis of the equation made using the model atmosphere from Gordon (1969). This corrected equation (Eq. 35 Appendix D) proved too complicated to

be easily used for the recovery of absorption optical thickness. Therefore it was not used as planned with the second data set.

Near-sun error correction. Both data sets also included an error in the sky radiances near the sun. For data set one, we proposed correcting the sky radiance data from the scanner and then comparing the resulting sky irradiance plus sun irradiance from the transmissometer to the total irradiance from the irradiometer. This analysis indicated the comparisons depended on the calibration period of the respective measurements. This was indicative of inter-instrumental calibration differences rather than a faulty correction method. The analysis on the first data set was not included in the submitted article (Appendix F), as it seemed extraneous. The correction method (given in detail in Appendix G) was also used on the second data set.

Single scattering albedo from horizon sky. We also proposed using a single scattering albedo method [Eq. 52, Appendix B based on work by Roessler and Faxfog (1981)] on the second data set. The 5° field of view of the scanner necessitated the use of a measurement at 87.5° rather than at 90°. This would have added an additional approximation to the method and would have meant that the single scattering albedo would apply to the entire atmosphere above the sensor, rather than to the altitude of measurement. Instead, another means of determining single scattering albedo within the haze layers was employed as is reported in Appendix G. The single scattering albedo method as given in Eq. 52 of Appendix B, should be applied to horizontal measurements with a smaller field of view, under conditions whereby a cloud free field of view can be verified. Neither of these conditions existed in data set two.

2. SUMMARY OF IMPORTANT RESULTS

The notation used is that adopted by the Visibility Laboratory as explained in Duntley, et al. (1957). It has been modified to correspond to the Optical Society of America recommendations in Sec. 1 of Driscoll and Vaughan (1978). An explanation of the specific symbols used in the body of this report are contained in a glossary in Sec. 6.

2.1 Development and Testing of New Methods

In order to get the maximum amount of information on the methods themselves, the first data set was restricted to those data obtained on optically stable days. In this way, a number of values could be obtained of a single constant quantity and standard deviations from the average value obtained as a measure of the precision of the method.

We discussed three of the methods: near-sun error correction, single scattering albedo from horizon sky, and the equation of transfer for scalar irradiance in the statement of problem section. We will now discuss the remaining four methods.

Aerosol optical thickness from solar almucantar radiances

The aerosol optical thickness can be obtained from solar almucantar

radiances at 55° and 125° scattering angle β from the sun by means of (Eqs. 17 and 44, Appendix C)

$$_{M}t_{\infty}(z)=4\pi[L^{*}_{\infty}(z,\theta_{s},55°\beta)-L^{*}_{\infty}(z,\theta_{s},125°\beta)/{}_{s}\varepsilon(z)m(\theta_{s}). \quad (1)$$

An explanation of the notation used in Eq. 1 is given in the glossary in Sec. 6. The theoretical development of the equation is given in Appendix C. Equation 1 is an abbreviated version of the method of Livshits and Pavlov (1970).

This method was tested (as reported in Appendix F) using the first data set with the sun scalar irradiance based on the Langley determination of the total optical thickness for the day. The aerosol optical thickness was found to be highly dependent on the accuracy or absolute calibration of the sky radiance values. When the absolute calibration was verifiable, the STD of the aerosol optical thickness was 0.0072. Comparison to the total scattering optical thickness from sky radiance ratios can be used as one test for the adequacy of the absolute calibration of the radiometer.

Scattering from sky radiance ratios

When the nephelometer data are graphed in the form of the ratio $\mathcal{Q}(z,\beta)$ (measured to Rayleigh volume scattering function) as a function of the optical scattering mixing ratio Q(z) (measured total to Rayleigh volume scattering coefficient), simple relationships emerge for each scattering angle. See Figs. 4 and 5 in Appendix B. All visible spectrum broad band measurements at all altitudes in the troposphere (based on ground-based to 6 km measurements) measured all over the world between 1968 and 1980 result in these predictable relationships. These relationships are derivable from the Barteneva (1960) catalog of proportional volume scattering functions. This is a tremendous simplification for modelers of the radiation field and of contrast transmittance. The Hering (1984) model for predicting contrast, contrast transmittance and sky radiance makes use of this simplification.

The method for obtaining scattering from sky radiance ratios is based on the above simplification and the Barteneva catalog of proportional volume scattering functions. The total scattering optical thickness can be obtained by means of the ratio of sky radiances measured at 55° scattering angle from the sun at two zenith angles (Eqs. 60 and 61, Appendix B)

$$L^{*}_{\infty}(z,\theta,55°\beta)/L^{*}_{\infty}(z,\theta',55°\beta)=[1-\exp(-{}_{s}t_{\infty}(z)m(\theta_{s})]/[1-\exp(-{}_{s}t_{\infty}(z)m(\theta'_{s})]. \quad (2)$$

The theoretical development of this equation is detailed in Appendix B. This is a further development of the nomographic method of Kushpil' and Petrova (1971).

This method was tested using the first data set. It was found to be accurate but not precise. The standard deviation (STD) of the total scattering optical thickness being 0.0269 as noted in Appendix F. Since the radiances are used in a ratio, absolute calibration errors are factored out but precision errors, and approximation errors due to the use of 55° β remain.

Absorption optical thickness

The absorption optical thickness for the visible spectrum can be obtained

by (Eq. 47, Appendix D)

$$_{a}t_{\Delta z}(z)=[\xi(z_o)-\xi(z)]/\overline{\varepsilon(z)}. \quad (3)$$

The theoretical development of this equation is given in Appendix D. It was based on a review of Duntley, et al. (1957), Chandrasekhar (1960), and Preisendorfer (1976).

Successful use of Eq. (3) requires optical stability during the time of measurement at two altitudes. The use of Eq. 3 was successfully tested on data set two and reported in Appendix G.

Critical scattering angle for radiometer error

When a day is optically stable it is possible to use solar almucantar values to determine the critical scattering angle from the sun β within which sky radiance measurements contain spurious sun reflections. This is an inversion of a method used by Pyaskovskaya-Fesenkova (1970) for checking for optical stability. This method is described in detail in Appendix C. It was further tested and used on data set one, determining in this case that the radiances closer than 15°β had consistent errors. This is described in detail in Appendix F. The method yielded consistent results regardless of the passband used.

2.2 Unproposed Material

The contract enabled the publication of one article (Appendix A) which had been written prior to the contract. A no-cost extension of the original two year contract period provided time for the writing and presentation of two unproposed papers, inclusion of additional unproposed material in another article (Appendix B) and the publication of one of the additional papers (Appendix E). One of the additional papers which concerned daytime visibility and was presented at a meeting of the Optical Society of America, October 1986, was rejected for publication. Because it has not yet been rewritten for submission, it has not been included in the appendices.

Appendix A

The equilibrium radiance model in Gordon (1969), which assumes constancy in the source function along the path of sight, predicts equilibrium radiance as a function of the angle from the sun. Measurements made at all altitudes in the troposphere of cloudless sky radiance in the visible spectrum consistently support this prediction. As a result, sky radiances can be used to obtain (1) vertical space-to-sensor scattering transmittance, (2) equilibrium radiance, and (3) path radiance through the atmosphere and in the troposphere. Comparisons are made of the constant equilibrium radiance model predictions of sky radiance, irradiance, and equilibrium, radiance to (1) other models for the Rayleigh atmophere, and (2) to measurements in the troposphere for thin atmospheres. The agreements are good.

Appendix B

Appendix B included equations derived for relating the integrating nephelometer measurements to the total volume scattering coefficient and the

volume scattering functions at 30° and 150°. These equations take into consideration the effects of non-uniformity of the light beam over the cross sectional area, variations from true cosine acceptance of the irradiometer, and truncation of the optical integration near scattering angles 0° and 180°. Although in use for some time, this material had never been published.

Appendix E

Appendix E was written as an invited paper for an international symposium on atmospheric transparency for sattelite applications held in Capri, Italy in September 1986. The bulk of the data for this paper came from the data set described in Appendix F.

Three data sets were presented. They ranged from data taken during the early development of the earth-to-space method to data taken to provide ground truth for remotely sensed measurements. Although these data were primarily measured to provide ground truth for specific remote sensing projects, they provide a sufficiently large data base with which to evaluate the expected range of variables as a function of solar zenith angle, wavelength, and over a number of seasons. Values were presented for vertical downward path reflectance, but they can be made applicable to downward slant paths of sight by means of a correction factor (a function of the radiance transmittance and slant path angle).

Path radiance is the radiance scattered into the path of sight from all 4π directions. This radiance is not generally the same in both directions along the same path, however, a method [Gordon, et al. (1973)] is available whereby the path radiance from earth to space can be predicted from ground-based measurements. Path reflectance combines the effects of path radiance, downwelling irradiance and radiance transmittance. An equation to determine apparent object reflectance was derived which relates the path reflectance to the masking effect of the veiling light scattered into the path of sight for any inherent object reflectance.

Path reflectance takes into consideration two concerns of atmospheric transparency determination: the loss of image forming light, and the veiling effect of scattered light. It is a convenient an powerful way of expressing both the loss and gain for the image forming signal.

2.3 Investigation Results

Our objective was to specify in detail the separate roles of absorption, emission and scattering as they relate to the atmosphere in the visible and near-infrared windows. Since the data were for the visible and very-near infrared, emission is negligible (see p. 275, Appendix D).

Hitherto, there has been no means of separating anything but Rayleigh scattering and ozone absorption from the total optical thickness in the broad passbands for the total atmosphere. In the past, very narrow pass bands were selected in order to hit windows where gas phase absorption bands could be avoided, in an attempt to isolate the total aerosol effect.

The first data set was taken at the Visibility Laboratory which is

situated on a point of land surrounded on 3 sides by water (the ocean and San Diego Bay) and somewhat removed from the city with its ever constant automobile exhausts. It was also measured at a time before heavy population buildup added to the local pollution. By restricting the analysis to optically stable days, the airmass tended to be continental, during Satanas or devil days. The second data set was deliberately chosen to represent measurements in a rather polluted atmosphere. Thus, we obtained a measure of the importance of the many small absorption bands above 550 nm for low concentration gases in the atmosphere using one data set and a measure of the absorption from gaseous and/or particulate pollution sources from the second data set.

For data set one, the combined measurements from a solar transmissometer and sky scanner allow the isolation of aerosol scattering and absorption optical thickness in the visible portion of the spectrum. With this combination one can obtain values for broad or narrow passbands, within or not within absorption windows. With an accurate value for aerosol scattering optical thickness available, the optical scattering mixing ratio and single scattering albedo help detail the state of the atmosphere.

Absorption

Actual values of absorption optical thickness for through the atmosphere (first data set) and for the primary and secondary haze layers (second data set) were obtained, a unique accomplishment.

The absorption recovery technique used in the second data set is limited to the visible spectrum or shorter wavelengths but may be used for broad or narrow passbands. Longer wavelengths require an emission term (see Eq. 46, Appendix D). The equations do not require an unobscured sun, only that the data from the two altitudes be consistent (that is, as if they had been measured simultaneously). One of the checks used was to compare the results by mean wavelength of the filter. Another was to compare the results for the total path and the path increments.

Each of the two data sets chosen included one passband below 550 nm, one above 550 nm and one photopic or near photopic. The photopic is such a broad passband it was hard to predict gaseous absorption without some direct measurements.

Gaseous absorption in the visible. The visible portion of the spectrum contains significant gaseous absorption due to continua. Not only is the Chappuis ozone continuum significant but the nitrogen dioxide continuum affects wavelengths from 300 to 550 nm according to Shaw (1976). In addition O_2 and water vapor have absorption bands in the visible and very near infrared which cannot be ignored as shown by King, et al. (1980) and as described in Appendix F.

Aerosol absorption optical thickness. In attempting to recover aerosol absorption, all the sources of gaseous absorption must be taken into account or bypassed, in the case of the band absorptions, by judicious selection of narrow passbands for the sensors. The aerosol single scattering albedo is a ratio important for understanding the effect of the aerosol

absorption relative to the total aerosol optical thickness.

In Appendix F (data set one) we found that aerosol absorption can be significant even on days of greater transparency than the average clear day. For the data for optically stable days, one could not predict the presence or absence of aerosol absorption on the basis of total optical thickness.

For the second data set (urban pollution), we were able to obtain a reasonable value of aerosol absorption for the secondary haze layer but not for the primary haze layer (Appendix G). Further knowledge of the types and amounts of polluting gases present would be needed to obtain an aerosol absorption value for the primary layer. Use of judiciously selected narrow passbands would aid in the identification of these gases and consequent isolation of the aerosol absorption optical thickness.

Aerosol scattering optical thickness

When aerosol scattering optical thickness is separated from the aerosol absorption, a modified Angstrom equation describes the data well

$$_{M}t_{\Delta z}(z)=\ln B' + c'\ln\lambda. \quad (4)$$

Not only that but the constant $\ln B'$ is a linear function of the slope c'

$$\ln B' = b + mc'. \quad (5)$$

This relationship only becomes apparent when the scattering and absorption of aerosols are separated. The relationship in the classical Angstrom (1929) equation, which relates the total aerosol optical thickness to wavelength, is distorted by the inclusion of the aerosol absorption optical thickness.

All the data from the two data sets fit these equations resulting in a single set of constants, $b=-3.243$ and $m=-7.108$ where the wavelength λ is in nm. See Fig. 2 in Appendix G. This applies to the complete visible spectrum 400 to 700 nm. The data are from cases of clearer than the average clear day to heavy urban pollution.

An alternate form of the Angstrom equation was developed (Eq. 10, Appendix G)

$$c' = (\ln {}_{M}t_{\Delta z}(z) - b)/(m + \ln\lambda), \quad (6)$$

where b and m are invariant. Thus a measurement of aerosol scattering optical thickness at one wavelength will predict the slope c' and allow a prediction of aerosol scattering optical thickness at other wavelengths.

The two data sets together encompass a large range of optical thickness and appear to define a relationship which is invariant whether the aerosol scattering optical thicknesses are for the entire atmosphere or for a haze layer or two. The methods of measuring the optical thicknesses for the two data sets are completely different. Both were visible spectrum data sets but employed different instruments, passbands and data collection procedures. The passbands used are not equivalent although they encompass about the same portion of the visible spectrum. The data are limited to passbands with mean

wavelengths between 459 and 664 nm but the results should apply to the entire visible spectrum 400 to 700 nm.

It is important to check these results further on additional data with particular emphasis on dust, smoke and aerosols with salt nuclei to see how general this relationship is.

3. PUBLICATIONS AND SCIENTIFIC PERSONNEL

3.1 List of Publications

J. I. Gordon and R. W. Johnson, "Equilibrium radiance model applications and comparisons to atmospheric measurements and Rayleigh models," Applied Optics 23, 3363-3372 (1984). See Appendix A.

J. I. Gordon and R. W. Johnson, "Integrating nephelometer: theory and implications," Applied Optics 24, 2721-2730 (1985). See Appendix B. Presented at the meeting of the Optical Society of America, October 1986.

J. I. Gordon, "New uses for the solar almucantar," Applied Optics 24, 3381-3389 (1985). See Appendix C.

J. I. Gordon, "Some implications of the equation of transfer," Journal of the Optical Society of America A 3, 274-283 (1986). See Appendix D. Presented as a poster paper at the meeting of the American Geophysical Union, December 1986.

J. I. Gordon and R.W. Johnson, "Equilibrium or path reflectance method of measuring atmospheric transparency in the visible and near infrared from ground stations: theory, instrumentation, data and applications," to be published in Proceedings of International Meeting on Atmospheric Transparency for Sattelite Applications, Capri, Italy, September 1986. See Appendix E. Presented as an invited paper at the international meeting, September 1986.

J. I. Gordon, "Aerosol scattering and absorption optical thickness I. From ground-based measurements during optically stable clear days," resubmitted to Applied Optics on 12 February 1987. See Appendix F. Presented at the International Meeting on Atmospheric Transparency for Sattelite Applications, Capri, Italy, September 1986.

J. I. Gordon, "Aerosol scattering and absorption optical thickness II. From airborne measurements in a pollutted atmosphere," submitted to Applied Optics on 12 February 1987. See Appendix G.

3.2 Scientific Personnel

Jacqueline I. Gordon
Viz. Ability, Inc., CODE IY 540
2941 NW Ashwood Drive
Corvallis, OR 97330-1255

4. ACKNOWLEDGMENTS

I wish to thank Judith Olson for technical writing and editing assistance.

I also wish to thank R. W. Johnson and the Visibility Laboratory, University of California at San Diego, for making the two data bases, early technical notes, pictures and sketches available for the writing of the methods and data analyses. The original data were collected by the Visibility Laboratory primarily for the U. S. Air Force Geophysics Laboratory.

I also wish to thank D. Fuhrer, Oregon State University, for programs to translate the binary data from an obsolete computer into useable form.

5. BIBLIOGRAPHY

Angstrom, A. (1929), "On the atmospheric transmission of sun radiation and on dust in the air," Geogr. Ann., 11, 156-166.

Barteneva, O. D. (1960), "Scattering functions of light in the atmospheric boundary layer", Bull. Acad. Sci. U.S.S.R., Geophys. Ser. (English edition translated by AGU) No. 12, 1237-1244.

Chandrasekhar, S. (1960), Radiative Transfer, (Dover Publ Inc., New York).

Driscoll, W. G. and W. Vaughan (1978), Eds., Handbook of Optics (McGraw-Hill, New York).

Duntley, S. Q., A. R. Boileau and R. W. Preisendorfer (1957), "Image transmission by the troposphere I," J. Opt. Soc. Am. 47, 499-506.

Gordon, J. I. (1969), "Model for a clear atmosphere," J. Opt. Soc. Am. 59, 14-18.

Gordon, J. I., J. L. Harris, Sr., and S. Q. Duntley (1973), "Measuring earth-to-space contrast transmittance from ground stations," Appl. Opt. 12, 1317-1324.

Gordon, J. I. (1982), "Implications of the equation of transfer within the visible and infrared spectrum," Scripps Institution of Oceanography, Visibility Laboratory, SIO Ref. 83-10, AFGL-TR-82-0223, NTIS No. ADA 133 979.

Gordon, J. I. and R. W. Johnson (1984), "Equilibrium radiance model applications and comparisons to atmospheric measurements and Rayleigh models," Appl. Opt. 23, 3363-3372.

Hering, W. S. (1984), "The FASCAT model performance under francional cloud conditions and related studies," Scripps Institution of Oceanography, Visibility Laboratory, SIO Ref. 85-7, AFGL-TR-84-0168.

Johnson, R. W. and J. I. Gordon (1982), "A review of optical data analysis related to the modelling of visible and optical infrared atmospheric

properties," Scripps Institution of Oceanography, Visibility Laboratory, SIO Ref. 83-5, AFGL-TR-82-0086, NTIS No. ADA 131 486.

King, M. D., D. M. Byrne, J. A. Reagan, and B. M. Herman (1980), "Spectral variation of optical depth at Tucson, Arizona between August 1975 and December 1977," J. Appl. Meteorol. 19, 723-732.

Kneizys, F. X., E. P. Shettle, W. O. Gallery, J. H. Chetwynd, Jr., L. W. Abrew, J. E. A. Selby, R. W. Fenn and R. W. McClatchey (1980), "Atmospheric transmittance/radiance: computer code LOWTRAN 5," Air Force Geophysics Laboratory, Hanscom AFB, Mass., AFGL-TR-80-0067.

Kushpil', V. I. and L. F. Petrova (1971), "Determination of the atmospheric transmittance from sky brightness distribution", Sov. J. Opt. Technol. 38, No. 4, 191-193.

Livshits, G. Sh. and V. E. Pavlov (1970), "Atmospheric transmittance and the interrelationships of certain optical parameters", in Atmospheric Optics, Nikolai B. Divari, Ed., translated by S. B. Dresner (Plenum, New York), pp. 53-56.

Preisendorfer, R. W. (1976), Hydrological Optics, (Environmental Research Laboratories, National Oceanicand Atmospheric Administration, U. S. Department of Commerce, Honolulu, Hawaii) Vols. I and II.

Prospero, J. M., R. J. Charlson, V. Mohnen, R. Jaenicke, A. C. Delany, J. Moyers, W. Zoller, and K. Rahn (1983), "The atmospheric aerosol system: an overview," Rev. Geophys. Space Phys. 21, 1607-1629.

Pyaskovskaya-Fesenkova, E. V. (1970), "Determining the transmission coefficient and degree of optical stability of the earth's atmosphere", in Atmospheric Optics, Nikolai B. Divari, Ed., translated by S. B. Dresner (Plenum, New York), pp. 151-156.

Roessler, D. M. and F. R. Faxvog (1981), "Visibility in absorbing aerosols", Atmos. Environ. 15, 151-155.

Shaw, G. E. (1976), "Nitrogen dioxide-optical absorption in the visible," J. Geophys. Res. 81, 5791-5792 (1976).

Tashenov, B. J. (1970), "Spectrophotometric studies of atmospheric transmittance and stability," in Atmospheric Optics, Nikolai B. Divari, Ed., translated by S. B. Dresner (Plenum, New York, pp. 70-79.

6. GLOSSARY

$E(z,d)$	total downwelling irradiance on a flat horizontal plate
$E(z,u)$	upwelling irradiance on a flat horizontal plate
$L^{*}_{\infty}(z,\theta,\beta)$	sky radiance or path radiance from out-of-the atmosphere to the altitude z
$L^{*}_{\infty}(z,\theta_s,\beta)$	solar almucantar sky radiance at altitude z, sun zenith angle θ, and scattering angle β
$m(\theta)$	relative optical airmass at zenith angle θ
$Q(z)$	optical scattering mixing ratio $Q(z) = s(z)/_{R}s(z)$
$\mathcal{Q}(z,\beta)$	volume scattering function ratio $\mathcal{Q}(z,\beta) = \sigma(z,\beta)/_{R}\sigma(z,\beta)$
$s(z)$	total volume scattering coefficient
$_{R}s(z)$	Rayleigh volume scattering coefficient
$_{a}t_{\Delta z}(z)$	absorption optical thickness for altitude increment Δz above altitude z
$_{M}t_{\infty}(z)$	aerosol scattering optical thickness from out-of-the atmosphere to altitude z
$_{M}t_{\Delta z}(z)$	aerosol scattering optical thickness for altitude increment Δz above altitude z
$_{s}t_{\infty}(z)$	scattering optical thickness from out-of-the atmosphere to altitude z
z	altitude
β	scattering angle
$_{s}\varepsilon(z)$	sun scalar irradiance at altitude z (irradiance unweighted by cosine of sun zenith angle)
$\overline{\varepsilon(z)}$	average total scalar irradiance in altitude increment above altitude z
$\xi(z)$	net irradiance, $\xi(z) = E(z,d)-E(z,u)$
θ	zenith angle
θ_s	sun zenith angle
λ	wavelength
$\sigma(z,\beta)$	volume scattering function at altitude z and scattering angle β
$_{R}\sigma(z,\beta)$	Rayleigh volume scattering function
$\emptyset$	azimuth

Reprinted from Applied Optics, Vol. 23, page 3363, October 1, 1984

Equilibrium radiance model applications and comparisons to atmospheric measurements and Rayleigh models

Jacqueline I. Gordon and Richard W. Johnson

Appendix A

The equilibrium radiance model, which assumes constancy in the source function along the path of sight, predicts equilibrium radiance as a function of the angle from the sun. Measurements made at all altitudes in the troposphere of cloudless sky radiance in the visible spectrum consistently support this prediction. As a result, sky radiances can be used to obtain (1) vertical space-to-sensor scattering transmittance, (2) equilibrium radiance, and (3) path radiance through the atmosphere and in the troposphere. Comparisons are made of the constant equilibrium radiance model predictions of sky radiance, irradiance, and equilibrium radiance to (1) other models for the Rayleigh atmosphere, and (2) to measurements in the troposphere for thin atmospheres. The agreements are good.

I. Introduction

A constant equilibrium radiance (source function) model of a cloud-free atmosphere for use in the visible spectrum was presented earlier.[1] It is based on two assumptions: (1) that the equilibrium radiance is constant along the path of sight, and (2) absorption is negligible. The scattering, however, is not assumed to be isotropic. There are other, more precise models for the atmosphere,[2,3] but the value of the equilibrium radiance model is that it leads to useful methods for obtaining scattering transmittance, equilibrium radiance, and path radiance from sky radiances. It also provides an equation for a simple fast prediction of irradiance, sky radiance, and equilibrium radiance.

The purpose of this article is to summarize work to date using the equilibrium radiance model equations in relation to measurements of optical properties of the atmosphere by the Visibility Laboratory. This has hitherto only been available in unrefereed reports. The notation used is that adopted by the Visibility Laboratory[4] and modified to correspond to OSA recommendations in Sect. 1 of Driscoll and Vaughan.[5]

Jacqueline Gordon is with Viz. Ability, 2941 NW Ashwood Drive, Corvallis, Oregon 97330, and R. W. Johnson is with University of California at San Diego, Visibility Laboratory, San Diego, California 92093.

Received 14 November 1983.
0003-6935/84/193363-10$02.00/0.

An important facet of the equilibrium radiance model is that the path radiance (light scattered into the path of sight that reaches the sensor) and hence sky radiance (path radiance for paths of sight from the boundary of the atmosphere to the sensor) are a function of the equilibrium radiance and the radiance transmittance of the path. The consistency of the resulting equation with various aspects of the real atmosphere will be reviewed.

Predictions using the model equations will be compared to the results from other models for the photopic Rayleigh atmosphere. Similar computations for the non-Rayleigh atmosphere using normalized volume scattering functions from Barteneva[6] will then be compared to atmospheric measurements.

Predictions have been made for a full range of sun zenith angles and ground albedos for the following ground level optical properties: equilibrium radiance and reflectance, sky radiance, downwelling irradiance and scalar irradiance (4π times the average intensity), vertical earth-to-space path radiance and reflectance, and path function. Only a small sample from these computations is presented here.

This concept of equilibrium radiance is a natural consequence of the equation of transfer [Eq. (10) Ref. 4]:

$$dL(z,\theta,\phi)/dr = -\alpha(z)L(z,\theta,\phi) + L_*(z,\theta,\phi). \quad (1)$$

This equation relates the incremental change in radiance $dL(z,\theta,\phi)$ at altitude z for the path of sight at zenith angle θ and azimuth ϕ, over the incremental path length dr to the attenuation (scattering plus absorption) coefficient $\alpha(z)$, the radiance $L(z,\theta,\phi)$, and the path function $L_*(z,\theta,\phi)$. The preceding equation applies to monochromatic radiation but can also be used in prac-

tice for certain broadband sensors in the visible spectrum. Equilibrium radiance $L_q(z,\theta,\phi)$ is defined as the radiance when $dL = 0$, therefore [Eq. (11) Ref. 4 and Eq. (40) Ref. 2]

$$L_q(z,\theta,\phi) = L_*(z,\theta,\phi)/\alpha(z). \tag{2}$$

Thus equilibrium radiance is equal to the source function,[2] a concept used earlier (but not named) by Barbier.[7]

Appendix A

II. Review of the Equilibrium Radiance Model

When the equilibrium radiance along a given path of sight is constant (first assumption), the equation of transfer can be integrated with the result that the path radiance (the scattered light which reaches the sensor) $L_r^*(z,\theta,\phi)$ is a function of the equilibrium radiance and the radiance transmittance [Eq. (11) Ref. 1]:

$$L_r^*(z,\theta,\phi) = L_q(z,\theta,\phi)[1 - T_r(z,\theta)]. \tag{3}$$

The subscript r refers to the path length. This equation applies to all paths of sight, upward or downward. The sky radiance $L_\infty^*(z,\theta,\phi)$ is the path radiance from the boundary of the atmosphere to the sensor pointed in an upward direction:

$$L_\infty^*(z,\theta,\phi) = L_q(z,\theta,\phi)[1 - T_\infty(z,\theta)]. \tag{4}$$

Figure 1 graphically depicts path function, path radiance, sky radiance, and equilibrium radiance.

The radiance transmittance is defined as

$$T_r(z,\theta) = \exp\left(-\int_0^r \alpha(z)dr\right), \tag{5}$$

where $\alpha(z)$ is the attenuation coefficient. Transmittance is expressed as a function of θ but not ϕ since the attenuation coefficient is assumed to be isotropic horizontally. The transmittance from space to sensor at zenith angle θ is a function of the vertical transmittance and the relative optical air mass $m_\infty(z,\theta)/m_\infty(z,0)$:

$$\begin{aligned}\ln[T_\infty(z,\theta)] &= [m_\infty(z,\theta)/m_\infty(z,0)]\ln[T_\infty(z,0)] \\ &= -[m_\infty(z,\theta)/m_\infty(z,0)]t.\end{aligned} \tag{6}$$

The optical thickness t is the negative of the natural log of the vertical transmittance. For the model calculations the relative air mass was computed using the equations froim Kasten.[8]

When there is no absorption (second assumption) the atmosphere is conservative, and the attenuation coefficient is equal to the scattering coefficient $s(z)$.

Given the above two assumptions an equation was developed for evaluating the equilibrium radiance from a knowledge of the sun scalar irradiance out of the atmosphere ${}_sE(\infty)$, the scalar albedo ${}_sA$ (upwelling scalar irradiance from the ground divided by the downwelling scalar irradiance), the normalized volume scattering function $\sigma(z,\beta)/s(z)$, the radiance transmittance from space to sensor and the sun zenith angle θ_s [Eq. (41) Ref. 1],

$$L_q(z,\theta,\phi) = {}_sE(\infty)T_\infty(z,\theta_s)\left[\sigma(z,\beta)/s(z) + {}_sA/(4\pi) + \frac{(1+{}_sA)\int_{2\pi}[\sigma(z,\beta)/s(z) + {}_sA/(4\pi)][1 - T_\infty(z,\theta)]d\Omega}{4\pi[1 - [(1+{}_sA)/(4\pi)]\int_{2\pi}[1 - T_\infty(z,\theta)]d\Omega]}\right]. \tag{7}$$

The first term in the braces is the direct scattering from the sun, this gives the directionality to the equilibrium radiance. The second term is the portion of the earth scalar irradiance due to the sun. The third term is the sky scalar irradiance and the reflectance from the earth of the light from the sky.

III. Aspects of the Real Atmosphere Well Represented by Eqs. (3) and (4) of the Equilibrium Radiance Model

For the model, the path radiance (and hence sky radiance) is a function of the equilibrium radiance and the radiance transmittance of the path, Eqs. (3) and (4). These equations are consistent with some aspects of the real atmosphere as described below.

A. Horizon Sky

In a cloud-free real atmosphere the radiance of the horizon sky is a function of the equilibrium radiance and the space-to-earth radiance transmittance [Ref. 9 Eq. (2.57)]:

$$L_\infty^*(z,90,\phi) = L_q(z,90,\phi)[1 - T_\infty(z,90)] \tag{8}$$

This is directly comparable with Eq. (4).

Ongoing work is establishing that when there is no absorption the sky radiance at 55° scattering angle conforms to Eq. (4). In addition, when there is no absorption and the sun is at a 70–80° zenith angle, the sky radiance at all angles in the solar almucantar (all sky radiances at the zenith angle of the sun) also conform to Eq. (4).

Thus, some portions of the sky in the real atmosphere conform to Eq. (4) particularly when there is no absorption (the second assumption of the equilibrium radiance model). This is true even without assuming equilibrium radiance constant for the path of sight.

B. Sky Radiance Along Almucantars

When cloud-free sky radiance measurements are graphed in the form of log sky radiance vs linear angle β from the sun, the curves formed by the different almucantars (constant zenith angle sky radiances) are nearly parallel. An example of this is given in Figs. 2 and 3. These sky radiances were measured with airborne instruments during flights[10] on 28 Oct. and 3 Nov. 1970. The sky radiances were measured with a filtered sensor having a mean wavelength of 478 nm and an effective passband of 19.9 nm. Kushpil and Petrova[11] describe similar near parallel curves and note that the separation of the curves is related to the transmittance due to scattering.

Cloud-free sky radiance may be used to compute equilibrium radiance by rearranging Eq. (4), thus,

$$L_q(z,\theta\phi) = L_\infty^*(z,\theta,\phi)/[1 - {}_sT_\infty(z,\theta)]. \tag{9}$$

where ${}_sT_\infty(z,\theta)$ is the scattering transmittance through the atmosphere at zenith angle θ.

When the equilibrium radiances computed using Eq. (9) are graphed as a function of angle from sun on the same grid as Figs. 2 and 3, the separations disappear. Thus equilibrium radiance is primarily a function of angle from sun and not of zenith angle. Figures 4 and 5 depict the equilibrium radiances computed from the sky radiances in Figs. 2 and 3. The fractional standard deviation of the individual equilibrium radiances from the average as a function of β is 0.16 for both Figs. 4 and 5.

Similar graphs were made for all the cloud-free sky radiance data from flights C-154 and C-155 (28 and 30 Oct. 1970). Sky radiances were measured at altitudes of ~4350, 2200, and 650 km with four filters. The fil-

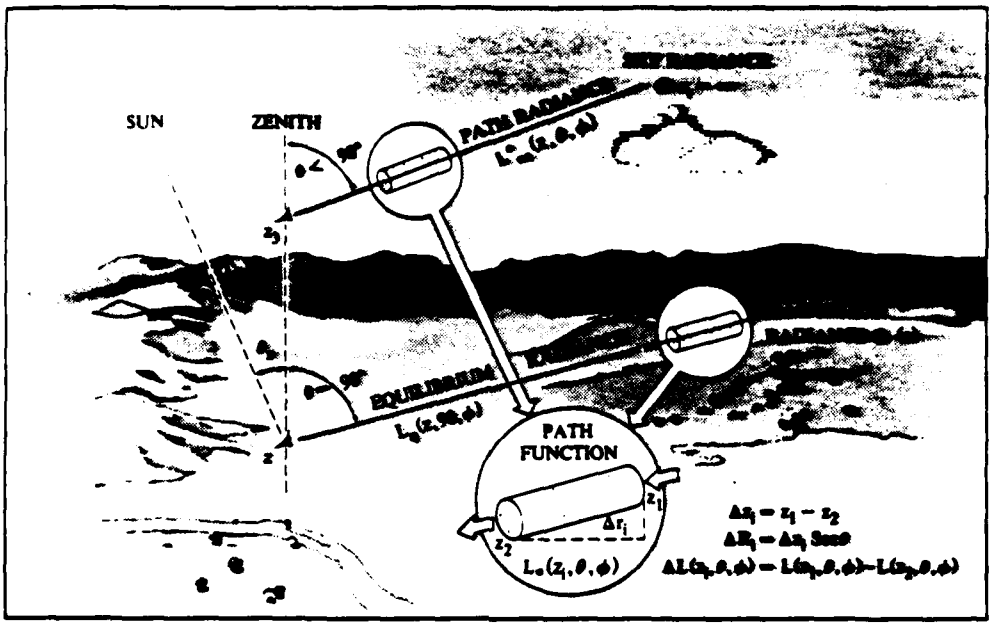

Fig. 1. Relationships between path function, path radiance, sky radiance, and equilibrium radiance. Path function is the radiance scattered toward the sensor by the atmospheric constituents within an incremental unit of path length. Path radiance is the cumulative transmitted radiance of the incremental path function elements along the specified path of sight. Sky radiance is a special form of path radiance in which the path of sight is between a sensor and the boundary of the atmosphere and is cloud free. Equilibrium radiance is a special form of path radiance, which is only directly observable along uniform horizontal paths of sight, in which an equilibrium exists between the radiance gained from an additional increment of path function and the radiance loss due to attenuation in the increment.

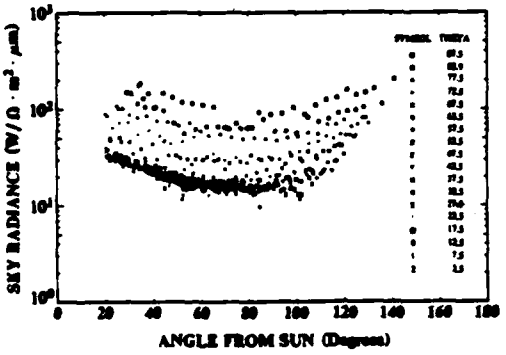

Fig. 2. Cloudless sky radiances along different almucantars as a function of angle from the sun for flight C-154, 4.375-km altitude above ground level, filter 2 mean wavelength of 478 nm. Flight was during the morning of 28 Oct. 1970 over a broad desert valley in central New Mexico. The solar zenith angle was 53°, the space-to-sensor vertical transmittance was 0.84 (optical thickness 0.17), and the scalar ground albedo was 0.23.

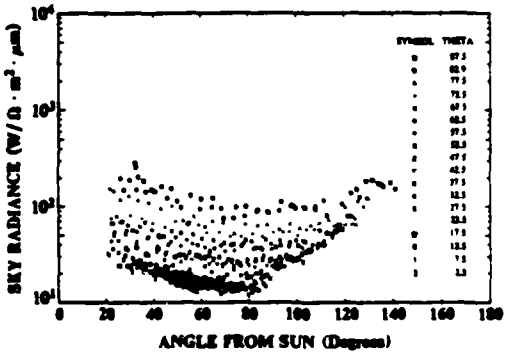

Fig. 3. Cloudless sky radiances along various almucantars as a function of angle from the sun for flight C-157, 2.229-km altitude above ground level, filter 2 mean wavelength of 478 nm. Flight was during the morning of 3 Nov. 1970. These sky radiances were measured during clear skies before clouds began appearing later in the flight. Flight was over a broad desert valley in central new Mexico. The solar zenith angle was 55°, the space-to-sensor vertical transmittance was 0.82 (optical thickness 0.20, and the scalar ground albedo was 0.15.

Appendix A

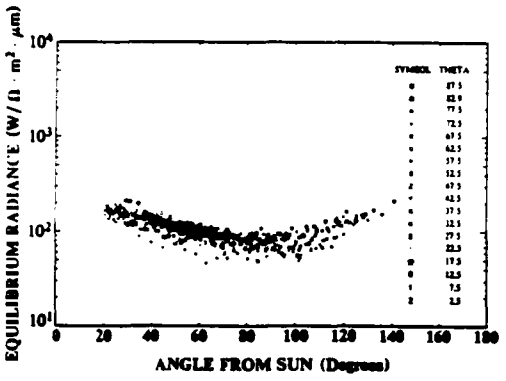

Fig. 4. Equilibrium radiance derived from sky radiances in Fig. 2 as a function of angle from the sun for flight C-154, 4.375-km altitude above ground level, filter 2.

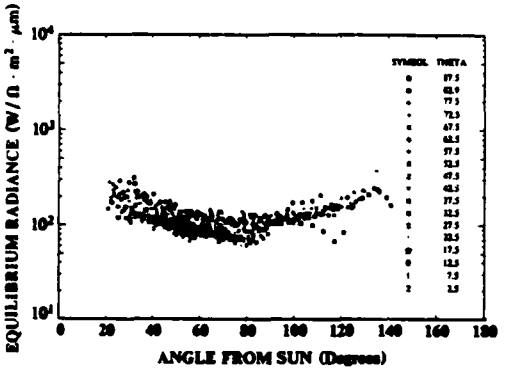

Fig. 5. Equilibrium radiance derived from sky radiances in Fig. 3 as a function of angle from the sun for flight C-157, 2.229-km altitude above ground level, filter 2.

tered sensor had mean wavelengths of 478, 557, 664, and 765 nm with effective passbands of 19.9, 78.5, 30.2, and 50.4 nm, respectively. The relative spectral response values for the four filtered sensors are graphed in Fig. 6. Except for two cases where the space-to-sensor transmittance was in error, the average fractional standard deviation of the individual equilibrium radiances from the average at each β was 0.21 with a range of 0.13–0.29.

Comparable graphs have been made for many ground-based measurements of sky radiance and for many airborne measurements at both low and high altitudes (0.5–6 km). The sky radiance measurements were made with various filtered sensors in the visible spectrum, including the photopically filtered sensor. These filtered sensors range in mean wavelength from 459 to 765 nm. Examples using photopic measurements of sky luminance are given in Fig. 1 of Ref. 1 and Figs. 2 and 3 of Ref. 12. The equilibrium radiances derived from cloud-free sky radiances using Eq. (9) when graphed as a function of angle from sun, always cluster as a fairly tight function of β, similar in shape to the volume scattering function $\sigma(z,\beta)$.

In the equilibrium radiance model, the directionality of the equilibrium radiance is assumed to be solely a function of the scattering angle from the sun. Thus from Figs. 4 and 5 we can see that, to a reasonable approximation, the real world has equilibrium radiances (derived from sky radiances) that are primarily a function of the scattering angle from the sun.

Additional validation of Eqs. (4) and (9) for the real atmosphere is implied by the method of obtaining scattering transmittance from sky ratios.

C. Scattering Transmittance from Sky Ratios

The method[13,14] for obtaining the scattering transmittance from sky radiance ratios stems from the suggested nomographic method of Kushpil and Petrova.[11] Equation (9) is divided by a similar equation for a second path of sight at zenith angle θ'. Both θ and θ' are upward paths of sight at the same scattering angle β,

$$L_s(z,\theta,\beta)/L_s(z,\theta',\beta) = [1 - {}_sT_a(z,\theta)]/[1 - {}_sT_a(z,\theta')]. \quad (10)$$

Equation (10) can also be put in terms of the relative air mass and the vertical space-to-earth scattering transmittance

$$\frac{L_s(z,\theta,\beta)}{L_s(z,\theta',\beta)} = \frac{1 - {}_sT_a(z,0)^{m_a(z,\theta)/m_a(z,0)}}{1 - {}_sT_a(z,0)^{m_a(z,\theta')/m_a(z,0)}}. \quad (11)$$

Although not solvable directly, Eq. (11) can be solved for vertical transmittance by iterative means.

An extensive body of solar transmissometer and sky scanner data collected during an early program at the Visibility Laboratory was used for the validation study.[14] Both sky radiance and solar transmissometer data were available for approximately 100 cases with clear skies for each of four filters. The filtered sensors had mean wavelengths of 459, 505, 560, and 661 nm, respectively. The relative spectral response values for the broadband filtered sensors used on the rooftop of the Visibility Laboratory are graphed in Fig. 7.

It is assumed that the total transmittance was the product of the scattering transmittance and transmittance due to ozone. The ozone transmittances were based on the total ozone for the U.S. Standard Atmosphere[15] and the spectral absorption values of Vigroux[16] which are in good agreement with the Inn and Tanaka[17] values.

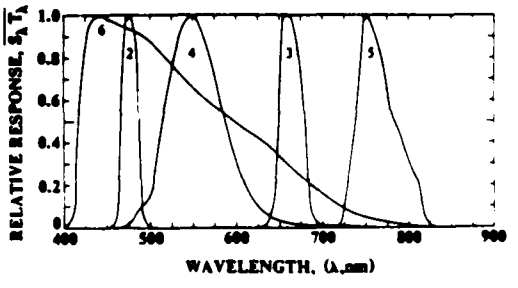

Fig. 6. Standard spectral responses for airborne filtered sensors. Peak wavelengths are 2 = 475 nm blue, 3 = 660 nm red, 4 = 550-nm photopic, 5 = 750-nm NIR, 6 = 440-nm S-20.

The ratios of the transmittance from sky radiance ratios times the ozone transmittance ${}_{a}T_{\infty}(0,0)$ divided by the transmittance from the solar transmissometer $[{}_{s}T_{\infty}(0,0){}_{a}T_{\infty}(0,0)/T_{\infty}(0,0)]$ were averaged for each filter; this average of the ratios is given in Table I, column 5. The fractional standard deviation is given in column 6.

The best comparisons between the sky ratio times ozone transmittance and the solar transmissometer values (the best average transmittance ratio) should be for filters 1 and 2 where the spectral responses are relatively unaffected by line or band absorption other than ozone. The average transmittance ratio for filters 1 and 2 is 0.98 with a fractional standard deviation of 0.05.

On the other hand H_2O absorption bands start at 688 nm so that the filter 4 solar transmissometer data may well be affected by water vapor in the atmosphere. This possibly accounts for the relatively high transmittance ratio of 1.06 for filter 4 mean wavelength 661 nm.

The validation experiments of the method for obtaining earth-to-space path radiance from sky radiances measured at ground stations provide further evidence of the validity of Eqs. (4) and (9) for the real atmosphere.

D. Earth-to-Space Path Radiances from Ground Stations

The method of measuring earth-to-space contrast transmittance from ground stations has been completely described (Ref. 12). It uses sky radiance to obtain the equilibrium radiance at the appropriate scattering angle for the downward path of sight from earth to space. If θ is the zenith angle of the downward path of sight and θ' is the zenith angle of a sky radiance at the same scattering angle β, the earth-to-space path radiance is

$$L_{*}(\infty,\theta,\beta) = L_{*}(z,\theta',\beta)[1 - T_{*}(\infty,\theta)]\,[1 - T_{*}(z,\theta')] \qquad (12)$$

This was derived by writing Eq. (9) in terms of θ and then θ' and then dividing the two equations and rearranging. Three experiments validated the method. In addition the method was used during the Gemini program[18] as part of a carefully controlled measurement of the visual capabilities of astronauts in earth orbit to discriminate test objects on the ground.

The method was found to be generally valid not only on cloud-free days but on days with some clouds as long as the path of sight and the sky radiance were cloud free.

When the β for the path of sight is larger than all the scattering angles available in the upper hemisphere (this happens most often when the sun zenith angle is small) an approximation is used of the sky radiance at $\beta = 90°$. This approximation was also used in the validation tests.

E. Practical Application

The agreement of the real clear-day atmosphere to the equilibrium radiance model is sufficient to suggest that a radiometer (such as a photopically filtered photometer) for measuring sky radiance in the visible spectrum could be used on clear days to obtain a reasonable estimate of path radiance for various paths of sight as follows:

First, the vertical scattering transmittance through the atmosphere would be obtained using Eq. (11) by measuring two sky radiances at equivalent angles from the sun. It is preferable to have θ as small as possible and θ' as large as possible in order to minimize the potential error. A minicomputer can easily do the computation necessary for solving Eq. (11).

Second, the scattering angle β from the sun at θ_s,ϕ_s for the desired path of sight at θ,ϕ is determined from

$$\cos\beta = \sin\theta \sin\theta_s \cos(\phi - \phi_s) + \cos\theta \cos\theta_s. \qquad (13)$$

Third, a sky radiance is measured at that scattering angle β. If the desired scattering angle is larger than the scattering angle for the horizon at 180° azimuth from the sun, a sky radiance at a scattering angle of 90° is used. This approximation was used successfully with the method for measuring earth-to-space path radiance from ground stations[12]; it should work equally as well for shorter path lengths.

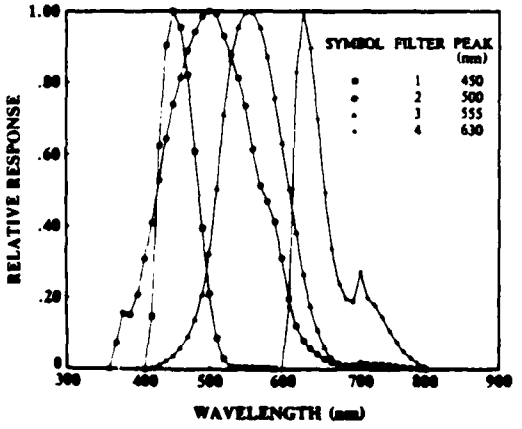

Fig. 7. Standard spectral responses for Visibility Laboratory rooftop 1964 filtered sensors.

Table I. Scattering Transmittance from Sky Radiance Ratios Times Ozone Transmittance Divided by Total Transmittance from Solar Transmissometer for all Cloudless Data from January–September 1964 at the Visibility Laboratory

Filter no.	Mean wavelength (nm)	Effective passband (nm)	Average total transmittance	Average ${}_{s}T_{\infty}T_{\infty}/T_{\infty}$	Fractional standard deviation	Number of cases	Ozone transmittance
1	459	58.1	0.713	0.985	0.051	110	0.996
2	505	151.9	0.750	0.981	0.047	103	0.984
3	560	106.8	0.782	1.030	0.058	105	0.970
4	661	61.4	0.821	1.062	0.078	96	0.978

Appendix A

Fourth, the equilibrium radiance $L_q(z,\theta,\phi)$ for the desired path of sight is computed using Eq. (9).

The final step for obtaining the desired path radiance is to measure or estimate the radiance transmittance for the path of sight of length r. The vertical transmittance through the atmosphere obtained above provides a limit against which estimates can be checked. Shorter paths should have transmittances less than $T_\infty(z,\theta)$. The path radiance would be computed using Eq. (3).

This method should be usable on all cloudless days for narrow or broadband sensors in the visible spectrum unless there is smoke which would indicate the presence of non-negligible absorption.

Now we will compare the equilibrium radiance model results using Eq. (7) to the models of the Rayleigh atmosphere and to atmospheric measurements for the photopic sensor.

IV. Equilibrium Radiance Model Predictions Using Eq. (7)

Predictions of equilibrium radiance, sky radiance, and downwelling irradiance have been made on the basis of Eq. (7) for both a Rayleigh atmosphere and for more realistic atmospheres using the Barteneva[6] scattering functions.

A. Homogeneous Rayleigh Atmosphere

Equilibrium radiance model atmosphere calculations can be made for the Rayleigh atmosphere since the volume scattering function and radiance transmittance are well specified. The approximate equation for the normalized volume scattering function for Rayleigh scattering is

$$_R\sigma(\beta)/_R\sigma = 3(1 + \cos^2\beta)/(16\pi); \quad (14)$$

Sky radiances or luminances have been computed for the photopic Rayleigh atmosphere by Coulson *et al.*,[19] Pyaskovskaya-Fesenkova,[20] and Tousey and Hulburt.[21] Comparison of the equilibrium radiance model was made to these other models.[22] The equilibrium radiance model computations were made with Eq. (7) using the same vertical radiance transmittance, solar irradiance out of the atmosphere, solar zenith angle, and albedo as for the other models. The results of the comparisons are depicted in Figs. 8–10.

The sky radiance values for Coulson *et al.* and the equilibrium radiance model for azimuths toward and away from the sun are graphed in Fig. 8. The comparison is best nearest the horizon in both azimuths. The values for the equilibrium radiance model near the zenith are slightly higher than for the Coulson model.

Pyaskovskaya-Fesenkova presented an isoluminance plot appropriate for albedos other than zero. The computations for the equilibrium radiance model were made using scalar albedos of 0.10 and 0.25. These are depicted as continuous curves in Fig. 9. The angular positions of the isoluminance values for the Pyaskovskaya-Fesenkova graph were estimated and are depicted in Fig. 9 as separate points. The curve for 0.25 albedo is close to the Pyaskovskaya-Fesenkova values near the horizon but higher near the zenith.

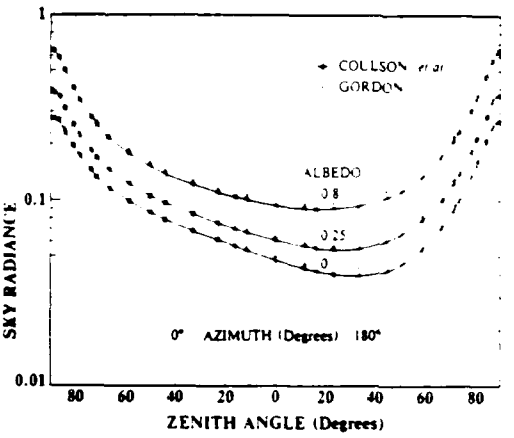

Fig. 8. Rayleigh sky radiance for Coulson *et al.*[19] and equilibrium radiance model using a vertical radiance transmittance of 0.861 (optical thickness 0.15), sun zenith angle of 36.8°, and a sun scalar irradiance of π.

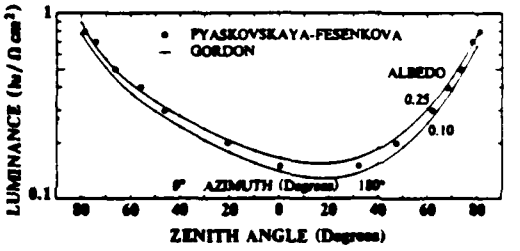

Fig. 9. Rayleigh sky luminances (lm/sr · cm² or stilbs) for Pyaskovskaya-Fesenkova[20] and equilibrium radiance model using vertical earth-to-space radiance transmittance of 0.861 (optical thickness 0.15), a sun illuminance out of the atmosphere of 13 lm/cm², and a sun zenith angle of 60°.

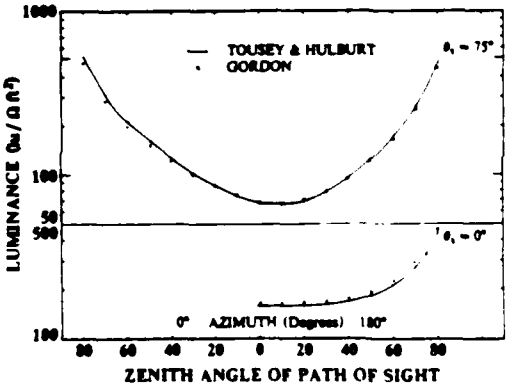

Fig. 10. Rayleigh sky luminance (lm/sr · ft² at 10,000 ft) for Tousey and Hulburt[21] and equilibrium radiance model for sun illuminance out of the atmosphere of 13,600 lm/ft², ground-level scattering coefficient of 0.017 km⁻¹, and an albedo of 0.20.

Table II. Transmittance and Scattering Function Specifications for Evaluation of Model Atmosphere Equations

Earth-to-space vertical transmittance	Barteneva scattering function class number								Total No. of cases
0.9	2	3							2
0.8	2	3	4	5					4
0.7		3	4	5	5'	6			5
0.6		3	4	5	5'	6			5
0.5			4	5	5'	6	6'	7	6
Total no. cases	2	4	4	4	3	3	1	1	22

The solid lines in Fig. 10 represent the values given by Tousey and Hulburt. The values for the equilibrium radiance model compare well near the zenith and are slightly lower near the horizon for the sun at a zenith angle of 75°. For the 0° sun zenith angle, the equilibrium radiance model values are consistently a little higher than the Tousey and Hulburt values, comparing best at the zenith.

In general, the photopic Rayleigh sky radiance values from the equilibrium radiance model compare reasonably well with the values of Coulson *et al.*, Pyaskovskaya-Fesenkova, and Tousey and Hulburt.

B. Comparison to Atmospheric Measurements

For comparison of the model to various Visibility Laboratory ground-based measurements, a value of $1.89E3$ W/m$^2\mu$m was used for the photopic solar irradiance out of the atmosphere. This value is based on the spectral solar irradiance values of Johnson[23] and the standard luminosity function.

Rayleigh. Calculations for the equilibrium radiance model were made[22] for the photopic Rayleigh atmopshere. The Rayleigh normalized volume scattering function was obtained from Eq. (14). The photopic Rayleigh vertical space-to-earth radiance transmittance of 0.907 was based on the spectral total volume scattering coefficients from Eq. (14) of Penndorf[24] and the sea level scale height for the U.S. Standard Atmosphere.

Barteneva. Equilibrium radiance model calculations were made[14] using the extensive catalog of photopic ground-level normalized volume scattering functions provided by Barteneva.[6] The twenty-two combinations of Barteneva scattering class functions and vertical space-to-earth radiance transmittances used for the model atmosphere computations are summarized in Table II.

1. Downwelling Irradiance

The downwelling irradiance is defined as

$$E(z,d) = \int_{2\pi} L(z,\theta,\phi)\cos\theta d\Omega, \qquad (1c$$

where the radiance array is for zenith angles from 0° to 90° including the sun or moon where appropriate.

Scalar albedo of 0.10 is representative of cultivated fields. It is also an intermediate albedo for non-snow-covered terrains. We will use the model values for 0.1 scalar albedo to compare to the measured irradiances when albedo is unspecified.

For the model calculations using 0.10 scalar albedo, the range of downwelling irradiance did not vary significantly with different normalized volume scattering functions when all other parameters were held constant. For 0.10 albedo the range of downwelling irradiance was within ±0.045 of the average for each sun zenith angle for each transmittance.

The average values from the model calculations of downwelling irradiance for 0.10 scalar albedo for each transmittance are graphed as a function of sun angle in Fig. 11(a). The irradiances for the photopic Rayleigh atmosphere for 0.10 scalar albedo are given as a solid curve. The second solid curve is for the Brown[25] average (photopic) irradiances based on over 12,000 measurements made between 1943 and 1947 all over the world. The Brown average values are generally used as an irradiance standard for a clear day. The Brown curve is similar to the average model values for 0.7 transmittance for sun zenith angles from 0° to 70° but is higher at 80° and 85° sun zenith angles. A vertical transmittance value of 0.7 is commonly used as the average clear-day photopic transmittance, therefore it is reasonable to assume the Brown values are representative of a transmittance of 0.7.

Thus the equilibrium radiance model results for downwelling irradiances are reasonably consistent with the Brown values.

The data bank of irradiance and vertical earth-to-space radiance transmittance and path radiance measured with portable instruments during the period from 1962 to 1967 (Ref. 22) contains ~370 photopic measurements. These data were measured in various locations throughout the United States on days with an unobscured sun for a large range of solar zenith angle. Photopic downwelling irradiances from this data bank are graphed in Fig. 11(b) as a function of sun zenith angle. The irradiance data are designated by symbols indicating the radiance transmittance in 0.10-transmittance increments; e.g., the symbol ⊙ indicates a transmittance of 0.85 ± 0.05 or values of transmittance from 0.800 to 0.899. These downwelling irradiances are all measured by an irradiometer. The two curves superimposed on the graph are the photopic Rayleigh atmosphere values for 1.0 albedo (conceived as an upper limit) and the average clear-day values of Brown.

The measured values of downwelling irradiance for the 1962–1967 period cluster about the average values of Brown and lie beneath the upper limiting values for the Rayleigh atmosphere. The measured irradiances show an approximate decrease as transmittance decreases similar to that shown in Fig. 11(a) for the average irradiances from the equilibrium radiance model.

The measured irradiances in Fig. 11(b) are for skies with an unobscured sun but with partially cloudy as well as clear skies. The model, however, represents a cloudless sky. Therefore for a more direct comparison, the data set was sorted to obtain zero cloud cover data within ±0.02 of the transmittances and ±2° of the sun

Appendix A

Appendix A

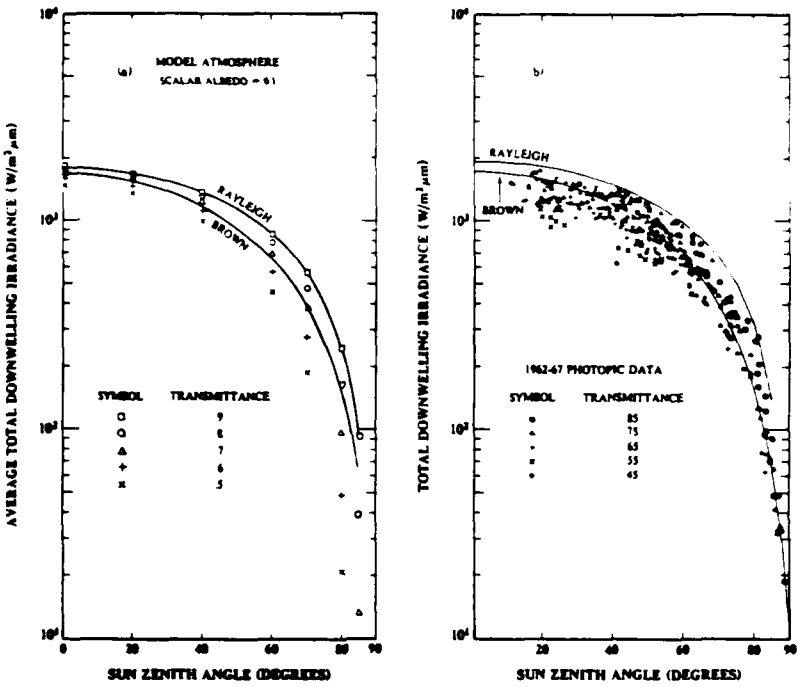

Fig. 11. Photopic downwelling irradiance data and equilibrium radiance model values compared to Brown.[25]

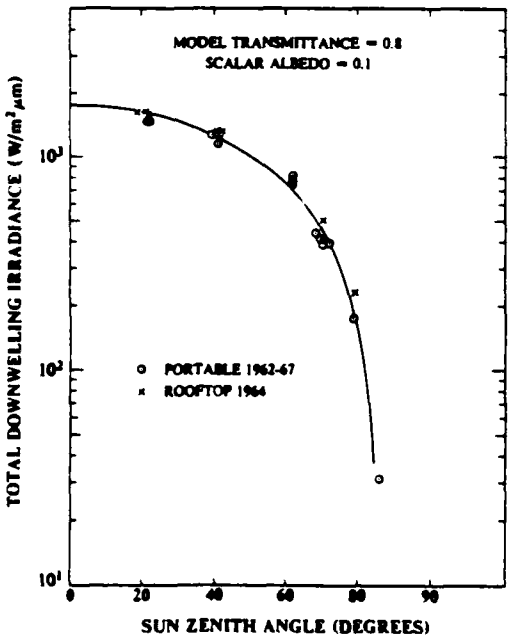

Fig. 12. Comparison of equilibrium radiance model to measured photopic irradiances for cloudless skies with vertical transmittances 0.8 ± 0.02 and sun zenith angles within ±2° of model calculations.

zenith angles used in the model computations. The bulk of these were for 0.8 transmittance. These are graphed in Fig. 12 along with similarly sorted data from the photopic irradiances measured with an irradiometer on the Visibility Laboratory rooftop during 1964.[14]

When the twenty-three measured values in Fig. 12 are divided by the average values from the model (graphed as a curve in Fig. 12), the average ratio is 0.999 with a standard deviation of 0.14. This is excellent agreement.

2. *Equilibrium Radiance*

Four of the model evaluations of equilibrium radiance were for a space-to-earth transmittance of 0.8, a sun zenith angle of 70°, and a scalar albedo of 0.1. The Barteneva scattering functions used were her gradual classes 2, 3, 4, and 5. These values are graphed in Fig. 13 as solid curves. Barteneva's measurements of normalized volume scattering function were for ground level and for scattering angles from 16° to 164°. Therefore we have limited the curves of equilibrium radiance to the scattering angles within the range of her measured values.

The data bank of sky radiances and solar transmittances measured on the Visibility Laboratory rooftop in 1964, Ref. 14, contained approximately 100 cloud-free photopic measurements. Four of these were within ±0.02 of the 0.8 transmittance and within ±2° of the sun zenith angle of 70°. The equilibrium radiances derived from the sky radiances in the 0° and 180° azimuths from the sun using Eq. (9) for these four cases are also

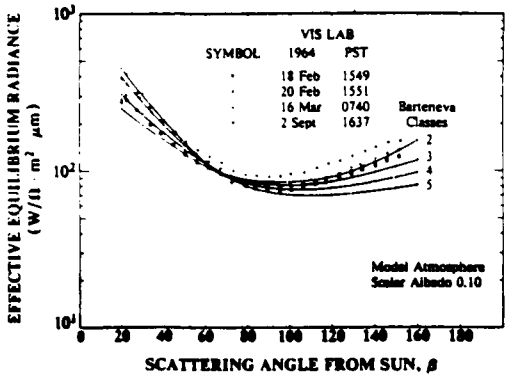

Fig. 13. Photopic equilibrium radiance derived from cloudless sky radiance data as a function of angle from the sun for 70 ± 2° sun zenith angles and space-to-earth vertical transmittances of 0.80 ± 0.02, compared with equilibrium radiance model atmosphere calculations using Barteneva[6] scattering functions.

graphed in Fig. 13. Although scalar albedo for these data sets is not available, an estimate of 0.1 is reasonable for the terrain surrounding the data site at the Visibility Laboratory.

The agreement between the curves for the model calculations and the equilibrium radiances based on the sky radiance and radiance transmittance measurements is quite good. Three of the four data sets compare quite closely to the model, with one data set slightly higher than the model at the larger scattering angles.

Similar graphs for seven other sun zenith angle transmittance combinations were drawn using altogether twenty-six data sets including those in Fig. 13. Most of the data sets (twenty-two) were for a transmittance of 0.8 ± 0.02, three sets were for 0.7 transmittance, and one for 0.6. The only large discrepancy between data sets and model was for the single data set for the low transmittance of 0.6 where absorption may be a problem.

On the basis of these limited data sets several trends were noted. The comparison between data sets and model for the 0.8 and 0.7 transmittances indicated generally good agreement at intermediate sun zenith angles. The model was slightly high at the small sun zenith angle of 20° and slightly low for the large sun zenith angle of 80°. When a fair number of data sets were available at one transmittance and sun zenith angle, the data sets sometimes showed more variability than the model. For example, for 0.8 transmittance and 80° sun zenith angle, two of the data sets compared closely to the model and four data sets were higher than the model.

The comparison of model to data sets is sufficiently good to warrant further use of Eq. (7) as a viable approximation for cloudless days in the visible portion of the spectrum for high transmittance. The observed differences between some of the data sets and the model, and the lack of data for comparison for lower transmittances indicate the need for further study with a larger number of data sets. One of the authors is currently attempting to set up a program which will make this study possible.

V. Summary

An equilibrium radiance model of a clear (cloud-free) atmosphere for use in the visible region of the spectrum was presented by one of the authors in an earlier paper.[1] This model was based on two assumptions: (1) the equilibrium radiance for a given path of sight is constant, and (2) absorption is negligible. The model predicts that path radiance (sky radiance) is a function of the equilibrium radiance and the radiance transmittance.

When equilibrium radiance is not constant for a path of sight, it is necessary to know the path function and attenuation coefficient values for each element of the path from 0 to r in order to obtain the path radiance. Assuming the equilibrium radiance to be constant allows the path radiance to be computed from the total path transmittance and the equilibrium radiance. Thus assuming equilibrium radiance constant represents a tremendous simplification.

A large body of cloudless sky radiance data in the visible spectrum indicates that equilibrium radiance can be derived from sky radiances when space-to-earth vertical radiance transmittance is known. This leads to a method for obtaining space-to-earth vertical scattering transmittance from sky radiance ratios. The sky radiance ratio method has been presented and validated herein. As a result, for the visible spectrum on cloudless days we can obtain from sky radiance measurements: (1) vertical space-to-sensor scattering transmittance, (2) equilibrium radiance for the path of sight, and, if an estimate or measure of path transmittance is available, (3) path radiance in the troposphere as well as through the atmosphere for upward and downward paths of sight.

Comparisons of predictions using Eq. (7) of the model to three other models for the photopic Rayleigh atmosphere indicate good agreement. Comparisons of predictions using Eq. (7) to atmospheric measurements when the transmittance is high using various broadband sensors in the visible spectrum during cloud-free days also indicate good agreement. Thus Eq. (7) can be used to quickly obtain approximations for equilibrium radiance, sky radiance, path radiance, and irradiance for very clear days.

This work was performed by the authors for the Air Force Geophysics Laboratory, Air Force Systems Command, United States Air force, under contract F19628-78-C-0200. Some of the writing of the article was done under the auspices of Viz. Ability. The publication is under the aegis of the U.S. Army Research Office. We wish to thank Judith Olson for technical editing assistance.

Appendix A

Appendix A

References

1. J. I. Gordon, "Model for a Clear Atmosphere," J. Opt. Soc. Am. 59, 14 (1969).
2. S. Chandrasekhar, *Radiative Transfer* (Dover, New York, 1960).
3. D. G. Collins and M. B. Wells, *Monte Carlo Codes for the Study of Light Transport in the Atmosphere* (Radiation Research Associates, Inc., Fort Worth, Tex., 1965), Vols. 1 and 2.
4. S. Q. Duntley, A. R. Boileau, and R. W. Preisendorfer, "Image Transmission by the Troposphere," J. Opt. Soc. Am. 47, 499 (1957).
5. W. G. Driscoll and W. Vaughan, Eds., *Handbook of Optics* (Mc-Graw Hill, New York, 1978).
6. O. D. Barteneva, "Scattering Functions of Light in the Atmospheric Boundary Layer," Bull. Acad. Sci. USSR Geophys. Ser. 1237 (1960).
7. D. Barbier, "Sur la Correction de Diffusion dans les Mesures d'Altitude des Couches Atmosphériques Émittant la Lumière du Ciel Nocturne," Ann. Geophys. 1, 144 (1944).
9. J. I. Gordon, U. California, San Diego, Scripps Institution of Oceanography, Visibility Laboratory, SIO Ref. 83-10, AFGL-TR-82-0223 (1982).
10. S. Q. Duntley, R. W. Johnson, and J. I. Gordon, U. California, Scripps Institution of Oceanography, Visibility Laboratory, SIO Ref. 72-71, AFCRL-72-0461, NTIS No. AD 751 936 (1972).
11. V. I. Kushpil and L. F. Petrova, "Determination of the Atmospheric Transmission from Sky Brightness Distribution," Opt. Technol. 38, No. 4, 191 (1971).
12. J. I. Gordon, J. L. Harris, Sr., and S. Q. Duntley, "Measuring Earth-to-Space Contrast Transmittance from Ground Stations," Appl. Opt. 12, 1317 (1973).
13. S. Q. Duntley, R. W. Johnson, and J. I. Gordon, U. California, Scripps Institution of Oceanography, Visibility Laboratory, SIO Ref. 72-82, AFCRL-72-0593, NTIS No. AD 754 898 (1972).
14. S. Q. Duntley, R. W. Johnson and J. I. Gordon, U. California, Scripps Institution of Oceanography, Visibility Laboratory, SIO Ref. 79-5, AFGL-TR-78-0286, NTIS No. ADA 073 121 (1978).
15. *U.S. Standard Atmosphere 1976* (Superintendent of Documents, U.S. GPO, Washington, D.C. 20402, 1976).
16. E. Vigroux, "Author, add title to the galleys," Ann. Phys. Paris 8, 742 (1953).
17. E. C. Y. Inn and Y. Tanaka, "Absorption Coefficient of Ozone in the Ultraviolet and Visible Regions," J. Opt. Soc. Am. 43, 870 (1953).
18. S. Q. Duntley, R. W. Austin, J. L. Harris, and J. H. Taylor, U. California, Scripps Institution of Oceanography, Visibility Laboratory, SIO Ref. 68-6 (1968); NASA, Washington, D.C., NASA CR-1134 (1968).
19. K. L. Coulson, J. V. Dave, and Z. Sekara, *Tables Related to Radiation Emerging from a Planetary Atmosphere with Rayleigh Scattering* (U. California Press, Berkeley, 1960).
20. E. V. Pyaskovskaya-Fesenkova, *Investigation of the Scattered Light in the Earth's Atmosphere*, (Acad. Nauk, U.S.S.R., 1957), p. 182. Polar plot of data also published by N. Robinson, ed., *Solar Radiation*, (Elsevier Publ. Co., Amsterdam, 1966), Fig. 3.14, p. 65.
21. R. Tousey and E. O. Hulburt, "Brightness and Polarization of the Daylight Sky at Various Altitudes Above Sea Level," Opt. Soc Am. 37, 78 (1947).
22. S. Q. Duntley, R. W. Johnson, and J. I. Gordon, U. California, Scripps Institution of Oceanography, Visibility Laboratory, SIO Ref 75-26, AFCRL-TR-75-0457, NTIS No. ADA 022 675 (1975).
23. F. R. Johnson, "The Solar Constant," J. Meteorol. 11, 431 (1954).
24. R. Penndorf, "Tables of the Refractive Index for Standard Air and the Rayleigh Scattering Coefficient for the Spectral Region Between 0.2 and 20.0 μ and their Application to Atmospheric Optics," J. Opt. Soc. Am. 47, 176 (1957).
25. D. R. E. Brown, *Natural Illumination Charts* (Department of the Navy, Bureau of Ships, Washington, D.C. 1962), Report 374-1, Project Ns-714-10.

Reprinted from Applied Optics, Vol. 24, page 2721, August 15, 1985

Integrating nephelometer: theory and implications

Jacqueline I. Gordon and Richard W. Johnson

Appendix B

The Visibility Laboratory integrating nephelometer measures the total volume scattering coefficient and volume scattering functions at 30° and 150° scattering angles. Equations for both measurements and calibration are derived and data reviewed. The ratio of measured to Rayleigh volume scattering function at each scattering angle is a simple function of the ratio of measured to Rayleigh total volume scattering coefficient regardless of altitude or wavelength in the visible spectrum. Methods are developed for obtaining the single scattering albedo from horizon sky radiance and the scattering optical thickness from sky radiance ratios at 55° scattering angle from the sun.

I. Introduction

The integrating nephelometer measures three scattering properties: the total volume scattering coefficient $s(z)$ at altitude z, and the volume scattering function $\sigma(z,\beta)$ at scattering angles β of 30° and 150°. A description of the instrument and the relationship of the measurements to daytime visibility has been previously published by one of the authors.[1] The purpose of this paper is to provide the theory behind these measurements and to describe some of the implications of concurrent measurements of the volume scattering function and the total volume scattering coefficient.

The theory and equations are for monochromatic radiation but applicability to radiation for broader passbands will be indicated where appropriate. The theory has hitherto been available only in unpublished technical notes. The notation used is that adopted by the Visibility Laboratory[2] and modified to correspond to OSA recommendations in Sec. 1 of Driscoll and Vaughan.[3]

The integrating nephelometer is based on one of the schemes suggested by Beuttell and Brewer.[4] It is essentially the optical inverse of the instrument described in full by Middleton[5] and used by Crosby and Koerber,[6] Charlson *et al.*,[7] and Horvath and Noll.[8] The integrating nephelometer uses a collimated light beam and a cosine-law collector to view the scattered flux. It has, in addition to an irradiometer, two narrow field radiometers for measurement of the volume scattering function at scattering angles of 30° and 150°. It is called an integrating nephelometer to reflect its multiple capabilities.

Jacqueline Gordon is with Viz. Ability, 2941 NW Ashwood Drive, Corvallis, Oregon 97330, and Richard Johnson is with University of California at San Diego, Visibility Laboratory, San Diego, California 92093.

Received 6 November 1984.
0003-6935/85/162721-10$02.00/0.

II. Derivation of Equations for the Integrating Nephelometer

The nephelometer has one sensor which time-shares three optical channels: the central irradiometer channel and the adjacent radiometers on either side (see Fig. 1). Each of these channels is calibrated using standard photometric techniques and an incandescent light source of radiant intensity traceable to the National Bureau of Standards. The ensuing derivations will relate the irradiance of the scattered flux to the total volume scattering coefficient and the radiance to the volume scattering function. In addition, the irradiance from a known reflecting surface placed in the light beam is used to further calibrate the device.

A. Irradiometer Measurements

A measurement of the irradiance due to the flux scattered from a well-collimated beam is related to the total volume scattering coefficient. If the irradiometer is placed immediately adjacent to the light beam, corrected for cosine-law response and truncation losses, the resulting optical integration will yield a direct measurement of the total scattering coefficient.

Figure 1 illustrates the positioning of the irradiometer immediately adjacent to the parallel light beam. Let us define a coordinate system centered on the surface of the irradiometer as shown in Fig. 2.

At the irradiometer surface, the incremental irradiance dE from one element of volume $dxdydz$ of the parallel light beam at point x, y, and z can be expressed as

$$dE(x,y,z) = L(x,y,z,\beta)\cos\theta d\Omega. \quad (1)$$

The θ is the angle between the normal from the irradiometer surface and the path of sight of the sensor (irradiometer) toward the incremental volume. The $L(x,y,z,\beta)$ is the radiance of the incremental volume at the scattering angle β from the light source and

$$\cos\theta = y/r, \quad (2)$$

$$r = (x^2 + y^2 + z^2)^{1/2}, \quad (3)$$

$$\beta = \cos^{-1}(z/r). \quad (4)$$

Appendix B

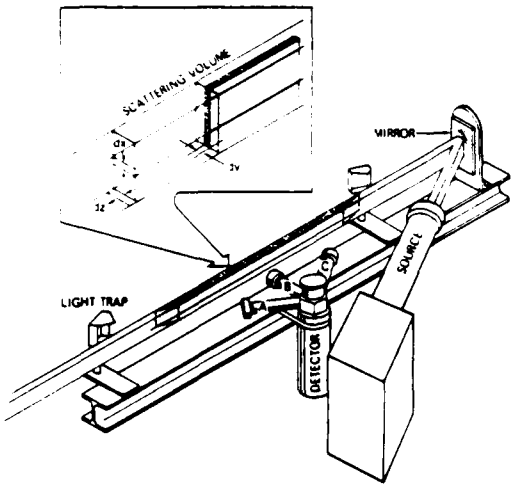

Fig. 1. Artists rendition of the integrating nephelometer and the volume of air providing scattered flux toward the irradiometer and radiometers. The light source is a high intensity, well-collimated projector: *A*, radiometer; *B*, irradiometer; and *C*, radiometer.

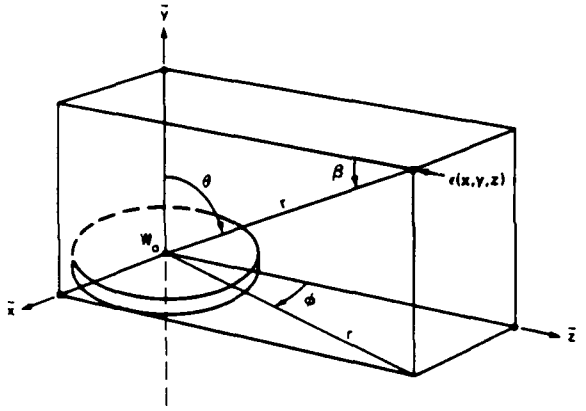

Fig. 2. Coordinate system centered on the surface of the irradiometer. The positive z direction is toward the light source.

By definition, scalar irradiance is the noncosine-weighted irradiance from any direction. The radiance of the incremental volume is equal to the scalar irradiance $\epsilon(x,y,z)$ of the light beam times the volume scattering function $\sigma(\beta)$ and the effective depth of the scattering volume $\sec\theta dy$:

$$L(x,y,z,\beta) = \epsilon(x,y,z)\sigma(\beta)\sec\theta dy. \tag{5}$$

Since the beam is parallel, the maximum change in scalar irradiance from the collimating lens to any point further along the beam is due to the radiance transmittance of the air column. The radiance transmittance $T = \exp(-\alpha\Delta z)$ where α is the attenuation coefficient and Δz is the distance along the beam from the lens to the point of measurement. The transmittance is reasonably close to 1.0 ($T \geqq 0.99$) even for fog if $\Delta z \leqq 2.37$ m. Thus the scalar irradiance does not change appreciably along the beam and can be designated by $\epsilon(x,y)$.

1. *Central Incremental Volume*

The compensation for scattering volume depth variation (see Fig. 1) by the cosine weighting of the irradiometer works perfectly for the central incremental volume of dx at $x = 0$ where the solid angle can be expressed as

$$d\Omega = \cos\theta y^{-1}dxd\theta \tag{6}$$

Assuming $\epsilon(x,y)$ is not a function of the x or y position in the light beam, combining Eqs. (1), (5), and (6) and integrating with respect to θ, we get

$$dE(0,y) = \epsilon y^{-1}\int_0^{\pi/2}\sigma(\beta)\cos\theta d\theta dxdy. \tag{7}$$

The contribution to the irradiance may be broken into two parts, the portion due to forward scattering in the beam and the portion due to backscattering in the beam. For the forward scattering, as θ goes from 0° to 90°, β goes from 90° to 0°, therefore $\cos\theta = \sin\beta$. For the back portion of the beam, as θ goes from 0° to 90°, β goes from 90° to 180° and again $\cos\theta = \sin\beta$. Now changing the integrating variable to β and substituting into Eq. (7) we get

$$dE(0,y) = \epsilon y^{-1}\int_0^{\pi}\sigma(\beta)\sin\beta d\beta dxdy. \tag{8}$$

The integral of the volume scattering function over 4π is equal to the total volume scattering coefficient. This can be written as

$$s = 2\pi\int_0^{\pi}\sigma(\beta)\sin\beta d\beta. \tag{9}$$

Substituting Eq. (9) into Eq. (8), it can now be written as

$$dE(0,y) = \epsilon s(2\pi y)^{-1}dxdy. \tag{10}$$

2. *Entire Height of Beam*

Equations (6)–(10) have assumed that the beam has depth (in the y dimension) but little height (in the x dimension). In actuality, the scattering from the incremental volumes where x is not zero does contribute significantly to the irradiance. In addition to this problem, the integration is truncated angularly near scattering angles 0° and 180° by baffles on the irradiometer to shield the irradiometer from the light source and the light trap. The ensuing equations correct these discrepancies as well as consider the effects of nonuniformity of the light beam over the cross-sectional area in the x and y dimensions and variations from true cosine acceptance of the irradiometer. The overall correction for these discrepancies is approximately a factor of 1.28 for the nephelometer. This correction was determined by comparing the K/F from the simplified a sumptions [obtained by setting dx equal to the beam height and dy equal to the beam depth in Eq. (10)] to the K/F computed from Eq. (26).

The solid angle is first expressed as a function of the apparent area a of the volume

$$d\Omega = a/r^2 = dxdz\cos\theta/r^2. \tag{11}$$

The scalar irradiance is then expressed as $\epsilon(x,y)$, a

function of cross-sectional position. In addition, the measured collection efficiency of the irradiometer $f(\theta)$ is substituted for $\cos\theta$ in Eq. (1). Now combining Eqs. (1), (5), and (11) with the above we get

$$dE(x,y,z) = \epsilon(x,y)\sigma(\beta)f(\theta)r^{-2}dxdydz. \quad (12)$$

The total irradiance is found by integrating over the limits defined by the light beam and the cutoff baffles for the irradiometer:

$$E = \int_{Z_b}^{Z_f}\int_{Y_1}^{Y_2}\int_{-X}^{X}\epsilon(x,y)\sigma(\beta)f(\theta)r^{-2}dxdydz. \quad (13)$$

The integrating limits are

X, the beam half-height;
Y_1, the distance from the irradiometer surface to the closest edge of the beam in the y dimension; and
Y_2, the distance from the irradiometr surface to the farthest edge of the beam in the y dimension.

The placement of cutoff baffles (see Fig. 3) limits the angles of incidence on the irradiometer. Thus the maximum θ is 85° in the forward direction at a scattering angle of 5°. In the backscattering direction the maximum θ is 80° at a scattering angle of 170° for data taken prior to summer 1976, and for data taken after that date the maximum θ is 82.5° at a scattering angle of 172.5°. When $x = 0$, the general equation for β becomes

$$\tan\beta = y/Z. \quad (14)$$

Solving for Z we get

$$Z = y/\tan\beta. \quad (15)$$

Equation (15) is also a reasonable approximation for all values of x for the cutoff angles used in the nephelometer.

Let us now define a factor F such that

$$F = \int_{Z_b}^{Z_f}\int_{Y_1}^{Y_2}\int_{-X}^{X}[\epsilon(x,y)/\epsilon(0,0)]\sigma(\beta)f(\theta)s^{-1}r^{-2}dxdydz. \quad (16)$$

Now an expression for the total volume scattering coefficient can be written by combining Eqs. (13) and (16):

$$s = E/[\epsilon(0,0)F]. \quad (17)$$

The factor F was evaluated for the nephelometer for a full range of scattering conditions by using the normalized volume scattering functions $\sigma(\beta)/s$ of Barteneva.[9] She provides a catalog containing 10 gradual functions labeled 1–10 ranging from near Rayleigh to heavy haze. (Her steep functions were for fog which are not applicable since the nephelometer was only used when weather was appropriate for flying under visual flight rules.) The factor decreased only slightly with increased scattering. Thus we used $F(5)$, the factor for Barteneva scattering function 5, as a reasonable approximation for all the data. For Rayleigh scattering, the factor increased by only 3% and for scattering function 10, the factor decreased by only 4% from $F(5)$.

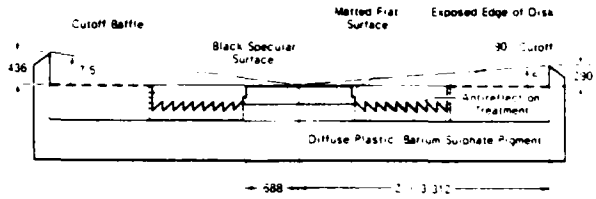

Fig. 3. Irradiometer flat plate collector. The antireflection treatment consists of 45° bevel circular grooves finished to a black specular surface. A flush-mounted, matted flat diffuse plastic surface is not a cosine surface for incident flux. This design was developed to increase the flux acceptance at angles >0°, the amount of the exposed edge of the disk being determined empirically. The outer cutoff at 8.412 cm (3.312 in.) is not a circular section but a rectangular plate (this is an edge view).

3. *Obtaining Scalar Irradiance*

The next step is to obtain a measurement of the scalar irradiance of the beam during operational sequences. Doing this near concurrently with the total volume scattering coefficient measurement minimizes absolute calibration errors and long-term sensor stability problems.

A reflecting surface is inserted normal to the beam at distance Z_r from the center of the irradiometer and the resultant irradiance is measured. The irradiance $E(x,y)$ falling on the calibrating surface is equal to the scalar irradiance since the surface is normal to the beam. The radiance of the calibrating surface $L(x,y,Z_r)$ is a function of the reflectance R of the surface and the scalar irradiance:

$$L(x,y,Z_r) = \epsilon(x,y)RT/\pi. \quad (18)$$

where T is the transmittance of an attenuator placed in the light beam in order to bring the measured reflected flux down into the appropriate range for measurement by the irradiometer. The incremental irradiance from the calibrating surface received by the irradiometer is defined by

$$dE(x,y,Z_r) = L(x,y,Z_r)f(\theta)d\Omega. \quad (19)$$

The solid angle may be expressed in terms of the incremental area of the calibrating surface,

$$d\Omega = \cos\gamma dxdy/r^2. \quad (20)$$

where γ is the angle between the normal from the surface and the light reflected toward the center of the irradiometer. Since the calibration surface is normal to the flux direction between the irradiometer and the light trap, the position of the surface Z_r is negative and

$$\cos\gamma = -Z_r/r. \quad (21)$$

Now combining Eqs. (18)–(20) we get

$$dE(x,y,Z_r) = \epsilon(x,y)RTf(\theta)\cos\gamma\pi^{-1}r^{-2}dxdy. \quad (22)$$

The total irradiance is then

$$E(Z_r) = RT\pi^{-1}\int_{Y_1}^{Y_2}\int_{-X}^{X}\epsilon(x,y)f(\theta)\cos\gamma^{-2}dxdy. \quad (23)$$

Let us now define a factor K such that

$$K = RT\pi^{-1}\int_{Y_1}^{Y_2}\int_{-X}^{X}[\epsilon(x,y)/\epsilon(0,0)]f(\theta)\cos\gamma r^{-2}dxdy. \quad (24)$$

Dividing Eq. (23) by Eq. (24) we get an expression for the scalar irradiance in the center of the beam:

$$\epsilon(0,0) = E(Z_r)/K. \quad (25)$$

4. Total Volume Scattering Coefficient

We now have everything needed for obtaining the total volume scattering coefficient. Substituting Eq. (25) into Eq. (17) we have

$$s = EK/[E(Z_r)F]. \quad (26)$$

Equation (26) is an expression for the total volume scattering coefficient in terms of the ratio of two measurable quantities and two computable factors.

Appendix B

B. Radiometer Measurements

A measurement of the radiance of a selected portion of the scattered flux can be related to the volume scattering function $\sigma(\beta)$. In the integrating nephelometer, radiance measurements are made at scattering angles of 30° and 150°. The incremental radiance $L(x,y,\beta)$ of the beam at angle β can also be expressed by rewriting Eq. (5) as

$$L(x,y,\beta) = \epsilon(x,y)\sigma(\beta)dxdydz/da, \quad (27)$$

where da is the apparent incremental area.

The field of view of the radiometer is 2°. Therefore $\sigma(\beta)$ may reasonably be assumed to be constant within the field of view and not a function of x, y, and z.

The field of view is sufficiently cylindrical such that it can be reasonably approximated by a cylinder of radius V. For a cylindrical field of view, the radiance can now be expressed as

$$L(\beta) = \sigma(\beta)2\pi^{-1}\int_{Y_1}^{Y_2}\int_{-V}^{V}\epsilon(x,y)V^{-2}\Delta z dxdy. \quad (28)$$

For each dy, the field of view describes an ellipse such that

$$x^2/V^2 + \Delta z^2/(V^2\csc^2\beta) = 1, \quad (29)$$

where Δz is the distance of the edge of the field of view from the center of the field of view in the z dimension. Solving Eq. (29) for Δz, we have

$$\Delta z = (V^2 - x^2)^{1/2}\cos\beta. \quad (30)$$

Now Eq. (28) can be rewritten as

$$L(\beta) = 2\sigma(\beta)\csc\beta\pi^{-1}\int_{Y_1}^{Y_2}\int_{-V}^{V}\epsilon(x,y)(V^2 - x^2)^{1/2}V^{-2}dxdy. \quad (31)$$

Let us define a factor G such that

$$G(\beta) = 2\csc\beta\pi^{-1}\int_{Y_1}^{Y_2}\int_{-V}^{V}[\epsilon(x,y)/\epsilon(0,0)] \times (V^2 - x^2)^{1/2}V^{-2}dxdy. \quad (32)$$

The factor $G(\beta)$ takes into consideration the nonuniformity of the light beam and the restriction of the field of view to only a portion of the beam in the x dimension.

1. Volume Scattering Function

Combining Eqs. (25), (31), and (32) we obtain an expression for the volume scattering function in terms of the radiance of the beam and the irradiance of the calibrating surface:

$$\sigma(\beta) = L(\beta)K.[E(Z_r)G(\beta)] \quad (33)$$

Equation (33) expresses the volume scattering function in terms of measurable quantities and computable factors.

All the preceding equations are for monochromatic radiation but they are reasonably applicable to broadband radiation for sensors in the visible and very near infrared portion of the spectrum.

III. Review of Integrating Nephelometer Data

The integrating nephelometer was first described in 1970 by Duntley *et al.*[10] This first nephelometer was essentially equivalent to that in Fig. 1 except that the flux path was not folded. (The light source was rotated and moved to the position of the mirror in Fig. 1.) Two instruments were fabricated: one for mounting on a C-130 aircraft and one for ground-based use. Measurements were made both on the ground and in flight by the Visibility Laboratory with these instruments from 1968 through 1974 in locations in Thailand, the continential United States, and in Europe. The airborne nephelometer was then redesigned with a folded path as depicted in Fig. 1 and described in 1975 by Duntley *et al.*[11] This folded path instrument was used in Europe to make similar measurements from 1976 through 1980.

The measurements between 1968 and 1980 were made with various narrowband and broadband spectral sensitivities in the visible spectrum and very near infrared, with mean wavelengths from 478 to 765 nm.

A. Nephelometer Procedure

The airborne procedure was to measure the total volume scattering coefficient, the volume scattering function at 30° and 150° scattering angles, and the irradiance from the calibration surface for each filter at the lowest altitude of level flight and the highest altitude of level flight. If the altitude difference was large, the procedure included similar measurements at one or two intermediate altitudes.

When it was possible to have a ground-based station beneath or near the flight area, similar ground-based measurements were made at the beginning of the flight and at the end. Intermediate ground-based measurements were made when the flight spanned a long interval.

B. Scattering Simplification

The dual measurements of total scattering coefficient and selected volume scattering function provided complementary data for use in evaluating the shape of the volume scattering function. When the integrating nephelometer data are put into the form of the ratio to

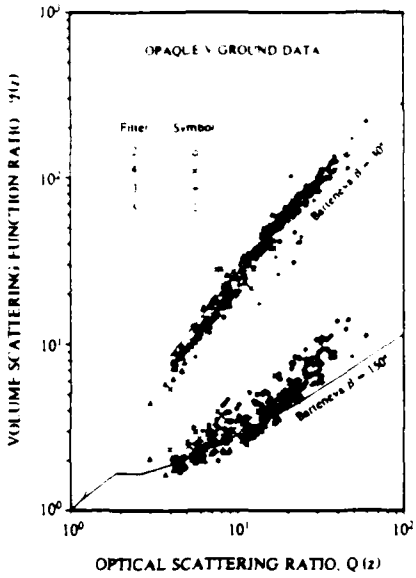

Fig. 4. Comparison of multispectral volume scattering function ratios measured by the Visibility Laboratory ground-based nephelometer with photopic ratios from Barteneva.[9] The OPAQUE V ground station operated in Sicily, Germany, and England during August and September 1978. The weather varied from clear with haze through scattered to broken clouds, to overcast. The deployment is described briefly in Ref. 13 and more fully in Ref. 14.

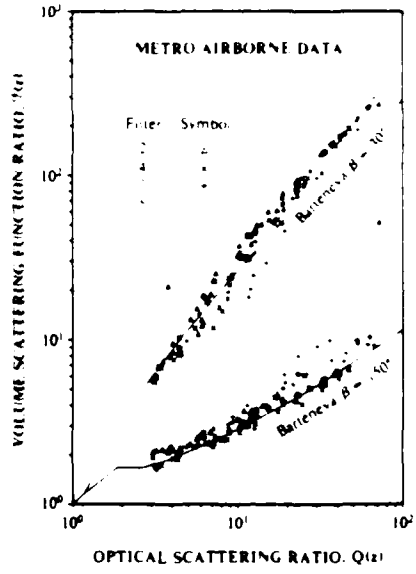

Fig. 5. Comparison of multispectral volume scattering function ratios measured by the Visibility Laboratory airborne nephelometer with photopic ratios from Barteneva.[9] The fourteen Metro flights were in the area of St. Louis, Illinois, from 11 to 24 Aug 1971. The sun was unobscured during the flights but the sky varied from clear to scattered or broken clouds, depending on the flight. The flights are described in Refs. 15 and 16.

the Rayleigh scattering, differences due to wavelength and air density changes with altitude disappear.[12]

Consider the ratio $2(z,\beta)$ of the measured volume scattering function to the Rayleigh volume scattering function ${}_R\sigma(z,\beta)$ where z is the altitude of measurement:

$$2(z,\beta) = \sigma(z,\beta)/{}_R\sigma(z,\beta) \tag{34}$$

Next consider the ratio $Q(z)$ of the measured total volume scattering coefficient to the Rayleigh total volume scattering coefficient ${}_Rs(z)$:

$$Q(z) = s(z)/{}_Rs(z) \tag{35}$$

When $2(z,\beta)$ is plotted vs $Q(z)$, simple relationships at each scattering angle emerge (see Fig. 4).

All the scattering function ratios graphed as a function of the total scattering ratios result in these simple relationships for each scattering angle regardless of the filter or altitude. The superimposed curves in Fig. 4 (ground level) and Fig. 5 (airborne) are from the Barteneva (Ref. 9) catalog of normalized volume scattering functions. Figure 6 contains a graph of the spectral response of the filtered sensor for the filters used in measuring the data in Figs. 4 and 5.

All departures from these simple relationships have disappeared on solution of instrumental problems. These relationships are derivable from the Barteneva catalog of scattering functions.

C. Barteneva Catalog

The Barteneva catalog is for the photopic sensor. This catalog is based on 624 ground-based measurements made with a nephelometer from 1955 through 1958 in various locations in the U.S.S.R. and at sea. For each normalized volume scattering function she gives a range of total volume scattering coefficients appropriate to that function.

The catalog contains values of normalized volume scattering function $\sigma(\beta)$'s for β from 0° to 180°. For our purposes we need the actual values of $\sigma(\beta)$ and s not the ratio. The median total volume scattering coefficients for each scattering class was obtained from the range given for each class. Then the ratio Q was com-

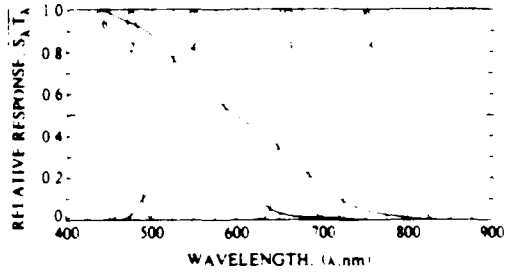

Fig. 6. Standard spectral responses for airborne filtered sensors.

Filter	Description	Mean wavelength (nm)	Effective passband (nm)
2	Blue	478	20
6	S-20 with UV cutoff	532	184
4	Pseudophotopic	557	78
3	Red	664	30
5	Near infrared	765	50

Appendix B

puted for these median s values. Similarly, the value of the median volume scattering function $\sigma(0,\beta)$ for 30° and 150° was computed by multiplying the normalized functions by the median s values. Then the ratio to Rayleigh $2(z,\beta)$ was calculated and the curves in Figs. 4 and 5 graphed for the Barteneva data.

All the integrating nephelometer data for total volume scattering and the scattering functions at 30° and 150° agree with the Barteneva catalog of gradual functions. Thus, it is reasonable to assume that the Barteneva catalog is appropriate for specifying the directional scattering for all the scattering angles from 0° to 180° for various sensors in the visible spectrum in the troposphere.

A graph of the normalized volume scattering functions as a function of scattering angle for the Barteneva catalog of gradual classes is given in Fig. 7.

Appendix B

D. Average Volume Scattering Function at 55°

The average normalized volume scattering function is

$$\int_{4\pi} [\sigma(\beta)/s]\,d\Omega \quad \int_{4\pi} d\Omega = 1/4\pi = 0.08. \tag{36}$$

The Rayleigh normalized volume scattering function can be computed from the approximation

$$_R\sigma(\beta)/_{RS} = 3(1 + \cos^2\beta)/(16\pi). \tag{37}$$

Equations (36) and (37) were combined and the ensuing equation solved to obtain the scattering angle at which the Rayleigh normalized volume scattering function is equal to the average values of $1/(4\pi)$. It was found to be 55°:

$$_R\sigma(55°)/_{RS} = 1/4\pi. \tag{38}$$

The graph in Fig. 7 is marked at scattering angle 55° and at the normalized volume scattering function equal to 0.08. From this graph we see that the scattering angle of 55° yields a reasonable approximation of the average volume scattering function for all the scattering functions except the gradual classes 9 and 10, that is,

$$\sigma(55°)/s \cong 1/4\pi) \tag{39}$$

Note that in Figs. 4 and 5 none of the total scattering coefficient ratios $Q(z)$ exceeds 100. Gradual classes 1 through 8 [$Q(8) = 114$] were encountered in the data measured from 1968 through 1981 but never 9 or 10 [$Q(9) = 201$ and $Q(10) = 237$]. Therefore, for modeling the atmospheres in the visible spectrum, it is reasonable to use Eq. (39) as part of the model assumptions.

IV. Obtaining Single Scattering Albedo from Horizon Sky Radiance

One of the implications of the measurements from the integrating nephelometer is that we can obtain the single scattering albedo from the horizon sky radiance. The single scattering albedo $u(z)$ is the total volume scattering coefficient divided by the attenuation coefficient

$$u(z) = s(z)/\alpha(z) \tag{40}$$

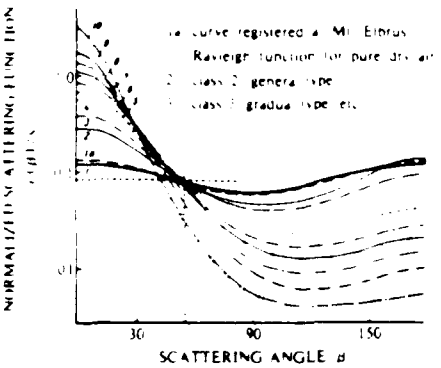

Fig. 7. Normalized volume scattering function for gradual classes from Fig. 1, Barteneva.[9]

The attenuation coefficient is the sum of the total volume scattering coefficient and the absorption coefficient

$$\alpha(z) = s(z) + a(z) \tag{41}$$

Roessler and Faxvog[17] developed equations for the horizon sky luminance as a function of the single scattering albedo after assuming both an isotropic scattering function and an isotropic luminance distribution. Their approach can be made more generally applicable to a nonisotropic scattering function and a nonisotropic radiance distribution (as well as a nonisotropic luminance distribution). We achieve this by developing equations for the horizon at a scattering angle of 55° from the sun.

A. Horizon Sky at 55° from the Sun

The path function is the radiance scattered toward the path of sight by the atmosphere within an increment of path length. Figure 8 graphically depicts path function, path radiance, sky radiance, and equilibrium radiance.

The equation for the path function $L_*(z,\theta,55°)$ at 55° scattering angle from the sun can be expressed with the sun component separate from the sky–terrain component in a manner similar to Eq. (3.2) of Ref. 18:

$$L_*(z,\theta,55°) = {}_sE(z)\sigma(z,55\beta) + \int_{4\pi} L(z,\theta',\phi')\sigma(z,\beta)\,d\Omega + L_*(z) \tag{42}$$

The θ is the zenith angle of the path of sight at scattering angle β, ${}_sE(z)$ is the sun scalar irradiance, $L(z,\theta',\phi')$ is the sky or terrain radiance at zenith angle θ' and azimuth ϕ', and $L_*(z)$ is the emitted path function due to absorption. Substituting Eq. (39) into Eq. (42) and assuming that the sky–terrain or diffuse scalar irradiance ${}_dE(z)$ is isotropic we get

$$L_*(z,\theta,55°) = {}_sE(z)s(z)/4\pi + {}_dE(z)s(z)/4\pi + L_*(z) \tag{43}$$

Since the total scalar irradiance $E(z)$ is the sun scalar irradiance plus the sky–terrain scalar irradiance, Eq. (43) can be written as

$$L_*(z,\theta,55\beta) = E(z)s(z)/4\pi + L_*(z) \tag{44}$$

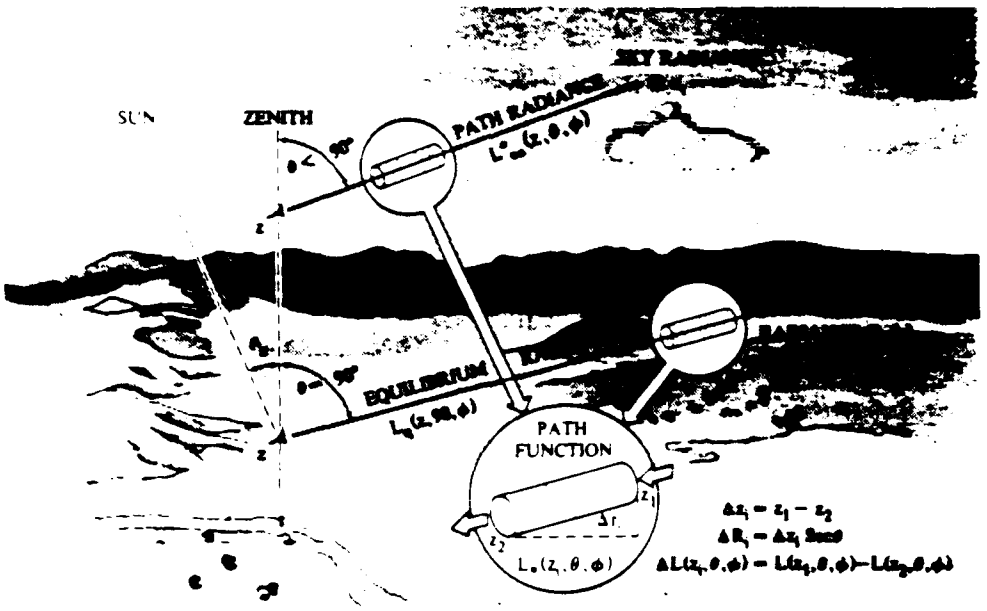

Fig. 4. Relationships between path function, path radiance, sky radiance and equilibrium radiance. Path function is the radiance scattered toward the sensor by the atmospheric constituents within an incremental unit of path length. Path radiance is the cumulative transmitted radiance of the incremental path function elements along the specified path of sight. Sky radiance is a special form of path radiance in which the path of sight is between a sensor and the boundary of the atmosphere and is cloud free. Equilibrium radiance is a special form of path radiance, which is only directly observable along uniform horizontal paths of sight, in which an equilibrium exists between the radiance gained from an additional increment of path function and the radiance loss due to attenuation in the increment.

The point function equilibrium radiance is equal to the path function divided by the attenuation coefficient [Eq. (11), Ref. 2]:

$$L_{eq}(z,90,55\overline{3}) = L_p(z,90,55\overline{3})/\alpha(z). \quad (45)$$

Also the emitted path function can be expressed as [Eq. (2.7), Ref. 18]:

$$L_p(z) = \alpha(z)L(\lambda,T). \quad (46)$$

The $L(\lambda,T)$ is the blackbody radiance which is a function of wavelength λ and absolute temperature T according to the classical blackbody equation.[19] Now, dividing both sides by the attenuation coefficient and expressing the emitted path function according to Eq. (46) we get an equation for the equilibrium radiance

$$L_{eq}(z,90,55\overline{3}) = \alpha(z)L(\lambda,T)/\alpha(z)4\pi = \omega(z)L(\lambda,T)/4\pi. \quad (47)$$

Equation (47) can be expressed in terms of the single scattering albedo ω [from Eqs. (40) and (41)] as

$$L_{eq}(z,90,55\overline{3}) = \omega(z)/4\pi = [1-\omega(z)]L(\lambda,T). \quad (48)$$

For a scattering, absorbing, and emitting atmosphere which is horizontally homogeneous, the general equation for the horizon sky radiance [Eq. (2.57), Ref. 18] can be written for the horizon at 55° scattering angle as

$$L_s(z,90,55\overline{3}) = L_{eq}(z,90,55\overline{3})[1-T_s(z,90)]. \quad (49)$$

The $T_s(z,90)$ is the horizontal radiance transmittance from out of the atmosphere to altitude z. Substituting Eq. (48) into Eq. (49), the horizon sky radiance at 55° becomes

$$L_s(z,90,55\overline{3}) = \omega(z)/4\pi + [1-\omega(z)]L(\lambda,T)[1-T_s(z,90)]. \quad (50)$$

Solving for the single scattering albedo we get

$$\omega(z) = \frac{L_s(z,90,55\overline{3})[1-T_s(z,90)]-L(\lambda,T)}{L(\lambda,T)4\pi[1-T_s(z,90)]}. \quad (51)$$

The above equation assumes that the attenuation coefficient is horizontally isotropic and therefore the horizon sky must be cloud free. With this equation the single scattering albedo can be obtained from a measurement of the horizon sky radiance, the temperature, the horizontal transmittance, and the total scalar irradiance.

B. Visible Spectrum

In the visible spectrum $L(\lambda,T)$ is negligible. Therefore Eq. (51) becomes

$$\omega(z) = L_s(z,90,55\overline{3})4\pi/E(z)[1-T_s(z,90)]. \quad (52)$$

Also for wavelengths ≤ 555 nm, the sea level $T_s(0,90)$ is always negligible even for a Rayleigh atmosphere. Thus Eq. (52) becomes

$$\omega(0) = L_s(0,90,55\overline{3})4\pi/E(0). \quad (53)$$

Therefore the single scattring albedo can be determined at sea level by measuring the horizon sky at 55° and the total scalar irradiance.

The above equations are the monochromatic radiation. However, they are also applicable to broadband

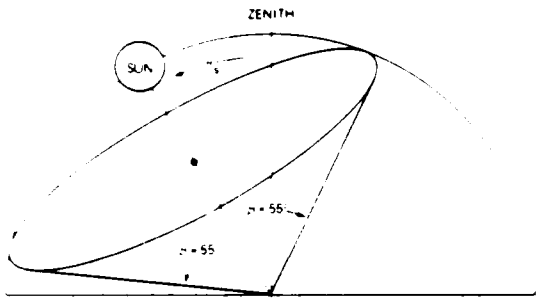

Fig. 9 Sketch of sky radiances at scattering angle from the sun of 55°.

radiation for sensors in the visible spectrum. Thus Eq. (53) applies to the photopic sensor as well as other sensors with mean wavelengths ≤555 nm.

V. Obtaining Scattering Transmittance from Sky Radiance Ratios

A second implication of the integrating nephelometer data utilizes the average volume scattering concept for obtaining space-to-earth scattering transmittance from sky radiance ratios.

A. Negligible Absorption

When absorption is negligible, the general equation for the equilibrium radiance at 55° scattering angle [Eq. (48)] reduces to

$$L_q(z,\theta,55b) = \epsilon(z)/(4\pi). \tag{54}$$

Rearranging the equilibrium radiance form of the equation of transfer [Eq. (2.17), Ref 18] we get

$$[L(z,\theta,55\beta) - L_q(z,\theta,55\beta)]^{-1} dL(z,\theta,55\beta) = -s(z)dr, \tag{55}$$

where dr is the incremental path length. The total scattering coefficient $s(z)$ has been substituted in Eq. (55) for the attenuation coefficient since aborption is negligible.

Multiplying the left side by $\epsilon(z)/\epsilon(z)$ and substituting in Eq. (54), Eq. (55) can be expressed in integral form as

$$\int_{L_{q\epsilon}}^{L_{\infty\epsilon}} \left[\frac{L(z,\theta,55\beta)}{\epsilon(z)} - 0.08\right]^{-1} d\left[\frac{L(z,\theta,55\beta)}{\epsilon(z)}\right] = -\int_0^r s(z)dr \tag{56}$$

Equation (56) can be integrated. The result of the integration is

$$\frac{L_\epsilon(z,\theta,55\beta)}{\epsilon(z)} = L_{0\epsilon}(z_t,\theta,55\beta)_s T_\epsilon(z,\theta)/\epsilon(z_t) + 0.08[1 - {}_sT_\epsilon(z,\theta)], \tag{57}$$

where ${}_sT_\epsilon(z,\theta)$ is the radiance transmittance due to scattering at angle θ over path length r.

For sky radiance at 55° scattering angle, the inherent radiance out of the atmosphere is equal to zero and Eq. (57) becomes

$$\frac{L_\epsilon(z\theta,55\beta)}{\epsilon(z)} = 0.08[1 - {}_sT_\epsilon(z,\theta)] \tag{58}$$

B. Sky Radiance Ratio at 55°

If we divide Eq. (58) by a similar equation written for a second path of sight at zenith angle θ', we get

$$L_\epsilon(z,\theta,55\beta)/L_\epsilon(z,\theta',55\beta) = [1 - {}_sT_\epsilon(z,\theta)]/[1 - {}_sT_\epsilon(z,\theta')] \tag{59}$$

The scalar irradiances drop out. Thus the ratio of two sky radiances at a scattering angle of 55° is solely a function of the scattering transmittance.

Slant path radiance transmittance can also be written as a function of the vertical transmittance and the relative air mass which we will abbreviate as $m(\theta)$, thus

$$L_\epsilon(a,\theta,55\beta)/L_\epsilon(z,\theta',55\beta) = [1 - {}_sT_\epsilon(z,0)^{m(\theta)}]/[1 - {}_sT_\epsilon(z,0)^{m(\theta')}] \tag{60}$$

Although Eq. (60) cannot be solved directly for vertical transmittance, it can be solved by iterative means. Error analysis indicates that the zenith angle difference $\theta - \theta'$ should be large to minimize the error in the resultant vertical transmittance. Figure 9 illustrates the position of sky radiances at 55° scattering angle for a sun zenith angle of 30°.

The scattering optical thickness ${}_st_\epsilon(z)$ is related to the vertical transmittance by

$${}_sT_\epsilon(z,0) = \exp[-{}_st_\epsilon(z)] \tag{61}$$

C. Visible Spectrum

In the visible spectrum, absorption is negligible except for ozone. The total vertical radiance transmittance $T_\epsilon(z,0)$ would thus be approximated by the product of the scattering transmittance times the ozone transmittance ${}_aT_\epsilon(z,0)$:

$$T_\epsilon(z,0) = {}_sT_\epsilon(z,0)_aT_\epsilon(z,0). \tag{62}$$

To illustrate the use of Eqs. (60) and (62), we refer to an extensive set of sky radiance and solar transmissometer data taken on the Visibility Laboratory rooftop in 1964 (described briefly in Ref. 13). The transmittances have been checked for consistency and validity. The spectral sensitivity of the sensor with the four different filters used to measure these data is illustrated in Fig. 10.

A day is considered to be optically stable when the vertical transmittance does not change with time. The atmosphere at the Visibility Laboratory on 2 Sept. 1964 was optically stable during the afternoon as verified in Sec. 3.3 of Ref. 18. Thus evaluation of the scattering transmittances throughout the afternoon should give us an estimate of the precision of the sky ratio estimation method for broadband sensors in the visible. Equation (60) was evaluated for all sky radiances at 55° ± 2.5° scattering angle for θ from 81.6° to 64.7° and θ' from 64.7° to 2.8°. Later error analyses indicated that some of these zenith angle combinations are less error prone than others. Hence, the average scattering

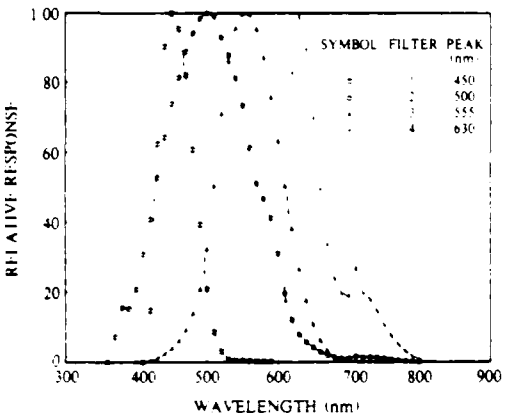

Fig. 10. Standard spectral responses for Visibility Laboratory rooftop 1964 filtered sensors.

Filter	Description	Mean wavelength (nm)	Effective passband (nm)
1	Blue	459	58
2	S-11	505	152
3	Photopic	560	107
4	Red	661	61

transmittances used to obtain the ratios in Table I are less accurate than can be obtained with a smaller yet better selection of zenith angle combinations for the sky radiance ratios. However, Table I is presented as a first approximation.

The transmittance ratios in Table I are the average scattering transmittances based on Eq. (60), times the ozone transmittance, divided by the transmittance from the solar transmissometer. The ozone transmittance is noted at the bottom of each column. The ozone vertical transmittances were based on the total ozone for the U.S. Standard Atmosphere[20] and the spectral ozone absorption values of Vigroux[21] (which are in good agreement with the Inn and Tanaka[22] values).

The average transmittance ratio is nearest to 1 (the ideal) for filter 1 which is a relatively narrowband filter whose spectral sensitivity is at wavelengths with the least atmospheric absorption. The near-noon (small sun zenith angle) data compare least well. The accuracy is, however, sufficient to warrant further development of the method to improve the precision level.

Use of sky radiances at 55° scattering angle should be an improvement on the sky ratio methods.[23] That method, which stemmed from the nomographic method of Kushpil and Petrova,[24] used sky radiances at all scattering angles. They suggested use of ratios at 57.2° scattering angle for the visible spectrum and 53.9° for the near-infrared portion of the spectrum but did not give a theoretical basis for their nomograph or for the selection of these angles. The use of 55° scattering angle in Eq. (60) is reasonably consistent with their angles.

VI. Summary

Equations were derived for relating the integrating nephelometer measurements to the total volume scattering coefficient and the volume scattering functions at 30° and 150°. These equations take into consideration the effects of nonuniformity of the light beam over the cross-sectional area, variations in true cosine acceptance of the irradiometer, and truncation of the optical integration near scattering angles of 0° and 180°.

When the nephelometer data are graphed in the form of the ratio $2(z,\beta)$ (measured to Rayleigh volume scattering function) as a function of the ratio $Q(z)$ (measured to Rayleigh total volume scattering coefficient), simple relationships emerge for each scattering angle. All visible spectrum broadband measurements at all altitudes in the troposphere (based on ground-based to 6-km measurements) measured all over the world between 1968 and 1980 result in these predictable relationships. These relationships are derivable from the Barteneva catalog of proportional volume scattering functions. This is a tremendous simplification for modelers of the radiation field and of contrast transmittance. The Hering model[25] for predicting contrast, contrast transmittance, and sky radiance makes use of this simplification.

It is not easy to obtain a measure of single scattering albedo or of scattering optical thickness. The inte-

Appendix B

Table I. Comparison of Transmittance Determination Procedures (Sky Radiance Ratio Method vs Solar Transmissometer)

Nominal sun zenith angle θ, (degrees)	Total transmittance ratio [From Eq. (60 and 62) and solar transmissometer measurements]			
	Filter 1 $\bar{\lambda}$ = 459 nm	Filter 2 $\bar{\lambda}$ = 505 nm	Filter 3 $\bar{\lambda}$ = 560 nm	Filter 4 $\bar{\lambda}$ = 661 nm
24	0.954	0.891	0.894	0.900
30	0.944	0.893	0.894	0.905
40	1.045	1.011	1.030	1.038
50	1.045	1.013	1.041	1.047
60	1.034	1.006	1.031	1.044
70	1.030	1.014	1.042	1.050
80	1.002	0.998	1.031	1.045
Average	1.008	0.975	0.995	1.004
Standard deviation	0.043	0.057	0.069	0.070
Ozone contribution ${}_oT_\infty(0,0)$	0.996	0.984	0.969	0.978

grating nephelometer has provided a data set, the analysis of which has led to simplifications and finally to the development of methods for obtaining single scattering albedo and scattering optical thickness.

The method for obtaining the single scattering albedo for broadband sensors in the visible uses a measurement of the horizon sky radiance at 55° scattering from the sun and a measurement of the total scalar irradiance. Nonvisible spectrum albedo requires additional measurements of ambient temperature and horizontal transmittance.

The method for obtaining scattering optical thickness uses measurements of sky radiance at 55° scattering angle from the sun, made at two disparate zenith angles. This method is appropriate for monochromatic or broadband measurements in the visible portion of the spectrum.

Appendix B

We wish to acknowledge the contribution to the theoretical analysis by Almerican Boileau and the development of the idea of the average volume scattering function at 55° by Wayne Hering. This work was performed by the authors at the Visibility Laboratory, University of California at San Diego, for the Air Force Geophysics Laboratory, Air Force Systems Command, United States Air Force, under contract F19628-78-C-0200. The writing and publication of this article was done at Viz. Ability under United States Army Research Office contract DAAG29-84-C-0014. We wish to thank Judith Olson for technical editing assistance.

References

1. R. W. Johnson, "Daytime Visibility and Nephelometer Measurements Related to its Determination," Atmos. Environ. **15**, 1835 (1981).
2. S. Q. Duntley, A. R. Boileau, and R. W. Preisendorfer," Image Transmission by the Troposphre I," J. Opt. Soc. Am. **47**, 499 (1957).
3. W. G. Driscoll and W. Vaughan, Eds., *Handbook of Optics* (McGraw-Hill, New York, 1978).
4. R. G. Beuttell and A. W. Brewer, "Instruments for the Measurement of the Visual Range," J. Sci. Instrum. **26**, 357 (1949).
5. W. E. K. Middleton, *Vision Through the Atmosphere* (U. Toronto Press, Toronto, 1952), Sec. 9.4.4.
6. P. Crosby and B. W. Koerber, "Scattering of Light in the Lower Atmosphre," J. Opt. Soc. Am. **53**, 358 (1963).
7. R. J. Charlson, H. Horvath, and R. F. Pueschall, "The Direct Measurement of Atmospheric Light Scattering Coefficient for Studies of Visibility and Pollution," Atmos. Environ. **1**, 469 (1967).
8. H. Horvath and K. E. Noll, "The Relationship Between Atmospheric Light Scattering Coefficient and Visibility," Atmos. Environ. **3**, 543 (1969).
9. O. D. Barteneva, "Scattering Functions of Light in the Atmospheric Boundary Layer," Bull. Acad. Sci. USSR Geophys. Ser. (English edition translated by AGU) No. 12, 1237 (1960).
10. S. Q. Duntley, R. W. Johnson, J. I. Gordon, and A. R. Boileau, "Airborne Measurements of Optical Atmospheric Properties at Night," U. California, Scripps Institution of Oceanography, Visibility laboratory, SIO Ref. 70-7, AFCRL-70-0137, NTIS No. AD 870 734 (1970).
11. S. Q. Duntley, R. W. Johnson, and J. I. Gordon, "Airborne Measurements of Optical Atmospheric Properties, Summary and Review II," U. California, Scripps Institution of Oceanography, Visibility Laboratory, SIO Ref. 75-26, AFCRL-TR-75-0477, NITIS No. ADA 022 675 (1975).
12. R. W. Johnson, W. S. Hering, J. I. Gordon, B. W. Fitch, and J. E. Shields, "Preliminary Analysis and Modeling Based upon Project OPAQUE Profile and Surface Data," U. California, Scripps Institution of Oceanography, Visibility Laboratory, SIO Ref. 80-7, AFGL-TR-79-0285, NTIS No. ADB 052 172L (1979) and Ref. 2.
13. S. Q. Duntley, R. W. Johnson, and J. I. Gordon, "Airborne Measurements of Optical Atmospheric Properties, Summary and Review III," U. California, Scripps Institution of Oceanography, Visibility Laboratory, SIO Ref 79-5, AFGL-TR-78-0286, NITS No. ADA 073 121 (1978).
14. R. W. Johnson and J. I. Gordon, "Airborne Measurements of Atmospheric Volume Scattering Coefficients in Northern Europe, Summer 1978," U. California, Scripps Institution of Oceanography, Visibility Laboratory, SIO Ref. 80-20, AFGL-TR-80-0207 (1980).
15. S. Q. Duntley, R. W. Johnson, and J. I. Gordon "Airborne Measurements of Optical Atmospheric Properties in Southern Illinois," U. California, Scripps Institution of Oceanography, Visibility Laboratory, SIO Ref. 73-24, AFCRL-TR-73-0422 (1973).
16. S. Q. Duntley, R. W. Johnson, and J. I. Gordon, "Airborne and Ground-Based Measurements of Optical Atmospheric Properties in Southern Illinois," U. California, Scripps Institution of Oceanography, Visibility Laboratory, SIO Ref. 74-25, AFCRL-TR-74-0298, NTIS No. ADA 013 14 (1974).
17. D. M. Roessler and F. R. Faxvog, "Visibility in Absorbing Aerosols," Atmos. Environ. **15**, 151 (1981).
18. J. I. Gordon, "Implications of the Equation of Transfer Within the Visible and Infrared Spectrum," U. California, Scripps Institution Oceanography, Visibility Laboratory, SIO Ref. 83-10, AFGL-TR-82-0223 (1982).
19. W. L. Wolfe, "Radiation Theory," in *The Infrared Handbook*, W. L. Wolfe and G. J. Zissis, Eds. (U.S. GPO, Washington, D.C., 1978).
20. *U.S Standard Atmosphere, 1976* (Superintendent of Documents, U.S. GPO, Washington, D.C. 20402, 1976).
21. E. Vigroux, "Etude experimentale de l'absorption de l'ozone," Ann. Phys. Paris **8**, 742 (1953).
22. E. C. Y. Inn and Y. Tanaka, "Absorption Coefficient of Ozone in the Ultraviolet and Visible Regions," J. Opt. Soc. Am. **43**, 870 (1953).
23. J. I. Gordon and R. W. Johnson, "Equilibrium Radiance Model Applications and Comparisons to Atmospheric Measurements and Rayleigh Models," Appl. Opt. **23**, 3363 (1984).
24. V. I. Kushpil and L. F. Petrova, "Determination of the Atmospheric Transmittance from Sky Brightness Distribution," Sov. J. Opt. Technol. **38**, 191 (1971).
25. R. W. Johnson and W. Hering, "Measurements of Optical Atmospheric Quantities in Europe and Their Application to Modelling Visible Spectrum Contrast Transmittance," AGARD Proceedings on Special Topics in Optical Propagation, AGARD-CP-300, pp. 14-1-14-12 (1981). Also, the Barteneva catalog is represented analytically in the form of Henyey-Greenstein functions in W. S. Herin, "Assessment of Operational Techniques for Estimating Visible Spectrum Contrast Transmittance," Proc. Soc. Photo-Opt. Instrum. Eng. **205**, 119 (1981).

Reprinted from Applied Optics, Vol. 24, page 3381, October 15, 1985

New uses for the solar almucantar

Jacqueline I. Gordon

Appendix C

The basic equation for the solar almucantar (same zenith angle as the sun) sky radiance is developed. Methods are reviewed for using the solar almucantar sky radiance to obtain space-to-sensor radiance transmittance and to test the optical stability of the atmosphere. Almucantar sky radiances on optically stable days can also be used to test for spurious sun reflectance in a sky radiance photometer. Examples of such a use are given. A new method is also developed for obtaining the aerosol optical thickness from solar almucantar radiances.

I. Introduction

The almucantar is the portion of the sky at a constant zenith angle. The solar almucantar is at the zenith angle of the sun θ_s. This is illustrated in Fig. 1. Solar almucantar sky radiances have special characteristics which make them useful for obtaining total optical thickness[1] and aerosol optical thickness.[2] Solar almucantar radiances can also be used to determine if the day is optically stable.[3]

The above methods provided the basis for developing two additional uses for the solar almucantar. Solar almucantar sky radiance measurements on an optically stable day can be used to test for internal reflectance problems in a radiometer. Finally, solar almucantar radiances at 55° and 125° from the sun can be used to obtain aerosol optical thickness.

The theory and equations are for monochromatic radiation, however applicability to radiance for broader passbands will be indicated where appropriate. The notation used is that adopted by the Visibility Laboratory[4] and modified to correspond to OSA recommendations in Sec. 1 of Driscoll and Vaughan.[5]

II. Solar Almucantar Sky Radiance

A. Basic Equation

A basic equation for the solar almucantar sky radiance can be developed from the general equation for path radiance. The sky radiance in the solar almucantar is the path radiance $L_a^*(z,\theta_s,\phi)$ from out-of-the atmosphere to the sensor at altitude z. The path of sight of the sensor is toward zenith angle θ_s of the sun and azimuth ϕ. The path radiance is the integral of the path function $L_*(z,\theta_s,\phi)$ times the intervening radiance transmittance [Ref. 4, Eq. (17)]:

$$L_a^*(z,\theta_s,\phi) = \int_{f(\infty)}^{f(z)} L_*(z_i,\theta_s,\phi)T_n(z,\theta_s)dr. \quad (1)$$

The differential path length dr is always non-negative. In the plane-parallel case (and in the curved earth case for paths of sight at zenith angles θ = 0–70° and 110–180°) the incremental path length Δr is defined as

$$\Delta r = \Delta z \sec\theta. \quad (2)$$

The Δz is defined as $z_1 - z_2$ (the subscripts increase in the flux direction), see Fig. 2.

I have expressed the limits of the integral in Eq. (1) as a function of the altitude at the beginning and end of the path length r since this will be helpful later in establishing some equivalencies.

The path function can be expressed as the sum of the scattered sun component, a scattered sky–terrain component and an emitted component $L_{*a}(z)$ [Eqs. (4) and (5), Ref 6 and Eqs. (2.3) and (2.4), Ref. 7]:

$$L_*(z,\theta_s,\phi) = {}_s\mathcal{E}(z)\sigma(z,\beta) + \int_{4\pi} L(z,\theta',\phi')\sigma(z,\beta')d\Omega + L_{*a}(z). \quad (3)$$

The ${}_s\mathcal{E}(z)$ is the sun scalar irradiance, $\sigma(z,\beta)$ is the volume scattering function, and β is the scattering angle. Factoring out the sun scalar irradiance, Eq. (3) becomes

$$L_*(z,\theta_s,\phi) = {}_s\mathcal{E}(z)\left[\sigma(z,\beta) + \int_{4\pi} L(z,\theta',\phi')\sigma(z,\beta')d\Omega/{}_s\mathcal{E}(z) + L_{*a}(z)/{}_s\mathcal{E}(z)\right]. \quad (4)$$

Let the last two terms be designated by the function $C(z)$ such that

$$C(z) = \int_{4\pi} L(z,\theta',\phi')\sigma(z,\beta')d\Omega/{}_s\mathcal{E}(z) + L_{*a}(z)/{}_s\mathcal{E}(z). \quad (5)$$

The author is with Viz. Ability, 2941 NW Ashwood Drive, Corvallis, Oregon 97330.
Received 3 May 1985.
0003-6935/85/203381-09$02.00/0.

Appendix C

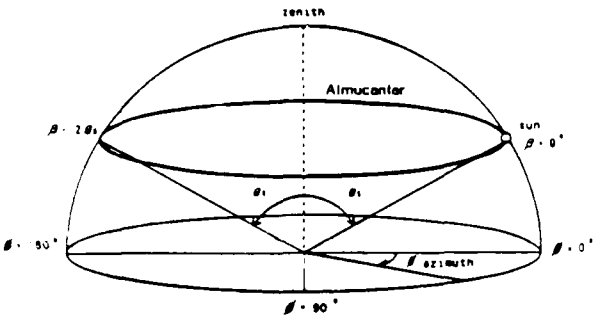

Fig. 1. Solar almucantar sky and radiance. Angle from sun β is found from $\cos\beta = \sin^2\theta_s \cos\phi + \cos^2\theta_s$.

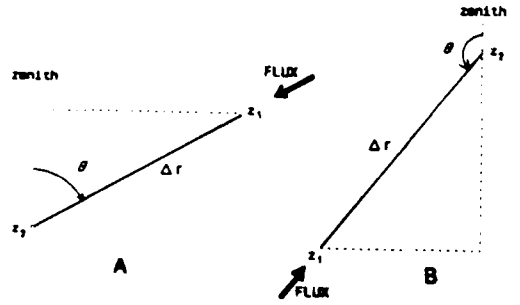

Fig 2. Incremental path length geometry for upward and downward paths of sight: $\Delta r = (z_1 - z_2)\sec\theta$; *A*, upward path of sight ($\theta < 90°$) with flux downward; *B*, downward path of sight ($\theta > 90°$) with flux upward.

Substituting Eqs. (4) and (5) into Eq. (1), it becomes

$$L_\infty^*(z,\theta_s,\phi) = \int_{f(\infty)}^{f(z)} {}_s\mathcal{E}(z_i) T_n(z,\theta_s)[\sigma(z_i,\beta) + C(z_i)]dr. \quad (6)$$

The sun scalar irradiance and the transmittance can be expressed as a function of the sun irradiance out-of-the atmosphere ${}_s\mathcal{E}(\infty)$ and the attenuation coefficient $\alpha(z)$ as follows:

$${}_s\mathcal{E}(z_i)T_n(z,\theta_s) = {}_s\mathcal{E}(\infty)\exp\left[-\int_{f(\infty)}^{f(z_i)}\alpha(z)dr - \int_{f(z_i)}^{f(z)}\alpha(z)dr\right]. \quad (7)$$

The two integrals can be combined and expressed in terms of the limits $f(\infty)$ to $f(z)$ which is equivalent to the total transmittance, thus

$${}_s\mathcal{E}(z_i)T_n(z,\theta_s) = {}_s\mathcal{E}(\infty)T_\infty(z,\theta_s) = {}_s\mathcal{E}(z). \quad (8)$$

Now substituting into Eq. (6), the sun irradiance can be taken out of the integral thus

$$L_\infty^*(z,\theta_s,\phi)/{}_s\mathcal{E}(z) = \int_{f(\infty)}^{f(z)} [\sigma(z,\beta) + C(z)]dr. \quad (9)$$

The quantity in the square brackets is a function of altitude and not of zenith angle, therefore

$$\int_{f(\infty)}^{f(z)} [\sigma(z,\beta) + C(z)]dr = [m_\infty(z,\theta_s)/m_\infty(z,0)] \int_\infty^z [\sigma(z,\beta) + C(z)]dz. \quad (10)$$

where $m_\infty(z,\theta_s)/m_\infty(z,0)$ is the relative optical air mass at θ_s. For sensor altitudes up to 6 km (Ref. 8) the sea level values of relative air mass can be used for sun zenith angles from 0° to 86°. So for convenience the air mass notation will be shortened to $m(\theta_s)$. Substituting back into Eq. (9) it becomes

$$L_\infty^*(z,\theta_s,\phi)/[{}_s\mathcal{E}(z)m(\theta_s)] = \int_\infty^z [\sigma(z,\beta) + C(z)]dz. \quad (11)$$

The right-hand term can be separated into two parts:

$$\int_\infty^z [\sigma(z,\beta) + C(z)]dz = \int_\infty^z \sigma(z,\beta)dz + \int_\infty^z C(z)dz. \quad (12)$$

Now let us define an optical thickness function $\tau_\infty(z,\beta)$ such that

$$\tau_\infty = \int_\infty^z \sigma(z,\beta)dz. \quad (13)$$

The integral of the optical thickness function over 4π is the optical thickness due to scattering ${}_st_\infty(z)$:

$${}_st_\infty(z) = \int_{4\pi} \tau_\infty(z,\beta)d\Omega, \quad (14)$$

since the optical thickness due to scattering is the integral of the total scattering coefficient with altitude:

$${}_st_\infty(z) = \int_\infty^z s(z)dz. \quad (15)$$

Substituting Eq. (13) into Eq. (11) it becomes

$$L_\infty^*(z,\theta_s,\phi)/[{}_s\mathcal{E}(z)m(\theta_s)] = \tau_\infty(z,\beta) + \int_\infty^z C(z)dz. \quad (16)$$

This is the basic equation for the radiance in the solar almucantar and how it relates to the sun scalar irradiance, the optical air mass, the optical thickness function and one additive component defined by Eq. (5).

For simplicity the right-hand ratio is defined[1,2] as a function $\mu(z,\beta)$:

$$\mu(z,\beta) = L_\infty^*(z,\theta_s,\beta)/[{}_s\mathcal{E}(z)m(\theta_s)]. \quad (17)$$

III. Optical Stability and Spurious Sun Reflectance

The method for determining spurious sun reflectance in a radiometer (when the day is optically stable) is based on the methods of testing optical stability. Therefore, we will start with a detailed review of the optical stability tests.

A. Optical Stability

The day is considered to be optically stable when the atmospheric radiance transmittance (or total optical thickness) does not change with time.

1. Transmittance from Solar or Solar Almucantar Radiances

When the day is optically stable, measurements of the apparent sun radiance ${}_sL_\infty(z,\theta_s,0)$ made over a large range of sun zenith angle yield a good measure of total transmittance $T_\infty(z,0)$ and the inherent sun radiance ${}_sL_0(\infty)$:

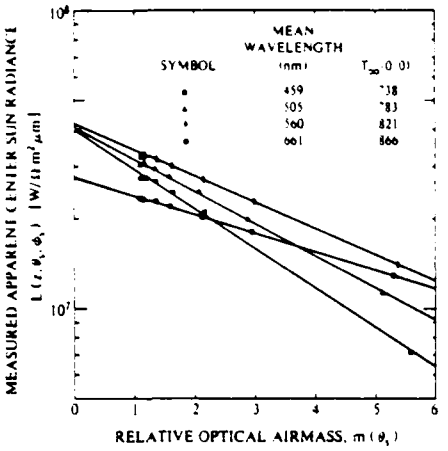

Fig. 3. Langley graph of measured apparent center sun radiance for 2 Sept. 1964.

$$ {}_{\lambda}L_{\infty}(z,\theta_s,0) = {}_{\lambda}L_{0}(\infty)T_{\infty}(z,0)^{m(\theta_s)}. \tag{18}$$

Taking the log of both sides of Eq. (18) it becomes

$$\log {}_{\lambda}L_{\infty}(z,\theta_s,0) = \log {}_{\lambda}L_{0}(\infty) + m(\theta_s)\log T_{\infty}(z,0), \tag{19}$$

Graphs of apparent sun radiance on semilog paper of log apparent sun radiance vs air mass yield the typical Langley (or Bouguer) graph where log inherent sun radiance is the intercept and log transmittance is the slope, see Fig. 3.

Variations of Eq. (16) give both another method for obtaining the total transmittance and several ways of checking the optical stability. Equation (16) can also be written as

$$L^{*}_{\infty}(z,\theta_s,\beta)/m(\theta_s) = T_{\infty}(z,0)^{m(\theta_s)}{}_{\lambda}\varepsilon(\infty)\left[\tau_{\infty}(z,\beta) + \int_{\infty}^{z} C(z)dz\right]. \tag{20}$$

Taking the log of both sides, Eq. (20) becomes

$$\log[L^{*}_{\infty}(z,\theta_s,\beta)/m(\theta_s)] = m(\theta_s)\log T_{\infty}(z,0) + \log A, \tag{21}$$

where

$$A = {}_{\lambda}\varepsilon(\infty)\left[\tau_{\infty}(z,\beta) + \int_{\infty}^{z} C(z)dz\right]. \tag{22}$$

For an optically stable day, A should be constant for a given angle from the sun. Thus, the sky radiance at a constant β in the solar almucantar can be used to obtain the radiance transmittance when measured over a large range of air mass values on an optically stable day. A semilog graph of $\log[L_{\infty}^{*}(z,\theta_s,\beta)/m(\theta_s)]$ vs air mass would be linear with a slope of log transmittance and an intercept at log A, see Fig. 4. The transmittance obtained from the sun radiance using Eq. (19) and the transmittance obtained from the sky radiance in the solar almucantar are then averaged to obtain the most accurate value.

Tashenov[1] used this method with measurements of the solar aureole to obtain spectral transmittance in the 410–735-nm region.

2. *Tests to Determine Optical Stability*

Pyasxovskaya-Fesenkova[3] outlines two tests for optical stability as well as a unique equation for transmittance which is valid only for optically stable days.

The first test is to graph the function $\mu(z,\beta)$ vs $m(\theta)$ for a constant scattering angle β. As can be seen from Eqs. (16) and (17), if the day is optically stable the right-hand term is constant. Therefore this graph should result in a horizontal straight line. Figure 5(a) is an example of this test. For an optically stable day, the function $\mu(z,\beta)$ is constant:

$$\mu(z,\beta) = B, \tag{23}$$

where

$$B = \tau_{\infty}(z,\beta) + \int_{\infty}^{z} C(z)dz. \tag{24}$$

O'Neill and Miller[9] used this test to indicate optical stability or lack thereof in conjunction with their solar beam and solar aureole measurements.

The second test for optical stability is to graph the ratio $[L_{\infty}^{*}(z,\theta_s,\beta)/{}_{\lambda}\varepsilon(z)]$ vs relative air mass for a constant β. The graph should result in a straight line going through the origin on an optically stable day. To understand this, Eq. (16) is rewritten in the form:

$$L^{*}_{\infty}(z,\theta_s,\beta)/{}_{\lambda}\varepsilon(z) = m(\theta_s)B. \tag{25}$$

The B is now the slope and the intercept is zero. Figure 5(b) is an example of this test.

If the day is optically stable a graph of solar almucantar radiance at a constant scattering angle vs air mass will yield a value of transmittance as follows. If Eq. (23) is written in the form

$$L^{*}_{\infty}(z,\theta_s,\beta) = {}_{\lambda}\varepsilon(\infty)T_{\infty}(z,0)^{m(\theta_s)}m(\theta_s)B \tag{26}$$

and differentiated (only the sky radiance and the air mass are variables, the inherent sun scalar irradiance B and the transmittance are constant), it becomes

$$dL^{*}_{\infty}(z,\theta_s,\beta) = B_{\lambda}\varepsilon(\infty)T_{\infty}(z,0)^{m(\theta_s)}dm(\theta_s)[1 + m(\theta_s)\ln T_{\infty}(z,0)]. \tag{27}$$

Equation (27) is only valid when the angle from sun is constant, the vertical transmittance from space to sen-

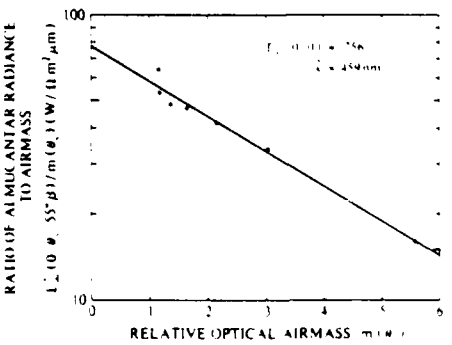

Fig. 4. Almucantar radiance to air mass ratio vs relative optical air mass for 2 Sept. 1964.

Appendix C

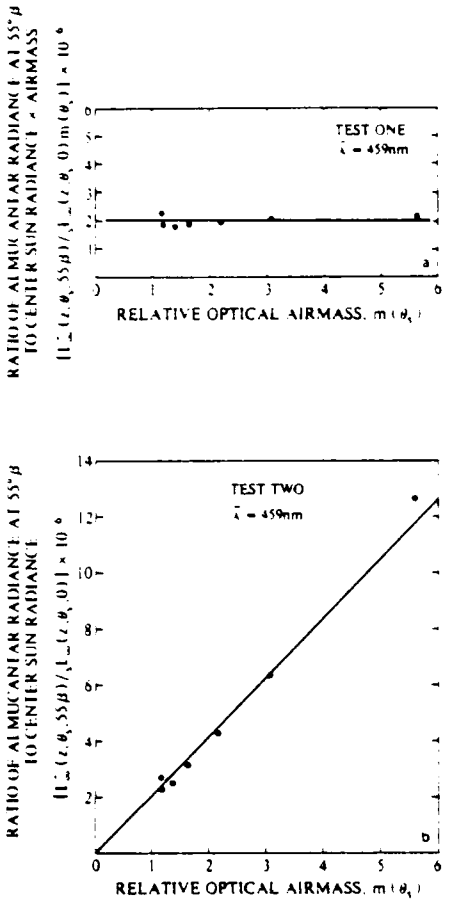

Fig. 5. Graphs to test atmospheric optical stability for 2 Sept. 1964, filter 1 (mean wavelength 459 nm): (a) test one, Eq. (30); (b) test two, Eq. (32).

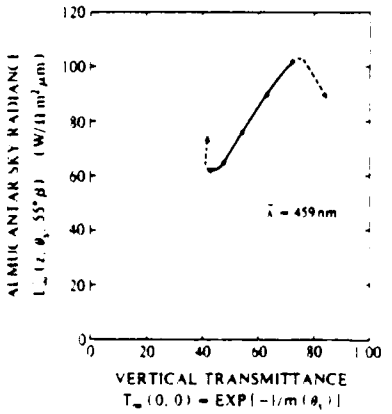

Fig. 6. Almucantar sky radiance at 55° vs vertical transmittance [Eq. (28)] for 2 Sept. 1964, filter 1 (mean wavelength 459 nm).

sor is constant, and the day is optically stable. Setting $dL_\infty^*(z,\theta_s,\beta)$ equal to zero and rearranging we get

$$\ln T_\infty(z,0) = -1/m(\theta_s'), \tag{28}$$

where θ_s' is the sun angle at the point where $L_\infty^*(z,\theta_s,\beta)$ is a maximum. Therefore a graph of solar almucantar radiance at a constant angle from the sun vs air mass will increase and then decrease with the maximum at $m(\theta_s')$ when the day is optically stable. Figure 6 is an example of this.

If the curve is reasonably well defined with sufficient air mass values, a reasonable transmittance value can be obtained. It can also be used as a third test for optical stability. The values of transmittance obtained by means of Eqs. (19), (21), and (28) should be in agreement for an optically stable day.

All the preceding equations are for monochromatic radiation but they are reasonably applicable to broadband radiation for sensors in the visible and very near infrared portion of the spectrum.

B. Method of Determining Spurious Sun Reflections

Pyaskovskaya-Fesenkova[3] also indicates that the two methods of checking for optical stability will falsely indicate instability if reflections in the radiometer telescope are not negligible.

Conversely, once it is established that the day is optically stable, the above tests for optical stability can be used to test whether a sky radiance measurement contains spurious sun reflection. Sky radiances near the sun are difficult to measure unless the sun can be occulted.

To illustrate the use of the above tests for optical stability and to test for spurious sun reflections in a sky radiance photometer, I have used a set of data[10] containing measurements with a solar transmissometer, a sky scanner, and an irradiometer. These measurements were made from January to September 1964 from a platform on the roof of one of the Visibility Laboratory buildings at Point Loma. The solar transmissometer measured both the center sun radiance and an aureole radiance 0.573° from the sun center. The general procedure was to make a set of measurements at each 10° increment of sun zenith angle and at noon.

The radiometers were fitted with four optical filters so that there were two narrow filtered-sensor passbands and two broad passbands. The two narrow passbands had mean wavelengths of 459 and 661 nm, the photopic passband had a mean wavelength of 560 nm, and a fourth broad passband represented an unfiltered sensor with a mean wavelength of 505 nm. Relative spectral response curves for the sensor with these filters are given in Fig. 7.

A graph of the apparent center sun radiance as a function of relative air mass for the afternoon of 2 Sept. 1964 was given in Fig. 3. The straight lines for each filter are the result of least-squares fits to the data. The correlation coefficients were high, ≥0.99, and the day is apparently optically stable. The least-squares transmissions are noted on the graph.

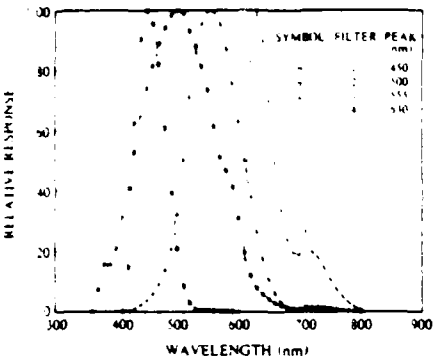

Fig. 7. Standard spectral response for Visibility Laboratory rooftop filtered sensor.

1. *Solar Almucantar at 55°*

To be certain to have an almucantar sky radiance measurement without sun reflection problems, an angle from sun of 55° was chosen. The sky scanner data are for a fixed set of zenith angles and azimuths ($\Delta\theta$ and $\Delta\phi = \pi/32$ or 5.625°). Therefore, the almucantar radiance used is from interpolations to the zenith angle of the sum and to the appropriate azimuth for 3 equal to 55°. The example is done only for filter 1 at a mean wavelength of 459 nm. The almucantar/$m(\theta_s)$ graph vs air mass [Eq. (21)] was given in Fig. 4. The transmittance from the almucantar is 0.756 compared with the transmittance from the center sun radiance of 0.738 thus there is only a 2.4% difference. The average 0.747 is considered the best measure of the transmittance if the day is optically stable.

Now, for the three tests for optical stability. Although there is no measure of the solar scalar irradiance $_sE(0)$, there is a measurement of the center sun radiance $_sL_\odot(0,\theta,0)$ which is related to the scalar irradiance by

$$_sE(0) = {}_sL_\odot(0,\theta_s,0)D(\bar{\lambda})\Omega_s, \tag{29}$$

where $D(\bar{\lambda})$ is the center to average sun radiance conversion factor or limb darkening factor for the filter and Ω_s is the solid angle subtended by the sun for 2 Sept. 1964. If the center sun radiance is substituted for the solar scalar irradiance in Eq. (23) it becomes

$$L^*_\odot(z,\theta_s,3)/[{}_sL_\odot(0,\theta_s,0)m(\theta_s)] = B', \tag{30}$$

where

$$B' = D(\bar{\lambda})\Omega_s B. \tag{31}$$

Similarly Eq. (25) becomes

$$L^*_\odot(z,\theta_s,3)/L_\odot(z,\theta_s,0) = m(\theta_s)B'. \tag{32}$$

Since $D(\bar{\lambda})$ is a constant for a filtered sensor and Ω_s is constant for any given day, the two tests can now be made using Eqs. (30) and (32) instead of Eqs. (23) and (25).

Figure 5 contained the appropriate graphs for the two tests. Although not perfect, the data in Fig. 5(a) are reasonably represented by a horizontal straight line. Similarly, the data in Fig. 5(b) are reasonably represented by a straight line going through the origin.

The third test is a plot of the almucantar sky radiance graphed against $\exp[-1/m(\theta_s)]$ from Eq. (28) as shown in Fig. 6. The maximum sky radiance should lie at a transmittance of ~0.75. Although the noon value of sky radiance is inconsistent with the rest (hooks upward near air mass 1), and there are no measured sky radiances at the exact θ_s', the sky radiances can be reasonably represented by a curve which maximizes at a transmittance of 0.75 (dashed line).

It can be seen that the atmosphere on 2 Sept. 1964 in the vicinity of the Visibility Laboratory was optically stable. This is apparent even though the almucantar sky radiances were interpolated. Thus it appears interpolation is a valid method for obtaining almucantar values for use in the preceding equations.

Now that it is established that the day is optically stable, these same equations will be used to test for sun reflections in the solar aureole photometer.

2. *Aureole Radiance*

The solar aureole radiance was measured 0.573° from the center of the sun without occulting the sun. A graph of the ratio of the apparent aureole radiance/relative air mass vs air mass is shown in Fig. 8. (There are no aureole data for filter 4.) The data for the three filters look reasonably linear and the correlation coefficients are 0.99. However, the least-squares transmittances, which are noted on the graph, vary markedly from the values derived from the sun radiance and the almucantar at 55° scattering angle.

The two tests for spurious sun reflection using Eqs. (30) and (32) fail miserably, see Figs. 9(a) and (b). In Fig. 9(a) the B' increases dramatically as air mass gets

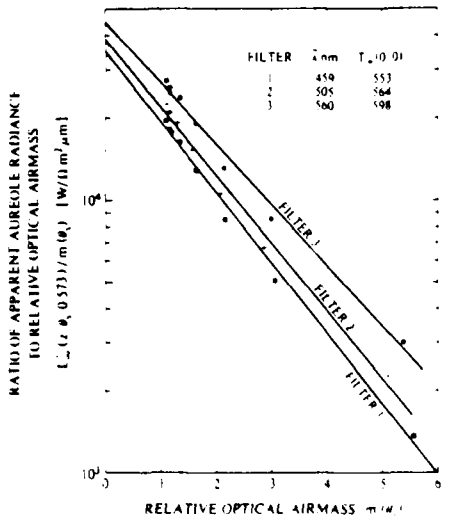

Fig. 8. Aureole radiance to air mass ratio vs relative optical air mass for 2 Sept. 1964.

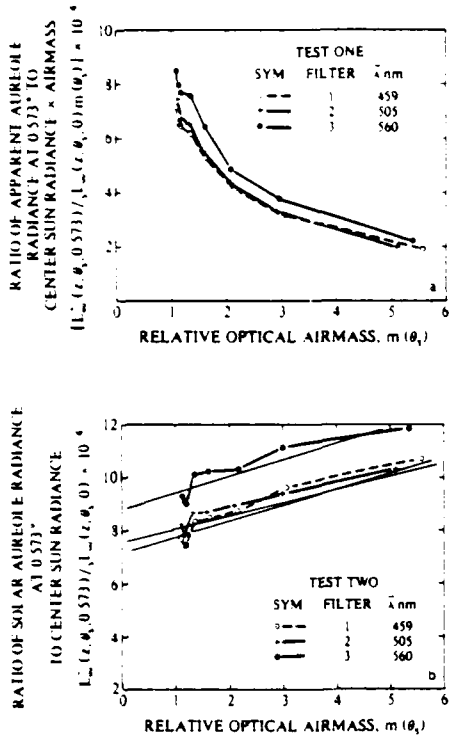

Fig. 9. Graphs to test for spurious sun reflections in aureole radiance measurements, 2 Sept. 1964: (a) test one, Eq. (30); (b) test two, Eq. (32).

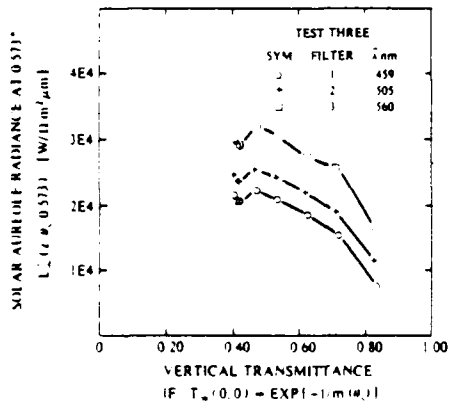

Fig. 10. Solar aureole radiance vs vertical transmittance [Eq. (28)] for 2 Sept. 1964.

near 1 instead of staying constant. In Fig. 9(b) the data can be fit to straight lines but they clearly do not go through the origin.

The final test is the graph of the solar aureole radiance as a function of $\exp[-1/m(\theta_s)]$ as shown in Fig. 10. The aureole peaks at transmittances still lower than the values derived using the aureole and noted in Fig. 8. The transmittances from Eqs. (19), (21), and (28) are clearly not in agreement. Thus it is apparent that the solar aureole measurements include a spurious sun reflection component in all three filters.

Any sky radiance measurement made near the sun without occultation of the sun may be questionable and should be tested in some fashion. The above method is a valid testing procedure.

IV. Aerosol Optical Thickness

The word aerosol is used herein to describe the liquid and/or solid particulates exclusive of the gas phase in which they are embedded. This is consistent with Prospero *et al.*[11] Levshits and Pavlo[2] developed a method for obtaining aerosol optical thickness. A shorter method, applicable to a larger range of sun zenith angle and requiring fewer measurements, was developed based on many of the same assumptions. Therefore we will review the long method in detail.

A. Long Method of Obtaining Aerosol Optical Thickness

The basic equation for the sky radiance in the solar almucantar Eq. (16) can be rewritten substituting in Eq. (17) and expressing the optical thickness function in two components, the Rayleigh or molecular ${}_R\tau_\infty(z,\beta)$ and the Mie or aerosol ${}_M\tau_\infty(z,\beta)$:

$$\mu(z,\beta) = {}_R\tau_\infty(z,\beta) + {}_M\tau_\infty(z,\beta) + \int_\infty^z C(z)dz. \tag{33}$$

If the almucantar has a large enough range of scattering angles from the sun, both sides of Eq. (33) can be integrated over 4π and Eq. (13) substituted in to obtain

$$2\pi \int_0^\pi \mu(z,\beta)\sin\beta d\beta = {}_Rt_\infty(z) + {}_Mt_\infty(z) + 2\pi \int_0^\pi \int_\infty^z C(z)dz \sin\beta d\beta, \tag{34}$$

where ${}_Rt_\infty(z)$ is the Rayleigh optical thickness and ${}_Mt_\infty(z)$ is the aerosol optical thickness. The last term in both Eqs. (33) and (34) is the diffuse component due to the contribution of the relatively nondirectional sky, apparent terrain radiance, and emission. In this section, all the equations up to this point are not approximations. They hold for an atmosphere with or without absorption and/or emission and thus are equally as valid in the infrared.

1. *Visible Portion of Spectrum*

Livshits and Pavlov[2] make several assumptions appropriate for the visible portion of the spectrum. The almucantar sky luminance or radiance for 90–180° scattering angles is assumed to be essentially a function of the Rayleigh optical thickness function and the diffuse component. They also assume that the diffuse component is the same for 0–90° as it is for 90–180° scattering angle. This assumes homogeneity in the almucantar and thus is limited to cloudless skies. It follows that, since the Rayleigh scattering is symmetrical about 90°,

$$2\left[2\pi \int_{\pi/2}^\pi \mu(z,\beta)\sin\beta d\beta\right] = {}_Rt_\infty(z) + 2\pi \int_0^\pi \int_\infty^z C(z)dz \sin\beta d\beta. \tag{35}$$

Also it follows that the aerosol optical thickness is the

integral of the forward portion of the function less the integral of the back portion

$$_M\tau_a(z) = 2\pi \int_0^{\pi/2} \mu(z,\beta) \sin\beta d\beta - 2\pi \int_{\pi/2}^{\pi} \mu(z,\beta) \sin\beta d\beta. \quad (36)$$

Livshits and Pavlov[2] also obtained the total optical thickness from

$$\tau_a(z) = {}_R\tau_a(z) + {}_M\tau_a(z) + {}_a\tau_a(z), \quad (37)$$

where ${}_a\tau_a(z)$ is the optical thickness due to absorption. They obtain the Rayleigh thickness theoretically and assume the absorption is primarily due to ozone in the visible wavelengths. Ozone absorption was assumed to be the yearly average value for a given wavelength. They obtained good comparisons to total optical thickness values obtained with the Langley or Bouguer method for short wavelengths where there are no other absorption bands. They did not compare as well at the longer wavelengths. I suspect the presence of absorption from sources other than ozone in the longer wavelengths in the visible rather than an error in the aerosol optical thickness was responsible for the discrepancy.

The disadvantage of Eq. (36) is the need for a large sun zenith angle so that a large range of scattering angles is available in the solar almucantar.

B. Short Method of Obtaining Aerosol Optical Thickness

1. Scattering Angle 55°

The ratio of the volume scattering function at 55° to the total scattering coefficient is $1/(4\pi)$ for Rayleigh scattering. It is also a reasonable approximation for the total scattering.[12] Therefore, it must also be $1/(4\pi)$ for aerosol scattering:

$$_R\sigma(z,55)/{}_R s(z) = \sigma(z,55)/s(z) = {}_M\sigma(z,55)/{}_M s(z) = 1/(4\pi). \quad (38)$$

Thus, the ratio of the optical thickness function at 55° to the optical thickness must be $1/(4\pi)$ for each component as well as for the total scattering

$$_R\tau_a(z,55)/{}_R\tau_a(z) = \tau_a(z,55)/{}_a\tau_a(z)$$

$$= {}_M\tau_a(z,55)/{}_M\tau_a(z) = 1/(4\pi). \quad (39)$$

Now the optical thickness function can be expressed in terms of the aerosol optical thickness by rearranging Eq. (39):

$$_M\tau_a(z,55) = {}_M\tau_a(z)/(4\pi). \quad (40)$$

Using the same rationale as Livshits and Pavlov,[2] the 90–180° angles in scattering angle describe the diffuse and Rayleigh components for the 0–90° angles. It can thus be said that

$$\mu(z,180\text{–}55) = {}_R\tau_a(z,55) + \int_0^z C(z)dz. \quad (41)$$

Writing Eq. (33) in terms of the scattering at 55°, we get

$$\mu(z,55) = {}_M\tau_a(z,55) + {}_R\tau_a(z,55) + \int_0^z C(z)dz. \quad (42)$$

Subtracting Eq. (41) from Eq. (42),

$$_M\tau_a(z,55) = \mu(z,55) - \mu(z,125). \quad (43)$$

Now combining with Eqs. (40) and (43) we get

$$_M\tau_a(z) = 4\pi[\mu(z,55) - \mu(z,125)]. \quad (44)$$

The solar almucantar contains both 55° and 125° scattering angles for sun zenith angles from 62.5° to 90°. Thus, for these solar zenith angles, measurements of the scalar sun irradiance and sky radiances in the solar almucantar at 55° and 125° from the sun would yield a value for the aerosol optical thickness through the atmosphere. As long as the sky radiance distribution shows brighter areas from 0° to 90° than from 90° to 180°, this scheme will work. Equation (44) also applies when atmospheric emission is present, as long as the emission does not swamp out the directional scattering effects.

2. Alternate Expression

An alternate equation can be developed for obtaining the aerosol optical thickness from sky radiances when no sun scalar irradiance measurement is available. Substituting Eq. (17) into Eq. (44) and rearranging, it becomes

$$_M\tau_a(z) = 4\pi[L_s^*(z,\theta_s,55\beta) - L_s^*(z,\theta_s,125\beta)]/[{}_s\bar{\mathcal{E}}(z)m(\theta_s)]. \quad (45)$$

The sun scalar irradiance can be obtained from the average sun irradiance out-of-the atmosphere ${}_s\bar{\mathcal{E}}(\infty)$ by

$${}_s\mathcal{E}(z) = {}_s\bar{\mathcal{E}}(\infty)T_a(z,0)^{m(\theta_s)}(\psi/\bar{\psi})^2 \quad (46)$$

where ψ is the solar diameter for that date and $\bar{\psi}$ the average solar diameter. Also the total transmittance can be expressed as a function of the component optical thicknesses from Eq. (37):

$$T_a(z,0) = \exp[-{}_R\tau_a(z) - {}_M\tau_a(z) - {}_a\tau_a(z)]. \quad (47)$$

Substituting Eqs. (46) and (47) into Eq. (45) and rearranging we get

$${}_M\tau_a(z)\exp[-{}_M\tau_a(z)m(\theta_s)] = 4\pi/[L_s^*(z,\theta_s,55\beta) - L_s^*(z,\theta_s,125\beta)]$$

$$/[{}_s\bar{\mathcal{E}}(\infty)m(\theta_s)(\psi/\bar{\psi})_2\exp|-m(\theta_s)[{}_R\tau_a(z) + {}_a\tau_a(z)]|]. \quad (48)$$

Equation (48) cannot be solved directly for the aerosol optical thickness but by iterative means it is readily solved. It assumes a reasonable estimate of absorption optical thickness can be made (such as assuming only ozone absorption in the visible) or that a value can be obtained through use of Program LOWTRAN[13] at other wavelengths.

3. Validation Studies

The two methods of obtaining the total optical thickness and hence transmittance from solar almucantar sky radiances at 55° and 125° using Eqs. (45) and (48) with Eq. (37) were tested using the 1964 Visibility Laboratory rooftop data previously described in Sec. III.B.

The scanner radiance grid included almucantar measurements within ±0.7° for all four filters for the 2 Sept. 1964 nominal 70° sun zenith angle data packages. The solar transmissometer value of transmit-

Table I. Spectral Characteristics Summary for Rooftop 1964 Filters

Spectral Characteristics				Inherent Sun Properties (Johnson (1954))			Rayleigh Atmosphere Properties (15°C)			Ozone Optical
Filter Code No	Peak Wavelength (nm)	Mean Wavelength (nm)	Effective Passband (nm)	Irradiance (W m^{-2} μm^{-1})	Radiance (W (Ω m^{-2} μm^{-1}) Average	Radiance (W (Ω m^{-2} μm^{-1}) Center	Attenuation Length (m)	Total Scattering Coefficient (per m)	Vertical Radiance Transmittance	Thickness $\tau_a(\infty,0)$
1	450	459	58.1	2.08E+03	3.04E+07	4.00E+07	4.11E+04	2.47E-05	0.812	3.70E-3
2	500	505	151.9	1.95E+03	2.86E+07	3.66E+07	5.94E+05	1.87E-05	0.852	1.60E-2
3	555	560	106.8	1.89E+03	2.77E+07	3.45E+07	9.22E+04	1.15E-05	0.907	3.07E-2
4	630	661	61.4	1.59E+03	2.33E+07	2.79E+07	1.80E+05	5.78E-06	0.952	2.20E-2

tance was used in Eq. (46) to obtain the value of scalar sun irradiance $_{s}\bar{e}(z)$ for use in Eq. (45).

The values of the scalar sun irradiance out-of-the atmosphere $_{s}\bar{e}(\infty)$, the Rayleigh vertical radiance transmittance, and the ozone optical thickness are given in Table I for each filter. The solar irradiances out-of-the atmosphere are based on the spectral solar irradiance values of Johnson.[14] The Rayleigh space-to-earth radiance transmittances are based on the spectral total volume scattering coefficients from Eq. (14) of Penndorf,[15] the refractive modulus from the dispersion formula of Edlen,[16] and the sea level scale height for the U.S. Standard Atmosphere 1976.[17] The ozone optical thicknesses are based on the total ozone for the U.S. Standard Atmosphere 1976 and the spectral absorption values of Vigroux[18] which are in good agreement with the Inn and Tanaka[19] values.

The total optical thickness $t_{\infty}(0)$ and total transmittance $T_{\infty}(0,0)$ from the solar transmissometer are given for each filter in Table II. The ratio of the optical thickness [derived using Eq. (45)] to the solar transmissometer value is given in column 4, and the ratio for eq. (48) in column 5. Similarly, the ratio of the derived transmittances to measured values are given in columns 7 and 8, respectively. The values compare well for the first three filters and less well for filter 4 with a mean wavelength of 661 nm, although even there the transmittances are within 2%. Livshits and Pavlov[2] similarly found closer comparisons at the shorter wavelengths for monochromatic measurements.

Thus, the shorter method, using the almucantar at 55° and 125° with or without an independent sun irradiance measurement, appears to be valid for narrowband and broadband sensors in the visible spectrum.

The alternate equation [Eq. (48)] is particularly useful with airborne scanner data where independent measurements of sun irradiance are not available.

Since this is an approximative method, the resultant aerosol optical thickness precision may not be high, but the resultant transmittances have high precision as can be seen in Table II. The method requires an unobscured sun and cloud-free sky at 55° and 125° from the sun in the almucantar.

V. Summary

Solar almucantar sky radiances have special characteristics which make them useful for a variety of tasks. A basic equation for the solar almucantar is derived which indicates it is a function of the solar scalar irradiance, the optical air mass, the optical thickness function and one additive component containing the contribution of the sky, the apparent terrain radiance, and the emission.

On optically stable days, solar almucantar radiances measured throughout the day at a set angle from the sun can be used to obtain vertical radiance transmittance (total optical thickness) but the radiometer must be free of internal reflections from the sun. Conversely, if the day is optically stable, these same solar almu-

Table II. Comparison of Transmittance Determination Procedures (Solar Almucantar Radiances vs Solar Transmissometer)

Filter Number	Mean Wavelength $\bar{\lambda}$ nm	TOTAL OPTICAL THICKNESS $t_{\infty}(z)$			TOTAL TRANSMITTANCE $T_{\infty}(0,0)$		
		Transmissometer Measurement	"Derived to Meas." Ratios Using Eq. (45)	Using Eq. (48)	Transmissometer Measurement	"Derived to Meas." Ratios Using Eq. (45)	Using Eq. (48)
1	459	296	96	95	743	1.01	1.01
2	505	241	1.02	1.03	786	99	99
3	560	200	95	1.02	819	1.01	1.00
4	661	143	86	84	867	1.02	1.02

cantar radiance measurements can be used to determine if the radiometer is free of internal reflectance problems or at what scattering angles they occur.

Finally, measurements made in the solar almucantar at scattering angles from the sun of 55° and 125° can be used to obtain a value for the aerosol optical thickness. This latter method can be used with or without a simultaneous measurement of the sun radiance or irradiance.

This work was performed by the author at the Visibility Laboratory, University of California San Diego, for the United States Air Force. The writing and publication of this article was done at Viz. Ability under U.S. Army Research Office contract DAAG29-84-C-0014. I wish to thank Judith Olson for technical editing assistance.

References

1. B. T. Tashenov, "Spectrophotometric Studies of Atmospheric Transmittance and Stability," in *Atmospheric Optics*, N. B. Divari, Ed. translated by S. B. Dresner (Plenum, New York, 1970), pp. 70–79.
2. G. S. Livshits and V. E. Pavlov, "Atmospheric Transmittance and the Interrelationships of Certain Optical Parameters," in *Atmospheric Optics*, see Ref. 1, pp. 53–56.
3. E. V. Pyaskovskaya-Fesenkova, "Determining the Transmission Coefficient and Degree of Optical Stability of the Earth's Atmosphere," in *Atmospheric Optics*, see Ref. 1, pp. 151–156.
4. S. Q. Duntley, A. R. Boileau, and R. W. Presisendorfer, "Image Transmission by the Troposphere I," J. Opt. Soc. Am. **47**, 499 (1957).
5. W. G. Driscoll and W. Vaughan, Eds., *Handbook of Optics* (McGraw-Hill, New York, 1978).
6. J. I. Gordon, "Some Implications of the Equation of Transfer," J. Opt. Soc. Am. A (1985), submitted.
7. J. I. Gordon, "Implications of the Equation of Transfer Within the Visible and Infrared Spectrum," Scripps Institution of Oceanography, Visibility Laboratory, SIO Ref. 83-10, AFGL-TR-82-0223, NTIS No. ADA 133 979 (1982).
8. This is based on air mass calculations using the *U.S. Standard Atmosphere Supplements, 1966* (Superintendent of Documents, U.S. GPO, Washington, D.C. 20402, 1966) as reported in Ref. 7, Sec. 1, Tables 2.1 and 2.2.
9. N. T. O'Neill and J. R. Miller, "Combined Solar Aureole and Solar Beam Extinction Measurements I: Calibration Considerations," Appl. Opt. **23**, 3691 (1984).
10. S. Q. Duntley, R. W. Johnson, and J. I. Gordon, "Airborne Measurements of Optical Atmospheric Properties, Summary and Review III," Scripps Institution of Oceanography, Visibility Laboratory, SIO Ref 79-5, AFGL-TR-78-0286, NTIS No. AD 073 121 (1978).
11. J. M. Prospero *et al.*, "The Atmospheric Aerosol System: an Overview," Rev. Geophys. Space Phys. **21**, 1607 (1983).
12. This is based on the catalog of scattering functions of O. D. Barteneva, "Scattering Functions of Light in the Atmospheric Boundary Layer," Bull. Acad. Sci. U.S.S.R., Geophys. Ser. (English edition translated by AGU) No. 12, 1237 (1960). The scattering functions are partially verified and given applicability to all filters in the visible and near infrared by the volume scattering function measurements at 30° and 50° of the Visibility Laboratory: R. W. Johnson, W. S. Hering, J. I. Gordon, B. W. Fitch, and J. S. Shields, "Preliminary Analysis and Modeling Based upon Project OPAQUE Profile and Surface Data," Scripps Institution of Oceanography, Visibility Laboratory, SIO Ref. 80-5, AFGL-TR-79-0285, NTIS ADB 052 1722 (1979); R. W. Johnson, "Daytime Visibility and Nephelometer Measurements Related to Its Determination," Atmos. Environ. **15**, 1835 (1981). This is summarized in Eqs. (4.5) and (4.6) in Ref. 7 and Eqs. (38) and (39) of J. I. Gordon and R. W. Johnson, "Integrating Nephelometer: Theory and Implications," Appl. Opt. **24**, 2721 (1985).
13. F. X. Kneizys *et al.*, "Atmospheric Transmittance/Radiance: Computer Code LOWTRAN 5," AFGL-TR-80-0067 (1980).
14. F. R. Johnson, "The Solar Constant," J. Meteorol. **11**, 431 (1954).
15. R. Penndorf, "Tables of the Refractive Index for Standard Air and the Rayleigh Scattering Coefficient for the Spectral Region Between 0.2 and 20.0 μ and Their Application to Atmospheric Optics," J. Opt. Soc. Am. **47**, 176 (1957).
16. B. Elden, "Dispersion of Standard Air," J. Opt. Soc. Am. **43**, 339 (1953).
17. *U.S. Standard Atmosphere, 1976* (Superintendent of Documents, U.S. GPO, Washington, D.C. 20402, 1976).
18. E. Vigroux, "Etude experimentale de l'absorption de l'ozone," Ann. Phys. (Paris) **8**, 742, 747 (1953).
19. E. C. Y. Inn and Y. Tanaka, "Ozone Absorption," J. Opt. Soc. Am. **43**, 872 (1953).

Appendix C

Reprinted from Journal of the Optical Society of America A, Vol. 3, page 274, February 1986

Some implications of the equation of transfer

Jacqueline I. Gordon

Visibility, Inc., 2941 NW Ashwood Drive, Corvallis, Oregon 97330

Received November 27, 1984; accepted September 30, 1985

The equation of transfer for radiance as it relates to a scattering, absorbing, and emitting medium is integrated with angle to obtain equations of transfer for irradiance and scalar irradiance. These equations are, in turn, integrated with respect to altitude. One major implication is that a measurement of the 4π radiance distribution at two altitudes in the atmosphere can yield a measure of absorption. Another implication is that there is an emission term in the irradiance equation but not in the scalar-irradiance equation of transfer.

Appendix D

INTRODUCTION

Early work in radiative transfer and the equation of transfer[1] generally lacks detailed specification of the separate roles of scattering, absorption, and emission as they relate to the atmosphere in the visible and the near-infrared wavelengths. Also, there appears to be no general development and integration of the equation of transfer for scalar irradiance.

This paper will deal with the basic monochromatic equation of transfer as it relates to radiance. It will detail the roles of scattering, absorption, and emission as they relate to the atmosphere in the visible and the near-infrared wavelengths. This will be followed by integration of the equation of transfer with angle to obtain the equations of transfer for irradiance and scalar irradiance. The basic equations developed herein are for monochromatic radiation. Applicability to radiation for broadband sensors will be discussed where appropriate.

The exact partial solution and the approximate full solution for integrating the equation of transfer for irradiance with altitude will be given. This solution is then used to evaluate a set of data for internal consistency and to obtain a measure of the absorption optical thickness for a broadband sensor in the visible portion of the spectrum for a 5.8-km-altitude interval in the troposphere. The data are part of a large body of hitherto unpublished data. They are used herein for illustrative purposes only.

The exact partial solution and an approximate full solution for integrating the equation of transfer for scalar irradiance are also given along with examples of the magnitude and the form of the two radiance distribution functions in the equations.

The notation used is that adopted by the Visibility Laboratory, University of California, San Diego,[1] and modified to correspond to Optical Society of America recommendations in Sec. 1 of Ref. 4. The integrals for solid angle will be expressed primarily in single-integral form for simplicity. Double integrals using two planar angles will be added occasionally for further clarification.

EQUATION OF TRANSFER FOR RADIANCE

Equation

The most basic equation in radiation theory is the equation of transfer [Eq. (10) of Ref. 1; Eq. (3), Sec. 3.15 of Ref. 2; and Eq. (46) of Ref. 3]:

$$dL(z, \theta, \phi)/dr = -\alpha(z)L(z, \theta, \phi) + L_*(z, \theta, \phi). \quad (1)$$

This equation relates the differential change in radiance $dL(z, \theta, \phi)$ at altitude z for the path of sight at zenith angle θ and azimuth ϕ, over the differential path length dr to the attenuation coefficient $\alpha(z)$, the radiance $L(z, \theta, \phi)$, and the path function $L_*(z, \theta, \phi)$.

The differential path length dr is always nonnegative, as is the incremental path length Δr. In the plane-parallel case (and in the curved-Earth case for paths of sight at zenith angles $\theta = 0°$–$70°$ and $110°$–$180°$) the incremental path length Δr is defined as

$$\Delta r = \Delta z \sec\theta. \quad (2)$$

The Δz is defined as $z_1 - z_2$ (the subscripts increase in the flux direction); see Fig. 1.

The attenuation coefficient is the sum of the total scattering coefficient $s(z)$ plus the absorption coefficient $a(z)$:

$$\alpha(z) = s(z) + a(z). \quad (3)$$

The path function is the sum of a scattered component and an emitted component:

$$L_*(z, \theta, \phi) = L_{*s}(z, \theta, \phi) + L_{*e}(z). \quad (4)$$

The emitted component is isotropic and hence is shown without direction modifiers.

Roles of Scattering, Absorption, and Emission

Scattering

The scattering coefficient has two components. Rayleigh or molecular scattering is highly wavelength dependent since it is proportional to the inverse fourth power of the wavelength, λ^{-4}. Mie or aerosol scattering is less wavelength dependent. Both tend to be smooth continuous functions with wavelength.

The word "aerosol" is used herein to describe liquid and/or solid particulates exclusive of the gas phase in which they are embedded. This is consistent with Ref. 5.

The scattering path function is the integral of the incoming radiance $L(z, \theta', \phi')$ in all 4π directions (including the Sun, where appropriate) times the volume scattering function $\sigma(z, \beta)$:

$$L_{*s}(z, \theta, \phi) = \int_{4\pi} L(z, \theta', \phi')\sigma(z, \beta)d\Omega$$
$$= \int_0^{2\pi}\int_0^{\pi} L(z, \theta', \phi')\sigma(z, \beta)\sin\theta' d\theta' d\phi'. \quad (5)$$

Appendix D

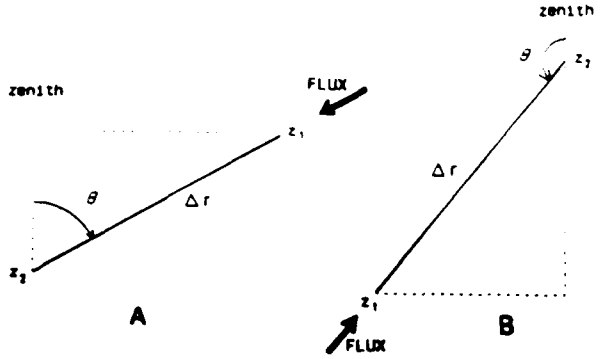

Fig. 1. Incremental-path-length geometry for upward and downward paths of sight, $\Delta r = (z_1 - z_2)\sec\theta$. A, Upward path of sight ($\theta < 90°$), with flux downward; B, downward path of sight ($\theta > 90°$), with flux upward.

The scattering angle β is a function of the incoming-radiance direction angles θ', ϕ' and the sensor direction angles θ, ϕ as follows:

$$\cos\beta = \sin\theta\sin\theta'\cos(\phi' - \phi) + \cos\theta\cos\theta'. \quad (6)$$

The integral of the volume scattering function over 4π is the total scattering coefficient

$$s(z) = \int_{4\pi} \sigma(z, \beta)d\Omega = 2\pi\int_0^{\pi} \sigma(z, \beta)\sin\beta d\beta. \quad (7)$$

Absorption and Emission

Atoms and molecules in the gas phase absorb and emit in line and band spectra. The atomic spectra are line spectra and tend to be at the shorter wavelengths. The band spectra are molecular and tend to be at the longer wavelengths. The continua are essentially part of the band spectra, weak but broad spectrally.

Molecules in the liquid or the solid phase cannot emit in line or band spectra but can emit only in a continuous spectrum, the distribution of which is determined by the ambient temperature, in other words, as a blackbody or a graybody (incomplete radiator). This implies that the absorption spectrum for liquids and solids is also continuous spectrally.

The atmosphere is a mixture of gas and aerosol. Thus it absorbs and emits as a spectral colored body.

Emission Mechanisms. The principal emission mechanisms above the mesosphere are electroluminescence and chemiluminescence resulting in line and band spectra. These emissions are called airglow. These are important in the visible part of the spectrum at twilight and at night but will not be dealt with herein.

The principal emission mechanism in the troposphere and in the atmosphere at or below the mesosphere is temperature radiation, which is photon emission caused by atomic or molecular collision. The atmosphere is assumed to be in local thermodynamic equilibrium; hence Kirchhoff's law applies.

The path function resulting from thermal emittance is thus [Eq. (38) of Ref. 3]

$$L_{*_e}(z) = L_{*_a}(z) = a(z)L(\lambda, T), \quad (8)$$

where $L(\lambda, T)$ is the blackbody radiance at wavelength λ and T is the temperature in degrees Kelvin. A blackbody in thermodynamic equilibrium absorbs and emits as a continuous function of wavelength and temperature according to the classical equation.[5]

Emission in the Visible Spectrum. Blackbody radiance and hence emittance is negligible in the visible spectrum. Even at 1 μm at 300 K (27°C or 80°F), the blackbody radiance L (1 μm, 300 K) is 1.76×10^{-7} W/μm. At shorter wavelengths (all the visible wavelengths) and/or lower temperatures (the normal range of temperature below the mesosphere), the thermal emittance is still less. Hence for the visible spectrum Eq. (4) becomes

$$L_*(z, \theta, \phi) = L_{*_s}(z, \theta, \phi). \quad (9)$$

INTEGRATING THE EQUATION OF TRANSFER WITH ANGLE

Definition of Multiangle Terms

Irradiance

The downwelling irradiance $E(z, d)$ is defined as the integral of the radiances from zenith angles 0°–90° weighted by the cosine of the zenith angle

$$E(z, d) = \int_{2\pi} L(z, \theta, \phi)\cos\theta d\Omega = \int_0^{2\pi}\int_0^{\pi/2} L(z, \theta, \phi)\cos\theta\sin\theta d\theta d\phi. \quad (10)$$

Similarly, the upwelling irradiance $E(z, u)$ is computed for angles 90° to 180° by using the cosine of the nadir angle (180 − θ). These are the irradiances on a flat surface oriented to receive the downward and the upward radiances, respectively.

The albedo $A(z)$ is defined as the ratio of the upwelling to the downwelling irradiance,

$$A(z) = E(z, u)/E(z, d). \quad (11)$$

Scalar Irradiance

A second type of irradiance is the scalar or nondirectional irradiance in which the cosine term is not present. The total scalar irradiance $\epsilon(z)$ is defined as

$$\epsilon(z) = \int_{4\pi} L(z, \theta, \phi)d\Omega = \int_0^{2\pi}\int_0^{\pi} L(z, \theta, \phi)\sin\theta d\theta d\phi. \quad (12)$$

The scalar albedo ${}_sA(z)$ is similarly the upwelling divided by the downwelling scalar irradiance

$${}_sA(z) = \epsilon(z, u)/\epsilon(z, d). \quad (13)$$

Scalar Exitance (Emittance)

Exitance (emittance) M is defined with the cosine term similar to the irradiance in Eq. (10). Let us define a second type of exitance as the scalar or nondirectional exitance in which the cosine term is not present. The scalar exitance that is due to absorption $m(\lambda, T)$ is defined as

$$m(\lambda, T) = L(\lambda, T)\int_{4\pi} d\Omega = 4\pi L(\lambda, T). \quad (14)$$

Scalar exitance per length $m_*(z)$ is the unweighted integral over 4π of the path function

$$m_{e_s}(z) = \int_{4\pi} L_{e_s}(z, \theta, \phi)\mathrm{d}\Omega = \int_0^{2\pi}\int_0^{\pi} L_{e_s}(z, \theta, \phi)\sin\theta\mathrm{d}\theta\mathrm{d}\phi. \tag{15}$$

When the scattering path function is integrated over 4π it can be expressed as a double integral by substituting in Eq. (5):

$$m_{e_s}(z) = \int_{4\pi}\int_{4\pi} L(z, \theta', \phi')\sigma(z, \beta)\mathrm{d}\Omega\mathrm{d}\Omega$$

$$= \int_0^{2\pi}\int_0^{\pi}\left[\int_0^{2\pi}\int_0^{\pi} L(z, \theta', \phi')\sigma(z, \beta) \times \sin\theta'\mathrm{d}\theta'\mathrm{d}\phi'\right]\sin\theta\mathrm{d}\theta\mathrm{d}\phi. \tag{16}$$

Since Eq. (16) is a double integral in which the paths of sight θ, ϕ vary over 4π and the incoming radiances θ', ϕ' also vary over 4π, each radiance $L(z, \theta', \phi')$ will be multiplied by $\sigma(z, \beta)$ over 4π for all β. Therefore Eq. (16) can be expressed as

$$m_{e_s}(z) = \int_0^{2\pi}\int_0^{\pi} L(z, \theta', \phi')\left[2\pi\int_0^{\pi}\sigma(z, \beta) \times \sin\beta\mathrm{d}\beta\right]\sin\theta'\mathrm{d}\theta'\mathrm{d}\phi'. \tag{17}$$

Substituting in Eq. (7) and taking it out of the integral, we get

$$m_{e_s}(z) = s\int_{4\pi} L(z, \theta', \phi')\mathrm{d}\Omega. \tag{18}$$

Now Eq. (12) can be substituted, and

$$m_{e_s}(z) = s(z)\epsilon(z). \tag{19}$$

Since the path function resulting from absorption is isotropic, the scalar exitance resulting from absorption is

$$m_{e_a}(z) = 4\pi a(z)L(\lambda, T) = a(z)m(\lambda, T). \tag{20}$$

Equation of Transfer for Irradiance

The equation of transfer for radiance can be used to obtain the equation of transfer for irradiance by integrating over 4π. In the plane-parallel case, similar to Eq. (2), the differential path length $\mathrm{d}r$ is expressed as

$$\mathrm{d}r = \mathrm{d}z\sec\theta. \tag{21}$$

Now let us rewrite Eq. (1) in terms of the separate components of absorption, scattering, and emission and express the incremental path length in terms of Eq. (21); thus

$$\mathrm{d}L(z, \theta, \phi)\cos\theta/\mathrm{d}z = -a(z)L(z, \theta, \phi) - s(z)L(z, \theta, \phi) + L_{e_s}(z, \theta, \phi) + L_{e_a}(z). \tag{22}$$

Multiplying both sides by $\mathrm{d}\Omega$ and expressing both sides as an integral over 4π, we get

$$\mathrm{d}\int_{4\pi} L(z, \theta, \phi)\cos\theta\mathrm{d}\Omega/\mathrm{d}z = -a(z)\int_{4\pi} L(z, \theta, \phi)\mathrm{d}\Omega - s(z) \times \int_{4\pi} L(z, \theta, \phi)\mathrm{d}\Omega + \int_{4\pi} L_{e_s}(z, \theta, \phi)\mathrm{d}\Omega + L_{e_a}(z)\int_{4\pi}\mathrm{d}\Omega. \tag{23}$$

This can be simplified by using Eqs. (10), (12), (19), and (20). The middle two terms drop out, and Eq. (23) becomes

$$\mathrm{d}[E(z, d) - E(z, u)]/\mathrm{d}z = -a(z)\epsilon(z) + a(z)m(\lambda, T). \tag{24}$$

This is the equation for the net irradiance $E(z, d) - E(z, u)$ change with altitude. Let us define $\xi(z)$ as the net irradiance

$$\xi(z) = E(z, d) - E(z, u). \tag{25}$$

Equation (24) can now be written as

$$\mathrm{d}\xi(z)/\mathrm{d}z = a(z)[m(\lambda, T) - \epsilon(z)]. \tag{26}$$

Note that Eq. (26) still has an emittance term $m(\lambda, T)$. The fourth term in Eq. (23) did not drop out. At longer wavelengths, such as in the infrared, the emittance makes an important contribution to the net irradiance. It ameliorates the loss that is due to absorption.

Visible Spectrum

In the visible spectrum where $L(\lambda, T)$ and hence $m(\lambda, T)$ are negligible, Eq. (26) can be written as

$$\mathrm{d}\xi(z)/\mathrm{d}z = -a(z)\epsilon(z). \tag{27}$$

Equation (27) is the same as Eq. (56), Chap. I of Ref. 3 and Eq. (10), Sec. 1.2 of Ref. 2, since the altitude differential $\mathrm{d}z$ as one descends in the atmosphere is the negative of the depth differential $\mathrm{d}d$ into the medium.

The net irradiance either stays constant with altitude, indicating no absorption, or decreases as altitude decreases. This can be used as a test for the internal consistency of visible-spectrum data.

Equation of Transfer for Scalar Irradiance

An expression for scalar irradiance can also be derived from Eq. (22) if we first multiply both sides by $\sec\theta$:

$$\mathrm{d}L(z, \theta, \phi)/\mathrm{d}z = -a(z)L(z, \theta, \phi)\sec\theta - s(z)L(z, \theta, \phi)\sec\theta + L_{e_s}(z, \theta, \phi)\sec\theta + L_{e_a}(z)\sec\theta. \tag{28}$$

Again, by multiplying both sides by $\mathrm{d}\Omega$ and expressing both sides as an integral over 4π, we get

$$\mathrm{d}\int_{4\pi} L(z, \theta, \phi)\mathrm{d}\Omega/\mathrm{d}z = -a(z)\int_{4\pi} L(z, \theta, \phi)\sec\theta\mathrm{d}\Omega - s(z) \times \int_{4\pi} L(z, \theta, \phi)\sec\theta\mathrm{d}\Omega + \int_{4\pi} L_{e_s}(z, \theta, \phi) \times \sec\theta\mathrm{d}\Omega + L_{e_a}(z)\int_{4\pi}\sec\theta\mathrm{d}\Omega. \tag{29}$$

The middle two terms on the right-hand side of Eq. (29) do not cancel each other as they did in Eq. (23). But, since $\sec(\pi - \theta) = -\sec\theta$, $\int_{4\pi}\sec\theta\mathrm{d}\Omega = 0$, and the fourth term drops out. Now, substituting in Eq. (12) and dividing the third term by $s(z)$, Eq. (29) can be written in terms of the change in scalar irradiance with altitude as

Appendix D

$$d\epsilon(z)\,dz = -a(z)\int_{4\pi} L(z,\theta,\phi)\sec\theta\,d\Omega - s(z)\left[\int_{4\pi} L(z,\theta,\phi)\sec\theta\,d\Omega - \int_{4\pi} L_{*s}(z,\theta,\phi)\sec\theta\,d\Omega/s(z)\right]. \quad (30)$$

Appendix D

In order to simplify Eq. (30), let us define two new functions.

Radiance Distribution Function

The first new function is the radiance distribution function $D(z)$. It is a seminormalized function of the 4π radiance distribution at altitude z:

$$D(z) = \int_{4\pi} L(z,\theta,\phi)\sec\theta\,d\Omega/\epsilon(z). \quad (31)$$

Dividing by the scalar irradiance $\epsilon(z)$ makes the function unitless. An alternative way of expressing Eq. (31) is to separate out the Sun term ${}_s\epsilon(z)$ and to express the more diffuse radiances as a radiance difference (sky minus terrain):

$$D(z) = {}_s\epsilon(z)\sec\theta_s/\epsilon(z) + \int_{2\pi}[L(z,\theta,\phi) - L(z,\pi-\theta,\phi)]\sec\theta\,d\Omega/\epsilon(z). \quad (32)$$

Equation (32) appears indeterminant because sec θ goes to infinity at 90°. However, the radiance difference $[L(z,\theta,\phi) - L(z,\pi-\theta,\phi)]$ goes to zero as sec θ goes to infinity; thus the equation is not indeterminant and can be evaluated with measured or model radiance distributions.

Scattered Radiance Distribution Function

The second function is the scattered radiance distribution function

$$D_s(z) = \int_{4\pi} L_{*s}(z,\theta,\phi)\sec\theta\,d\Omega/[\epsilon(z)s(z)] = \int_{4\pi}\int_{4\pi} L(z,\theta',\phi')[\sigma(z,\beta)/s(z)]d\Omega\sec\theta\,d\Omega/\epsilon(z). \quad (33)$$

Dividing by both the scalar irradiance and the total volume scattering coefficient makes this function unitless.

An alternative way of expressing Eq. (33) is to separate out the Sun term as in Eq. (32):

$$D_s(z) = {}_s\epsilon(z)\int_{4\pi}[\sigma(z,\beta)/s(z)]\sec\theta\,d\Omega/\epsilon(z) + \int_{4\pi}\int_{4\pi} L(z,\theta',\phi')[\sigma(z,\beta)/s(z)]d\Omega\sec\theta\,d\Omega/\epsilon(z). \quad (34)$$

Equation for Scalar Irradiance

Now Eq. (30) can be rewritten as

$$d\epsilon(z)/[\epsilon(z)dz] = -a(z)D(z) - s(z)[D(z) - D_s(z)]. \quad (35)$$

Thus the change in scalar irradiance with altitude is a function of both the absorption and the scattering coefficients, the radiance distribution, and the shape of the proportional volume scattering function $\sigma(z,\beta)/s(z)$.

Examples

We can explore the magnitude and the form of the two distribution functions through examples of the ground-level and the out-of-the atmosphere cases.

Out of the Atmosphere. At the top of the atmosphere, the sky radiances (θ = 0° to 90°) are zero. Thus the second or diffuse term in Eq. (32) is negative, and $D(z)$ is less than the Sun component or first term. A reasonable approximation for $D(\infty)$ assumes the upwelling radiance to be constant (Lambertian) and thus equal to the upwelling scalar irradiance divided by 2π:

$$D(\infty) = {}_s\epsilon(\infty)\sec\theta_s/\epsilon(\infty) + \epsilon(\infty,u)\int_{2\pi}\sec\theta\,d\Omega/[2\pi\epsilon(\infty)]. \quad (36)$$

The downwelling scalar irradiance is equal to the Sun scalar irradiance since there is no sky irradiance. Thus the upwelling scalar irradiance can be expressed, using Eq. (13), as ${}_sA(\infty){}_s\epsilon(\infty)$, and the total scalar irradiance is

$$\epsilon(\infty) = {}_s\epsilon(\infty)[1 + {}_sA(\infty)]. \quad (37)$$

Combining Eqs. (36) and (37) and evaluating sec $\theta d\Omega$ for a 5° resolution grid,[7] we get

$$D(\infty) = [\sec\theta_s - 4.4\,{}_sA(\infty)]/[1 + {}_sA(\infty)]. \quad (38)$$

Figure 2 depicts the radiance distribution function computed by using Eq. (38) with a range of Sun zenith angles and scalar albedos. It should be remembered that the ${}_sA(\infty)$ is the apparent albedo and not the inherent albedo. The two are not usually equivalent.

The scattering path function $L_{*s}(\infty,\theta,\phi) = 0$, since out of the atmosphere is by definition above the scattering layer. Therefore the scattering distribution function for out of the atmosphere is also zero:

$$D_s(\infty) = 0. \quad (39)$$

Rayleigh Scattering. It is relatively easy to see that the first term on the right-hand side of Eq. (34) becomes zero for Rayleigh scattering. The $\sigma(z,\beta)/s(z)$ is symmetrical about β = 90° and thus has equal forward scattering and backscat-

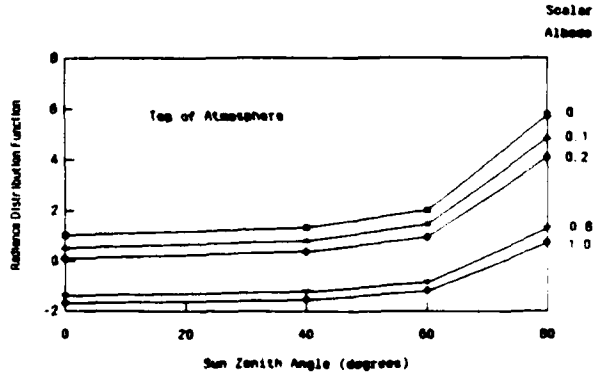

Fig. 2. Radiance distribution function at the top of the atmosphere as a function of Sun zenith angle and scalar albedo.

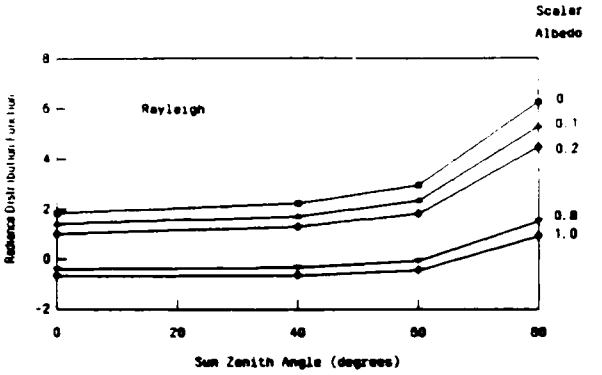

Fig. 3. Photopic Rayleigh radiance distribution function for ground level, $T_\infty(0, 0) = 0.907$.

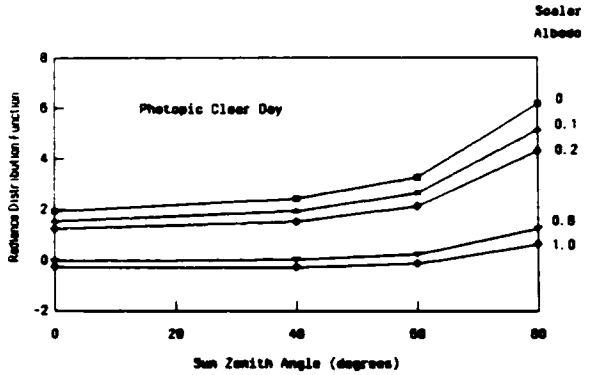

Fig. 4. Ground-level radiance distribution function for a photopic clear day, $T_\infty(0, 0) = 0.7$.

tering. Therefore the scattering from the Sun into the upward hemisphere is equal to the scattering into the lower hemisphere, and the weighting by sec θ makes the first term in Eq. (34) equal to zero. The same thing is true for the scattering from each sky- and/or terrain-radiance element. Therefore, for the Rayleigh atmosphere,

$$ {}_RD_s(z) = 0. \tag{40}$$

Equation (40) was verified by doing the integrals in Eq. (34) by discrete summation using a resolution of 5°. These were computed for several ground-level Rayleigh-model sky- and terrain-radiance distributions (several Sun zenith angles and several albedos). The Rayleigh sky-radiance distributions were computed by using model-atmosphere equations that assume equilibrium radiance to be constant with altitude.[8,9] The terrain radiance was assumed to increase toward the horizon and to be textured so that the largest reflectance was at 180° azimuth from the Sun.

For the Rayleigh case, Eq. (35) can be written as

$$ d\epsilon(z)/[\epsilon(z)dz] = -[a(z) + s(z)]D(z) = -\alpha(z)D(z). \tag{41}$$

The above equations are for monochromatic radiation. They are, however, reasonable engineering approximations for broadband radiation when the absorption is primarily in broadband continua and not in line or band spectra or when absorption is due to suspended particles or water droplets. This holds reasonably well in the visible portion of the spectrum in the atmosphere. It may also be useful for relatively narrow-band radiation in a window in the near infrared.

Figure 3 depicts sample Rayleigh radiance distribution functions. These examples are for ground level $D(0)$ for a range of Sun zenith angle and scalar albedo for the photopic case of Earth-to-space radiance transmittance $T_\infty(0, 0)$ equal to 0.907. These were computed by using Rayleigh sky-radiance distributions based on the equilibrium-radiance model atmosphere with the terrain described as above. The difference between using this textured terrain and a constant-radiance terrain affected $D(0)$ less than 3%. Scalar albedos, zero and one, provide the lower and the upper limiting cases. Scalar albedo 0.1 represents an average terrain of fields and crops, 0.2 represents desert, and 0.8 represents fresh snow.

The ground-level radiance distribution function for the photopic Rayleigh case is generally greater than the out-of-the-atmosphere case in Fig. 2. However, the two functions in Figs. 2 and 3 are of the same general form.

Photopic Clear Day. For a non-Rayleigh example, we will use a space-to-Earth radiance transmittance $T_\infty(0, 0)$ of 0.7. This is considered a standard clear day for the photopic sensor. For the proportional volume scattering function we will use the Barteneva[10] class 5 function values. We use sky radiances based on the equilibrium-radiance model atmosphere and the same type of terrain as described above.

The total downwelling irradiances computed from these sky radiances agree well (see Ref. 9) with the total downwelling illuminances (converted to irradiances) from Brown.[11] The Brown average illuminances as a function of Sun zenith are based on over 12,000 measurements made between 1943

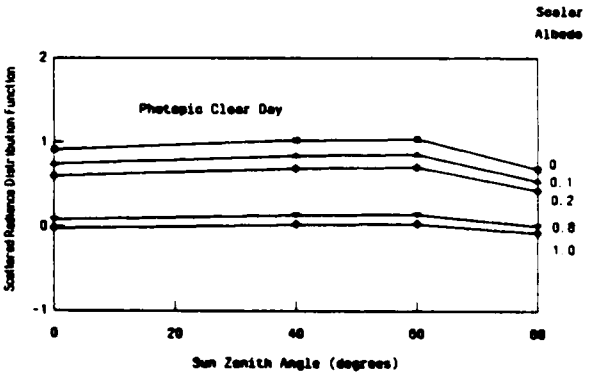

Fig. 5. Ground-level scattered radiance distribution function for a photopic clear day.

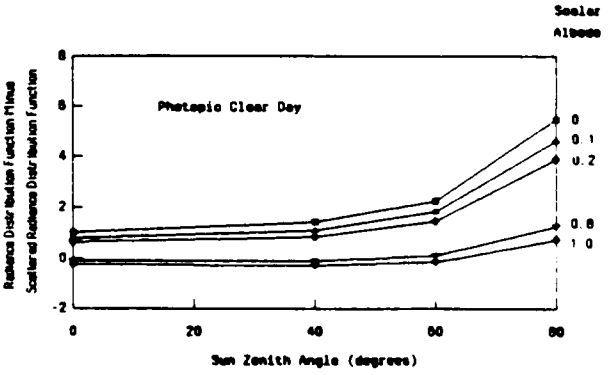

Fig. 6. Difference between the radiance and the scattered radiance distribution functions $[D(0) - D_s(0)]$ for a photopic clear day.

Appendix D

Appendix D

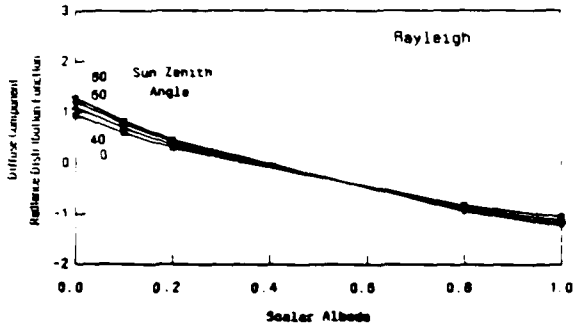

Fig. 7. Diffuse component of the Rayleigh radiance distribution function.

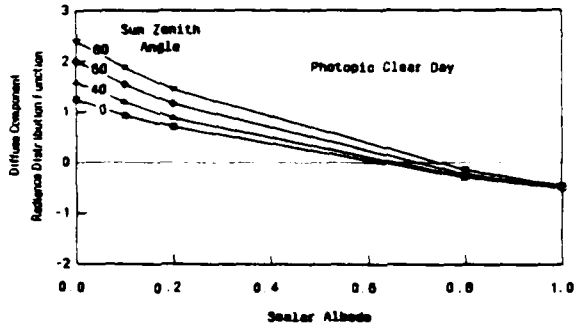

Fig. 8. Diffuse component of the radiance distribution function for a photopic clear day.

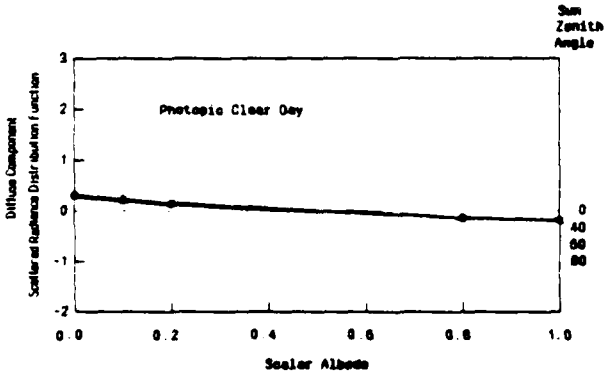

Fig 9. Diffuse component of the scattered radiance distribution function for a photopic clear day.

and 1947 all over the world. The Brown average values are generally used as an illuminance standard for a clear day.

Figure 4 depicts values of the radiance distribution function $D(0)$ for the photopic average clear-day case based on the model-atmosphere calculations. Figure 5 depicts the scattered radiance distribution function (note change of scale), and Fig. 6 depicts the difference between the radiance distribution function and the scattered radiance distribution function $[D(0) - D_s(0)]$. The two distribution functions were evaluated for the same range of albedos and Sun zenith angles as before.

The radiance distribution function for the average clear day (Fig. 4) is generally larger than the values for the Rayleigh case (Fig. 3), except at the largest Sun zenith angle 80°. However, the distribution-function difference $[D(0) - D_s(0)]$ for the average clear day is closer to zero than the Rayleigh distribution function. This is due to the effect of subtracting the scattered radiance distribution function (which is zero for the Rayleigh case).

Diffuse Component of the Distribution Functions. The first or Sun term in Eqs. (32) and (34) is always positive, but the second or diffuse term varies from positive to negative as albedo increases. In the out-of-the-atmosphere case, the diffuse component varies from zero for albedo zero to −2.2 for albedo 1.0.

Figures 7 and 8 depict the diffuse component of the radiance distribution function as a function of albedo for the photopic Rayleigh and standard clear day, respectively. The Rayleigh case became negative at lower albedos than did the distribution function for the photopic clear day. In Fig. 9 the diffuse component of the scattered radiance distribution function is depicted for the photopic clear day.

INTEGRATING THE EQUATION OF TRANSFER WITH ALTITUDE

Irradiance Integration

The equation of transfer for irradiance, Eq. (26), can be integrated with respect to altitude. The limits of integration are between z_0 and z as we descend into the atmosphere so that z_0 is greater than z:

$$\int_{\xi(z_0)}^{\xi(z)} d\xi(z) = \int_{z_0}^{z} a(z)[m(\lambda, T) - \epsilon(z)]dz. \tag{42}$$

The left-hand term is easily integrated, but the right-hand term is not. Partially integrated Eq. (42) becomes

$$\xi(z) - \xi(z_0) = \int_{z_0}^{z} a(z)[m(\lambda, T) - \epsilon(z)]dz. \tag{43}$$

This equation defines the irradiance divergence.

Approximate Solution

A reasonable approximation to the integration can be obtained if we assume that the change in the difference $[m(\lambda, T) - \epsilon(z)]$ is small enough from z_0 to z such that an average value $\overline{[m(\lambda, T) - \epsilon(z)]}$ can be substituted. Substituting in the average difference between the exitance and the scalar irradiance, it can now be taken out of the integral, and we get

$$\xi(z) - \xi(z_0) = \overline{[m(\lambda, T) - \epsilon(z)]} \int_{z_0}^{z} a(z)dz. \tag{44}$$

The integral of the absorption with altitude is the optical thickness that is due to absorption ${}_a t_{\lambda z}(z)$; therefore

$$\xi(z) - \xi(z_0) = {}_a t_{\lambda z}(z)\overline{[m(\lambda, T) - \epsilon(z)]}. \tag{45}$$

This is an approximate equation for the net irradiance change with altitude.

An expression for the absorption optical thickness can be obtained by rearranging Eq. (45):

$${}_a t_{\lambda z}(z) = [\xi(z) - \xi(z_0)]/\overline{[m(\lambda, T) - \epsilon(z)]}. \tag{46}$$

The error in the resultant optical thickness is probably less than the variability of the difference $[m(\lambda, T) - \epsilon(z)]$ from the average value.

Thus, if one has a measure of ambient temperature and downwelling and upwelling and scalar irradiance at two alti-

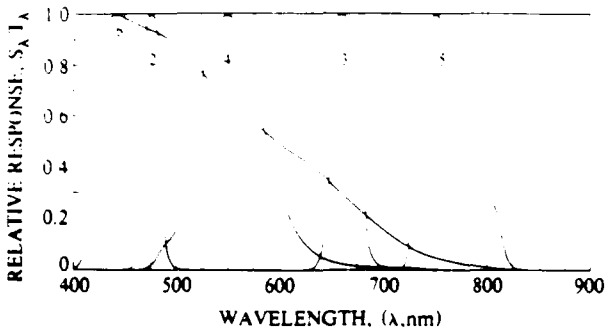

Fig. 10. Standard spectral responses for airborne filtered sensors.

Filter	Description	Mean Wavelength (nm)	Effective Passband (nm)
2	Blue	478	20
6	S-20	532	184
4	Pseudophotopic	557	78
3	Red	664	30
5	Near infrared	765	50

tudes z_0 and z, the absorption optical thickness can be obtained.

Visible-Spectrum Example

In the visible spectrum, the emission is negligible; therefore Eq. (46) simplifies to

$$ {}_a t_{\Delta z}(z) = [\xi(z_0) - \xi(z)]/\overline{\epsilon(z)}. \quad (47)$$

For an example, we will refer to measurements made during flight C-466 in Meppen, Germany.[12] Airborne measurements were made for a 4π coverage of sky and terrain radiances (measured with a 5° field of view), total volume scattering coefficient, and downwelling and upwelling irradiance. The example uses the sky and terrain radiances measured for filter 2. See Fig. 10 for the filtered sensor spectral characteristics.

The altitude z_0 was chosen as the highest altitude flown (6 km), and the z used was for the lowest altitude flown (0.2 km). Thus Δz equals 5.8 km. The Sun was unobscured at both altitudes, but there were scattered cirrus clouds.

Subsequent scanner tests indicated a spurious Sun reflection in sky-radiance measurements near the Sun. Therefore the first step was to correct the scanner data in the region 0°–25° scattering angle from the Sun. The correction method used was similar to the Barteneva[10] method for extrapolating the volume scattering function near the zero-degree scattering angle. Log sky radiance at each zenith angle was assumed to be linear with cos β from 0° to 30° in β. The slope of the line was established by the values near the 30° scattering angle.

The next step was to obtain a measure of radiance transmittance appropriate for the unobscured Sun. This was done by using solar almucantar sky radiances and a modification[13,14] of the Livshits–Pavlov[15] method.

As a check, the computed irradiances were compared to the E meter (irradiometer) measurements. The irradiances computed from the sky–terrain scanner measurements are given in Tables 1 and 2 together with the ratios to the E meter values. The ratio of computed to measured upwelling irradiances can be used as a control to evaluate the sky-radiance corrections since the terrain radiances required no correction. The ratio of computed to measured downwelling irradiances are as close or closer to one (the ideal) than the control ratios. Thus the corrected sky radiances were considered reasonable.

The evaluation of Eq. (47) is also shown in Table 3. The estimated error is ±8% based on the variability of the $\epsilon(z)$ at each altitude from the average $\overline{\epsilon(z)}$. No attempt was made to correct for the Sun zenith angle change from 41° to 47° between the measurements at 6 and 0.2 km.

The above sample indicates that the method appears usable on tropospheric measurements of this sort.

Table 1. Computed Scalar Irradiances for Flight C-466, Filter 2 $\bar{\lambda}$ = 478 nm

Specific Irradiance Component	Computed Scalar Irradiances (W/m² μm) At 6 km $\epsilon(6)$	At 2 km $\epsilon(0.2)$	Average over Altitude $\overline{\epsilon(\Delta z)}$	Change over Altitude
Sun ${}_s\epsilon(z)$	1796	1113		
Sky ${}_d\epsilon(z, d)$	338	838		
Upwelling $\epsilon(z, u)$	424	227		
Total $\epsilon(z)$	2558	2178	2368	8%
Albedo ${}_sA$	0.199	0.119		

Table 2. Computed Flat-Plate Irradiances for Flight C-466, Filter 2, λ = 478 nm

Specific Irradiance Component	Computed Flat-Plate Irradiances (W/m² μm) At 6 km E(6) Calculated from Scanner	At 2 km E(0.2) Calculated from Scanner
Sun ${}_sE(z)$	1359	757
Sky ${}_dE(z, d)$	114	380
Total downwelling $E(z, d)$	1473	1137
Total upwelling $E(z, u)$	187	77
Albedo $A(z)$	0.127	0.069
Net $\xi(z)$	1286	1060
Calculated–measured ratios		
Downwelling (scan/irrad)	1.04	1.02
Upwelling (scan/irrad)	0.96	1.11

Table 3. Computed Absorption Optical Thickness

Computational Procedure	Computed Absorption Optical Thickness $a(5.8^{(0.2)})$
From net irradiance	0.0954

Appendix D

Appendix D

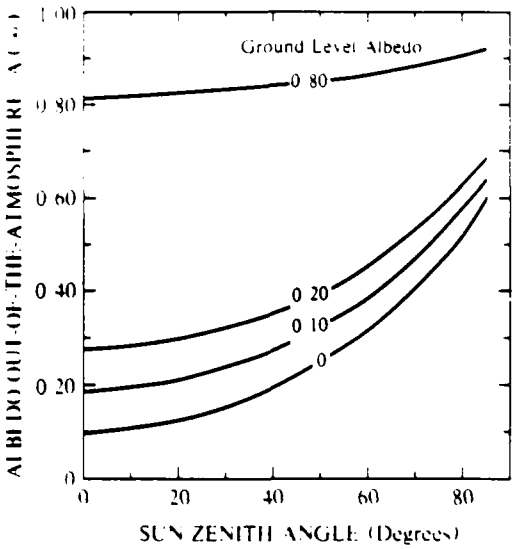

Fig. 11. Albedo out of the atmosphere for a nonabsorbing atmosphere based on Ref. 11 and Eq. (52).

No Absorption

When there is no absorption and hence no emission, Eq. (45) becomes

$$\xi(z) - \xi(z_0) = 0, \tag{48}$$

or, substituting in Eq. (25),

$$E(z, d) - E(z, u) = E(z_0, d) - E(z_0, u). \tag{49}$$

When there is no absorption the net irradiance does not change with altitude.

Substituting Eq. (11) into Eq. (49), we get an expression in terms of downwelling irradiance and the albedo:

$$E(z, d)[1 - A(z)] = E(z_0, d)[1 - A(z_0)]. \tag{50}$$

Thus the apparent albedo change with altitude is directly linked to the downwelling-irradiance change with altitude when there is no absorption.

The albedo out-of-the-atmosphere $A(\infty)$ can be computed when the albedo and the downwelling irradiance at altitude z are known, since the downwelling irradiance out of the atmosphere is the solar scalar irradiance ${}_s\epsilon(\infty)$ times the cosine of the Sun zenith angle

$$E(\infty, d) = {}_s\epsilon(\infty)\cos\theta_s. \tag{51}$$

Substituting Eq. (51) into Eq. (50) and rearranging, we get

$$A(\infty) = 1 - E(z, d)[1 - A(z)]/[{}_s\epsilon(\infty)\cos\theta_s]. \tag{52}$$

If we assume the photopic clear day to have negligible absorption, for example, we can use the illuminances from Brown[11] to compute the albedo out of the atmosphere by assuming various albedos at ground level. Using a Sun illuminance out of the atmosphere of 1.37×10^5 lm/m^2 based on the spectral irradiances from Johnson,[16] with the Brown illuminances converted to the same units; the results are shown in Fig. 11 for various ground-level albedos. A ground-level albedo of 0.1 is probably the most reasonable in relation to the Brown illuminances.

Scalar-Irradiance Integration

The equation of transfer for scalar irradiance, Eq. (35), can also be integrated. Integrating from z_0 to z, we get

$$\int_{\epsilon(z_0)}^{\epsilon(z)} \epsilon(z)^{-1}\,d\epsilon(z) = -\int_{z_0}^{z} a(z)D(z)dz - \int_{z_0}^{z} s(z)[D(z) - D_s(z)]dz. \tag{53}$$

Again, the left-hand term is easily integrated, but the right-hand term is not, which results in

$$\ln[\epsilon(z)/\epsilon(z_0)] = -\int_{z_0}^{z} a(z)D(z)dz - \int_{z_0}^{z} s(z)[D(z) - D_s(z)]dz. \tag{54}$$

This is the partially integrated equation for the change of scalar irradiance with altitude.

Approximate Solution

A reasonable approximation to the integration can be obtained if we assume that the changes in $D(z)$ and $[D(z) - D_s(z)]$ are small between z_0 and z. Thus the average values can be substituted and taken out of the integrals:

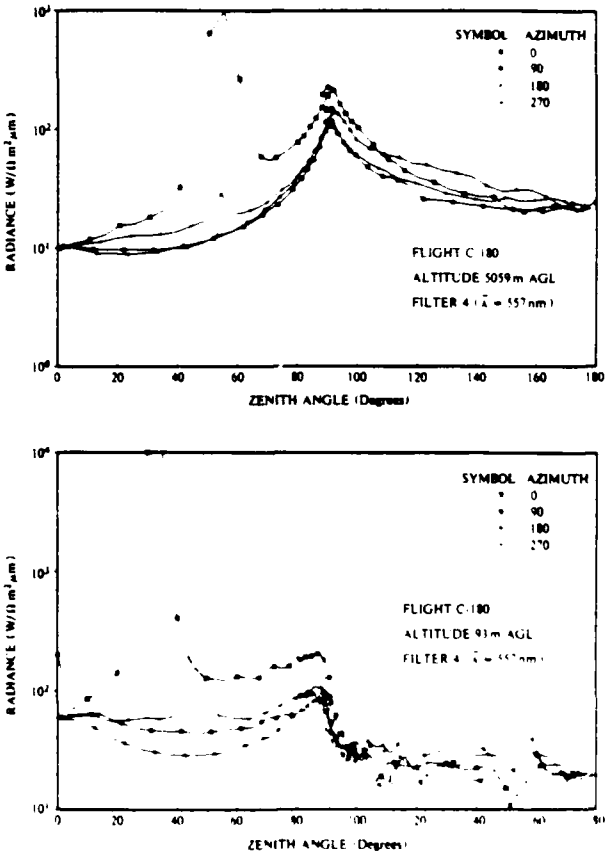

Fig. 12. Measured sky and terrain radiances for high and low altitude for the pseudophotopic filter 4 during flight C-180. Flight was in the afternoon on August 11, 1971, over farmlands north of St. Louis with scattered cumulus clouds dissipating and a layer of thin cirrostratus forming during the flight.

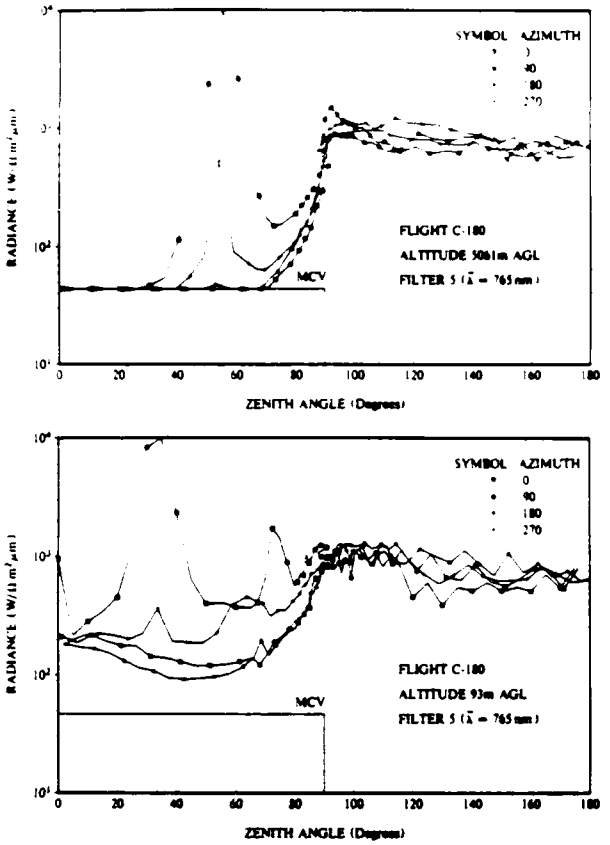

Fig. 13. Measured sky and terrain radiances for high and low altitude for filter 5 during flight C-180. MCV is the minimum calibratable value for the upper-hemisphere scanner radiance measurements using filter 5.

$$\ln[\epsilon(z)/\epsilon(z_0)] = -\overline{D(z)}\int_{z_0}^{z} a(z)\mathrm{d}z - [\overline{D(z) - D_s(z)}]\int_{z_0}^{z} s(z)\mathrm{d}z, \tag{55}$$

or, in terms of the optical thicknesses,

$$\ln[\epsilon(z)/\epsilon(z_0)] = -\overline{D(z)}_a t_{\Delta z}(z) - [\overline{D(z) - D_s(z)}]_s t_{\Delta z}(z). \tag{56}$$

This is an approximate solution for the change of scalar irradiance with altitude.

Effect of Altitude on the Radiance Distribution Function

Let us speculate at this point on the relationship between the Sun and the diffuse terms in Eq. (32) as a function of altitude. We can do this by looking at sample data for the troposphere. We will refer to airborne data from the only series of flights in the atmospheric optical data bank of the Visibility Laboratory that are in and near a large metropolitan area with considerable air pollution.[17] The data are thus expected to indicate measurable absorption from gaseous and/or particulate pollution sources.

Figure 12 contains two graphs for the pseudophotopic filter 4. One graph is for high altitude and one for low altitude of measured sky and terrain radiances for azimuths from the Sun of 0°, 90°, 180°, and 270°. These graphs are typical of terrains with scalar albedos of approximately 0.1 at low altitude. Typically, the apparent albedo of these terrains increases with altitude.

The sky radiances (θ = 0°–90°) are generally lower than the apparent terrain radiances (θ = 90°–180°) at high altitude and generally greater than the terrain radiances at low altitude. Thus the diffuse component of the radiance distribution function would be negative at high altitude and positive at low altitude. At high altitude, the total $D(z)$ is less than the first or Sun term. At some intermediate altitude, the $D(z)$ is equivalent to the Sun term since the diffuse term becomes zero. At low altitude, the $D(z)$ is greater than the Sun term since the second term becomes positive.

On the same flight, graphs (and albedos) for broadband filters 2 and 3 with mean wavelengths of 478 and 664 nm, respectively (see Fig. 10), were similar to Fig. 12. In contrast, filter 5 had a consistently higher albedo and higher overall radiance transmittance, space to sensor. The high- and low-altitude graphs for the broadband filter 5 (mean wavelength 765 nm with an albedo of 0.3) are given in Fig. 13. These graphs show sky radiance lower than terrain radiance at both low and high altitude, indicating that the diffuse component of $D(z)$ would be negative at all altitudes.

The above analysis is reasonably consistent with the analysis of the diffuse component of the radiance distribution function based on the model-atmosphere computations, as depicted in Figs. 7 and 8. In the model calculations, the diffuse component became negative with increased albedo. It also became negative at lower albedos for the thinner Rayleigh atmosphere.

SUMMARY

Absorption optical thickness between two altitudes of measurement can be obtained from measurements of 4π radiance by using the equation of transfer for irradiance. Absorption values would be of use to modelers of radiance fields and contrast transmittance and of some interest to those concerned with visibility and pollution. Equation (46) provides a means for obtaining absorption optical thickness values from extant tropospheric visible-spectrum data. The equation of transfer for irradiance has absorption and emission terms but no scattering terms. This becomes apparent only when the path function is broken into its two (scattered and emitted) components.

The equation of transfer for scalar irradiance has absorption and scattering terms but no emission term. Both the absorption and the scattering are affected by a radiance distribution function. The scattering is also affected by a scattered radiance distribution function, except for the Rayleigh case. The equation of transfer for scalar irradiance is necessary for understanding the radiation field and how it changes with altitude.

The equations were derived for monochromatic radiation in the atmosphere below the mesosphere. They are appropriate for broadband radiation in the visible spectrum. They are also probably applicable to a relatively narrow-band radiation operating in an absorption window in the near infrared.

These irradiance and scalar-irradiance equations can be used, provided that the medium is in a steady state during the measurements. In the visible, Eq. (47) can also be used as a test to indicate whether a steady state exists. The

Appendix D

equations require not an unobscured Sun but only that the data from the two altitudes be consistent (that is, as if they had been measured simultaneously).

ACKNOWLEDGMENTS

I wish to acknowledge a debt to the two reviewers who criticized the development of the scalar-irradiance equation, thus correcting a serious error. This correction led to the current form of Eq. (35).

This work was begun by the author at the Visibility Laboratory, University of California, San Diego, for the U.S. Air Force. Further development as well as the writing and the publication of this article was done at Viz. Ability under U.S. Army Research Office contract no. DAAG29-84-C-0014. I wish to thank Judith Olson for technical editing assistance.

Appendix D

REFERENCES AND NOTES

1. S. Q. Duntley, A. R. Boileau, and R. W. Preisendorfer, "Image transmission by the troposphere I," J. Opt. Soc. Am. 47, 499–506 (1957).
2. R. W. Preisendorfer, *Hydrological Optics* (Environmental Research Laboratories, National Oceanic and Atmospheric Administration, U.S. Department of Commerce, Honolulu, Hawaii, 1976), Vols. I and II.
3. S. Chandrasekhar, *Radiative Transfer* (Dover, New York, 1960).
4. W. G. Driscoll and W. Vaughan, *Handbook of Optics* (McGraw-Hill, New York, 1978).
5. J. M. Prospero, R. J. Charlson, V. Mohnen, R. Jaenicke, A. C. Delany, J. Moyers, W. Zoller, and K. Rahn, "The atmospheric aerosol system: an overview," Rev. Geophys. Space Phys. 21, 1607–1629 (1983).
6. W. L. Wolfe, "Radiation theory," in *The Infrared Handbook*, W. L. Wolfe and G. J. Zissis, eds. (U.S. Government Printing Office, Washington, D.C., 1978).
7. The 5° resolution for the summative grid was chosen to correspond to the resolution of the measured and model sky-radiance arrays used in ensuing analyses.
8. J. I. Gordon, "Model for a clear atmosphere," J. Opt. Soc. Am. 59, 14–18 (1969).
9. J. I. Gordon and R. W. Johnson, "Equilibrium radiance model applications and comparisons to atmospheric measurements and Rayleigh models," Appl. Opt. 23, 3363–3372 (1984).
10. O. D. Barteneva, "Scattering functions of light in the atmospheric boundary layer," Bull. Acad. Sci. USSR Geophys. Ser. 12, 1237–1244 (1960).
11. D. R. I. Brown, *Natural Illumination Charts* (Bureau of Ships U.S. Department of the Navy, Washington, D.C., 1952), Rep. 374-1, Project Ns-714-100.
12. Flight C-466 was made on August 15, 1978. It is described by R. W. Johnson and J. I. Gordon, "Airborne measurements of atmospheric volume scattering coefficients in northern europe, summer 1978," ADA 097 134 (National Technical Information Service, Springfield, Va., 1980).
13. J. I. Gordon, "Implications of the equation of transfer within the visible and infrared spectrum," ADA 1133 979 (National Technical Information Service, Springfield, Va., 1982).
14. J. I. Gordon, "New uses for the solar almucantar," Appl. Opt. 24, 3381–3389 (1985).
15. G. Sh. Livshits and V. E. Pavlov, "Atmospheric transmittance and the interrelationships of certain optical parameters," in *Atmospheric Optics*, Nikolai B. Divari, ed. (Plenum, New York, 1970), pp. 53–56 (translated by S. B. Dresner).
16. F. R. Johnson, "The solar constant," J. Meteorol. 11, 431–439 (1954).
17. The measurements were made using instrumentation on board an AFGL C-130 aircraft in the area of St. Louis, Illinois. The METRO deployment was designed to sample the turbid character of the heavy summer atmosphere in the vicinity of a densely urbanized population center. The Metropolitan Meteorological Experiment (METROMEX) was being coordinated for the St. Louis area during the same interval, as reported by S. A. Changnon, F. A. Huff, and R. G. Semonin, "METROMEX: an investigation of inadvertent weather modification," Bull. Am. Meteorol. Soc. 52, 958–967 (1971). The airborne optical data for filters 2–4 are reported in S. Q. Duntley, R. W. Johnson, and J. I. Gordon, "Airborne measurements of atmospheric properties in southern Illinois," AD 774 597 (National Technical Information Service, Springfield, Va., 1973); "Airborne and ground-based measurements of optical atmospheric properties in southern Illinois," ADA 013 164 (National Technical Information Service, Springfield, Va., 1974).

Appendix E

JACQUELINE I. GORDON
Viz. Ability, Inc., 2941 NW Ashwood Dr., Corvallis, Oregon 97330
and
RICHARD W. JOHNSON
Visibility Laboratory, Scripps Institution of Oceanography
University of California, San Diego, La Jolla, California 920093

Equilibrium or path reflectance method of measuring atmospheric transparency in the visible and near infrared from ground stations: Theory, instrumentation, data and applications.

Abstract

Two concerns of atmospheric transparency determination are the loss of image forming light and the veiling effect of scattered light. Path reflectance takes both into consideration. The veiling light which masks the signal received by sensors on satellites can be and has been measured from the ground. An instrument was designed and has been in use for some 20 years providing ground truth for remote sensing from space. A reasonably broad sample from this data base, including data from passbands with mean wavelengths between 459 nm and 882 nm is presented and discussed.

1. INTRODUCTION

The radiance transmittance through the atmosphere is the same for inverse directions for any path of sight. That is, the vertical upward transmittance is equivalent to the vertically downward transmittance, and the transmittance for the path of sight at zenith angle 60° azimuth 0° is equivalent to the transmittance for the path of sight at zenith angle 120° azimuth 180°. Thus values of transmittance or

optical thickness measured on the surface of the earth are directly applicable to the transmittance for the downward paths of sight, both being the vertical transmittance $T_\infty(0,0)$ to the power of the relative optical airmass $m(\theta)$ for the appropriate zenith angle θ

$$T_\infty(0,\theta)=T_\infty(0,0)^{m(\theta)}. \quad (1)$$

Appendix E

The path radiance is the radiance scattered into the path of sight from all 4π directions. This radiance is not generally the same in both directions along the same path since the angle of scattering from the principal light source, the sun or moon, is generally not equivalent for the two paths of sight. However, a method[1] is available whereby the path radiance can be predicted from ground-based measurements.

This paper will primarily be concerned with the veiling effect of intervening path radiance or path reflectance and how it can be and has been measured from ground stations to provide the ground truth for remote sensing. Three data sets will be presented. These will be designated Rooftop, Portable and Sea Air. They range from data taken during the earlier development of the earth-to-space method to data taken to provide ground truth for remotely sensed measurements.

The notation used is that adopted by the Visibility Laboratory, University of California, San Diego,[2] and modified to correspond to Optical Society of America recommendations in Sec. 1 of Driscoll and Vaughn[3].

2. THEORY

2.1 Path Radiance

The basic equation for the apparent radiance of an object on the surface of the earth as measured by a sensor in earth orbit is

$$L_\infty(\infty,\theta,\emptyset)=L_0(0,\theta,\emptyset)T_\infty(\infty,\theta) + L^*_\infty(\infty,\theta,\emptyset) \quad (2)$$

where $L_\infty(\infty,\theta,\emptyset)$ is the apparent radiance as measured at range $r=\infty$, at altitude $z=\infty$, for the path of sight at zenith angle θ and azimuth $\emptyset$. The $L_0(0,\theta,\emptyset)$ is the inherent radiance at range $r=o$ and altitude $z_t=0$. The initial signal is degraded by the radiance transmittance $T_\infty(\infty,\theta)$ and the veiling path radiance $L^*_\infty(\infty,\theta,\emptyset)$. The optical thickness $t_\infty(0)$ is related to the radiance transmittance by

$$\ln T_\infty(0,0) = -t_\infty(0). \quad (3)$$

The method of measuring earth-to-space path radiance from ground stations has been completely described (Ref. 1). It uses sky radiance $L^*_\infty(0,\theta',\emptyset')$ to obtain the effective equilibrium radiance $L_q(0,\beta)$ at the appropriate scattering angle β for the downward path of sight from earth to space

$$L_q(0,\beta) = L^*_\infty(0,\theta',\emptyset')/[1-T_\infty(0,\theta')]. \quad (4)$$

If θ is the zenith angle of the downward path of sight and θ' is the zenith angle of the sky radiance at the same scattering angle β from the principal light source such as the sun or moon, the earth-to-space path radiance is (Eq. 8 Ref. 1)

$$L^*_\infty(\infty,\theta,\beta) = L^*_\infty(z,\theta',\beta)[1-T_\infty(\infty,\theta)]/[1-T_\infty(z,\theta')]. \quad (5)$$

Figure 1 illustrates the scattering angle relationships for a vertically downward path of sight.

Three experiments validated the method. In addition, the method was used during the Gemini program[4] as a part of a carefully controlled measurement of the visual capabilities of astronauts in earth orbit to discriminate test objects on the ground.

The method was found to be generally valid, not only on cloud-free days but on days with some clouds, as long as the path of sight and the sky radiance were cloud free.

When the β for the path of sight is larger than all the scattering angles available in the upper hemisphere (this happens most often when the sun zenith angle is small) an approximation is used of the sky radiance at $\beta = 90°$. This approximation was used and validated in the three experiments.

2.2 Path Reflectance

Path reflectance was defined by Duntley[5] as (Eq. 4, Ref 5)

$$R^*_\infty(\infty,\theta,\emptyset) = \pi L^*_\infty(\infty,\theta,\emptyset)/[E(0,d)T_\infty(\infty,\theta)], \quad (6)$$

where $E(0,d)$ is the total downwelling irradiance at the object altitude. We have expressed Eq. 6 in terms of the orbital downward path of sight. It combines the effects of path radiance, downwelling irradiance and path transmittance in such a way that the equation for contrast transmittance can be written as (Eq. 3, Ref. 5)

$$C_\infty(\infty,\theta,\emptyset)/C_0(0,\theta,\emptyset) = [1+R^*_\infty(\infty,\theta,\emptyset)/{}_bR_0(0,\theta,\emptyset)]^{-1}, \quad (7)$$

Appendix E

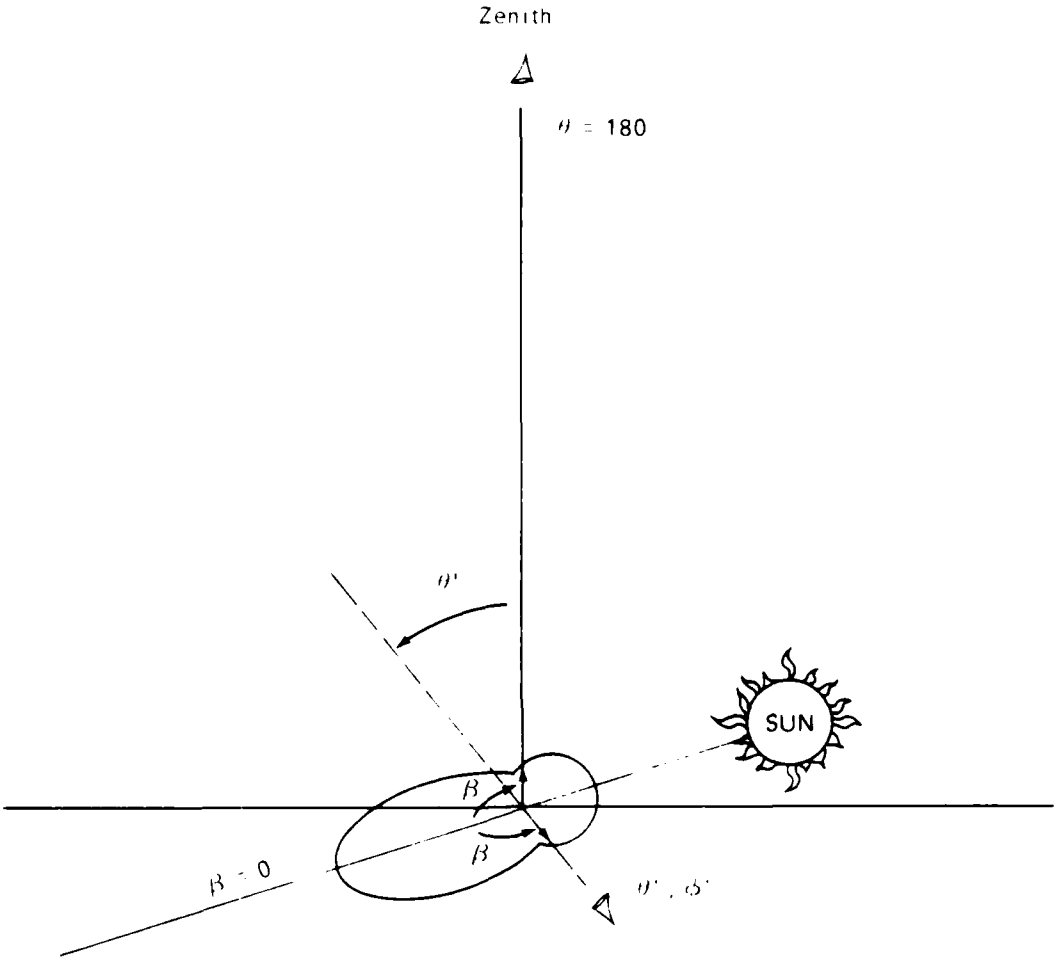

Fig. 1. Scattering angle β relationships for vertical downward path of sight.

where ${}_bR_o(0,\theta,\emptyset)$ is the inherent background reflectance. The inherent contrast $C_o(0,\theta,\emptyset)$ is defined by

$$C_o(0,\theta,\emptyset) = {}_tL_o(0,\theta,\emptyset)/{}_bL_o(0,\theta,\emptyset) - 1$$
$$= {}_tR_o(0,\theta,\emptyset)/{}_bR_o(0,\theta,\emptyset) - 1 \quad (8)$$

where ${}_tL_o(0,\theta,\emptyset)$ is the inherent object radiance and ${}_tR_o(0,\theta,\emptyset)$ the inherent object reflectance. Apparent contrast $C_\infty(\infty,\theta,\emptyset)$ is similarly related to the apparent object and background radiances and reflectances appropriate for an orbital sensor.

The contrast transmittance is related to the ratio of the path reflectance to the inherent background reflectance in Fig. 2 (Fig. 3, Ref. 5). When the ratio is one, the contrast transmittance is 0.5. When the background reflectance is smaller than the path reflectance, the ratio is greater than one and the contrast transmittance is less than 0.5. Conversely, when the background reflectance is greater than the path reflectance, the ratio is less than one and the contrast transmittance lies between 0.5 and 1.0.

2.3 Additional Substantiation

The method for obtaining earth-to-space path radiance was based on empirical evidence and not on theory. Additional empirical evidence has indicated that there is a theoretical basis as well[6]. The point function equilibrium reflectance $R_q(z,180°)$ for the vertically downward path of sight was found to be constant with altitude for 26 (80%) out of 33 separate tropospheric profiles measured during one field trip. These profiles were measured during mostly cloudy conditions but the flights were always in cloud free segments of the path.

When equilibrium reflectance for a given path of sight is a constant it is possible to integrate the equation of transfer to obtain an equation similar to Eq. 2 (Eq. 44, Ref. 6)

$$R_\infty(\infty,\theta,\emptyset) = R_o(0,\theta,\emptyset)T_\infty(\infty,\theta) + R_q(0,\theta,\emptyset)[1-T_\infty(\infty,\theta)]. \quad (9)$$

The path reflectance then becomes

$$R^*_\infty(\infty,\theta,\emptyset) = R_q(0,\theta,\emptyset)[1-T_\infty(\infty,\theta)]/T_\infty(\infty,\theta)$$
$$= R_q(0,\theta,\emptyset)[T_\infty(\infty,\theta)^{-1}-1]. \quad (10)$$

Appendix E

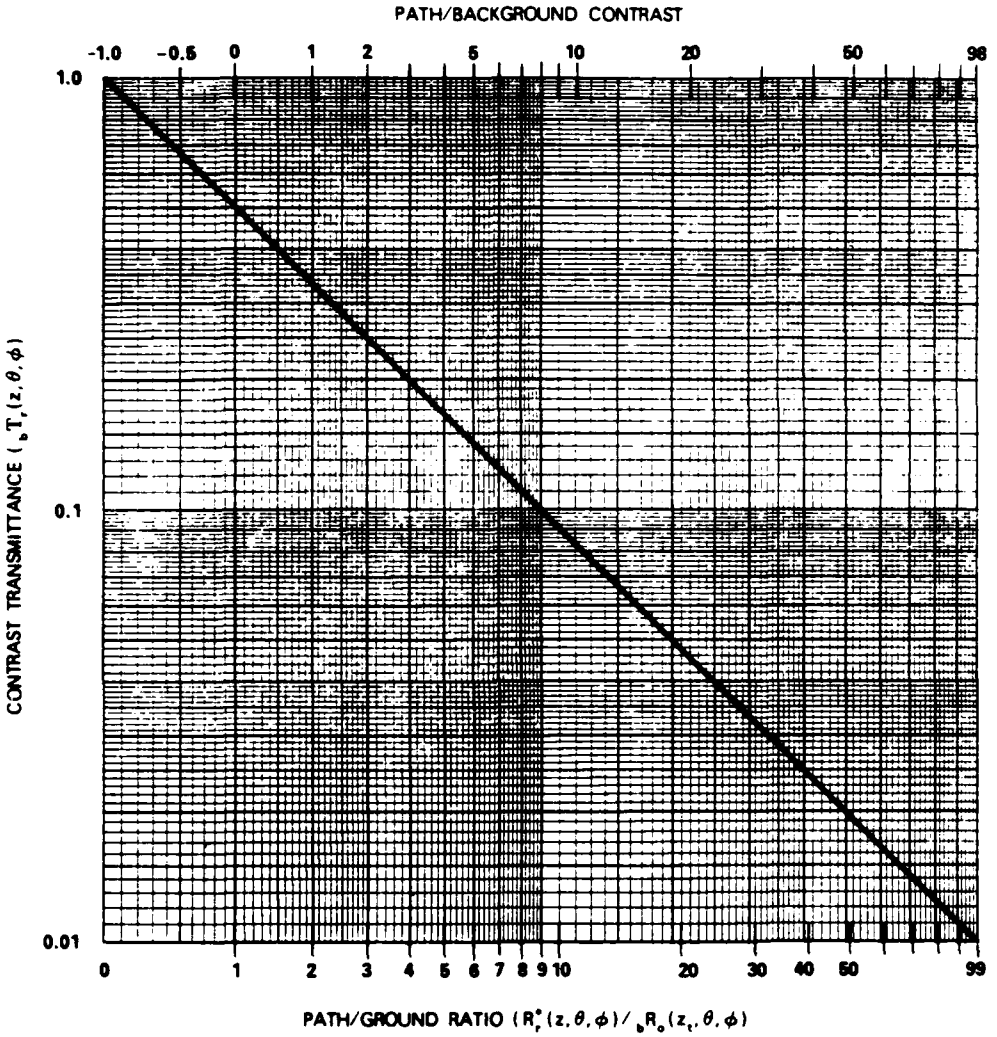

Fig. 2. Contrast transmittance as a function of the path to background reflectance ratio.

2.4 Caveat

Recent data analyses indicate that the transmittance in Eqs. 4 and 5 is the transmittance due to scattering alone ${}_sT_\infty$ and does not include any absorption[7,8,9]. When absorption is small, this can probably be ignored. Therefore, Eqs. 5, 9 and 10 are appropriate in the windows where absorption is relatively negligible.

Appendix E

3. INSTRUMENTATION

3.1 Early Instrumentation

The instrumentation used to develop the method of obtaining earth-to-space path reflectance was primarily a solar transmissometer with a field of view of 4 minutes of arc (Fig. 3), a sky scanning telephotomer with a five degree field of view (Fig. 4), and an irradiance meter (upper portion of Fig. 5). The Rooftop data set used these instruments and the Pahrump, Nevada experiment in the Portable data set used a similar portable set of instruments. The Portable scanner pattern was different but a 5° field of view was still used in a 2π scan pattern.

The vertical transmittance was obtained from the measurements of apparent center sun radiance ${}_sL_\infty(0,\theta_s,0)$ as follows

$$T_\infty(z,0)=[{}_sL_\infty(0,\theta_s,0)/{}_sL_0(\infty,\theta_s,0)]^{1/m(\theta_s)}. \quad (11)$$

The empirical expression for airmass was taken from Kasten[10]. The inherent solar radiance ${}_sL_0$ for each spectral passband was obtained for the Rooftop data set by means of a Langley graph on an optically stable day in each calibration period. Theoretical inherent sun values were used for the other two data sets. The theoretical values and their computation will be described later.

Occulting Irradiometer

During one of the field experiments included in the Portable data set (at the Naval Ordinance Test Station, China Lake, California (NOTS) in 1962), an irradiometer with an occulting metal strap (lower portion of Fig. 5) was used to obtain both the transmittance and the downwelling irradiance. Since the two occulted sky portions are very nearly equal in irradiance, the difference between the downwelling measurement E'(0,d) when the strap is near the azimuth of the sun and

Appendix E

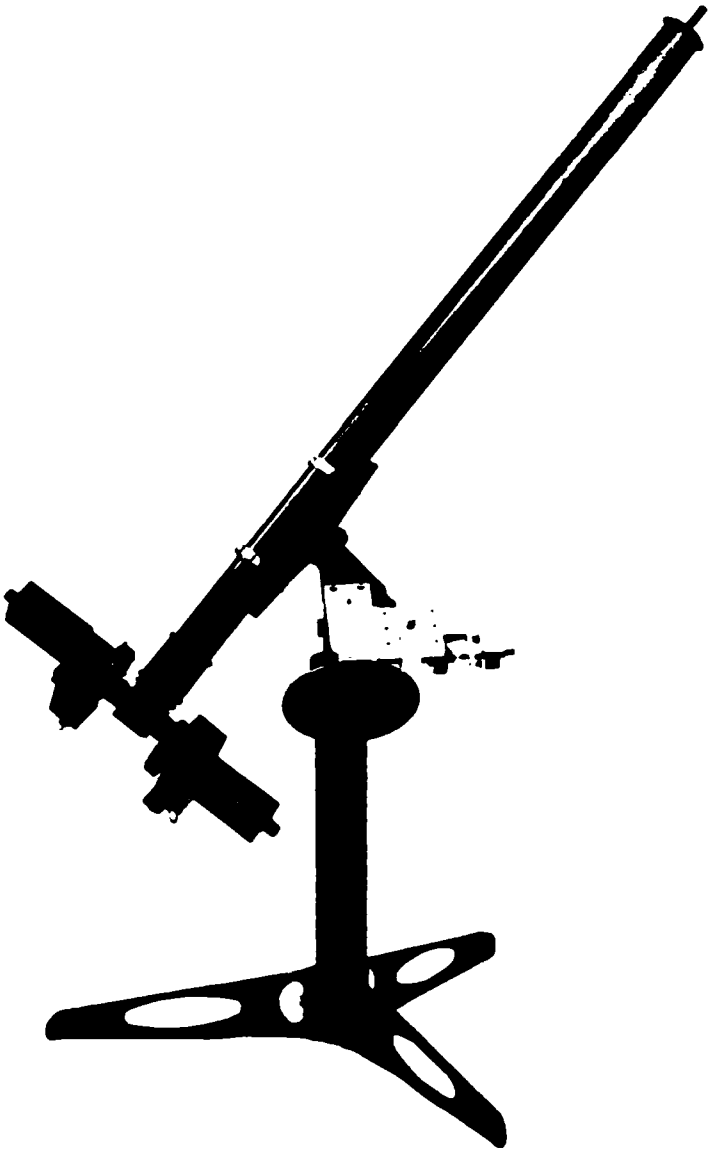

Fig. 3. The transmissometer shown in this figure is on a portable equatorial mount for field use. For the Rooftop data set, the transmissometer was mounted on a large diameter steel post with a carefully machined polar axis accurately surveyed and locked in position. The transmissometer was aligned by a clock drive and the alignment checked by an attendant immediately prior to collection of each data package.

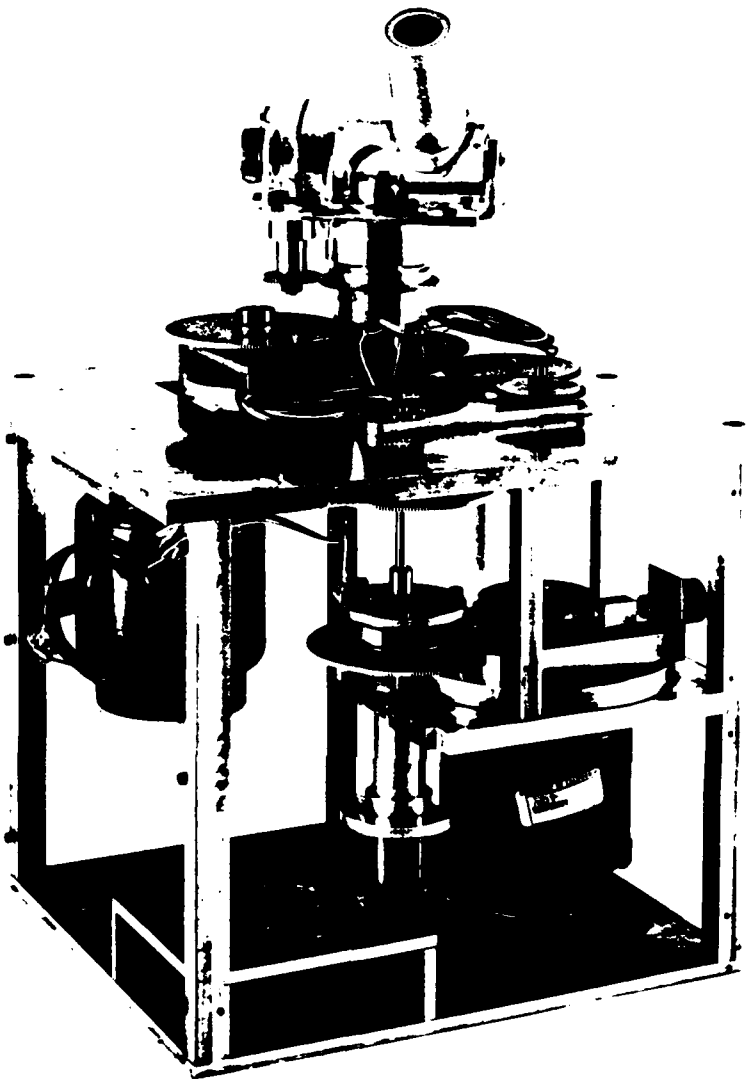

Fig. 4. The sky scanning telephotometer had a 5° field of view. At the beginning of the scan pattern the telephotometer was pointed in the direction of the azimuth of the sun, 87.1875° in zenith angle (2.8125° above the horizontal). It moved azimuthally counterclockwise in 64 discrete steps ($\Delta\emptyset$ = 5.625°). Then it decreased in zenith angle by 5.625°, and repeated the pattern. After rotating azimuthally at 16 zenith angles, the pattern was complete, and the scanner returned to the initial position.

Appendix E

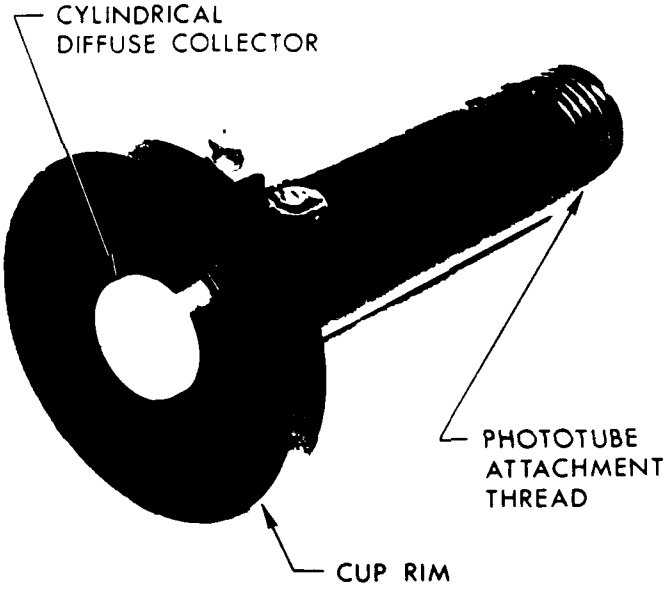

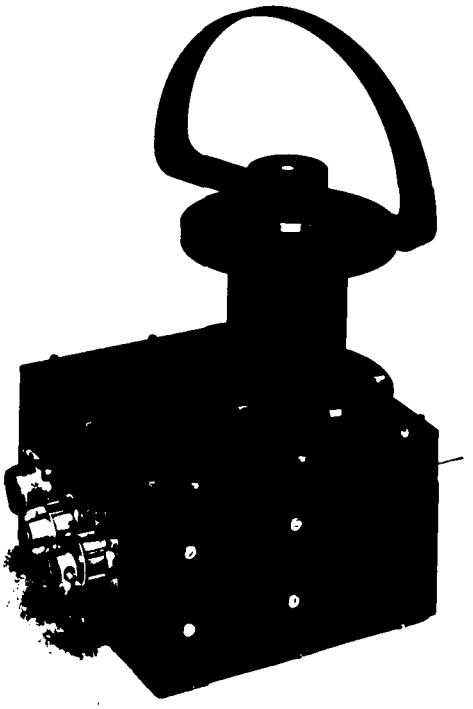

Fig. 5. Irradiometer and shadow intensity. The collector cap of the irradiometer is shown on the top. It is designed so that the outer surface of the white plastic diffuser is in the same plane as the outer rim of the cup. The extent of the diffuser side exposure and the diameter of the cup are determined empirically to obtain the cosine collection within ±2 percent for all zenith angles out to 90°. The purpose of the serrated grooves is to prevent unwanted flux from being reflected from the bottom of the cup to the side of the diffuser. The metal strap which rotates azimuthally is shown in the bottom picture.

the sky irradiance measurement with the sun azimuth occulted ${}_kE'(0,d)$ is the sun irradiance ${}_sE(0,d)$,

$${}_sE(0,d) = E'(0,d) - {}_kE'(0,d). \quad (12)$$

The corrected sky irradiance ${}_kE(0,d)$ was obtained by multiplying the measured value by a factor C to correct for occultation by the metal strap. A reasonable estimate of the factor C was obtained by assuming a constant radiance for the sky and integrating over the solid angle of the strap Ω_m to obtain the contribution from the occulted portion. The contribution from a constant radiance sky if there were no stap is π, therefore

$$C=\pi/[\pi - \int_{\Omega_m} \cos\theta d\Omega]. \quad (13)$$

The total downwelling irradiance is the sum of the sun irradiance and the corrected sky irradiance.

3.3 Contrast Reduction Meter (CRM)

An instrument was developed specifically for obtaining the path radiance and reflectance for the vertically downward path of sight. This instrument was designated the contrast reduction meter or the CRM. A sketch of the geometrical relationships involved, assuming that $\beta=90°$ is the appropriate sky radiance to be measured, is given in Fig. 6. A photograph of the device is given in Fig. 7 and a sketch of the layout of the CRM in Fig. 8. The device is essentially a solar transmissometer with a 2 minute field of view, a sky radiance photometer with a five degree field of view and total downwelling irradiance meter combined into one instrument. A detailed description of the instrument is given by Duntley, et al.[11].

The CRM has been the principal instrument used by the Visibility Laboratory to gather ground-truth information for remote sensing. All the reported Portable data except that taken at NOTS and Pahrump were measured with the CRM, as were all the Sea Air data.

3.4 Spectral Specifications for Measurements

The standard spectral response $\overline{S}_\lambda$ of the sensor times the appropriate filter transmittance $\overline{T}_\lambda$ for the four passbands used for the Rooftop experiment are depicted in Fig. 9 as relative values. The relative spectral response $\overline{S}_\lambda\overline{T}_\lambda$ for filter 3 is the photopic luminosity function.

Appendix E

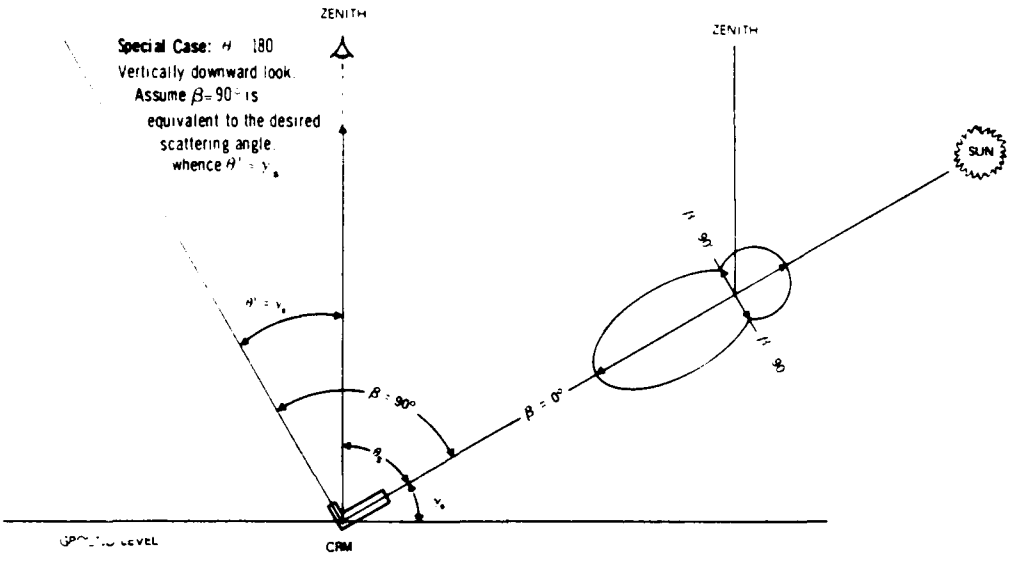

Fig. 6. Scattering angle relationships for typical CRM operations.

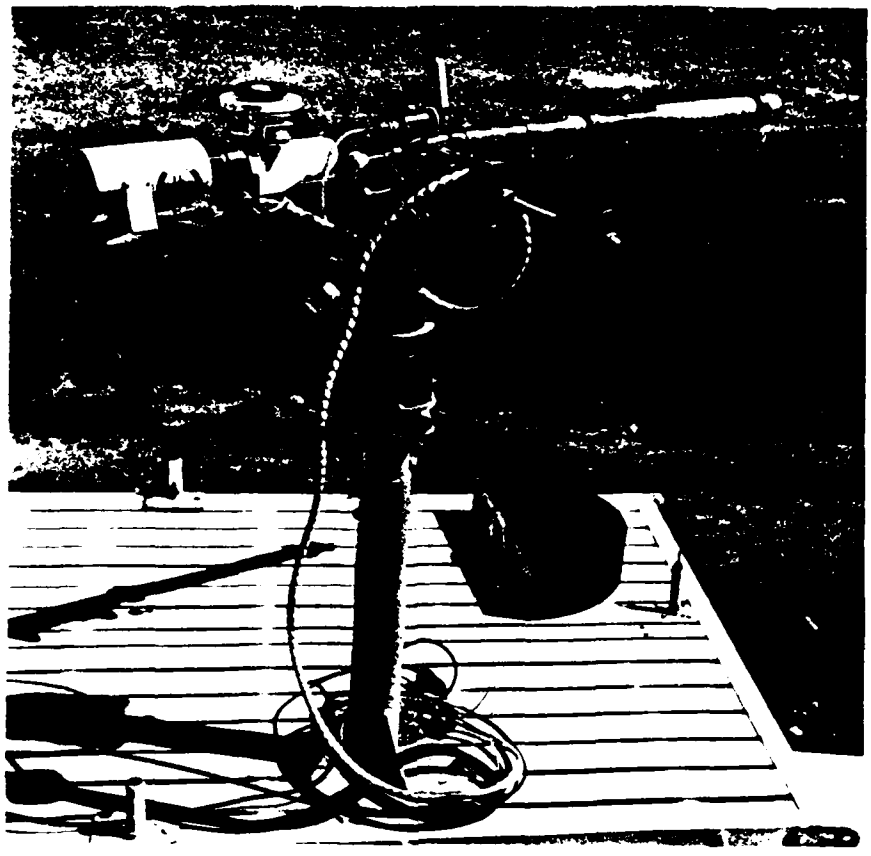

Fig. 7. Contrast Reduction Meter. The instrument has incorporated in it two optical systems, one having a field of view of 2 minutes of arc for measuring apparent radiance of the sun, and the second system having a field of view of 5° for measuring radiance in any direction. A flat plate collector mounted on the sunshade of the second optical system (as shown in this figure) converts the telephotometer into an irradiometer. The multiplier phototube, which is enclosed in a thermoelectric junction temperature control unit (in the cylindrical aluminum cover), is coupled to the optical unit (painted white) by an optical filter unit (the short black anodized cylinder). The instrument is mounted on an equatorial mount to permit easy tracking of the sun.

Appendix E

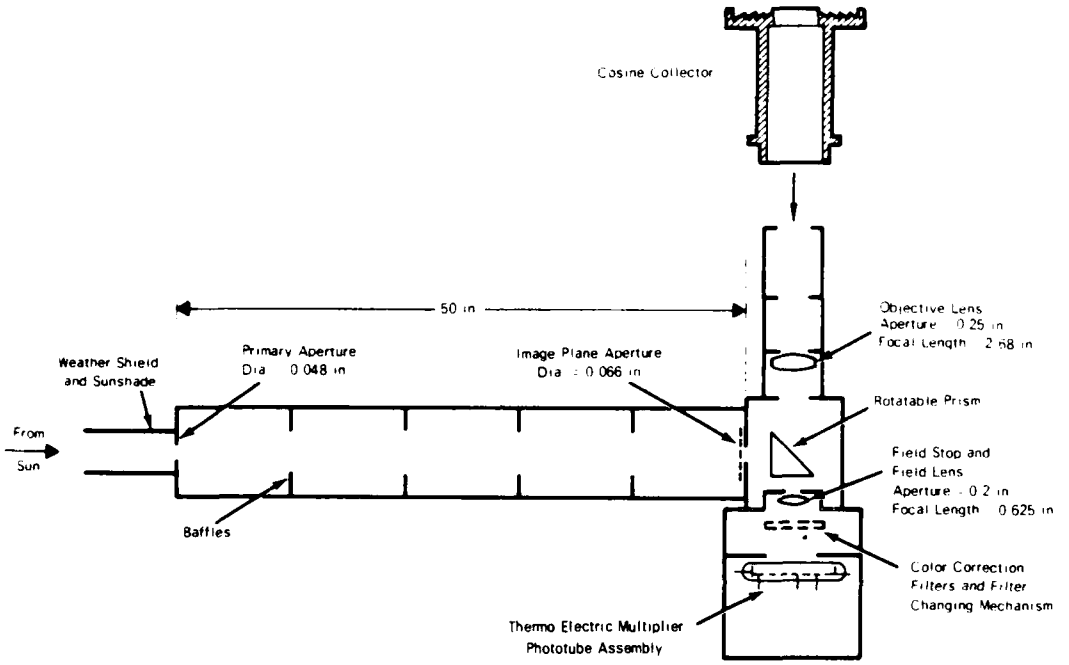

Fig. 8. Schematic of collection optics for the CRM.

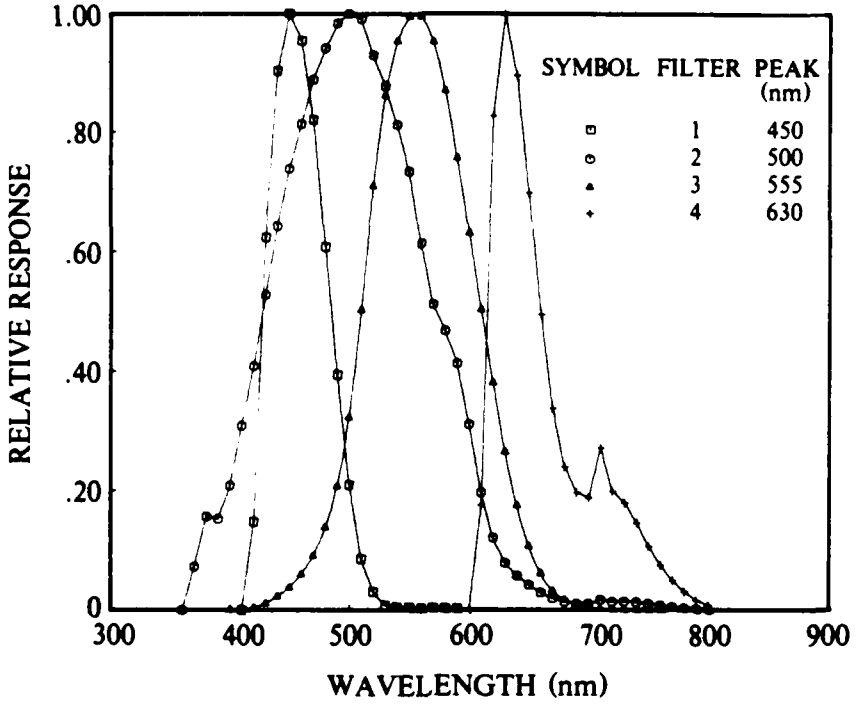

Fig. 9. Relative spectral response of the four passbands for the Rooftop data set. The passband for filter 2 was the broadest, followed by the photopic passband filter 3. The two remaining passbands are relatively narrow, 60 ±1.9 nm.

Appendix E

Although the Portable data set included some measurements for 6 passbands in the visible, only the values for the photopic passband filter 3, are included herein.

The Sea Air data set used two passbands, Filter 1 photopic, and Filter 2 in the near Infrared. The relative spectral responses for these two filters are presented in Fig. 10.

The effective passband and meanwavelength for each filter are presented in Table 1. The mean wavelength $\bar{\lambda}$ is

$$\bar{\lambda}=\Sigma\lambda\bar{S}_{\lambda}\bar{T}_{\lambda}\Delta\lambda/\delta\lambda \qquad (14)$$

where the cumulative product is between 380 and 1150 nm and $\Delta\lambda$ is 5 nm. The effective passband $\delta\lambda$ is the area under the relative spectral response curve.

The remaining four columns are theoretical solar and atmospheric properties appropriate for these passbands. The sun irradiance for out-of-the atmosphere was computed using the spectral solar irradiance values of Johnson[12]. The inherent center sun radiance is based on the solar spectral irradiances of Johnson and the spectral limb darkening functions of *Minnaert*[13]. The Rayleigh vertical radiance transmittance is based upon the spectral total volume scattering coefficients from Eq. 14 of Penndorf[14] using the refractive modulus from the dispersion formula of Edlen[15] and the sea level scale height for the U. S. Standard Atmosphere 1976[16]. The mean ozone optical thickness values are based on the spectral values per cm of Vigroux[17] which are in good agreement with the Inn and Tanaka[18] values. The mean value of ozone in cm is for the Visibility Laboratory site as taken from Wilcox, et al[19]. These computations are described in more detail in Gordon[9].

4. DATA

4.1 Description of Data Sets

Details of site location and experiment dates for the three data sets are summarized in Table 2. The data reported herein include partially cloudy as well as cloudless day data. In all cases the sun was unobscured as was the portion of the sky used for the orbital vertical path radiance prediction. In addition to optical

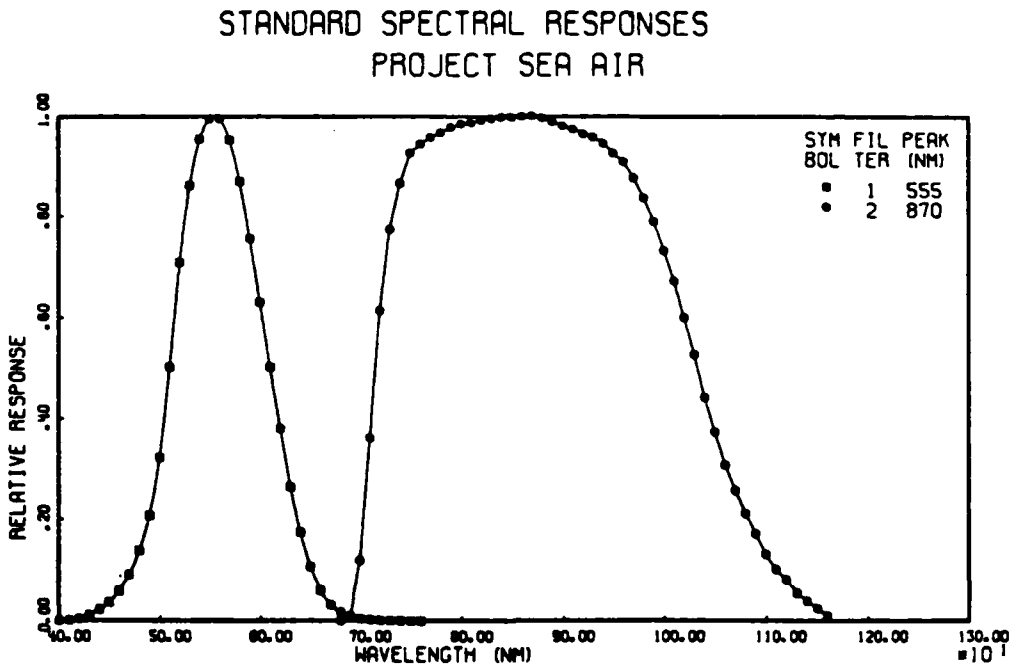

Fig. 10. Relative spectral response of the two passbands for the Sea Air data set. The passband for filter 1 is photopic.

Appendix E

Table 1 Spectral characteristics summary for passbands used for Rooftop, Portable and Sea Air data sets.

	Spectral Characteristics			Solar		Rayleigh	Mean
Filter Designation	Peak Wavelength (nm)	Mean Wavelength (nm)	Effective Passband (nm)	Irradiance Out-of-Atmosphere ($W/m^2\mu m$)	Center Sun Radiance ($W/\Omega m^2\mu m$)	Vertical Radiance Transmittance	Ozone Optical Thickness
Photopic							
*	555	560	106.8	1890	3.45×10^7	0.907	0.0258
Non-Photopic							
Rooftop							
1	450	459	58.1	2080	4.00×10^7	0.812	0.0031
2	500	505	151.9	1950	3.66×10^7	0.852	0.0134
4	630	661	61.8	1590	2.79×10^7	0.952	0.0185
Sea Air							
2	870	882	313.6	967	1.42×10^7	0.982	0.0001

* The photopic passband filter designations are Rooftop 3, Portable 3 and Sea Air 1. The value for the photopic passband is expressed in radiometric terms. The irradiance may be converted to illuminance or radiance to luminance by multiplying by 72.62 luμm/W.

TABLE 2. Site locations and dates of measurement for the three data sets.

Experiment Title	Location	Latitutude (Degrees)	Longitude (Degrees)	Dates Begin	End
Rooftop Data Set					
Rooftop	San Diego, CA	32.70 N	117.24 W	23Jan64	4Sep64
Portable Data Set					
NOTS	China Lake, CA	35.75 N	117.75 W	16Jul62	9Aug62
Pahrump	Nevada	36.66 N	115.50 W	7Oct63	19May64
Laredo 1	Texas	27.50 N	99.50 W	21Dec64	25Jan65
Laredo 2	Texas	27.50 N	99.50 W	26Jan65	14Feb65
Australia	Carnarvon,Aust	26.19 S	114.70 E	15Aug65	27Aug65
Laredo-Gem	Texas	28.20 N	99.80 W	22Aug65	6Dec65
Crater Lake	Oregon	42.88 N	122.01 W	2Aug66	4Aug66
Colo Springs	Colorado	39.00 N	105.00 W	8Sep66	13Sep66
Ramey AFB	Puerto Rico	18.25 N	67.00 W	19Sep66	19Sep66
Montgom Fld	San Diego,CA	32.81 N	117.01 W	17Feb67	6Apr67
CRM Rooftop	San Diego,CA	32.70 N	117.24 W	26Apr67	2Jun67
Sea Air Data Set					
Vis Lab	San Diego,CA	32.70 N	117.24 W	30Sep69	29Jun70
San Clemente	California	32.94 N	118.53 W	18Nov69	1Apr70
Whites Point	Los Angeles,CA	33.74 N	118.32 W	27Jul71	30Jul71
Santa Catalina	California	33.44 N	118.50 W	4Aug71	5Aug71

measurements, historical weather records in the form of local surface observations, radiosonde data, and surface and 500 mb charts were obtained.

Rooftop

Ground-based automatic instrumentation was developed and experimental data taken in 1964 for a project concerning ocean surveillance from satellites by the Visibility Laboratory at the University of California, San Diego. A large body of data (937 observations) was measured over a relatively long period of time (23 January to 4 September), covering the diurnal daytime solar cycle. This data set contains measurements of vertical radiance transmittance, sky radiance and downwelling irradiance. Measurement of downwelling irradiance began in April. The downwelling irradiances for January through March were computed from the scanner radiances and the total radiance transmittance.

The weather records, from nearby Lindbergh field, were supplemented by all-sky pictures. About 100 data packages for each of the four passbands were measured on cloudless days. An analysis of the relationship between the meteorological and atmospheric optical properties has been reported for the photopic cloud-free data by Edgerton[20]. Also an analysis of the data for optically stable days has been reported by Gordon (Ref. 9).

Portable

During the period 1962 to 1967, portable instrumentation was used at a number of ground stations to obtain measurements for determining total transmittance, downwelling irradiance and earth-to-space path reflectance. No sky radiances were measured therefore no path reflectances are available for the NOTS field experiment. About half the Portable data were for the photopic passband (353 observations of transmittance and irradiance, 236 observations of path reflectance).

Some of the early data (Pahrump) were used for the verification of the path reflectance method, Ref. 1. Some of the data (Laredo 1, Laredo 2, Australia, Laredo Gem) were measured in conjunction with the Gemini project reported in Ref. 4. This data set contains all the photopic earth-to-space transmittance measurements made with portable

Appendix E

instruments between 1962 and 1967. Except for NOTS and Pahrump, the measurements were made with a CRM.

Sea Air

This data set was obtained with a CRM, between 30 September 1969 and 5 August 1971, for a NASA project concerning the remote sensing of sea surface roughness. The data for the near infrared passband were reported by Duntley, et al.[21] The bulk of the measurements (1062 data packages) were made at the Visibility Laboratory. Two other locations were channel islands off the coast of California [San Clemente (70 observations) and Santa Catalina (26 observations)] and the remaining location (Whites Point, 70 observations) was on the mainland near the Los Angeles sewer outfall west of the harbor at San Pedro.

Appendix E

4.2 Photopic Measurements

Each of these three data sets contain photopic measurements, comprising the largest readily available data based for any one passband. The photopic passband data describe the atmospheric limitations on the capabilities of astronauts to see objects on the surface of the earth.

Transmittance

The photopic earth-to-space radiance transmittance values as a function of solar zenith angle are summarized in Fig. 11. The horizontal line is the Rayleigh transmittance. The right hand scale on each graph indicates the optical thickness.

The symbols in the Rooftop graph indicate the month of the measurement. The clustering of the data at even 10° increments of zenith angle clearly indicate the measurement procedure (data taken every 10° in solar zenith angle). Values were also measured at solar noon, therefore the values at the smaller solar zenith angles show less clustering. It is appropriate that the measured photopic transmittances are always less than the Rayleigh, since the upper limit is actually 0.884 [the Rayleigh (0.907) times the mean ozone absorption transmittance (0.974)].

In the graphs for the Portable and Sea Air data, the symbols indicate the geographical location of each measurement. The Portable

Appendix E

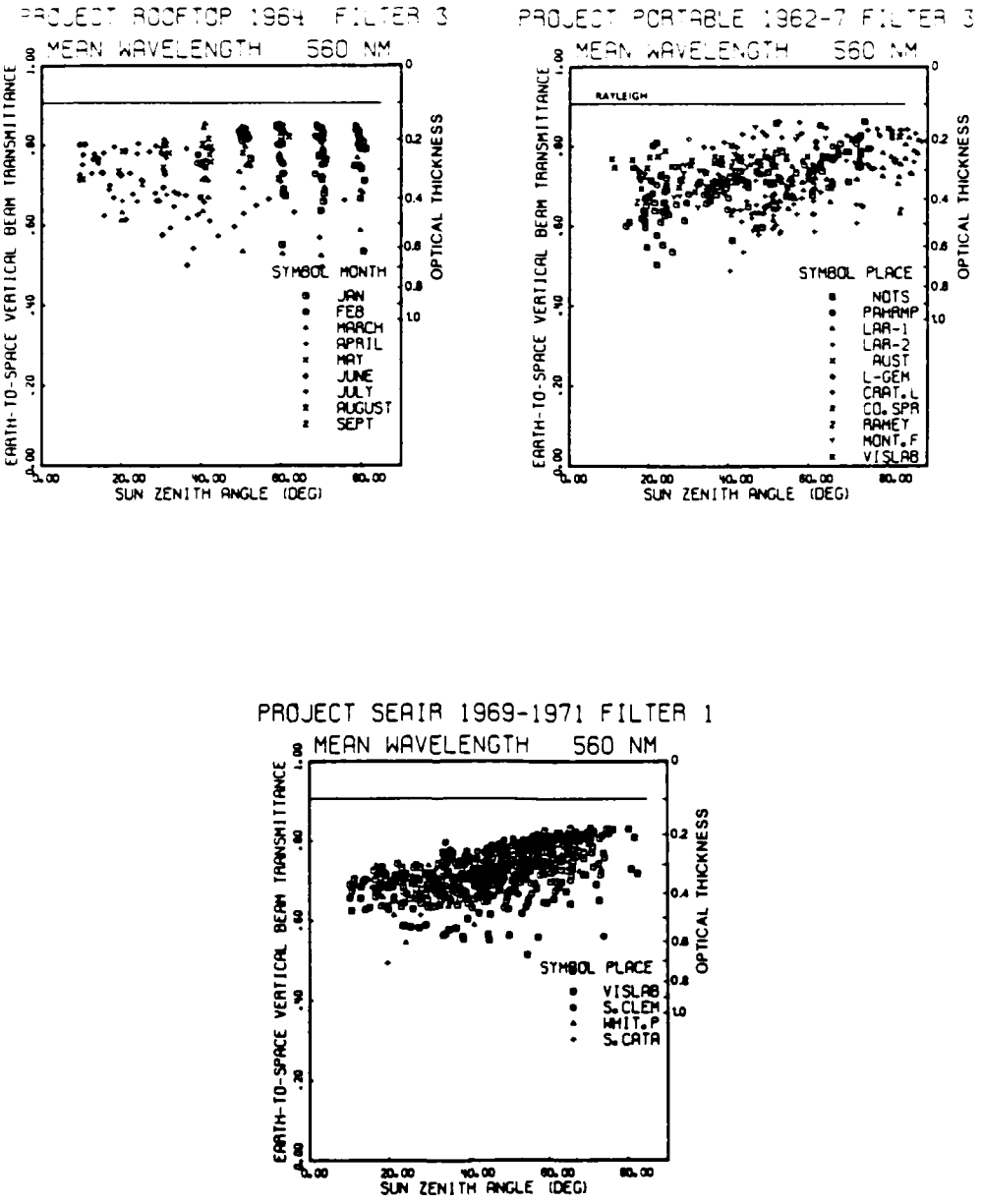

Fig. 11. Photopic earth-to-space vertical radiance transmittance.

and Sea Air transmittances indicate an apparent decrease of transmittance with decrease of solar zenith angle. This is expected for pyroheliometer data on days when the monochromatic transmittance is constant as a function of solar zenith angle (the day is optically stable), because transmittance is a function of wavelength[22]. This effect is small, however, for the photopic filter (less than 3% for a transmittance of 0.7 and less than 1% for a Rayleigh transmittance). Examination of the Portable data indicates that most of it is morning data, indicating that for these cases the transmittance decreased from morning to noon. The Sea Air data were taken both morning and afternoon.

A vertical transmittance of 0.7 (0.36 optical thickness) is commonly used as the average clear-day photopic transmittance. The average transmittance for the Rooftop was 0.75 and the average for the Portable data was 0.72.

Irradiance

The photopic total downwelling irradiance values are graphed in Fig. 12 for the three data sets. These graphs are coded in terms of transmittance. The lower curve is for the Brown[23] average photopic irradiances based on over 12,000 measurements made between 1943 and 1947 all over the world. The Brown average values are generally used as an irradiance standard for a clear day. The upper curve on each graph is for the Rayleigh atmosphere, with an albedo of 1.0 in an attempt to provide an upper limit. The photopic Rayleigh irradiances were computed using the equilibrium radiance model atmosphere equations[24,7]. Most of the measured downwelling irradiances lie between these two curves for the Rooftop data set and cluster about the Brown curve for the Portable and Sea Air data sets.

Path Reflectance

The photopic path reflectance for the earth-to-space vertical path is graphed as a function of solar zenith angle in Fig. 13. These values are also coded in terms of transmittance. The solid curve is for the photopic Rayleigh atmosphere with an albedo equal to zero assuming a scattering angle of 90°. Again, this was computed using

Appendix E

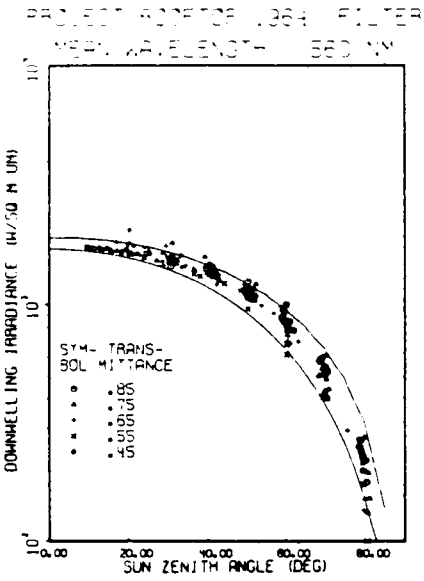

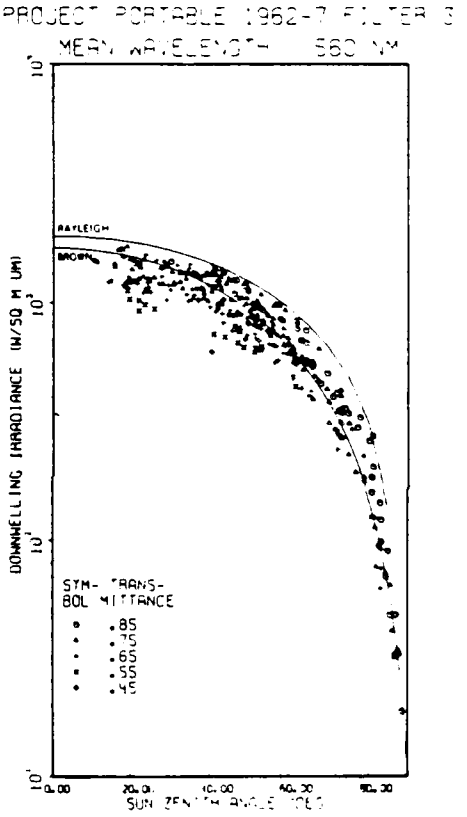

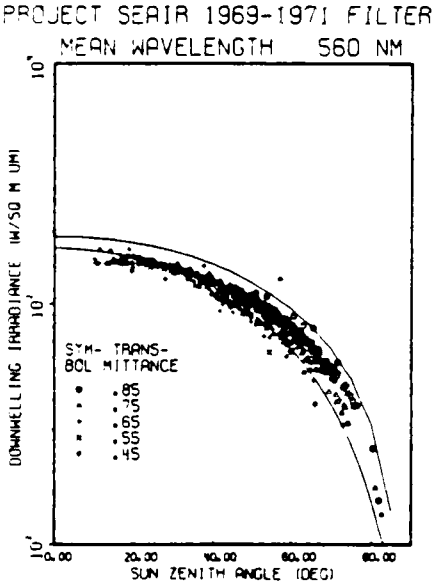

Fig. 12. Photopic downwelling irradiance.

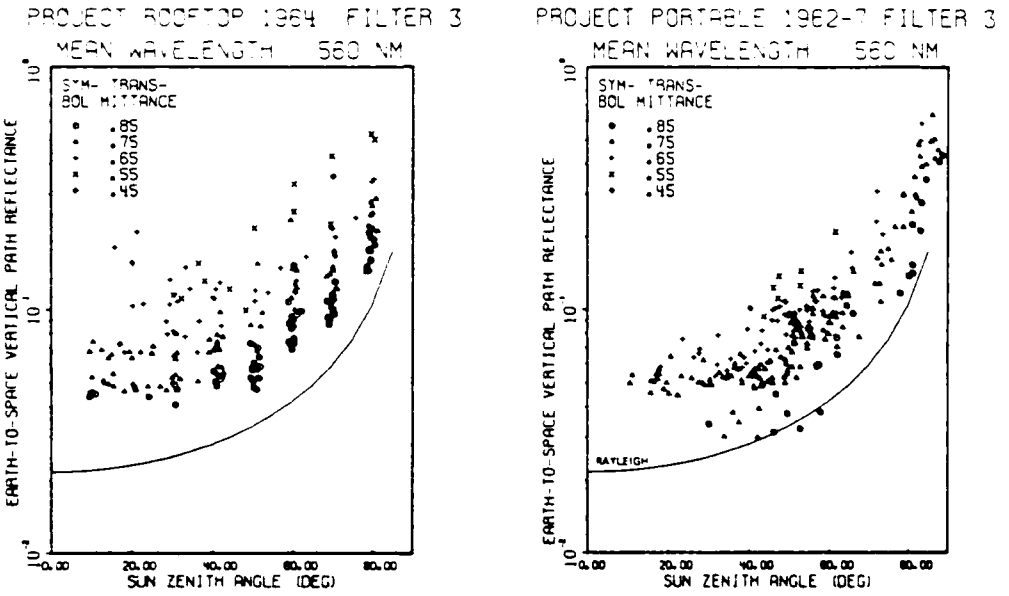

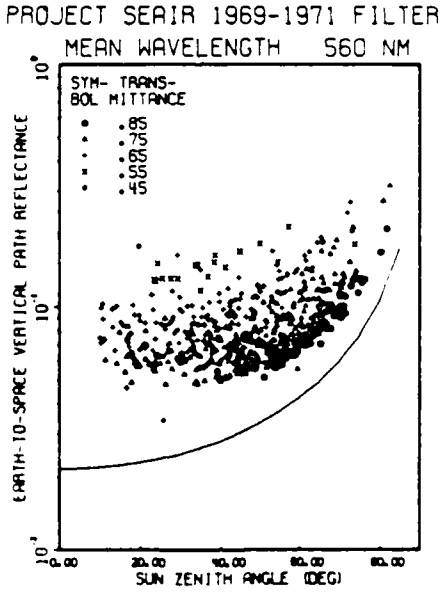

Fig. 13. Photopic earth-to-space vertical path reflectance.

the equilibrium radiance model equations. Most of the data clearly lie above the Rayleigh values. The path reflectance is strongly a function of solar zenith angle and transmittance.

It is useful at this point to compare these values to the average vertical earth-to-space reflectance for $\beta=90°$ computed using the equilibrium radiance model atmosphere equations (Refs. 24 and 7) with a scalar albedo 0.10. A scalar albedo of 0.1 can be considered an average terrain albedo for fields. The proportional volume scattering functions used are from Barteneva[25]. The Barteneva function classes for each transmittance are summarized in Table 3. The ratio of maximum to minimum values for any given transmittance and solar zenith angle was small (1.08 to 1.37) therefore only the averages are graphed in Fig. 14.

Appendix E

Note that the Barteneva scattering function values for transmittance 0.9 are less than the Rayleigh values (which are also for albedo 0.1) but not by much. This is due to scattering function shape differences. The model values clearly indicate the dependence of path reflectance upon both sun zenith angle and transmittance.

4.3 *Non-photopic* Measurements

The sample non-photopic measurements are taken from the Rooftop data set filters 1, 2 and 4 and Sea Air data set filter 2. The mean wavelengths are 459, 505, 661 and 882 nm with effective passbands of 58, 152, 62 and 314 nm respectively. Thus both of the filter 2 passbands (mean wavelenghts 505 and 882 nm) are even broader band than the photopic passband.

Transmittance

The earth-to-space radiance transmittance values as a function of solar zenith angle for the non-photopic passbands are summarized in Fig. 15. As before the Rooftop data are coded in terms of month of measurement but the Sea Air data are coded in terms of location of measurement.

Since the passbands with mean wavelengths of 505 and 882 nm are broader in passband than the photopic, the transmittance on optically stable days might be expected to decrease with solar zenith angle more than for the photopic. However, the decrease with solar zenith angle is similar to the photopic for each data set and so probably this

Table 3.

Transmittance and Scattering Function Specifications for Evaluation of Model Atmosphere Equations

Earth-to-space vertical transmittance	Barteneva scattering function class number								Total No. of cases
0.9	2	3							2
0.8	2	3	4	5					4
0.7		3	4	5	5'	6			5
0.6		3	4	5	5'	6			5
0.5			4	5	5'	6	6'	7	6
Total no. cases	2	4	4	4	3	3	1	1	22

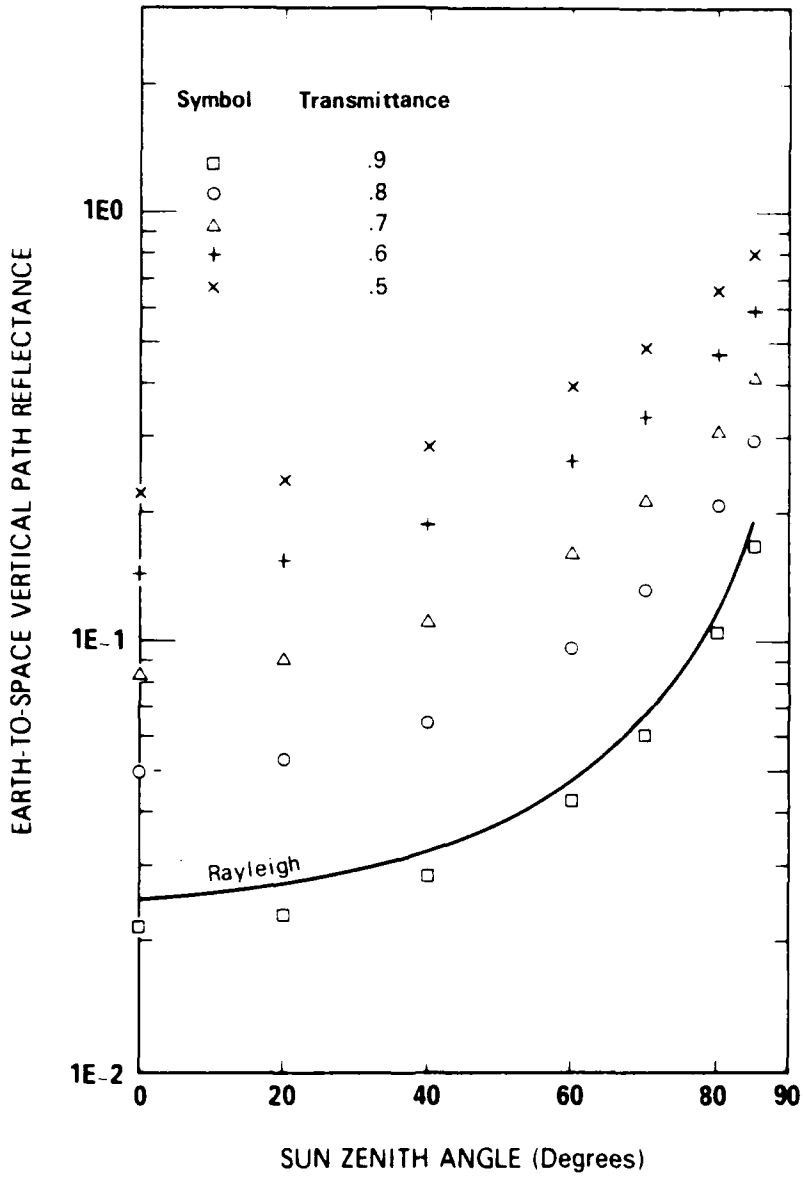

Fig. 14. Average photopic vertical earth-to-space vertical path reflectance for $\beta=90°$ for model calculations assuming scalar albedo 0.1 using the Barteneva scattering functions and the Rayleigh scattering function (transmittance 0.907).

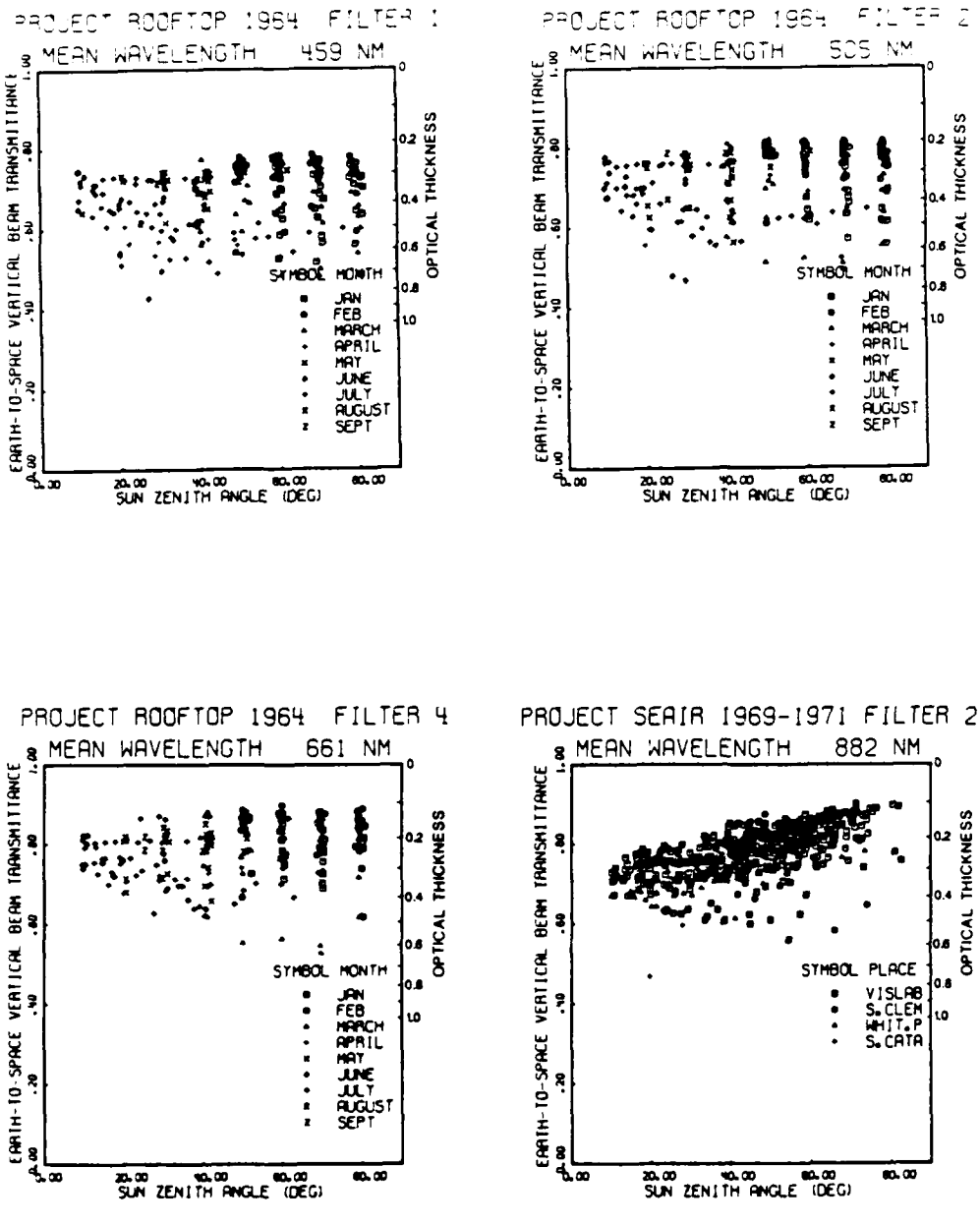

Fig. 15. Non-photopic earth-to-space vertical radiance transmittance.

effect is small at best.

The Rayleigh times mean ozone transmittance values are 0.809, 0.841, 0.935 and 0.982 respectively and all transmittances are less than these values. However, the two passbands with mean wavelengths of 661 and 882 nm can be expected to be affected by O_2 and H_2O gas phase absorption bands as well as the ozone continuum. A useful graph to evaluate the potential absorption from gas phase sources (atomic and molecular absorption) in the visible spectrum is given in Fig. 16 from King, et al[26]. The passband with mean wavelength 661 nm contains two oxygen absorption bands as well as a small water vapor absorption band. The passband with mean wavelength 882 nm contains one strong oxygen absorption band and two strong water vapor absorption bands. All the measured transmittances for these two passbands are sufficiently below the Rayleigh times ozone transmittance values to allow for the additional absorption.

Appendix E

Irradiance

The total downwelling irradiance values for the non-photopic passbands are graphed in Fig. 17. These graphs are coded in terms of transmittance. The values for the passbands with mean wavelengths 459 and 505 are very similar to the photopic values. If the graphs are superimposed, the values lie between the two curves on the photopic graph at the smaller solar zenith angles.

The values for the passbands with mean wavelength 661 and 882 nm are clearly less than the photopic values. The decrease with mean wavelength is similar to the decrease in sun irradiance out of the atmosphere with mean wavelength. The values for passband meanwavelength 661 nm lie below the Brown values at the smaller zenith angles but are still above 10^3 W/m$^2\mu$m. However, the 882 nm passband values are all less than 10^3 W/m$^2\mu$m.

The irradiance values for all four non-photopic passbands vary strongly as a function of sun zenith angle in a manner similar to the photopic Brown curve.

Path Reflectance

The path reflectance for the earth-to-space vertical path is graphed as a function of solar zenith angle for the non-photopic

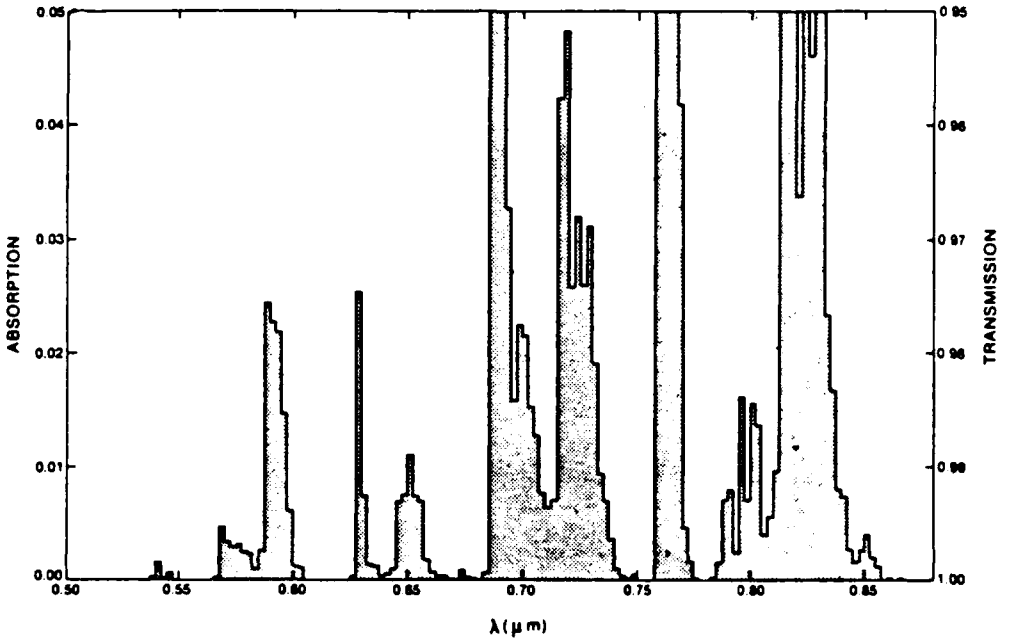

Fig. 16. (Fig. 1 from Ref. 26) Slant path absorption and transmission through the atmosphere (at a resolution of 2.5 nm) as obtained from high resolution spectra in the Utrecht Photometric Atlas (after Moore, et al., Ref. 27). Bands at 0.63, 0.69 and 0.76 μm are due to oxygen absorption while all remaining bands are due to water vapor absorption. The air mass varies with wavelength λ but is everywhere less than 2.22.

Appendix E

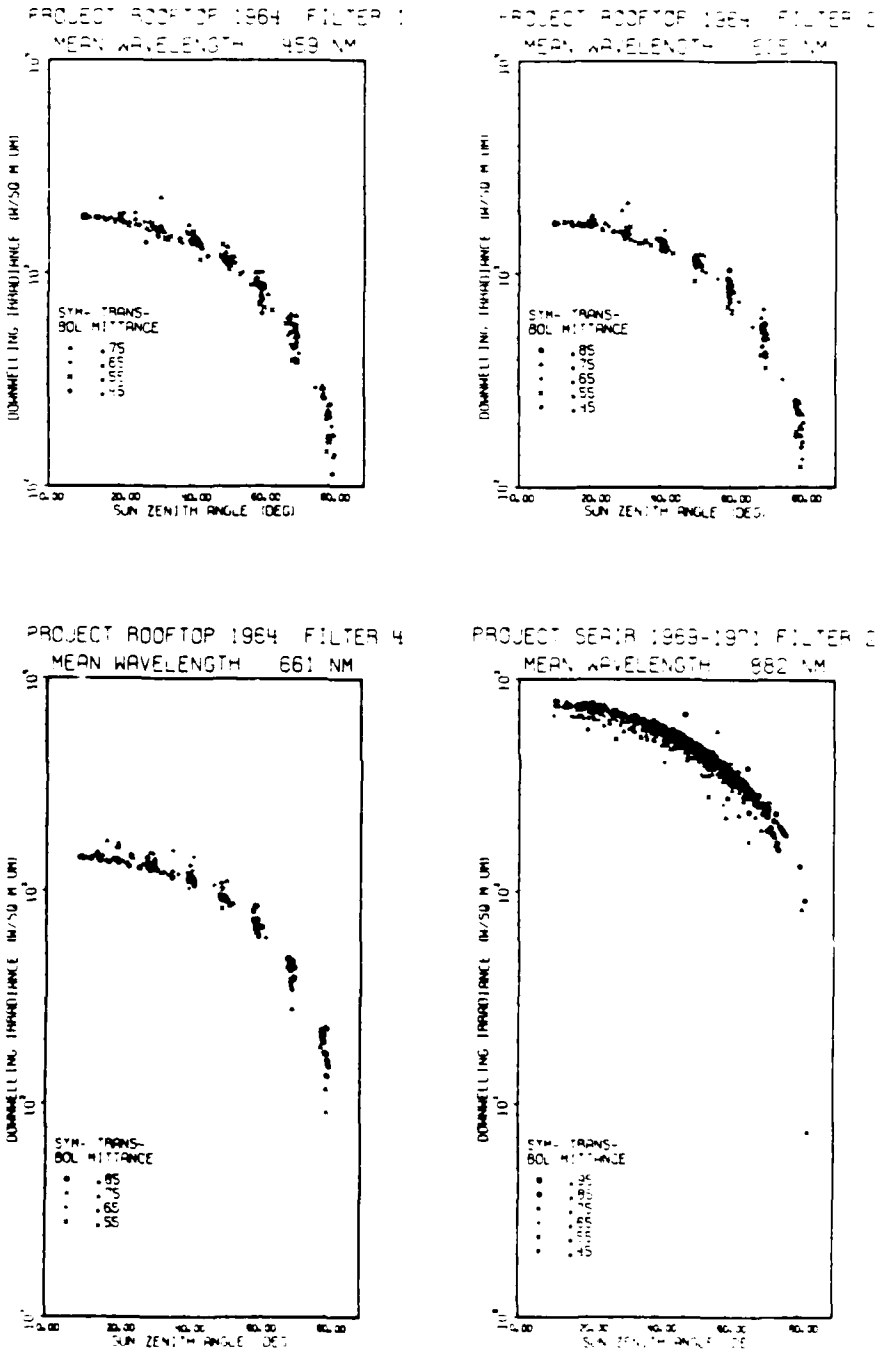

Fig. 17. Non-photopic downwelling irradiance.

passbands in Fig. 18. These are again coded in terms of transmittance. The decrease of path reflectance with mean wavelength of filter is pronounced, being roughly a factor of 4 to 1 from mean wavelength 459 to mean wavelength 661. The non-photopic path reflectances clearly indicate the dependence upon both sun zenith angle and transmittance as did the photopic.

5. APPLICATIONS

Although these data were primarily measured to provide ground truth for specific remote sensing projects, they provide a sufficiently large data base with which to evaluate the expected range of variables as a function of solar zenith angle, wavelength, and over a number of seasons.

By combining Eq. 10 with Eq. 9 we get an equation which relates the path reflectance to the masking effect of the veiling light scattered into the path of sight

$$R_\infty(\infty,\theta,\emptyset)=[R_0(0,\theta,\emptyset)+R^*_\infty(\infty,\theta,\emptyset)]T_\infty(\infty,\theta). \quad (15)$$

This equation separates the signal received at orbital altitude into the proportion which is image forming light and the proportion due to the veiling effect of the atmosphere. Thus if the path reflectance is equal to or greater than the inherent reflectance of the object, the resultant signal will be half or more than half scattered light.

We have presented values for vertical path reflectance. They can be made applicable to other downward paths of sight with scattering angles $\geq 90°$ by multiplying by the ratio $[T_\infty(\infty,\theta)^{-1}-1]/[T_\infty(\infty,180)^{-1}-1]$

$$R^*_\infty(\infty,\theta,\emptyset)=R^*_\infty(\infty,180°)[T_\infty(\infty,\theta)^{-1}-1]/[T^*_\infty(\infty,180°)^{-1}-1]. \quad (16)$$

This ratio has been evaluated neglecting earth curvature and refraction effects for vertical transmittances 0.95 through 0.5 and paths of sight 150° through 115° and is presented in Fig. 19. The factor is less than 2 for paths of sight 150° and 135° but is greater than 2 for 120° and 115°. Earth curvature and refraction effects would be negligible for orbital altitudes up to 200 km for zenith angles 150° and 135°.

Appendix E

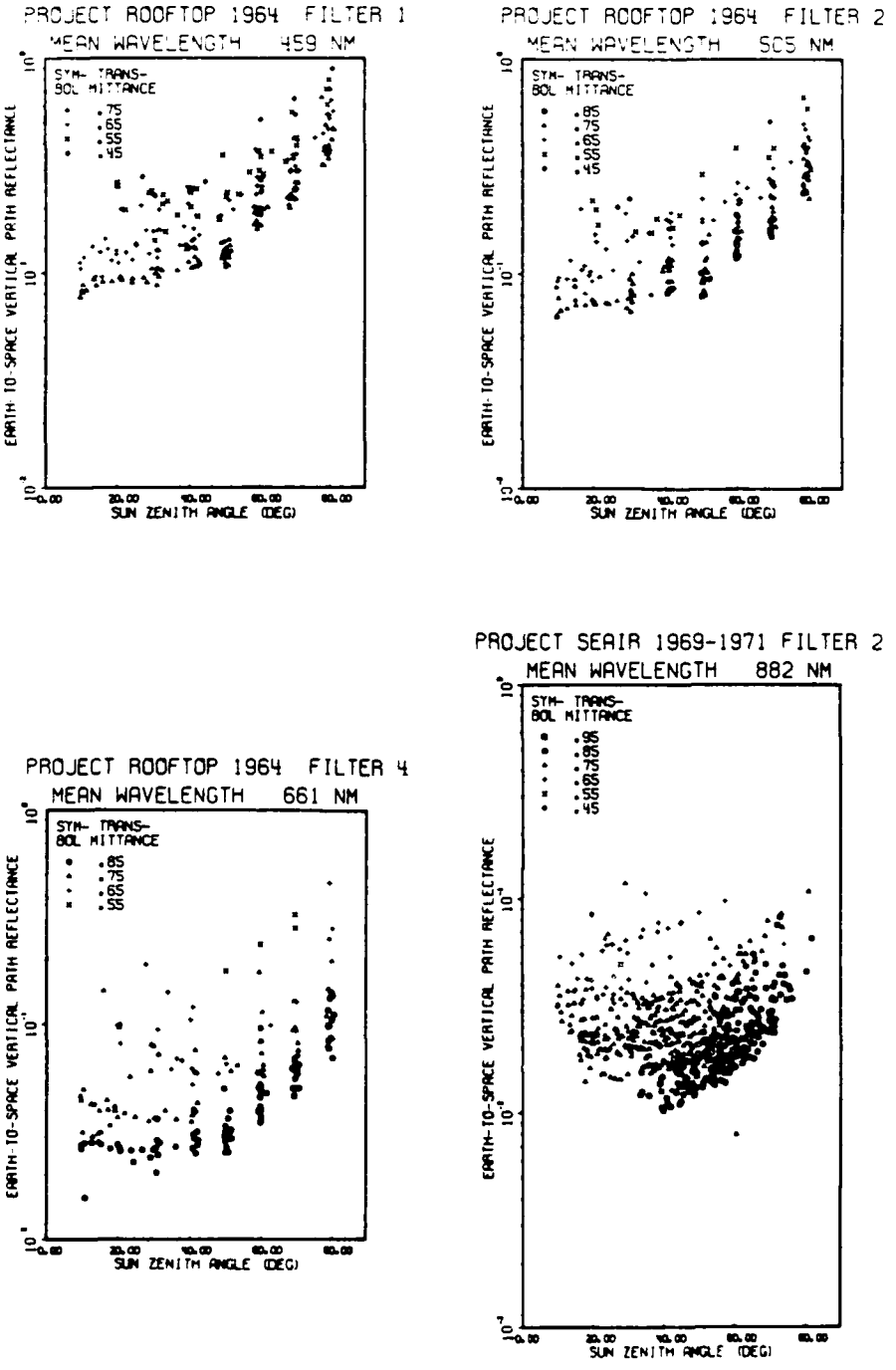

Fig. 18. Non-photopic earth-to-space vertical path reflectance.

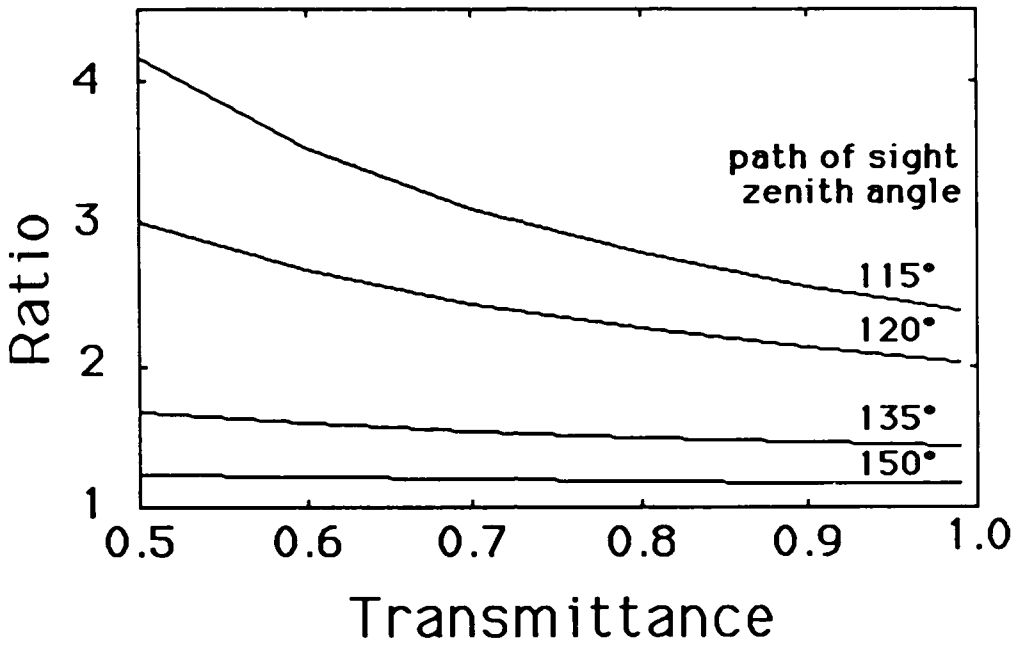

Fig. 19. Ratio to apply to vertical path reflectance in order for it to become applicable to slant paths of sight. Ratio presented as a function of vertical radiance transmittance and slant path angle for various earth-to-space downward paths of sight.

Appendix E

J. I. GORDON AND R. W. JOHNSON

6. SUMMARY

Path radiance is the radiance scattered into the path of sight from all 4π directions. This radiance is not generally the same in both directions along the same path, however, a method[1] is available whereby the path radiance from earth to space can be predicted from ground-based measurements. Path reflectance combines the effects of path radiance, downwelling irradiance and radiance transmittance. An equation to determine apparent object reflectance was derived which relates the path reflectance to the masking effect of the veiling light scattered into the path of sight for any inherent object reflectance.

An instrument, developed specifically for obtaining the path radiance and reflectance for the vertically downward path of sight, has been in use for some 20 years. The contrast reduction meter or CRM was designed for gathering ground-truth information for satellite problems and has been the principal instrument used by the Visibility Laboratory for this purpose.

Three data sets were presented. They ranged from data taken during the early development of the earth-to-space method to data taken to provide ground truth for remotely sensed measurements. Values were presented for vertical downward path reflectance, but they can be made applicable to downward slant paths of sight by means of a correction factor (a function of the radiance transmittance and slant path angle).

Although these data were primarily measured to provide ground truth for specific remote sensing projects, they provide a sufficiently large data base with which to evaluate the expected range of variables as a function of solar zenith angle, wavelength, and over a number of seasons.

Path reflectance takes into consideration two concerns of atmospheric transparency determination: the loss of image forming light, and the veiling effect of scattered light. It is a convenient and powerful way of expressing both the loss and gain for the image forming signal.

ACKNOWLEDGMENTS

The writing of this article was done at Viz. Ability, Inc. under U. S. Army Research Office contract no. DAAG29-84-C-0014. We wish to thank Judith Olson for editing assistance.

The data for the three data sets were collected, assembled and evaluated by the Visibility Laboratory under various contracts for the U. S. Navy, NASA, and the U. S. Air Force Geophysics Laboratory. The experiments were conducted under the technical supervision of R. W. Austin, A. R. Boileau, S. Q. Duntley, C. F. Edgerton, J. I. Gordon, J. L. Harris, R. W. Johnson, and T. J. Petzold.

Appendix E

REFERENCES AND FOOTNOTES

1. J. I. Gordon, J. L. Harris, Sr. and S. Q. Duntley, "Measuring earth-to-space contrast transmittance from ground stations," Appl. Opt. 12, 1317-1324 (1973).
2. S. Q. Duntley, A. R. Boileau, and R. W. Preisendorfer, "Image Transmission by the Troposphere I," J. Opt. Soc. Am. 47, 499-506 (1957).
3. W. G. Driscoll and W. Vaughan, Eds., Handbook of Optics (McGraw-Hill, New York, 1978).
4. S. Q. Duntley, R. W. Austin, J. L. Harris, and J. H. Taylor, "Experiments on visual acuity and the visibility of markings on the ground in long duration earth-orbital space flight," University of California at San Diego, Scripps Institution of Oceanography, Visibility Laboratory, SIO Ref. 68-6 (1968); also published as NASA, Washington, D. C., NASA CR-1134 (1968).
5. S. Q. Duntley, "Directional reflectance of atmospheric path of sight," Duntley Report No. 69-1, (1969) also Appendix D in University of California at San Diego, Scripps Institution of Oceanography, Visibility Laboratory, SIO Ref. 70-7, AFCRL-70-0137 (1970).
6. J. I. Gordon and R. W. Johnson, "Equilibrium-reflectance model for clear or cloudy atmosphere," J. Opt. Soc. Am. A 1, 860-868 (1984).

7. Because Eqs. 4 and 5 do not include absorption, they are the basis for the sky ratio method of measuring the total scattering optical thickness as described in J. I. Gordon and R. W. Johnson, "Equilibrium radiance model applications and comparisons to atmospheric measurements and Rayleigh models," Appl. Opt. 23, 3363-3372 (1984) and in Refs. 8 and 9.

8. J. I. Gordon and R. W. Johnson, "Integrating nephelometer: theory and implications," Appl. Opt. 24, 2721-2730 (1985).

9. J. I. Gordon, "Aerosol scattering optical thickness from ground-based measurements," submitted to Applied Optics August 7, 1986.

10. F. Kasten, "A New Table and Approximation Formula for the Relative Optical Air Mass", Arch., Met. Geophys. Bioklim. B14, 206-233 (1965).

11. S. Q. Duntley, R. W. Johnson. and J. I. Gordon, "Airborne and ground-based measurements of optical atmospheric properties in centeral New Mexico," University of California at San Diego, Scripps Institution of Oceanography, Visibility Laboratory, SIO Ref. 72-71, AFCRL-72-0461 (1972).

12. F. R. Johnson, "The Solar Constant," J. Meteorol. 11, 431-439 (1954).

13. M. Minnaert, "The Photosphere," Chapter 3 in The Sun, G. P. Kuiper, Ed., (University of Chicago Press, 1953).

14. R. Penndorf, "Tables of the Refractive Index for Standard Air and the Rayleigh Scattering Coefficient for the Spectral Region Between 0.2 and 10.0 μm and Their Application to Atmospheric Optics," J. Opt. Soc. Am. 47, 176-182 (1957).

15. B. Edlen, "Dispersion of Standard Air," J. Opt. Soc. Am. 43, 339 (1953).

16. U. S. Standard Atmosphere, 1976 (Superintendent of Documents, U.S. GPO, Washington, D.C. 20402, 1976).

17. E. Vigroux, "Etude experimentale de l'absorption de l'ozone," Ann. Phys. (Paris) 8, 742-743, 747 (1953).

18. E. C. Y. Inn and Y. Tanaka, "Ozone Absorption," J. Opt. Soc. Am. 43, 872 (1953).

Appendix E

19. R. W. Wilcox, G. D. Nastrom and A. D. Belmont, "Periodic Variations of Total Ozone and of Its Vertical Distribution," J. Appl. Meteorol. 16, 290-298 (1977).

20. C. F. Edgerton, "Relationship between Meterorological Conditions and Optical Properties of the Atmosphere," Scripps Institution of Oceanography, Visibility Laboratory, SIO Ref. 67-27 (1967).

21. S. Q. Duntley, C. F. Edgerton, and T. J. Petzold, "Atmospheric limitations on remote sensing of sea surface roughness by means of reflected daylight," University of California at San Diego, Scripps Institution of Oceanography, Visibility Laboratory, SIO Ref. 70-27 (1970).

22. N. Robinson, Solar Radiation (Elsevier Pub. Co.,Amsterdam/London/New York, 1966), p. 95-96.

23. D. R. E. Brown, Natural Illumination Charts (Department of the Navy, Bureau of Ships, Washington, D. C. 1952), Report 374-1, Project Ns-714-10.

24. J. I. Gordon, "Model for a clear atmosphere," J. Opt. Soc. Am. 59,14 (1969).

25. O. D. Barteneva, "Scattering functions of light in the atmospheric boundary layer," Bull. Acad. Sci. USSR Geophys. Ser. 1237 (1960).

26. M. D. King, D. M. Byrne, J. A. Reagan, and B. M. Herman, "Spectral Variation of Optical Depth at Tucson, Arizona between August 1975 and December 1977," J. Appl. Meteorol. 19, [illegible] (1980).

27. C. E.Moore, M. G. J. Minnaert and J. Houtgast, The 2935Å to 8770 Å; Second Revision of Rowland's Preliminary Table of Solar Spectrum Wavelengths. Nat. Bur. Standards No. 61 (U. S. GPO, Washington, DC, 1966), 34 p.

AD-A178 590 NEW METHODS FOR OBTAINING SCATTERING AND ABSORPTION FROM TROPOSPHERIC VIS (U) VIZ ABILITY CORVALLIS OR J I GORDON 28 FEB 87 VA187-1 ARO-21655 8-GS-S 2/2

UNCLASSIFIED DAAG29-84-C-0014 F/G 20/6 NL

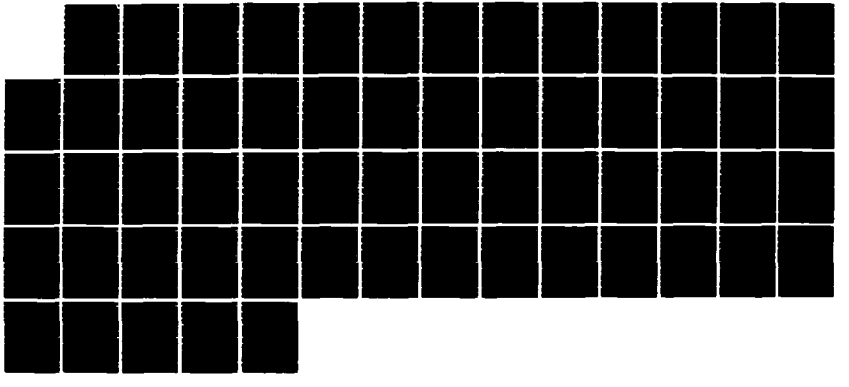

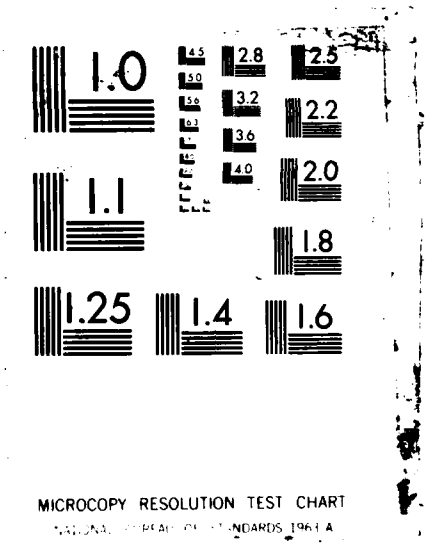
1.0
1.1
1.25
1.4
1.6
1.8
2.0
2.2
2.5
2.8
3.2
3.6
4.0
4.5
5.0
5.6
6.3
MICROCOPY RESOLUTION TEST CHART
NATIONAL BUREAU OF STANDARDS 1963 A

Aerosol scattering and absorption optical thickness I.

From ground-based measurements during optically stable clear days.

By

Jacqueline I. Gordon

Viz. Ability, Inc., 2941 NW Ashwood Drive, Corvallis, Oregon 97330-1255

Appendix F

ABSTRACT

This is the first paper of a two part series. The combined measurements from a solar transmissometer and sky scanner allow the isolation of aerosol scattering and absorption optical thickness in the visible portion of the spectrum. With this combination one can obtain values for broad or narrow passbands, within or not within absorption windows. With an accurate value for aerosol scattering optical thickness available, the optical scattering mixing ratio, modified Angstrom equation, and total and aerosol single scattering albedo help detail the state of the atmosphere. We found that aerosol absorption can be significant even on days of greater transparency than the average clear day.

1. INTRODUCTION

This is the first paper of a two part series investigating aerosol scattering and absorption in the visible. A method for obtaining aerosol scattering optical thickness for the total atmosphere was described earlier by the author[1], a simplification of the work of Livshits and Pavlov[2]. This method uses a combination of the sky scanner and solar transmissometer to obtain values of aerosol scattering optical thickness for broad or narrow passbands, within or not within absorption windows.

The data set used, though old, is sufficiently complete that new methods of data retrieval could be applied to obtain values of total optical thickness, aerosol scattering optical thickness, and aerosol absorption

optical thickness. Prior investigations using the data ignored the separate roles of aerosol scattering and absorption.

Our study will show that there can be measureable absorption in portions of the visible spectrum generally thought to be windows. The notation used is that adopted by the Visibility Laboratory[3] and modified to correspond to Optical Society of America recommendations in Sec. 1 of Driscoll and Vaughan[4].

Appendix F

Data Set Description

Automatic equipment was developed and the experimental data were taken apropos ocean surveillance from satellites by the Visibility Laboratory at University of California, San Diego in 1964. Ground-based observations were made between 23 January and 4 September (covering the diurnal daytime solar cycle). Only the data from optically stable days will be used and discussed in this article. There are 9 optically stable days, comprised of 228 measurement packages.

In addition to historical weather records from the nearest weather station, optical measurements were supplemented by all sky pictures. An analysis of the relationship between the meteorological and the atmospheric optical properties has been reported for the photopic cloud-free data by Edgerton[5].

2. INSTRUMENTATION

Since there is no report describing the instruments, a brief description will be given here. A sky scanner, solar transmissometer, sun azimuth computer, and all-sky camera were placed on the rooftop of a building at the Visibility Laboratory (124 m above sea level) on Point Loma, a penninsular area in San Diego, California.

2.1 Radiometric Systems

Each radiometric instrument had a photoelectric system consisting of a optically filtered multiplier phototube and a pseudo-logarithmic Sweet type photometer circuit.

Solar Transmissometer

The telephotometer measured the apparent radiance of the center of the sun. The instrument was designed so that diffraction effects were small. Two small holes separated by 50 inches formed a Gershun tube with a small field of view (approximately 4 minutes of arc). The transmissometer was aligned by a clock drive and the alignment checked by an attendant immediately prior to the collection of each data package.

Sky Scanner

A sky scanning telephotometer was used to measure the sky radiance distribution. This unit was basically a small telescope with a sunshade and baffles to reduce stray light. The unit had a 5° field of view.

Two movable prisms driven by stepping motors scanned optically. At the beginning of the scan pattern the telephotometer was pointed toward the azimuth of the sun. When one revolution (64 steps in azimuth) was complete, the zenith angle unit took a 1/64 of a revolution step. A complete hemisphere scan took 1.71 minutes and consisted of 1024 discrete positions. Data from 340 overlapping fields of view were suppressed.

2.2 Subsidiary Instruments

The scanner "home" position was slaved via a follow-up servo to information provided by the sun azimuth computer. The sun azimuth computer was a small analog computer which continually computed the azimuth and zenith angles of the sun and started an automatic data logger at each 10° interval of solar zenith angle and at solar noon.

Appendix F

The automatic data logger took data in the following spectral order: filter 2, 4, 3 then 1; mean wavelengths 505, 661, 560, and 459 nm respectively. The entire process for the four spectral regions took 6 minutes and 57.2 seconds. Once during each data period the automatic data logger triggered an all sky camera for a photographic record of the sky condition.

2.3 Spectral Specifications of Radiometric Data

The standard spectral responses $\overline{S}_\lambda \overline{T}_\lambda$ for the radiometric measurements for filters 1, 2, and 4 were based upon the tube sensitivity S_λ and the filter transmittance T_λ for the solar transmissometer. The spectral response for filter 3 is the photopic luminosity function $\overline{y}_\lambda$. The spectral passbands for the two instruments were equivalent.

The effective passband and mean wavelength for each passband are presented in Table 1. The mean wavelength $\overline{\lambda}$ is

$$\overline{\lambda} = \Sigma \lambda \overline{S}_\lambda \overline{T}_\lambda \Delta\lambda / \delta\lambda. \qquad (1)$$

where the cumulative product is between 380 and 1100 nm and $\Delta\lambda$ is 5 nm. Effective passband $\delta\lambda$ is the area under the relative spectral response curve. The relative spectral responses of the four passbands are presented in Fig. 1.

The remaining four columns in Table 1 are solar and atmospheric properties appropriate for these broad passbands. The details of the derivation of the solar and atmospheric properties will be explained later.

2.4 Radiometric Calibrations

The calibration procedure used standard photometric practices, a 3-meter optical bench, and incandescent standards of luminous intensity traceable to the National Bureau of Standards. Each instrument was calibrated five times during the experiment period. The linearity calibrations extended over a radiance span of 5 log cycles. At the center of the span, the precision was

estimated to be 1%.

An independent measure of the absolute calibration precision and accuracy, and change within a given calibration period can be obtained for the solar transmissometer. Inherent center sun radiance values were obtained from measured apparent center sun radiances using the Langley method on optically stable days. The ratio of these values to the average per calibration period per passband had a standard deviation (STD) of 0.035 (using a total of 32 ratios or n=32). This an indication of the day-to-day variability of the absolute calibration of the phototube.

Appendix F

A theoretical value for the inherent center sun radiance in each passband is given in Table 1. The ratio of the average inherent center sun radiance obtained by the Langley method for each calibration period to the theoretical value was computed. This ratio can be either an indicator of the adequacy of the theoretical value or the accuracy of the absolute calibration. The ratio was clearly a function of the passband. The average ratio per passband was 0.978, 1.073, 1.125 and 1.009, with an STD per passband of 0.014, 0.023, 0.034 and 0.039 for the passbands with mean wavelengths 459, 505, 560 and 661 nm respectively.

3. DATA ANALYSES

The cloud-free data packages were tested to determine the optically stable days. The data from the optically stable days were then used to evaluate various methods for obtaining optical thickness. Because the data were from optically stable days, estimates of precision could be obtained in the form of the STD from the average for each filter for each day as well as for all four filters.

3.1 Optically Stable Days

A day is considered to be optically stable when the atmospheric radiance

transmittance $T_\infty(z,0)$ [or total optical thickness $t_\infty(z)$] does not change with time. The transmittance is related to the optical thickness by

$$t_\infty(z) = -\ln[T_\infty(z,0)] \quad . \tag{2}$$

There were 9 optically stable days in the rooftop data set with measurements over a sufficiently large range of sun zenith angle such that a least squares fit to a Langley (or Bouger) equation (Eq. 19, Ref. 1) could be employed,

$$\ln {}_sL_\infty(z,\theta_s,0) = \ln {}_sL_o(\infty) - m(\theta_s)\, t_\infty(z). \tag{3}$$

The ${}_sL_\infty(z,\theta_s,0)$ is the apparent radiance of the sun as measured by the solar transmissometer at altitude z=0, zenith angle of the sun θ_s, and azimuth from the sun ϕ=0. The ${}_sL_o(\infty)$ is the inherent radiance of the sun, and $m(\theta_s)$ is the relative optical airmass[6]. The average correlation coefficient of the data to the above equation was -0.998. The coefficients for all four filters for all the optically stable days were averaged (a total of 36 coefficients or n=36).

Values of total optical thickness based on the least squares fits to Eq. 3 are given in Table 2 for all four filters on the nine optically stable days. The vertical radiance transmittance in the photopic ranged from 0.777 to 0.854. A vertical transmittance of 0.7 is commonly used as the average clear-day photopic transmittance. Thus all nine days were more transparent than the average clear day.

Solar Almucantar

An almucantar is the portion of the sky at a constant zenith angle. The solar almucantar is the sky at the constant zenith angle of the sun θ_s. When a day is optically stable it is possible to use solar almucantar values to determine the scattering angle from the sun β at which sky radiance measurements contain spurious sun reflections for a photometer (Ref. 1). This also demonstrates optical stability.

Since the sky radiance values were measured at set azimuth and zenith angles rather than at set scattering angles, values of sky radiance at scattering angles 10° through 55°, $\Delta\beta$=5°, were first interpolated for the solar almucantar from azimuths from the sun 0° to 180° and 180° to 360° and then averaged. The three tests illustrated in Figures 2, 3 and 4 for photopic sky radiances on February 21, 1964, were applied to all the interpolated sky radiances for all four spectral passbands.

Appendix F

Test One. A graph of $\mu(z,\beta)$ versus $m(\theta_s)$ should be a horizontal straight line (Eq. 3 and Fig. 5a, Ref. 1). The $\mu(z,\beta)$ is defined as

$$\mu(z,\beta) = L^*_{\infty}(z,\theta_s,\beta)/[_s\varepsilon(z)m(\theta_s). \quad (4)$$

The $_s(z)$ is the sun scalar irradiance. A scalar irradiance is not weighted by the cosine as is the irradiance. Solar scalar irradiance was computed from

$$_s\varepsilon(z) = {}_s\bar{\varepsilon}(\infty)\ \exp[-t_{\infty}(z)m(\theta_s)]\ (\psi/\bar{\psi})^2. \quad (5)$$

The total optical thicknesses are the values from Table 2 based on Eq. 3. The ψ is the solar radius for the date of measurement and $\bar{\psi}$ is the mean solar radius. (This is equivalent to using the ratio of the square of the solar distances.)

The $_s\bar{}(\infty)$ is the solar irradiance out-of-the atmosphere at mean solar distance. Values for each passband are given in Col. 5 of Table 1. The values for each passband were computed from

$$_s\bar{\varepsilon}(\infty) = \Sigma\ {}_s\bar{\varepsilon}_\lambda\bar{S}_\lambda\bar{T}_\lambda\Delta\lambda/\delta\lambda\ , \quad (6)$$

where $_s\bar{\varepsilon}_\lambda$ is the spectral solar irradiance from Johnson[7].

Test Two. This is really only a variant of Test One. A graph of $L^*_{\infty}(z,\theta,\beta)/{}_s\varepsilon(z)$ versus $m(\theta_s)$ should be a straight line with intercept at the origin (Eq. 2.5 and Fig. 5b, Ref. 1).

Test Three. A graph of the solar almucantar sky radiance for a constant angle from sun β versus $\exp[1/m(\theta_s)]$ should maximize at the solar zenith

angle θ_s'. In Eq. 28 and Fig. 6 of Ref. 1,

$$\exp[-1/m(\theta_s')] = T_\infty(0,0). \quad (7)$$

The vertical radiance transmittance $T_\infty(0,0)$ is 0.854 for the data graphed in Fig. 4. Therefore θ_s' should be 81.275° which is slightly larger than the sun zenith angle for any of the photopic measurements on 21 February.

Appendix F

These three tests for all four passbands for all 9 optically stable days consistently indicated that the sky radiances from 15° through 55° scattering angle from the sun are valid but that the 10° β radiances contained spurious sun reflections. A second series of interpolated solar almucantar radiances for 11° through 14°, $\Delta\beta$=1°, indicated that the interpolated values from 11° to 14° were less consistent as to the onset of spurious sun reflections. This inconsistency is probably due to these being interpolated rather than directly measured values. To be consistent, the critical angle for the sky radiance photometer was assumed to be 15° and all sky radiance values measured at closer angles to the sun were assumed to contain a spurious component.

Obtaining optical thickness from solar almucantar radiances could be considered a fourth test for spurious sun reflections.

Total Optical Thickness from Solar Almucantar Radiances

On optically stable days the total optical thickness can also be obtained from the solar almucantar radiance at a set angle from the sun (Eq. 21, Ref. 1)

$$\log[L_\infty^*(z,\theta_s,\beta)/m(\theta_s)] = m(\theta_s)\ \log T_\infty(z,0°) + \log A, \quad (8)$$

where A is a constant. Figure 5 contains a graph of the log of the ratio of the solar almucantar divided by the airmass plotted versus the airmass. The slope of the straight line is a function of the optical thickness [$\log T_\infty(z,0°) = t_\infty(z)/2.303$].

Thus the values interpolated from 15° to 55° every 5° in β could be used to obtain the optical thickness as illustrated in Fig. 5. The average correlation coefficient of the interpolated almucantar values to the above

equation was -0.972 (n=324). The fractional STD of the transmittance for each β from the average per day per filter was 0.8%. The average ratio of the transmittance from the solar almucantar (Eq. 8) to that derived from the solar transmissometer radiances (Eq. 3) was 1.017.

Figure 5 also illustrates what happens when the 10° β data containing spurious sun reflections are in this form. The curve is not a straight line, the correlation coefficient is low, and the slope is not equivalent to the optical thickness obtained from the sun radiance measurements.

3.2 Components of Total Optical Thickness

The total optical thickness has two basic components, the scattering optical thickness ${}_{s}t_{\infty}(z)$ and the absorption optical thickness ${}_{a}t_{\infty}(z)$. In addition, each of these components can be divided into a gas phase component and an aerosol component. The word aerosol is used herein to describe the liquid and/or solid particulates exclusive of the gas phase in which they are embedded. This is consistent with Prospero, et al.[8]

Total Scattering Optical Thickness

The total scattering optical thickness can be obtained from the ratio of sky radiances measured at 55° scattering angle from the sun (Eq. 59, Gordon and Johnson[9])

$$L^{*}_{\infty}(z,\theta,55\beta)/L^{*}_{\infty}(z,\theta',55\beta)=[1-{}_{s}T_{\infty}(z,\theta)]/[1-{}_{s}T_{\infty}(z,\theta')]. \qquad (9)$$

Although this equation cannot be solved directly, it can be solved by iteration. The total scattering optical thickness is then computed from the resultant scattering transmittance using Eq. 2. Since the sky radiances were not measured directly at β equal to 55°, the sky radiances for each zenith angle were interpolated as described earlier. The sky radiances for zenith angle 82.5° were used for the θ in Eq. 9. For θ', the almucantars for all zenith angles from 2.5 to 47.5 were tested and used if they contained β=55°.

The resultant scattering transmittances based upon each almucantar were then averaged for each sun zenith angle.

The values of scattering transmittance for each solar zenith angle were divided by the average for the day. The overall fractional STD was 0.0269 (n=214). This is equivalent to the STD for the optical thickness.

Appendix F

Comparison to Total Optical Thickness. One test of the accuracy and precision of any scattering optical thickness method is to compare the average for each optically stable day to the total optical thickness values in Table 2. The difference should be the total absorption

$$ {}_{a}t_{\infty}(z) = t_{\infty}(z) - {}_{s}t_{\infty}(z). \qquad (10) $$

Approximately a quarter of the resultant absorptions when the total scattering is based on Eq. 9, were negative indicating that the precision of the derived optical thickness is inadequate for obtaining reasonable individual absorption values. This is not surprising since the STD 0.0269 is of the same order of magnitude as the expected absorption values.

The total scattering optical thickness can also be expressed as the sum of the Rayleigh optical thickness and the aerosol scattering optical thickness.

Rayleigh Scattering Optical Thickness

The gas phase scattering (the molecular or Rayleigh scattering) is readily obtainable by computation. Appropriate values of Rayleigh vertical radiance transmittances ${}_{R}T_{\infty}(0,0)$ for the four passbands computed using

$$ {}_{R}T_{\infty}(0,0) = \frac{\Sigma \exp(-{}_{R}s_{\lambda}H)\,{}_{s}L_{\lambda}\bar{S}_{\lambda}\bar{T}_{\lambda}\Delta\lambda}{\Sigma\, {}_{s}L_{\lambda}\bar{S}_{\lambda}\bar{T}\Delta\lambda} \qquad (11) $$

are given in Col. 7 of Table 1. The spectral total volume scattering coefficients ${}_{R}s_{\lambda}$ are from Eq. 14 of Penndorf[10] using the refractive modulus from the dispersion formula of Edlen[11]. The sea level scale height H is for the U. S. Standard Atmosphere 1976[12].

The Rayleigh transmittance obtained from Eq. 11 is for use with the measurements from the solar transmissometer which measured the center sun radiance ${}_{s}L$. The center sun values for each passband are computed from

$${}_{s}L_{\lambda} = {}_{s}\bar{\varepsilon}_{\lambda}/({}_{s}\Omega D_{\lambda}). \quad (12)$$

The ${}_{s}\Omega$ is the solid angle of the sun at mean solar distance and D_{λ} is the spectral limb darkening factor based on limb darkening functions of Minnaert[13].

Aerosol Scattering Optical Thickness

The aerosol scattering optical thickness can be obtained from solar almucantar radiances using Eq. 44 from Ref. 1

$${}_{M}t_{\infty}(z) = 4\pi\,[\mu(z,55) - \mu(z,125)], \quad (13)$$

where $\mu(z,\beta)$ is defined by Eq. 4. Although this is an approzimative method it is powerful since it yields an answer directly in aerosol scattering optical thickness rather than transmittance.

Since the radiances were not measured directly for the solar almucantar at 55° and 125° scattering angle, these values were obtained by interpolation as described earlier. Since the largest β is at 180° azimuth, 62.5° is the smallest solar zenith angle for which 125° β can be obtained. Thus, for each day, fewer values of aerosol optical thickness were obtained than values of other optical thicknesses.

Dependence on Absolute Calibration. Error analysis of Eq. 13 indicates that the error of the aerosol scattering optical thickness is directly dependent on the error in the absolute calibration of the sky radiance photometer. All the previous methods, for obtaining the total optical thickness Eqs. 3 and 8 and the total scattering optical thickness Eq. 9, were independent of the absolute calibration of the instrument. In the first two methods the slope of the line is the optical thickness; in the last, the ratio of two sky radiances is used.

Appendix F

There were three indications of an unacceptably large absolute error in the sky radiance photometer calibration for March 9 and 11. First, no measurements of sky radiance for filter 4 were available for a large section of the sky near the azimuth 180° from the sun (approximately half of the sky) where the lowest radiances should have been recorded. Second, the absorption optical thickness obtained using Eq. 10 was negative for two of the measureable passbands for March 9 and substantially negative for all three measureable passbands for March 11. Third, total scattering optical thickness computed from the aerosol scattering optical thickness and the Rayleigh values

$$_{s}t_{\infty}(z) = {}_{M}t_{\infty}(z) + {}_{R}t_{\infty}(z) \qquad (14)$$

did not compare well to the values derived by the sky ratio method (Eq. 9) for March 9 and 11.

Thus the aerosol scattering optical thickness values are only available for seven days. These values are given in Table 2. The individual values of aerosol scattering optical thickness were divided by the average for the day. The resultant fractional STD was 0.147. Since the average aerosol scattering optical thickness was 0.0492, this translates to a STD of 0.0072 (n=75).

For comparison purposes, the scattering optical thickness from the sky ratio (Eq. 9) was divided by the values obtained using Eq. 14 as was described above. The average ratio for the seven days for filter 3 was 1.014 with an STD of 0.054 (which translates to a STD in optical thickness of 0.008 which is similar to the STD for the aerosol scattering optical thickness). The overall average ratio for all four filters is a bit higher, 1.11 with a STD of 0.141 (which translates to an STD in optical thickness of 0.0277 which is similar to the STD for the total scattering optical thickness derived by the sky ratio method). The ratio of the two scattering values for March 9 and 11 was well beyond the STD based upon the data for the other seven days.

From here on only the data from these seven days will be used and discussed. Scattering optical thicknesses will be based on Eq.s 13 and 14. The accuracy and precision of these data (STD 0.0072) substantiates the validity of the aerosol scattering optical thickness values even though the actual thickness values are quite small. With the aerosol scattering optical thickness value thus available, a better picture of the state of the atmosphere can be obtained.

Effective Optical Scattering Mixing Ratio. The optical scattering mixing ratio is one means of describing aerosol effects. The optical scattering mixing ratio is defined by Hering[14] as

$$Q(z) = s(z)/_{R}s(z). \quad (15)$$

This ratio is one when there is no aerosol, and the amount greater than one indicates the proportion of aerosol scattering relative to the Rayleigh scattering.

Let us define an effective optical scattering mixing ratio which is applicable to the entire atmosphere above the sensor as

$$Q_{\infty}(z) = {}_{s}t_{\infty}(z)/_{R}t_{\infty}(z). \quad (16)$$

Values of the optical scattering mixing ratio were computed using the measured values of aerosol scattering optical thickness (Eq. 13) and the theoretical values of Rayleigh optical thickness. These are graphed as a function of the mean wavelength of the four filters in Fig. 6. The values increase consistently with wavelength and are generally well behaved. The effective optical scattering mixing ratio is directly useful with models of sky radiance and contrast transmittance through the atmophere such as the model used in the FASCAT computer code (Ref. 14).

Angstrom Coefficients. The turbidity of the atmosphere (effect of the aerosol content) is typically evaluated by means of the Angstrom[15] equation

$$ {}_{M}t_{\infty}(z) + {}_{A}t_{\infty}(z) = \beta \lambda^{-\alpha} \quad (17) $$

where ${}_{A}t_{\infty}(z)$ is the aerosol absorption optical thickness. Care is generally taken to eliminate any gaseous sources of absorption by selection of appropriate windows in the spectrum, and by subtracting out the Rayleigh scattering. However, the remaining aerosol optical thickness is a composite of the aerosol scattering and aerosol absorption.

Appendix F

The aerosol scattering optical thickness method allows us to separate these two components of aerosol optical thickness. The coefficients derived from the aerosol scattering alone should give better information on the nature of the aerosol. Thus we suggest a modified form of the Angstrom equation as follows

$$ {}_{M}t_{\infty}(z) = B' \lambda^{c'}. \quad (18) $$

or

$$ \ln {}_{M}t_{\infty}(z) = \ln B' + c' \ln \lambda. \quad (19) $$

We have obtained best fit values of lnB' and c' with λ in nanometers for the aerosol scattering optical thickness values in Table 2. The average correlation coefficient for these fits is -0.943 STD 0.064.

In addition the lnB' was found to be a linear function of c', that is

$$ \ln B' = b + mc'. \quad (20) $$

A best fit to Eq. 20 produced a slope m=6.429, an intercept b=-3.512 and a correlation coefficient of -0.996. The individual values of lnB' and c' and the best fit line are depicted in Fig. 7. For these data, a measurement of aerosol scattering optical thickness at one wavelength will predict the slope c' and hence aerosol scattering optical thicknesses at other wavelengths in the visible spectrum.

Absorption Optical Thickness

The difference between the total optical thickness and the total

scattering optical thickness is the absorption.

Effective Single Scattering Albedo. The single scattering albedo is important for understanding the effect of absorption relative to the total attenuation. The single scattering albedo is defined as

$$w(z) = s(z)/\alpha(z) \tag{21}$$

where $\alpha(z)$ is the attenuation coefficient (which is the absorption plus the scattering) at altitude z.

Let us similarly define an effective single scattering albedo which is applicable to the entire atmosphere above the sensor as

$$w_\infty(z) = {}_s t_\infty(z)/t_\infty(z). \tag{22}$$

Values of the effective single scattering albedo were computed based upon the aerosol scattering and total optical thickness values in Table 2. The total scattering was computed using Eq. 14. These albedos are graphed as a function of the mean wavelength of the filters in Fig. 8. The values decrease consistently with mean wavelength and are again generally well behaved.

Ozone Absorption Optical Thickness Absorption due to ozone is reasonably well documented. In the visible part of the spectrum there is a relatively strong ozone continuum. The spectral values of ozone absorption optical thickness per cm ${}_z t_\lambda$ for the Chappuis bands are taken from the tabular values of Vigroux[16] which are in good agreement with the Inn and Tanaka[17] values. The absorption values for each passband were computed from

$${}_z t = \frac{\Sigma_z t_{\lambda s} \bar{\epsilon}_\lambda \bar{S}_\lambda \bar{T}_\lambda \Delta\lambda}{\Sigma_s \bar{\epsilon}_\lambda \bar{S}_\lambda \bar{T}_\lambda \Delta\lambda} . \tag{23}$$

The mean value of total ozone for the Visibility Laboratory site was taken from Wilcox, et al.[18] to be 0.290 cm. Values of mean ozone optical thickness for the four passbands are given in Col. 8 of Table 1.

Appendix F

The seasonal variation in the ozone thickness n(x) was computed using Eq. 6 from King, et al.[19]

$$n(x) = \bar{n} + A \sin(2\pi x - P). \quad (24)$$

The $\bar{n}$ is the mean ozone thickness, A the amplitude (0.024 for the latitude of the site based on Ref. 18), P the phase lag (0.72 from Ref. 19 for Tucson at a similar latitude to the Visibility Laboratory) , and x the fractional day in the year [day/365].

Non-ozone Absorption Optical Thickness If one has aerosol scattering, Rayleigh scattering, ozone absorption and total optical thickness, one can obtain a non-ozone absorption optical thickness. The non-ozone absorption thickness ${}_{x}t_{\infty}(z)$ is

$${}_{x}t_{\infty}(z) = {}_{a}t_{\infty}(z) - {}_{z}t_{\infty}(z), \quad (25)$$

where ${}_{a}t_{\infty}(z)$ is based upon Eq. 10 and ${}_{s}t_{\infty}(z)$ based on the aerosol scattering optical thickness values in Table 2 from Eq. 14. Non-ozone absorption optical thickness values for the seven optically stable days are graphed in Fig. 9. In the few cases which are negative, the negative amounts are within or nearly equivalent to the STD (±0.0072) of the aerosol optical thickness values from which the absorptions are derived.

The non-ozone absorption optical thickness source depends on the passband. A useful graph to evaluate the potential absorption from gas phase sources (atomic and molecular absorption) in the visible spectrum is given in Fig. 10 taken from Ref. 19 and based on Ref. 20. The spectral region to which the passbands apply is 365 to 800 nm. King et al. indicate that surface based optical thickness measurements in the spectral region 365 to 540 are essentially free from gaseous absorption except for the ozone and NO_2 continua. The primary bands appearing between 540 and 800 nm in Fig. 10 are for O_2 near 630, 690 and 760 nm, with the remainder due to H_2O.

The NO_2 continuum[21] affects measurements made in the spectral region 300 to 550 nm, peaking at 390 nm. Thus the passbands for filters 1 and 2 are affected to a significant extent. The NO_2 burden varies by an order of magnitude but the heaviest burden occurs during heavy pollution, which is not the case for optically stable days. Also the non-ozone absorption values for filters 1 and 2 already show some negative values. Therefore it is reasonable to assume a minimum NO_2 burden of 0.4×10^{-3} cm. The NO_2 absorption optical thickness was computed for the four passbands for 0.4×10^{-3} cm from

$$N^t = \frac{\Sigma_N t_{\lambda s} \bar{L}_\lambda \bar{S}_\lambda \bar{T}_\lambda \Delta\lambda}{\Sigma_s \bar{L}_\lambda \bar{S}_\lambda \bar{T}_\lambda \Delta\lambda} \quad . \tag{26}$$

The ${}_N t_\lambda$ values were taken from Hall and Blacet[22]. The ${}_s L_\lambda$ is the center sun radiance from Eq. 12. The NO_2 absorption optical thicknesses for 0.4 cm of NO_2 are 0.0047, 0.0028 and 0.0006 for the passbands for filters 1, 2 and 3 respectively.

Thus the passbands for filter 1 and filter 2 (which has 71 percent of its passband below 540) will indicate little gaseous absorption except for ozone and NO_2. The photopic effective passband (507 to 613 nm) contains several H_2O absorption bands. The filter 4 effective passband (630 to 692 nm) includes two oxygen bands and an H_2O band, therefore it should indicate a constant O_2 absorption at all times and a variable H_2O absorption.

Aerosol Absorption Optical Thickness Let us assume that aerosol absorption is constant with wavelength within the precision limits of our recovery method. Thus the average of the absorption values for filters 1 and 2, after both ozone and NO_2 have been subtracted, provide the best value for aerosol absorption. The average small negative values for Feb 14, Feb 21 and 2 Sept are approximately equal to the STD for the aerosol thickness values

so they can be assumed equal to zero. We can then subtract the average aerosol absorption from the non-ozone absorption thickness values for filters 3 and 4.

Appendix F

On 2 Sept, filter 3 indicates zero remaining absorption. Therefore, the remaining absorption for filter 3 on the other days is due to H_2O vapor absorption. The O_2 absorption should not vary significantly day to day whereas the H_2O vapor absorption for filter 4 should vary similarly to that of filter 3. Therefore, the remaining absorption for filter 4 (0.0146) on 2 Sept should be due to O_2. Subtracting that value from the remaining absorption for filter 4 leaves values not only similar in trend to those for filter 3, but also fortuitously similar in magnitude.

A tabular summary of the above is given in Table 3. The averages for filters 1 and 2 provided the aerosol absorption optical thickness values, and the averages from filters 3 and 4 (after subtracting the O_2 absorption from Filter 4) provide the H_2O vapor absorption optical thickness values.

The February period shows a fairly consistent picture in terms of absorption. As the gas phase H_2O absorption decreases, the aerosol absorption (which would include water droplets) increases until on 21 Feb there is suddenly no aerosol absorption, perhaps due to overnight dewfall.

Aerosol Single Scattering Albedo The aerosol single scattering albedo is important for understanding the effect of aerosol absorption relative to the total aerosol optical thickness. It is defined as

$$ {}_{M}w_{\infty}(z) = {}_{M}t_{\infty}(z)/[{}_{M}t_{\infty}(z) + {}_{A}t_{\infty}(z)]. \qquad (27) $$

The aerosol single scattering albedo based on the aerosol scattering values in Table 2 and the aerosol absorption values in Table 3 are graphed in Fig. 11.

Relative Importance of Aerosol Scattering and Absorption Optical Thickness

Two graphs illustrate the relative importance of the various components of total optical thickness. Figure 12 is a graph for January 31 for which

aerosol absorption optical thickness but little H_2O vapor absorption was indicated. Optical thickness values are graphed as a function of the mean wavelength of the four filters. Curves are given for the Rayleigh scattering, total scattering, scattering plus gaseous absorption, and total optical thickness. The space between the Rayleigh and the total scattering curve indicates the aerosol scattering optical thickness. The space between the total optical thickness and the scattering plus gaseous absorption is the aerosol absorption optical thickness. The various components are of approximately equal importance for filter 4, whereas for filter 1, the Rayleigh scattering predominates.

Appendix F

Figure 13 is a similar graph for only filters 1 and 4, but for all seven optically stable days for which we could obtain aerosol scattering and absorption optical thickness. The order of the days is in decreasing order of total optical thickness. The STD of the aerosol measurements is noted near the origin, in order to give a perspective on the importance or lack of importance of small differences.

Figure 13 illustrates that the relative proportions of the aerosol scattering and the aerosol absorption cannot be predicted fully on the basis of the total optical thickness values. Although the two days with aerosol absorption were among the higher total optical thickness values, so was September 2 which indicated no aerosol absorption. The almucantar method for obtaining aerosol scattering provides a means for separating the aerosol scattering from the aerosol absorption optical thickness.

4. CONCLUSIONS

Hitherto, there has been no means of separating anything but Rayleigh scattering and ozone absorption from the total optical thickness in the broad passbands. In the past, very narrow pass bands were selected in order to hit

windows where gas phase absorption bands could be avoided, in an attempt to isolate the total aerosol effect. Modelers, however, need to know how much of this aerosol optical thickness is scattering and how much is absorption. With the combination of the sky scanner and solar transmissometer, one can isolate the aerosol scattering optical thickness, obtaining values for broad or narrow passbands, within or not within absorption windows.

Appendix F

We found that the aerosol absorption can be significant, even on days of greater transparency than the average clear day. The aerosol single scattering albedo is a ratio important for understanding the effect of the aerosol absorption relative to the total aerosol optical thickness.

A modified Angstrom equation relates the aerosol scattering optical thickness to the wavelength. For this limited data set, a linear relationship was found between the natural log of the Angstrom constant and the slope (or power) of the wavelength for the aerosol scattering.

Separation of aerosol scattering and absorption leads to a more thorough understanding of the state of the atmosphere in terms appropriate for use in the equation of transfer, for prediction and for modeling.

ACKNOWLEDGMENTS

The data analyses and writing of this article were done at Viz. Ability, Inc. under U. S. Army Research Office contract no. DAAG29-84-C-0014. I wish to thank Judith Olson for technical writing and editing assistance.

I wish to thank R. W. Johnson and the Visibility Laboratory for making the data base, early technical notes, pictures and sketches available for the data analysis and this article. The data were collected by the Visibility Laboratory under various contracts for the Bureau of Ships, NASA, and the U. S. Air Force Geophysics Laboratory.

REFERENCES AND FOOTNOTES

1. J. I. Gordon, "New uses for the solar almucantar," Appl. Opt. 24, 3381-3389 (1985).

2. G.S. Livshits and V. E. Pavlov, "Atmospheric Transmittance and the Interrelationships of Certain Optical Parameters," in Atmospheric Optics, N. B. Divari, Ed. translated by S. B. Dresner (Plenum, New York, 1970), pp. 53-56.

3. C. F. Edgerton, "Relationship between Meterorological Conditions and Optical Properties of the Atmosphere," Scripps Institution of Oceanography, Visibility Laboratory, SIO Ref. 67-27 (1967).

4. S. Q. Duntley, A. R. Boileau, and R. W. Preisendorfer, "Image Transmission by the Troposphere I," J. Opt.Soc. Am. 47, 499 (1957).

5. W. G. Driscoll and W. Vaughan, Eds., Handbook of Optics (McGraw-Hill, New York, 1978).

6. The empirical expression for airmass was taken from F. Kasten, "A New Table and Approximation Formula for the Relative Optical Air Mass", Arch., Met. Geophys. Bioklim. B14, 206-233 (1965).

7. F. R. Johnson, "The Solar Constant," J. Meteorol. 11, 431-439 (1954).

8. J. M. Prospero, R. J. Charlson, V. Mohnen, R. Jaenicke, A. C. Delany, J. Moyers, W.Zoller, and K. Rahn, "The Atmospheric Aerosol System: an Overview," Rev. Geophys. Space Phys. 21, 1607-1629 (1983).

9. J. I. Gordon and R. W. Johnson, "Integrating nephelometer: theory and implications," Appl. Opt. 24, 2721-2730 (1985).

10. R. Penndorf, "Tables of the Refractive Index for Standard Air and the Rayleigh Scattering Coefficient for the Spectral Region Between 0.2 and 10.0 μm and Their Application to Atmospheric Optics," J. Opt. Soc. Am. 47, 176-182 (1957).

11. B. Edlen, "Dispersion of Standard Air," J. Opt. Soc. Am. 43, 339 (1953).

12. U. S. Standard Atmosphere, 1976 (Superintendent of Documents, U.S. GPO, Washington, D.C. 20402, 1976).

13. M. Minnaert, "The Photosphere," Chapter 3 in The Sun, G. P. Kuiper, Ed., (University of Chicago Press, 1953).

14. W. S. Hering, "The FASCAT Model Performance under Fractional Cloud Conditions and Related Studies," Scripps Institution of Oceanography, Visibility Laboratory, SIO REf. 85-7, AFGL-TR-84-0168.

15. A. Angstrom, "On the atmospheric transmission of sun radiation and on dust in the air," Geogr. Ann., 11,156-166 (1929).

16. E. Vigroux, "Etude experimentale de l'absorption de l'ozone," Ann. Phys. (Paris) 8, 742-743, 747 (1953).

17. E. C. Y. Inn and Y. Tanaka, "Ozone Absorption," J. Opt. Soc. Am. 43, 872 (1953).

18. R. W. Wilcox, G. D. Nastrom and A. D. Belmont, "Periodic Variations of Total Ozone and of Its Vertical Distribution," J. Appl. Meteorol. 16, 290-298 (1977).

19. M. D. King, D. M. Byrne, J. A. Reagan, and B. M. Herman, "Spectral Variation of Optical Depth at Tucson, Arizona between August 1975 and December 1977," J. Appl. Meteorol. 19, 723-732 (1980).

20. C. E.Moore, M. G. J. Minnaert and J. Houtgast, The Solar Spectrum 2935 Å to 8770 Å; Second Revision of Rowland's Preliminary Table of Solar Spectrum Wavelengths. Nat. Bur. Stnd. Monogr. No. 61 (U. S. GPO, Washington, DC, 1966), 349 pp.

21. G. E. Shaw, "Nitrogen dioxide-optical absorption in the visible," J. Geophys. Res. 81, 5791-5792 (1976).

22. T. C. Hall, Jr., and F. E. Blacet, "Separation of the absorption spectra of NO_2 and N_2O_4 in the range of 2400-5000A," J. Chem. Phys. 20, 1745-1749 (1952).

Table 1 Spectral characteristics summary for Rooftop 1964 filters.

Filter	Spectral Characteristics: Peak Wavelength (nm)	Mean Wavelength (nm)	Effective Passband (nm)	Solar Irradiance Out-of-Atmosphere ($W/m^2\mu m$)	Inherent Center Sun Radiance ($W/\Omega m^2\mu m$)	Rayleigh Vertical Transmittance	Mean Ozone Optical Thickness (0.29cm)	NO_2 Optical Thickness (0.004cm)
1	450	459	58.1	2080	4.00×10^7	0.812	0.00311	0.0047
2	500	505	151.9	1950	3.66×10^7	0.852	0.0134	0.0028
3	555	560	106.8	1890*	3.45×10^7	0.907	0.0258	0.0006
4	630	661	61.8	1590	2.79×10^7	0.952	0.0185	0

* The value for the photopic filter 3 is expressed in radiometric terms. The radiance and irradiance may be converted to luminance and illuminance by multiplying by 72.62 lu μm/W.

Appendix F

Table 2 Optical thickness for the optically stable days.

Date 1964	Air Mass Type*	No. θ_s	Total Optical Thickness Filter 1	2	3	4	No. θ_s	Aerosol Scattering Optical Thickness** Filter 1	2	3	4
Jan 31	STK	3	0.298	0.255	0.202	0.152	2	0.0552	0.0568	0.0516	0.0405
Feb 14	STK	8	0.292	0.236	0.195	0.143	2	0.0730	0.0640	0.0547	0.0435
Feb 17	STK	8	0.270	0.218	0.178	0.128	4	0.0437	0.0395	0.0356	0.0288
Feb 18	STK	3	0.271	0.231	0.178	0.134	2	0.0525	0.0518	0.0416	0.0326
Feb 20	STK	8	0.308	0.272	0.223	0.182	4	0.0621	0.0599	0.0615	0.0548
Feb 21	STK	7	0.242	0.198	0.158	0.116	3	0.0312	0.0320	0.0309	0.0269
Mar 9	MPK	6	0.296	0.241	0.200	0.147					
Mar 11	ST-MPK	6	0.353	0.306	0.252	0.198					
Sep 2	CTK	8	0.303	0.245	0.189	0.144	2	0.0911	0.0790	0.0710	0.0620
	Total	57					19				

* STK Superior (warm, dry airmass having origin aloft) Tropical Cooler
MPK Maritime Polar Cooler
ST-MPK Superior Tropical - transitional to - Maritime Polar Cooler
CTK Continental Tropical Cooler
Zero days with one airmass aloft and another at lower levels.

** Not available for March 9 and 11

Table 3 Absorption optical thickness for aerosol (average of filters 1 and 2) and H_2O vapor (average of filters 3 and 4).

	Aerosol	H_2O Vapor
31 Jan	0.0243	0.0040
14 Feb	0	0.0167
17 Feb	0.0060	0.0116
18 Feb	0.0027	0.0132
20 Feb	0.0327	0.0085
21 Feb	0	0.0045
2 Sep	0	0

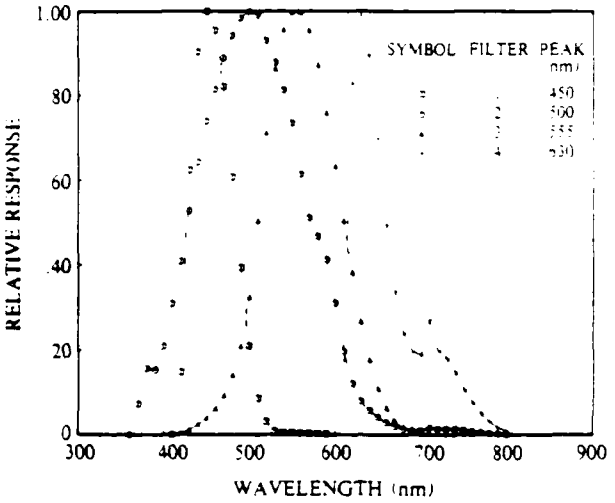

Fig. 1 Relative spectral response of the four passbands. Filter 2 was the broadest passband, followed by filter 3, photopic. The two remaining passbands are relatively narrow, 60 ±1.9 nm.

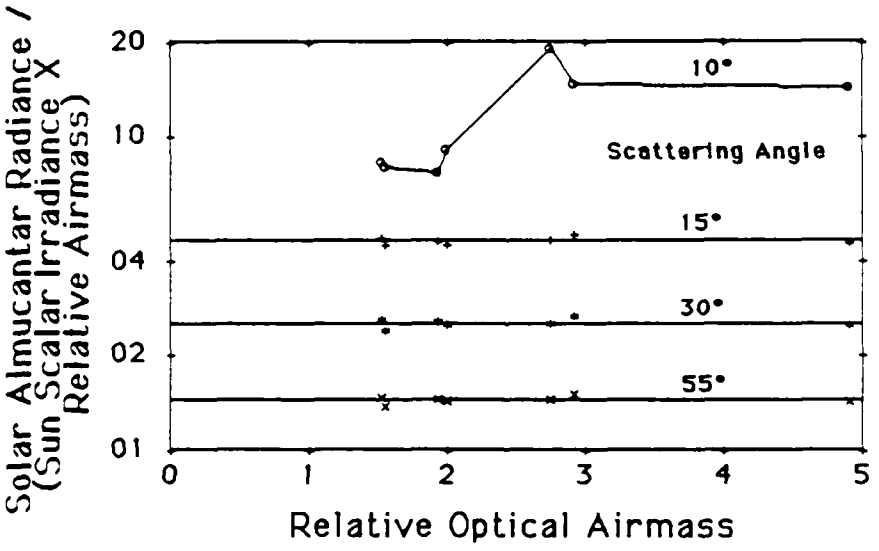

Fig. 2 Test One for photopic sky radiances on 21 February 1964. The log scale for the ratio emphasizes the consistency of the fractional standard deviation from the horizontal straight line for scattering angles 15° through 55°.

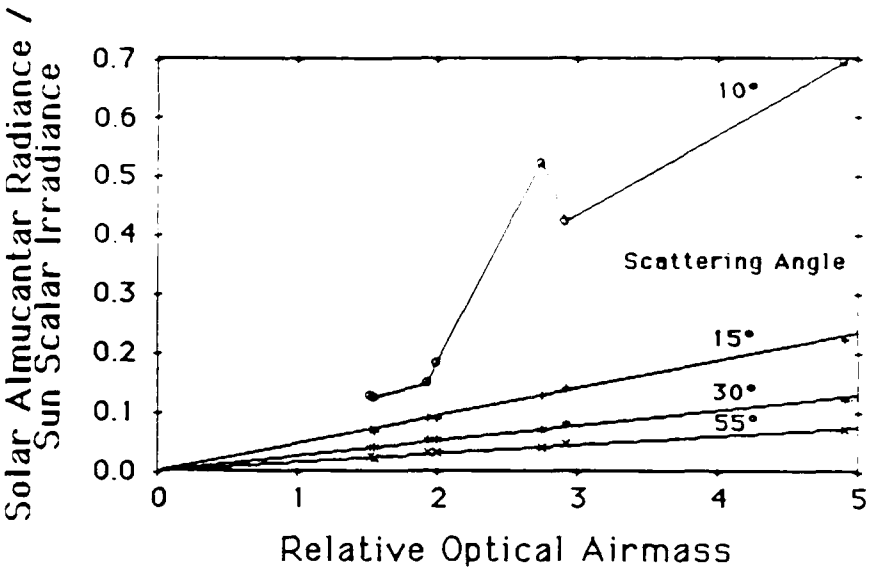

Fig. 3 Test Two for photopic sky radiances on 21 February 1964. The values for scattering angles 15° through 55° $\Delta\beta$ = 5° consistently fit a straight line through the origin.

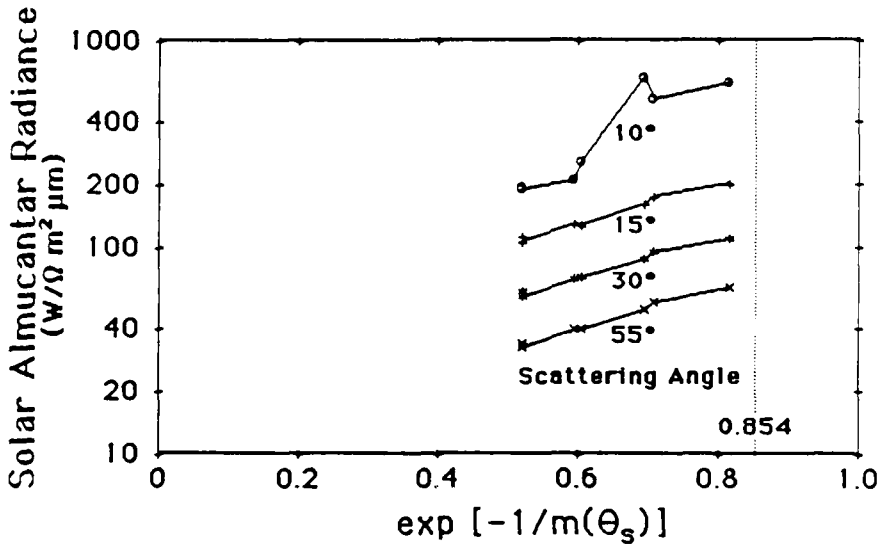

Fig. 4 Test Three for photopic sky radiances on 21 February 1964. The radiances for the solar almucantar at scattering angles 15° through 55° $\Delta\beta$ = 5° consistently rise towards the expected maximum at vertical transmittance = 0.854. The solar almucantar for 10° is less consistent, showing a maximum at transmittance 0.695 and apparently rising again.

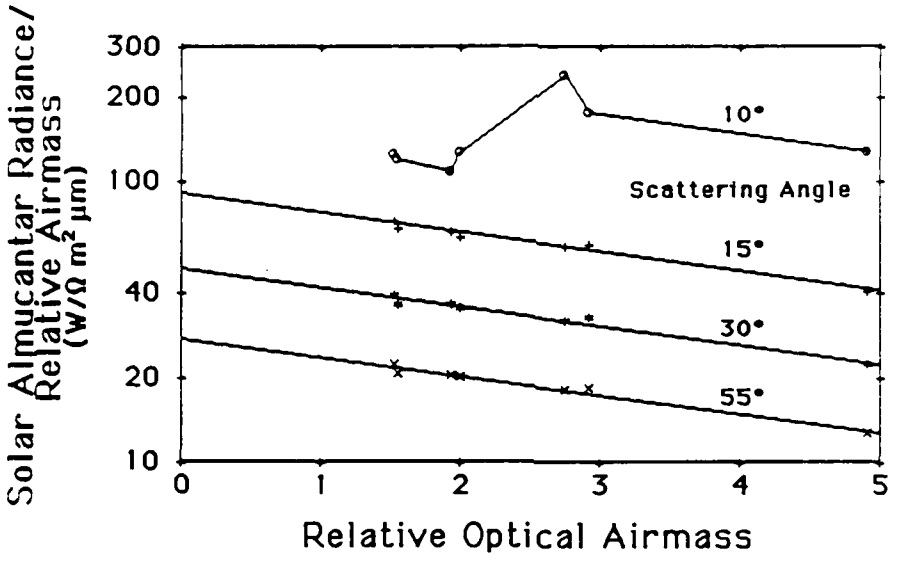

Fig. 5 Log of the ratio of the photopic solar almucantar radiance divided by the airmass graphed versus relative optical airmass for 21 February 1964. The slope of the straight line is the optical thickness. The optical thickness based on the average slope, from scattering angles 15° through 55° $\Delta\beta$ = 5°, is 0.155. This compares well to 0.158 which is the slope obtained from the apparent sun radiances measured with the solar transmissometer.

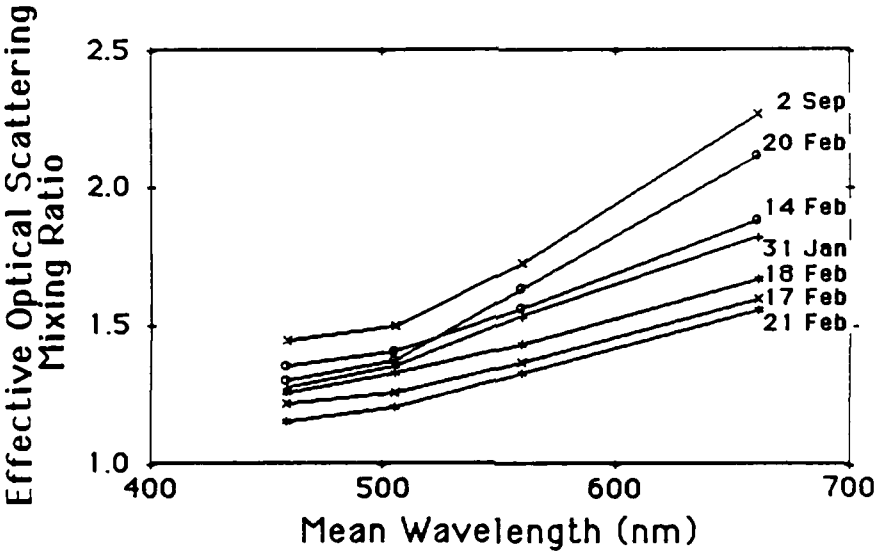

Fig. 6 Effective optical scattering mixing ratio $Q_{\infty}(z)$ as a function of the passband mean wavelength for the seven optically stable days.

Appendix F

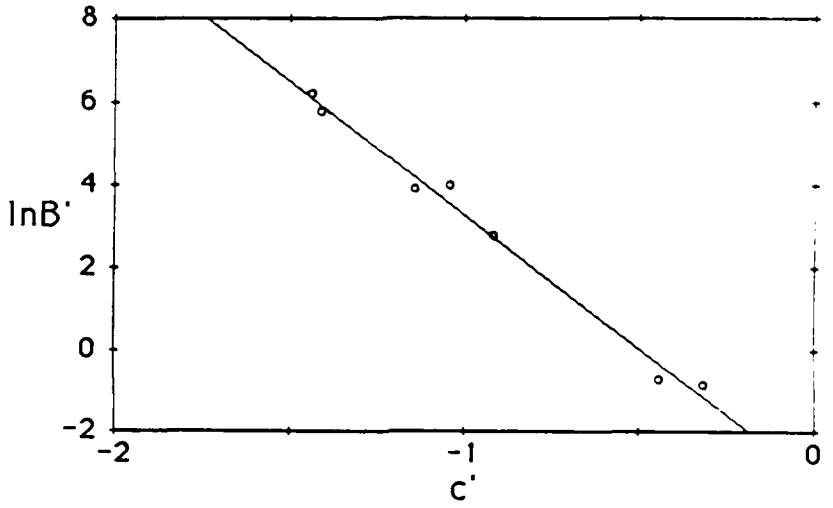

Fig. 7 Relationship of Angstrom constant (lnB') to the slope or power c' for aerosol scattering optical thickness values in the visible spectrum, wavelength in nm. The line is from the equation lnB' = -3.512 -6.429c'.

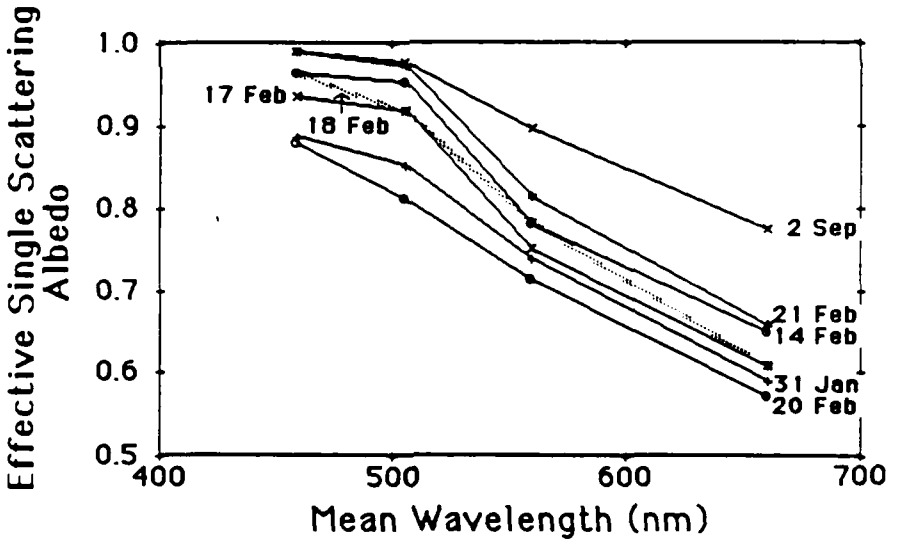

Fig. 8 Effective single scattering albedo $w_{\tilde{s}}(z)$ as a function of the passband mean wavelength for the seven optically stable days.

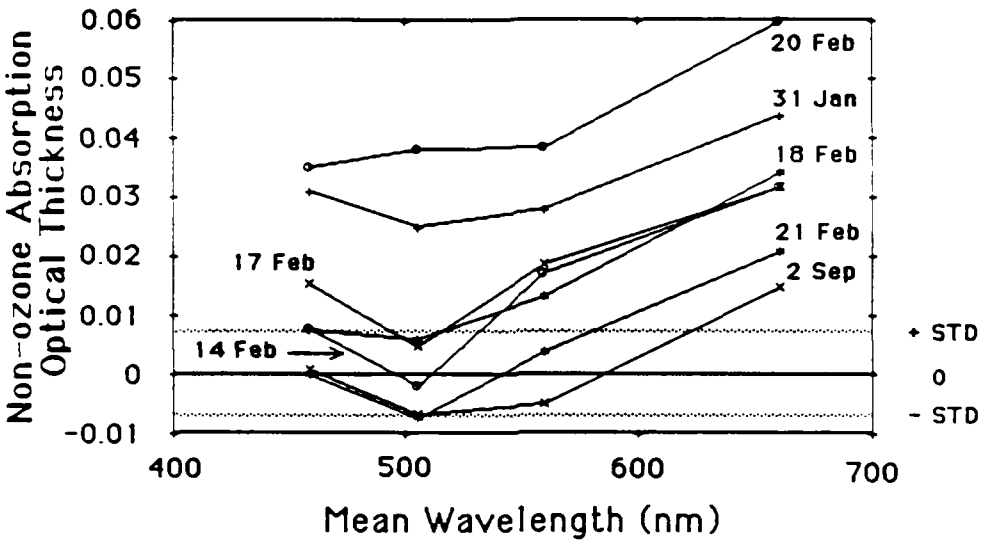

Fig. 9 Non-ozone absorption optical thickness $t_x(z)$ as a function of the passband mean wavelength for the seven optically stable days. The horizontal lines indicate ±0.0072 which is the STD for the aerosol optical thickness values upon which the absorptions are based.

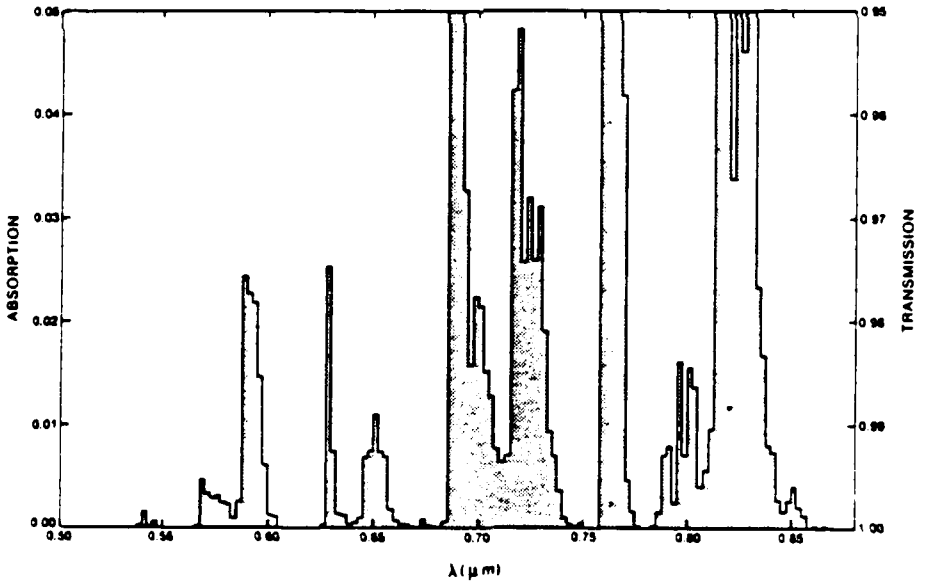

Fig. 10 (Fig. 1 from Ref. 19) Slant path absorption and transmission through the atmosphere (at a resolution of 2.5 nm) as obtained from high resolution spectra in the Utrecht Photometric Atlas (after Moore et al., Ref. 20). Bands at 0.63, 0.69 and 0.76 μm are due to oxygen absorption while all remaining bands are due to water vapor absorption. The air mass varies with wavelength but is everywhere less than 2.22.

Appendix F

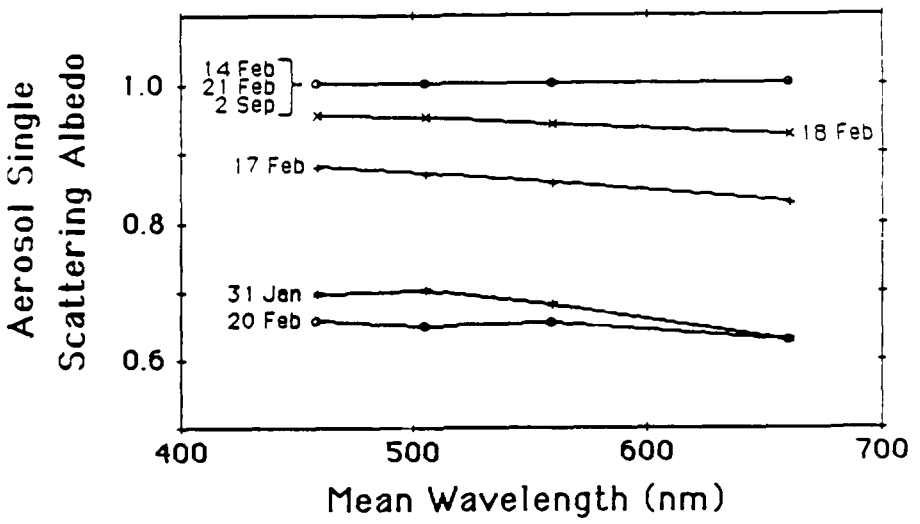

Fig. 11 Effective aerosol single scattering albedo $_{M}w_{o}(0)$ as a function of the passband mean wavelength for the seven optically stable days.

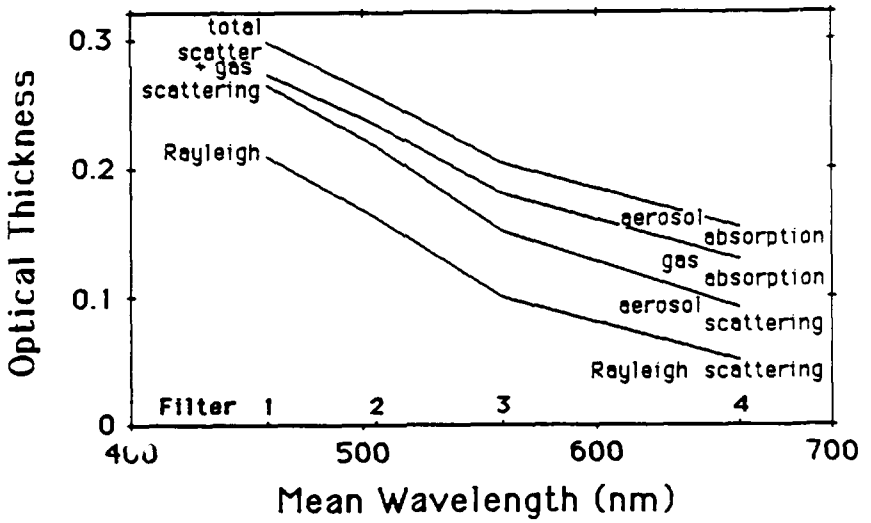

Fig. 12 Components of total optical thickness for Janary 31, 1964.

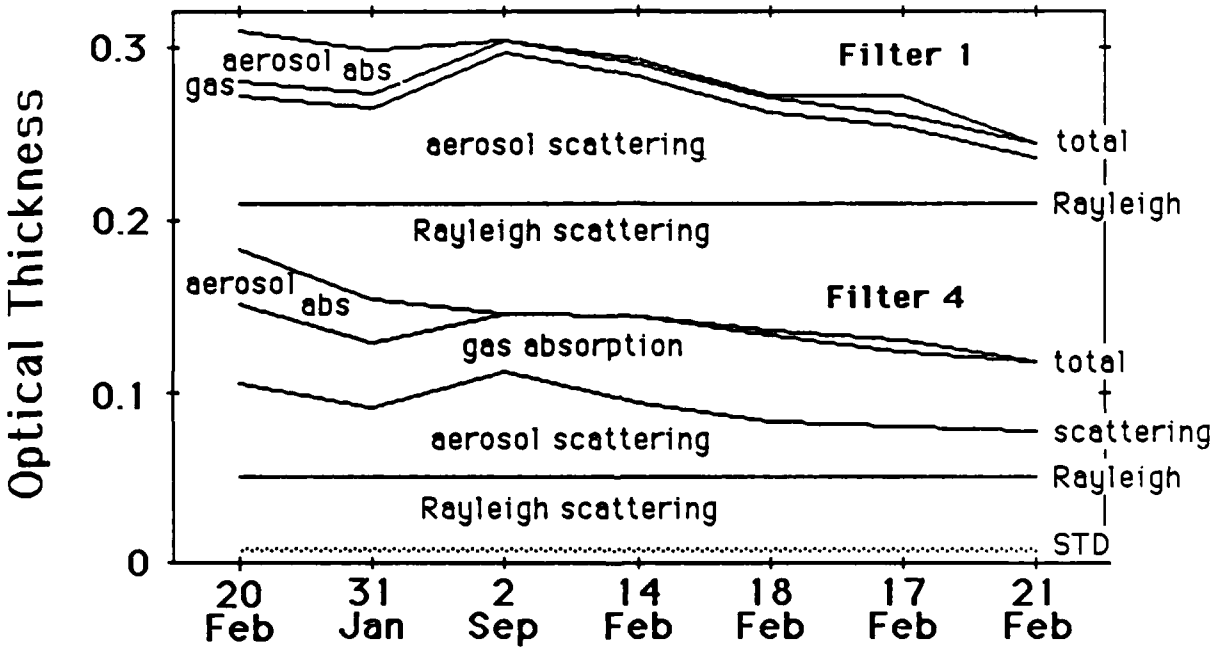

Fig. 13 Components of total optical thickness for filters 1 and 4 for all seven optically stable days, in order by decreasing total optical thickness.

Aerosol Scattering and Absorption Optical Thickness II.

From airborne measurements in a polluted atmosphere.

By

Jacqueline I. Gordon

Viz. Ability, Inc., 2941 NW Ashwood Drive, Corvallis, Oregon 97330-1255

Appendix G

ABSTRACT

This paper concludes a two part series. With measurements of aerosol scattering and absorption optical thickness available, the optical scattering mixing ratio, modified Angstrom equation and single scattering albedo detail the state of a polluted urban atmosphere. The Angstrom equation for aerosol scattering is further developed for any altitude interval. A relationship between the Angstrom constant and Angstrom coefficient was discovered for the combined data from the two part series. Any single aerosol scattering measurement at any wavelength in the visible can be used to predict all other aerosol scattering values at all other wavelengths in the visible.

1. INTRODUCTION

This is the second paper of a two part series. The first paper[1] used a data base of ground-based measurements made during optically stable days that were optically thinner than a standard clear day. This second paper uses a data base consisting of airborne data for a polluted atmosphere near a large metropolitan area. Although the data bases are relatively old, the data analyses are completely new, using newly developed methods. Both were visible spectrum data sets but employed different instruments, passbands and data collection procedures.

The data reported herein are for 14 flights made during the METROMEX field project[2] with an instrumented C-130 during 8 days in August 1971 near St. Louis, Missouri. The data are for three visible spectrum broad

passbands, mean wavelengths 478, 557 and 664 nm. The early reports on the data base[3,4] give a complete description of instruments, data gathering procedures, total scattering coefficient and path radiance for various downward paths of sight, but no information on absorption or aerosol scattering.

Appendix G

The notation used is that adopted by the Visibility Laboratory[5] and modified to correspond to Optical Society of America recommendations in sec. 1 of Driscoll and Vaughan[6].

2. INSTRUMENTATION AND DATA PROCEDURES

The instruments used in the data collection were an integrating nephelometer, a dual irradiometer for measuring upwelling and downwelling irradiance, and two 2π scanners for measuring the sky and the terrain radiances, respectively. Pictures were taken with two fisheye-lens cameras to document the upper and lower hemispheres. In addition, ambient pressure, temperature and dewpoint temperature were measured.

2.1 Procedures

The first element of a flight was level at the lowest altitude AGL (above ground level) feasible. The average low level flight altitude for the 14 flights was 0.15 km AGL, STD (standard deviation) 0.05 km. During level flight, measurements were made with all three radiometric instruments using one passband. When the entire 4π lighting distribution was recorded, measurements were repeated for the other two passbands. During level flight, the data were always taken in the filter order 2, 3 then 4, mean wavelengths 478, 664 and 557 respectively.

As the plane ascended to the top of the primary haze layer (determined visually), the integrating nephelometer recorded a vertical profile using the filter 2 passband. The level flight element was then repeated. The average

second level flight altitude for the 14 flights was 1.3 km AGL, STD 0.2 km. A second vertical profile was recorded while ascending to an average altitude of 2.2 km AGL, STD 0.9 km, for a third level flight element. The aircraft then descended to the lowest altitude while recording with the integrating nephelometer using the filter 3 passband, and ascended to the top altitude recording the filter 4 passband.

Most of the flights contained three level flight elements. Two of the flights contained two and one flight contained four level flight elements. The data on all but two of the flights were taken near noon so that changes in solar zenith angle over the flight duration were minimized. On six of the days, two flights were flown in succession, one on either side of the city, in an attempt to record measurements upwind and downwind of the city.

The optical thicknesses which will be described herein are for the altitude intervals between level flight elements. These provide a description of the primary haze layer and the secondary haze layer. The average altitude interval for the primary haze layer was 1.1 km, STD 0.2 km. The average altitude interval for the secondary haze layer measurements was 1.2 km, STD 0.2 km. This latter measurement interval was arbitrary. The secondary haze layer, in actuality, continued to much higher altitudes.

2.2 Radiometric systems

The basic detector was a multiplier phototube with an S-20 spectral response. The phototube assembly and isolite photometric reference sources were mounted within a temperature control housing. This maintained the relative spectral sensitivity of the phototubes[7] and ensured the temperature stability of the reference sources.

Integrating Nephelometer

The integrating nephelometer was mounted on top of the aircraft fuselage.

The nephelometer measured the flux scattered from a collimated beam. An irradiometer mounted adjacent to the beam collected the flux scattered from angles 5° to 170°.

By remote control, a reflecting surface was periodically inserted into the beam on the side away from the projector and a direct measure of the beam flux taken. The nephelometer thus became a ratio device, no longer dependent on the absolute calibration. Details of the design and calibration equations are given by Gordon and Johnson[8].

Appendix G

Dual Irradiometer

The dual irradiometer was mounted on a wing tip such that the two flat plate optical collectors could receive the radiant flux from the upper and lower 2π hemispheres. A rotating prism directed the collected flux to a single phototube. The position of the prism was controlled by an operator within the aircraft.

Scanners

Two identical scanners were used for measuring the sky and the terrain radiances. The sky scanner was mounted on top of the fuselage and the terrain scanner beneath the fuselage. Each scanner had a small moveable telescope with a 5° field of view. The telescopes continually moved in a spiral pattern which covered the full hemisphere in 160 seconds. Radiances were sampled at a rate of 60 per second. Azimuth and elevation angle positions were sampled at a rate of 15 per second and 3 per second respectively.

2.3 Spectral Specifications of Radiometric Data

The standard relative spectral responses for the radiometric measurements are depicted in Fig. 1. These are the normalized curves of the spectral response of the standard phototube $\overline{S_\lambda}$ times the standard transmittance $\overline{T_\lambda}$ of the filter. The spectral passbands for the three instruments were equivalent.

The effective passband (or area under the relative response curve) and the mean wavelength for each passband are presented in Table 1. The remaining four columns in Table 1 are solar and atmospheric properties appropriate for each passband, the details of obtaining these solar and atmospheric properties were explained in detail in Ref. 1.

2.4 Radiometric Calibrations

The calibration procedure used standard photometric practices, a 3-meter optical bench, and incandescent standards of luminous intensity traceable to the National Bureau of Standards. The linearity calibrations extended over a radiance span of 5 log cycles. The precision depended upon the portion of the range in use. At the center of the span a readout precision of ±1% of the reading was achieved. The measurements for the three passbands tended to be in the central portion of the span. Typical standard deviations for the calibration constants are on the order of ±5%.

The linearity and absolute calibrations were conducted prior to and following the field trip. During the calibration procedure and during the flights, each phototube was periodically exposed to an Isolite internal reference source. The long term stability of each detector was thus monitored and automatic adjustments made to its calibration constants.

3. DATA ANALYSES

The total optical thickness has two basic components, the scattering optical thickness ${}_{s}t_{\Delta z}(z)$ and the absorption optical thickness ${}_{a}t_{\Delta z}(z)$. The z is the measurement altitude, the subscript Δz indicates the altitude interval to which the thickness t applies.

In addition, the scattering and absorption components can each be divided into a gas phase component and an aerosol component. The word aerosol is used herein to describe the liquid and/or solid particulates exclusive of the gas

phase in which they are embedded. This is consistent with Prospero, et al.[9]

3.1 Scattering Optical Thickness

Appendix G

The total scattering optical thickness is the integral of the total volume scattering coefficient s(z) over the altitude interval Δz

$$s^{t}_{\Delta z}(z) = \int_{\Delta z} s(z)dz. \qquad (1)$$

The total volume scattering coefficient s(z) was measured by the integrating nephelometer during the vertical flight profiles flown between the straight and level flight elements and was available for each 30 m increment in altitude. The total scattering optical thickness for the altitude interval between the level flight elements was computed for each passband using the trapazoidal rule.

Rayleigh Scattering Optical Thickness

The gas phase scattering (the molecular or Rayleigh scattering) is readily obtainable by computation. Appropriate values of Rayleigh volume scattering coefficient for sea level, 15°C are given in Table 1 for the three passbands.

The Rayleigh optical thickness for the atmosphere above the altitude z was computed using

$$R^{t}_{\infty}(z) = {}_{R}s(0,15°C)H(0,15°C)P(z)/P(0,15°C) = {}_{R}s(0,15°C)P(z)8.3244 \qquad (2)$$

where H(0,15°C) is the scale height in meters for sea level at a temperature of 15°C, and P(z) is the measured pressure in millibars at altitude z. The scale height and sea level pressure were taken from the U. S. Standard Atmosphere[10].

The Rayleigh optical thickness for the haze layer in altitude increment Δz is found from

$$R^{t}_{\Delta z}(z) = {}_{R}t_{\infty}(z_1) - {}_{R}t_{\infty}(z_2) \qquad (3)$$

where altitude z_1 is lower than z_2.

Aerosol Scattering Optical Thickness

The aerosol scattering optical thickness ${}_M t_{\Delta z}(z)$ for each layer can be obtained from the total scattering optical thickness (derived from nephelometer data) less the Rayleigh optical thickness

$$ {}_M t_{\Delta z}(z) = {}_s t_{\Delta z}(z) - {}_R t_{\Delta z}(z). \quad (4) $$

The aerosol scattering optical thickness values from the ground-based data set were obtained from almucantar sky radiance values at 55° and 125° scattering from the sun β divided by the solar scalar irradiance at ground level and the relative optical airmass (Eq. 14, Ref. 1).

Unfortunately, we were unable to use this same method on the airborne data set because it requires solar zenith angles of 62.5° or greater. All the airborne data except for one altitude for one flight were for solar zenith angles of less than 62.5° (most of the data were taken near noon in the summer at mid-latitude). Therefore, a comparison of the two methods of obtaining aerosol scattering optical thickness on a single data set was not possible.

Angstrom Equation. The turbidity of the atmosphere (effect of the aerosol content) is typically evaluated by means of the Angstrom[11] equation which relates the total aerosol optical thickness to the wavelength. In ref. 1 we suggested a modified form of the Angstrom equation as follows

$$ {}_M t_{\infty}(z) = B' \lambda^{c'}. \quad (5) $$

This relationship can be generalized for the aerosol scattering optical thickness for any altitude interval and written in the form

$$ \ln {}_M t_{\Delta z}(z) = \ln B' + c' \ln \lambda. \quad (6) $$

We have obtained best fit values of lnB' and c' with λ in nanometers from the aerosol scattering optical thickness values derived from the nephelometer values for the haze layers and for the total altitude interval flown. The

average correlation coefficient for these fits is -0.976, STD 0.043.

In the first article of this two part series (Ref. 1), we found that lnB' was a linear function of c' thus

$$\ln B' = b + mc'. \qquad (7)$$

A best fit to Eq. 7 for the data set in Ref. 1 produced a slope m=-6.429, an intercept b=-3.152 and a correlation coefficient of -0.996. This was based on 7 days of data measured on optically stable days. The four passbands used had mean wavelengths of 459, 505, 560 and 661 nm.

Appendix G

Fitting the slopes c' and intercepts lnB' derived from the nephelometer data to Eq. 7 we again obtained a good linear fit with a similar slope and intercept and a correlation coeficient of -0.972.

Fig. 2 shows the slopes c' and intercepts lnB' of the combined sets of data. The best fit to this combined data set yields a slope m=-7.108, an intercept b=-3.243 and a correlation coefficient of -0.983. Data set 1 (shown as circles) contains optical thicknesses through the entire atmosphere appropriate for days more transparent than the average clear day. Data set 2 (shown as x for the primary haze layer, + for the secondary haze layer and * for the total altitude interval of each flight) contains the large aerosol scattering optical thicknesses expected from haze layers in a fairly polluted atmosphere. Some of the data from the secondary haze layers overlap the values from data set 1.

The unmodified Angstrom equation for the total aerosol optical thickness is (from Eq. 6.6.1 of Ref. 12)

$$_{M}t_{\infty}(z) + {}_{A}t_{\infty}(z) = \beta \lambda^{-\alpha}, \qquad (8)$$

where ${}_{A}t_{\infty}(z)$ is the aerosol absorption optical thickness. The average slope α is 1.3 ±0.5 for most natural atmospheres[12]. The slope α (for total aerosol optical thickness) equals the slope -c' (for aerosol

scattering optical thickness) when there is no aerosol absorption. The slopes in Fig. 2 exceed the range for $-\alpha$ in both directions.

The methods of measuring aerosol scattering optical thicknesses for the two data sets are completely different. The passbands used are not equivalent although they encompass about the same portion of the visible spectrum. Together, the two data sets encompass a large range of conditions and appear to define a relationship which is invariant whether the aerosol scattering optical thicknesses are for the entire atmosphere or for one or two haze layers.

Thus, the constant in the modified Angstrom equation can be predicted for a wide range of aerosol scattering optical thickness values if the power (or slope) c' in Eq. 7 is known.

Combining Eqs. 6 and 7 we get

$$\ln {}_{M}t_{\Delta z}(z) = b + c'(m + \ln\lambda), \tag{9}$$

or

$$c' = (\ln {}_{M}t_{\Delta z}(z) - b)/(m + \ln\lambda), \tag{10}$$

where b and m are invariant. Thus a measurement of aerosol scattering optical thickness at one wavelength will predict the slope c' and allow a prediction of aerosol scattering optical thickness at other wavelengths.

The data in Fig. 2 are limited to passbands with mean wavelengths between 459 and 664 nm but the results should apply to the entire visible spectrum 400 to 700 nm.

Effective Optical Scattering Mixing Ratio. The effective optical scattering mixing ratio (eq. 17, ref. 1) is another means of describing aerosol scattering effects

$$Q_{\infty}(z) = {}_{S}t_{\infty}(z)/{}_{R}t_{\infty}(z). \tag{11}$$

This ratio is one when there is no aerosol, and the amount greater than one indicates the proportion of aerosol scattering relative to the Rayleigh

scattering.

We can further develop the effective optical scattering mixing ratio to be applicable to haze layers or the entire atmosphere

$$Q_{\Delta z}(z) = {}_{s}t_{\Delta z}(z)/{}_{R}t_{\Delta z}(z). \quad (12)$$

This is a useful quantity since the Rayleigh optical thickness is readily derivable for any altitude increment if the altitudes, temperatures and pressures are known or can be estimated. Thus the aerosol scattering effect can be accounted for and the total scattering optical thickness obtained by multiplying the Rayleigh optical thickness by the ratio Q.

Appendix G

Values of effective optical scattering mixing ratio were computed for each haze layer using the total scattering optical thicknesses from the nephelometer and the Rayleigh optical thicknesses from Eq. (4). These are graphed as a function of the mean wavelength of the three passbands for the primary haze layer in Fig. 3 and for the secondary haze layer in Fig. 4. The curves are labeled with the flight numbers, C180 through C188B.

There is some overlap between the two figures; in these cases the primary haze layer is thinner optically than the secondary haze layer at another location and time. The increase of Q with wavelength is typical. The effective optical scattering mixing ratios $Q_{\infty}(0)$ from Ref. 1 were much smaller. They ranged from 1.2 to 1.5 at 459 nm to 1.5 to 2.3 at 661 nm.

To get an estimate of the variability of Q(z) within the haze layers, we first computed Q(z) from (Eq. 15 Ref 1)

$$Q(z) = s(z)/{}_{R}s(z). \quad (13)$$

The ${}_{R}s(z)$ was computed from the values in Table 1 times the density ratio. The density for each altitude was based on the measured pressure and temperature. Then we computed the fractional standard deviation from the average for each haze layer. The average fractional standard deviation was

0.276 with an STD from that average of 0.273.

Values of the optical scattering mixing ratio should be more useful than the actual values of the aerosol scattering optical thickness for each haze layer. The aerosol scattering optical thickness is directly affected by variations in the altitude interval Δz and the pressure and temperature (density) profile with altitude of the interval. In contrast, the optical scattering mixing ratio has these differences factored out, as a ratio to the Rayleigh optical thickness which takes density and altitude interval into consideration.

Appendix G

3.2 Absorption Optical Thickness

In the visible portion of the spectrum, the absorption optical thickness for a haze layer can be determined from

(Ref. 13, Eq. 47)

$$ {}_{a}t_{\Delta z} = [\xi(z_0) - \xi(z)]/\overline{\epsilon(z)} \qquad (14) $$

where z_0 is greater than z. The net irradiance (or net flux) $\xi(z)$ is the difference between the downwelling irradiance E(z,d) and the upwelling irradiance E(z,u)

$$ \xi(z) = E(z,d) - E(z,u). \qquad (15) $$

The net flux difference $\xi(z_0) - \xi(z)$ is also called the flux divergence. The $\overline{\epsilon(z)}$ is the average total scalar irradiance for the altitude incrementbetween z_0 and z. The total scalar irradiance is defined as

$$ \epsilon(z) = {}_{s}\epsilon(z) + {}_{4\pi}\int L(z,\theta,\phi)d\Omega, \qquad (16) $$

where ${}_{s}\epsilon(z)$ is the solar scalar irradiance at altitude z.

Computation Procedures

The data set included downwelling and upwelling irradiance measurements made by a single photometer (thus minimizing absolute error effects). It also

included the 4π radiance distribution $L(z,\theta,\emptyset)$ as measured by the two scanning telephotometers. Unfortunately the sky scanner contained internal reflection errors in the measurements of radiance within 25° of the sun.

Sky Radiances Near Sun. The scanner internal reflectance handicap was overcome by assuming the log of the sky radiance $L^*_\infty(z,\theta_s,\beta)$ to be linear as a function of the cosine of the angle from sun β, from 0° to 30° in the solar almucantar (at solar zenith angle θ_s)

$$\ln L^*_\infty(z,\theta_s,\beta) = A + M\cos\beta. \quad (17)$$

Average values of solar almucantar radiance for 25° and 30° in β were computed and used to solve for the intercept A and slope M for each level altitude and passband.

The sky radiances for $\beta<25°$ for zenith angles less than and greater than the sun zenith angle were computed by assuming the sky radiance to be a function of the effective equilibrium radiance $L_q(z,\beta)$ and the scattering transmittance ${}_sT_\infty(z,\theta)$ (Eq. 9, Ref. 14)

$$L_q(z,\beta) = L^*_\infty(z,\theta,\emptyset)/[1 - {}_sT_\infty(z,\theta)]. \quad (18)$$

The scattering transmittance at any zenith angle θ is a function of the total scattering optical thickness and the relative optical airmass $m(\theta)$[15],

$${}_sT_\infty(z,\theta) = \exp[-{}_st_\infty(z)\, m(\theta)]. \quad (19)$$

Equilibrium radiance is in turn assumed to be primarily a function of the scattering angle β. Using the solar almucantar radiances to indicate the equilibrium radiance as a function of β, the sky radiance at other zenith angles could be computed from

$$L^*_\infty(z,\theta,\emptyset) = L^*_\infty(z,\theta_s,\beta)[1-{}_sT_\infty(z,\theta)]/1-{}_sT_\infty(z,\theta_s)]. \quad (20)$$

The scattering transmittance was computed from (Eq. 60, Ref. 8)

$$L^*_\infty(z,\theta,55°\beta)/L^*_\infty(z,\theta_s,55°\beta)=[1-{}_sT_\infty(z,\theta)]/[1-{}_sT_\infty(z,\theta_s)]. \quad (21)$$

Although not solvable directly, Eq. 21 is readily solved by iteration. The sky radiances used for the ratio were from the solar almucantar θ_s and for θ=82.5°. Although the precision of the scattering optical thickness recovered by this method is not high (Ref. 1), it is adequate for the purpose of correcting the sky radiances near the sun.

Sun Scalar Irradiance. The solar irradiance ${}_sE(z,d)$ was computed from the measured downwelling irradiance $E(z,d)$ and the computed sky irradiance as follows

$$ {}_sE(z,d) = E(z,d) - {}_{2\pi}\int L^*_\infty(z,\theta,\phi)\cos\theta\, d\Omega. \qquad (22) $$

The sun scalar irradiance is then

$$ {}_s\varepsilon(z) = {}_sE(z,d)/\cos\theta_s. \qquad (23) $$

For the actual computation of the absorption optical thickness, an average solar zenith angle for the given passband and altitude interval was used both for the computation of total scalar irradiance and the flux difference. This involved modifying the contribution of the sun for both the downwelling irradiance and the total scalar irradiance. In order to do this, an estimate of the total optical thickness was necessary so that the relative optical airmass differences due to sun zenith angle change could be applied. The total optical thickness was computed from

$$ t_\infty(z) = [{}_s\varepsilon(z)/{}_s\varepsilon(\infty)]\cos\theta_s. \qquad (24) $$

The sun irradiance out-of-the-atmosphere ${}_s\varepsilon(\infty)$ was obtained from the mean value in Table 1 for each passband, times the square of the ratio of the solar diameter ψ for each date to the mean solar diameter

$$ {}_s\varepsilon(\infty) = \overline{{}_s\varepsilon(\infty)}(\psi/\bar{\psi})^2. \qquad (25) $$

Flux Error Estimate. The above procedures forced the downwelling irradiance computed from the scanner radiances to be equivalent to the downwelling irradiance as measured by the irradiometer. This insured the

appropriateness of the scalar sky irradiance computed from the scanner values. The portion of the total scalar irradiance contributed by the terrain scanner had no such forcing. An estimate of that error was computed.

Appendix G

The proportional error P contributed by the upwelling flux to the total flux was assumed to be equivalent to the scalar albedo ${}_sA$ (the ratio of the upwelling scalar irradiance to the downwelling scalar irradiance); times the ratio of the upwelling irradiance ${}_cE(z,u)$ (computed from the scanner radiances) divided by the upwelling irradiance (from the irradiometer), minus one

$$P = {}_sA\,[{}_cE(z,u)/E(z,u) - 1]. \qquad (26)$$

The average proportional error to the total flux contributed by using the upwelling scalar irradiance computed from the terrain scanner radiances was 0.009, STD 0.020.

Absorption Optical Thickness Values

Use of Eq. (14) to obtain absorption optical thickness assumes an instant in time and measurements differing in position only vertically. Thus the atmosphere had to be homogeneous along the flight track and stable over the period of the data measurement sequence for the results to be reasonable.

Various tests were used to indicate homogeniety and stability during the entire flight. First, absorption thickness values for the primary haze layer must be positive for all passbands (flights C181, C182A, C183B, C185B, C186A and C187A did not pass this test). Second, small negative values for the secondary haze layer were acceptable but not large negative values of absorption optical thickness (flight C185A had large negative values). Third, absorption values for the primary haze layer should be generally larger than the absorption values for the secondary haze layer (flight C188A did not pass this test). Fourth, the total optical thickness values obtained using Eq. 24

should make sense spectrally and should compare reasonably to the sum of the total scattering optical thickness from the nephelometer values and the absorption optical thickness from Eq. 14 (flight C187B failed this test).

Five flights passed all four tests, and two of these flights passed all the tests for both the primary and the secondary haze layer. The other three had one or more small negative absorption values for the secondary haze layer. The absorption optical thickness values for the primary haze layer are depicted in Fig. 5 for these five flights.

Figure 6 shows the absorption optical thickness values for the two flights where reasonable values for the secondary haze layer were obtained. The values for the primary layer are denoted by x, the secondary layer by o and the total flight altitude interval by *. Note the change in scale from Fig. 5. The altitudes of measurement for the haze layers for these flights are given in Table 2.

Single Scattering Albedo. The single scattering albedo $w_{\Delta z}(z)$ for each haze layer and the total altitude interval was computed from

$$w_{\Delta z}(z) = {}_{s}t_{\Delta z}(z)/[{}_{s}t_{\Delta z}(z) + {}_{a}t_{\Delta z}(z)]. \qquad (27)$$

Eq. 27 is a further development of the effective single scattering albedo in Ref. 1 allowing the concept to apply to any altitude interval. The values for the primary haze layer are graphed as a function of the mean wavelength of the passbands in Fig. 7. The single scattering albedo for both haze layers individually and in sum is given in Fig. 8 for flights C183A and C186B.

Values of the single scattering albedo should be more useful than the actual values of absorption optical thickness. The absorption optical thickness is directly affected by variations in the altitude interval Δz, and the pressure and temperature (or density) profile with altitude within that interval. In contrast, the single scattering albedo has these differences

factored out by being a ratio to the total optical thickness.

Aerosol Absorption Optical Thickness

Aerosol absorption optical thickness is expected to be relatively neutral spectrally.

Appendix G

For the secondary haze layer we can probably assume that absorption for the filter 2 passband (effective passband 468 to 488 nm) is aerosol absorption. This passband lies in the spectral region 365 to 540 nm which is essentially free from gaseous absorption except for the ozone and NO_2 continua for atmospheric optical thickness measurements. Ozone and NO_2 continua absorptions are in the spectral region of the filter 2 passband as noted in Table 1. However, ozone and NO_2 are primarily in the boundary layer (primary haze layer) or above the troposphere. Therefore the effect of these continua can probably be neglected for the secondary haze layer.

Note that the secondary haze layer absorption values in Fig. 6 are relatively neutral spectrally. We can probably assume that the absorption in the secondary haze layer for these two flights is primarily aerosol absorption for all three passbands. The two passbands above 540 nm were narrow enough and so placed in the spectrum (filters 4 and 3 effective passbands 518 to 596 and 649 to 679 respectively) that they miss the strong O_2 absorption bands at 630 and 690nm. All the secondary haze layers and above were cloud free, so that H_2O vapor which might affect the passbands for filters 4 and 3 would be at a minimum.

The higher absorption optical thickness values in the primary haze layers for the passbands for filters 4 and 3 compared to filter 2 can be expected to be heavily due to gaseous absorption from H_2O plus various pollutents. However the absorption values for the filter 2 passband would probably include NO_2[16] and ozone absorption. Therefore aerosol absorption for the

primary layer and the total altitude interval are probably less than the total absorption for the filter 2 passband in each case.

Aerosol Single Scattering Albedo. Let us assume that the total absorption values for all three passbands are a reasonable indication of aerosol absorption for the secondary haze layer. Using this assumption, we computed the aerosol single scattering albedo from

$$_{M}w_{\Delta z}(z) = {}_{M}t_{\Delta z}(z)/[{}_{M}t_{\Delta z}(z) + {}_{a}t_{\Delta z}(z)]. \quad (28)$$

These are given in Fig. 9 for the two flights with valid absorption values for the secondary haze layer.

Appendix G

4. CONCLUSIONS

This two part article series used new methods for recovery of aerosol scattering and absorption optical thickness on available optical data. The first paper used a data base of ground-based measurements made during optically stable days that were optically thinner than a standard clear day[1]. This second paper used a data base consisting of airborne data for a polluted atmosphere near a large metropolitan area. Both were visible spectrum data sets but employed different instruments, passbands and data collection procedures.

Actual values of absorption optical thickness for through the atmosphere (first data set) and for the primary and secondary haze layers (second data set) were obtained, a unique accomplishment. Previous through-the-atmosphere research isolated the aerosol effect as a combination of aerosol scattering and aerosol absorption. In the first article we were able to derive aerosol scattering optical thickness in addition to total optical thickness and therefore obtain absorption optical thickness. Previous troposphere researchers[17] determined the flux divergence (change in net flux with altitude) as an indicator of absorption but did not obtain actual absorption

optical thickness values. In the second data set, by having a total scalar irradiance value concurrent with flux divergence, a direct measure of total absorption optical thickness was obtainable.

The absorption recovery technique used in the second data set is limited to the visible spectrum or shorter wavelengths but may be used for broad or narrow passbands. Longer wavelengths require an emission term[18].

In the first article (first data set) we found aerosol absorption could be significant even on some days of greater transparency than the average clear day. For the second data set (urban pollution), we were able to obtain a reasonable value of aerosol absorption for the secondary haze layer but not for the primary haze layer. Further knowledge of the types and amounts of polluting gases present would be needed to obtain an aerosol absorption value for the primary layer. Use of judiciously selected narrow passbands would aid in the identification of these gases and consequent isolation of the aerosol absorption optical thickness.

The Angstrom equation was further modified to describe the aerosol scattering optical thickness for any altitude interval. For both data sets, we found that the natural log of the constant was a linear function of the slope. This relationship only becomes apparent when the scattering and absorption of aerosols are separated. The relationship in the classical Angstrom equation, which relates the total aerosol optical thickness to wavelength, is distorted by the inclusion of the aerosol absorption optical thickness.

An alternate form of the Angstrom equation was developed;

$$c' = (\ln_M t_{\Delta z}(z) - b)/(m + \ln\lambda), \qquad (10)$$

where b and m are invariant. Thus a measurement of aerosol scattering optical thickness at one wavelength will predict the slope c' and allow a prediction

of aerosol scattering optical thickness at other wavelengths. An important question to be asked is, how general is the relationship? Do dust, smoke, and salt nuclei of marine air also fit this modified Angstrom equation for aerosol scattering optical thickness?

The two data sets together encompass a large range of optical thickness and appear to define a relationship which is invariant whether the aerosol scattering optical thicknesses are for the entire atmosphere or for a haze layer or two. The methods of measuring the optical thicknesses for the two data sets are completely different. The passbands used are not equivalent although they encompass about the same portion of the visible spectrum. The data are limited to passbands with mean wavelengths between 459 and 664 nm but the results should apply to the entire visible spectrum 400 to 700 nm.

ACKNOWLEDGMENTS

The data analyses and writing of this article were done at Viz. Ability, Inc. under U. S. Army Research Office contract no. DAAG29-84-C-0014. I wish to thank Judith Olson for technical writing and editing assistance.

I wish to thank R. W. Johnson and the Visibility Laboratory for making the data base, early technical notes, pictures and sketches available for the data analysis and this article. The original data were collected by the Visibility Laboratory for the U. S. Air Force Geophysics Laboratory.

Appendix G

REFERENCES AND FOOTNOTES

1. J. I. Gordon, "Aerosol scattering and absorption optical thickness I. From ground-based measurements during optically stable clear days," submitted to Applied Optics.

2. S. A. Changnon, F. A. Huff and R. G. Semonin, "METROMEX: an investigation of inadvertent weather modification," Bull. Amer. Meteor. Soc. 52, 958-967 (1971).

3. S. Q. Duntley, R. W. Johnson and J. I. Gordon, "Airborne measurements of optical atmospheric properties in southern Illinois," University of California at San Diego, Scripps Institution of Oceanography, Visibility Laboratory, SIO Ref. 73-24, AFCRL-TR-73-0422 (1973).

4. S. Q. Duntley, R. W. Johnson and J. I. Gordon, "Airborne and ground-based measurements of optical atmosphereic properties in southern Illinois," University of California at San Diego, Scripps Institution of Oceanography, Visibility Laboraory, SIO Ref. 74-25, AFCRL-74-0298 (1974).

5. S. Q. Duntley, A. R. Boileau, and R. W. Preisendorfer, "Image Transmission by the Troposphere I," J. Opt.Soc. Am. 47, 499 (1957).

6. W. G. Driscoll and W. Vaughan, Eds., Handbook of Optics (McGraw-Hill, New York, 1978).

7. R. W. Austin, "Techniques of measurement" Section VII in "Visibility" by Duntley, et al. App. Opt. 3, 584-587 (1964).

8. J. I. Gordon and R. W. Johnson, "Integrating nephelometer: theory and implications," Appl. Opt. 24, 2721-2730 (1985).

9. J. M. Prospero, R. J. Charlson, V. Mohnen, R. Jaenicke, A. C. Delany, J. Moyers, W.Zoller, and K. Rahn, "The Atmospheric Aerosol System: an Overview," Rev. Geophys. Space Phys. 21, 1607-1629 (1983).

10. U. S. Standard Atmosphere, 1976 (Superintendent of Documents, U.S. GPO, Washington, D.C. 20402, 1976).

11. A. Angstrom, "On the atmospheric transmission of sun radiation and on dust in the air," Geogr. Ann., 11, 156-166 (1929).

12. M. Eqbal, An Introduction to Solar Radiation (Academic Press, New York, 1983) p. 118.

13. J. I. Gordon, "Some implications of the equation of transfer," J. Opt. Soc. Am. A, 3, 274-283 (1986).

14. J. I. Gordon and R. W. Johnson, "Equilibrium radiance model applications and comparisons to atmospheric measurements and Rayleigh models," App. Opt. 23, 3363-3372 (1984).

15. The empirical expression for airmass was taken from F. Kasten, "A New Table and Approximation Formula for the Relative Optical Air Mass", Arch., Met. Geophys. Bioklim. B14, 206-233 (1965).

16. The NO_2 burden for the total atmosphere varies from 0.0004 to 0.005 cm according to G. E. Shaw "Nitrogen dioxide-optical absorption in the visible," J. Geophys. Res. 81, 5791-5792 (1976).

17. F. P. J. Valero, W. J. Y. Gore, and L. P. M. Giver, "Radiative flux measurements in the troposphere," Appl. Opt. 5, 831-838 (1982).

18. See Eq. 26 in Ref. 13.

Appendix G

Table 1 Spectral characteristics summary for airborne passbands.

Filter	Spectral Characteristics: Peak Wavelength (nm)	Mean Wavelength (nm)	Effective Passband (nm)	Solar Irradiance Out-of-Atmosphere ($W/m^2 \mu m$)	Rayleigh Scattering Coefficient (0,15°C) (per km)	Ozone Absorption Optical Thickness (per 0.1cm)	NO_2 Absorption Optical Thickness (per 0.001cm)
2	475	478	19.9	2140	0.0207	0.00166	0.0098
4	550	557	78.5	1900	0.0115	0.00893	0.0012
3	660	664	30.2	1570	0.00541	0.00052	0

Table 2 The measurement altitudes and altitude intervals for the haze layers for which absorption optical thicknesses were obtained.

Flight	Primary Haze Layer: Lowest Altitude	Primary Haze Layer: Interval	Secondary Haze Layer: Lowest Altitude	Secondary Haze Layer: Interval
Number	(km)	(km)	(km)	(km)
C180	0.10	1.29		
C182B	0.09	1.29		
C183A	0.12	1.16	1.28	1.23
C186B	0.20	1.20	1.40	1.20
C188B	0.23	1.19		

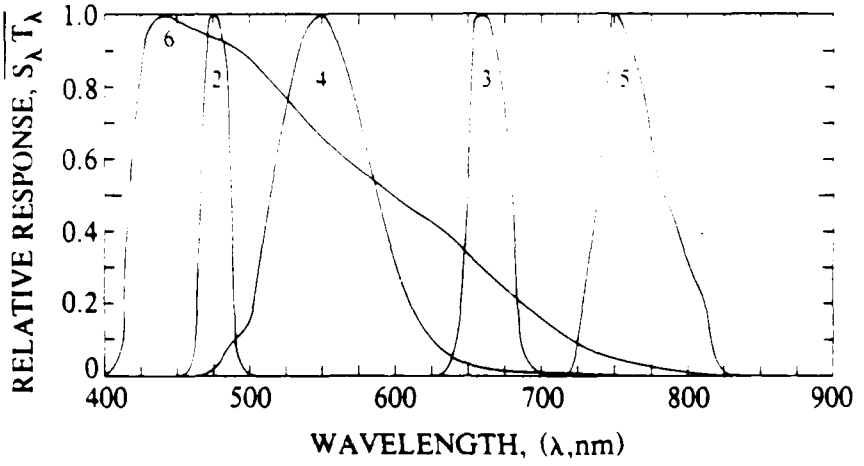

Fig. 1 Relative spectral response of the three passbands.

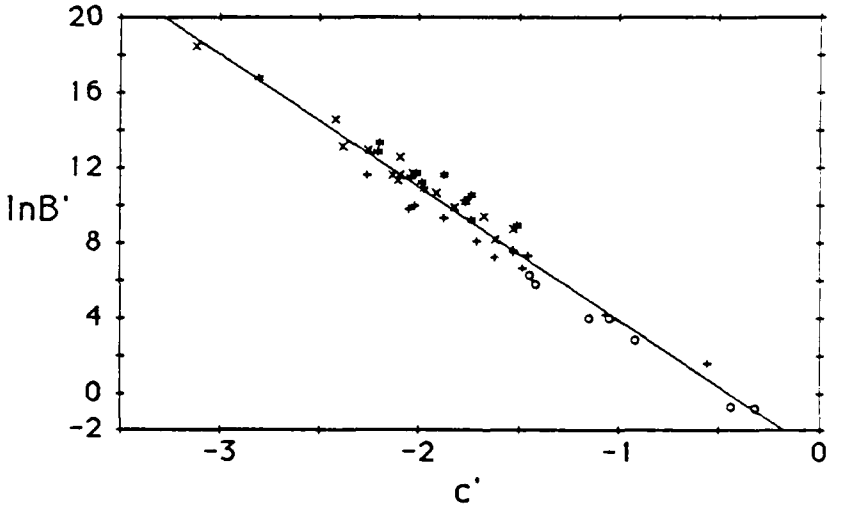

Fig. 2 Relationship of the Angstrom constant (ln B') to the slope or power c' for aerosol scattering optical thickness values in the visible spectrum, $\ln \tau_{M,\Delta z}(z) = \ln B' + c' \ln \lambda nm$. Data from Ref. 1 are shown as circles, airborne data from data set 2 are shown as + for the primary haze layer, x for the secondary haze layer, and * for the combined altitude interval measured. The line is from the equation lnB' = -3.243 -7.108c'.

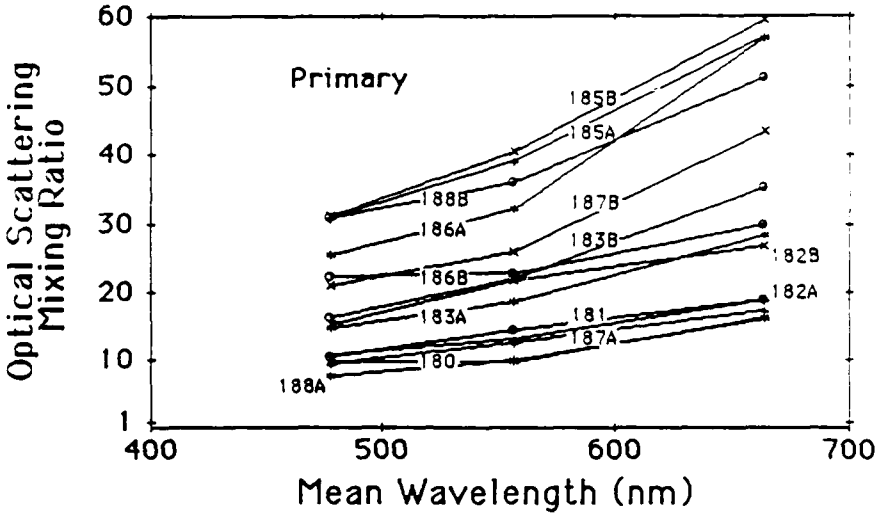

Fig. 3 Optical scattering mixing ratio $Q_{Az}(z)$ as a function of passband mean wavelength for the primary haze layer.

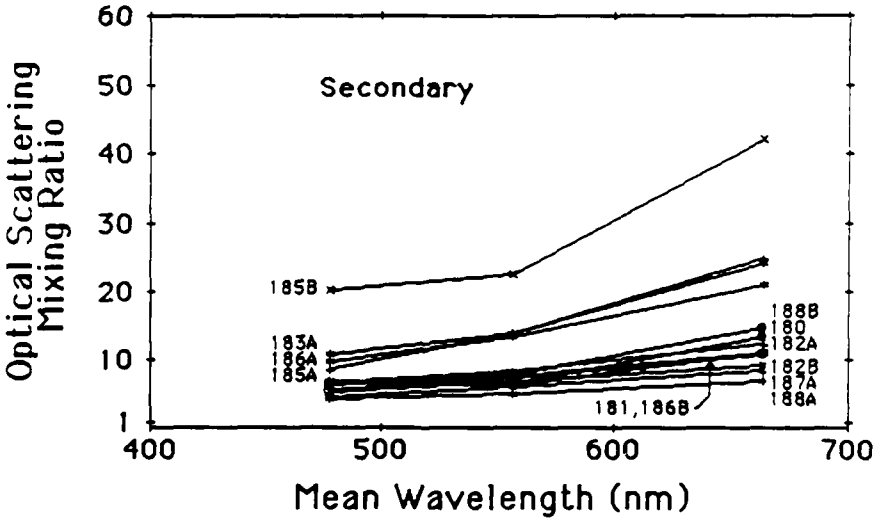

Fig. 4 Optical scattering mixing ratio $Q_{Az}(z)$ as a function of passband mean wavelength for the secondary haze layer.

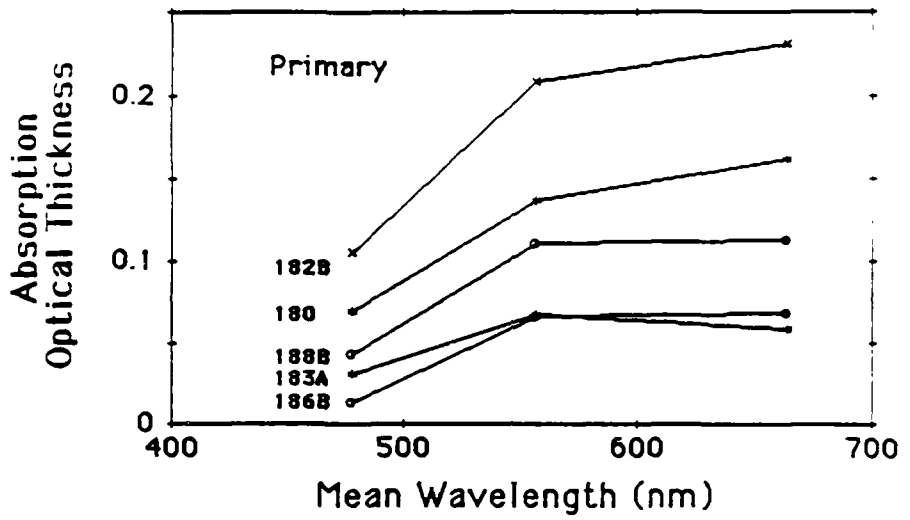

Fig. 5 Absorption optical thickness $\Delta\tau_{a\Delta z}(z)$ as a function of passband mean wavelength for the primary haze layer for five flights.

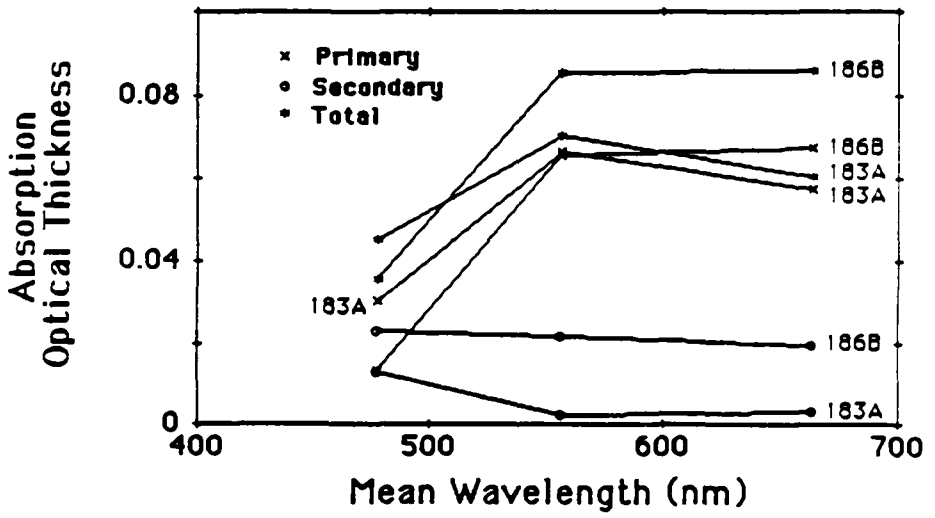

Fig. 6 Absorption optical thickness $\Delta\tau_{a\Delta a}(z)$ as a function of passband mean wavelength for the primary x, secondary o, and total altitude interval * for two flights.

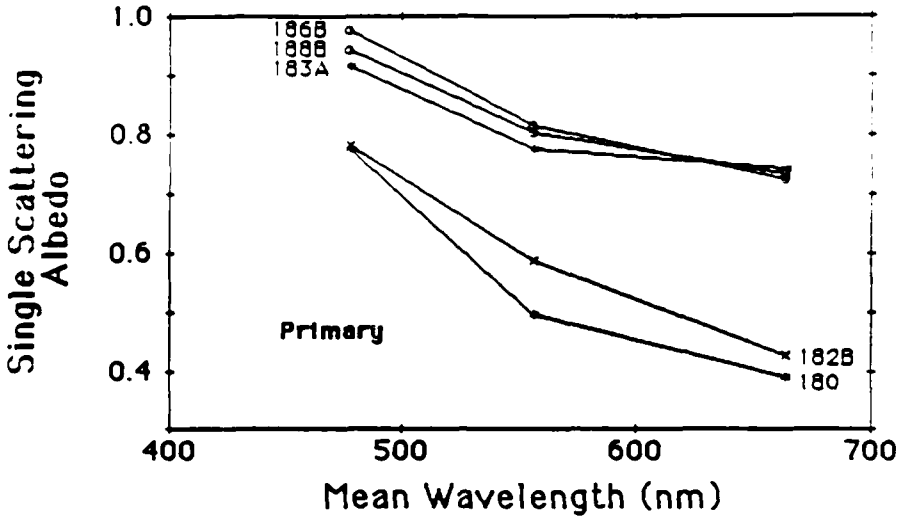

Fig. 7 Single scattering albedo $w_{\Delta z}(z)$ as a function of passband mean wavelength for the primary haze layer for five flights.

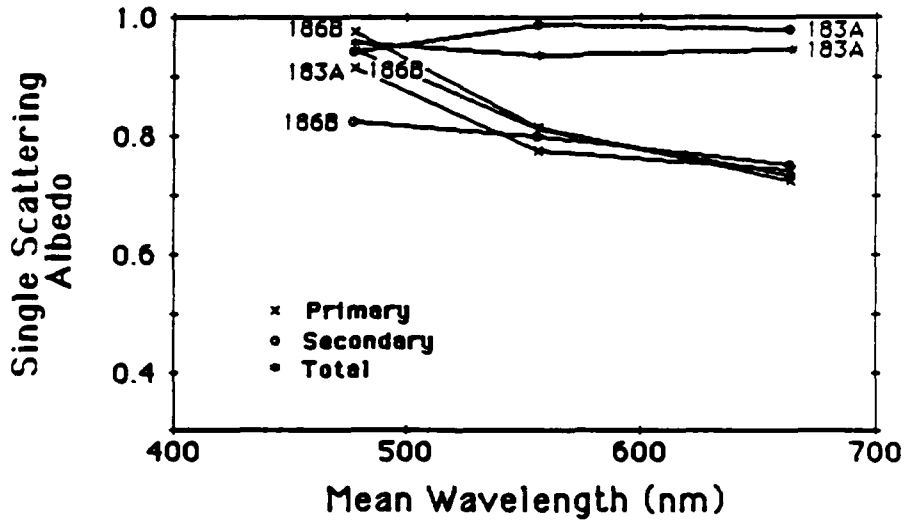

Fig. 8 Single scattering albedo $w_{\Delta z}(z)$ as a function of passband mean wavelength for the primary haze layer x, secondary haze layer o, and total altitude interval * for two flights.

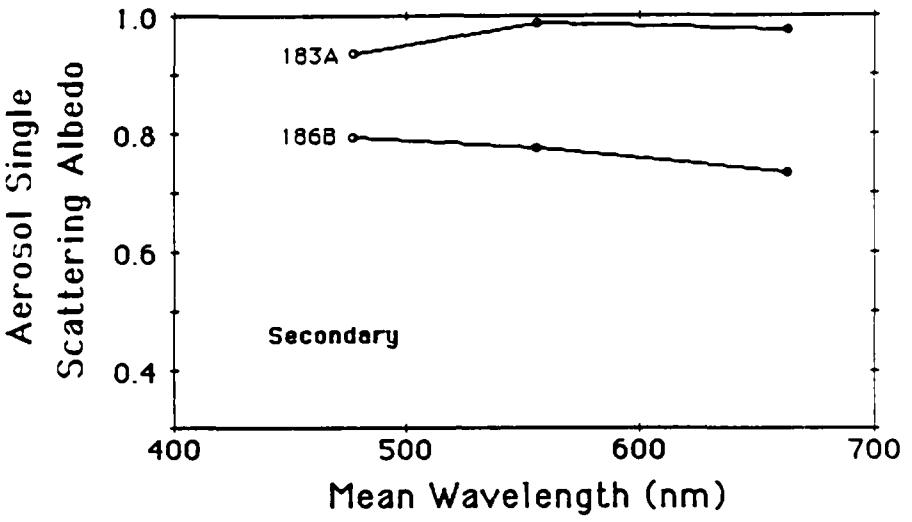

Fig. 9 Aerosol single scattering albedo $_{M}w_{Az}(z)$ as a function of passband mean wavelength for the secondary haze layer for two flights.

FMD

5-87

DTIC